CORRELATING LOST CIRCULATION MATERIALS' SIZE AND SHAPE WITH SEALING EFFECTIVENESS IN A LAB SETTING

By

Walter H. Baker

A thesis submitted to the Faculty and the Board of Trustees of the Colorado School of Mines in partial fulfillment of the requirements the degree of Master of Science (Petroleum Engineering).

Golden, Colorado

Date ______________________________

Signed: ______________________________
Walter H. Baker

Signed: ______________________________

Alfred William Eustes, Ph.D.
Thesis Advisor

Golden, Colorado

Date ______________________________

Signed: ______________________________

Jennifer L Miskimins, Ph.D.
Professor and Head
Department of Petroleum Engineering

ABSTRACT

The uncontrolled loss of fluid during drilling operations has been an existing and costly issue throughout the history of the Oil and Gas industry. The cost and frequency of lost circulation (LOC) events is exacerbated when drilling through producing and depleted plays while exploring deeper source rock. The severity of LOC events varies in scale as a function of drilling fluid rheology, density, wellbore and pore pressure, and rock properties. Fluid loss may occur in pore space, fractures (occurring naturally or induced), or subsurface caverns. The most often severe or “total loss” events typically occur in the natural and induced fracture intervals.

Currently the industry lacks common testing data and practices to engineer mitigation techniques to address these lost circulation events, specifically losses in fracture networks (induced and natural).

The purpose of this research is to provide size, shape and testing data using common lost circulation materials found in the field. Materials were provided by major oil and gas service companies. A lost circulation study laboratory was created on the main Colorado School of Mines campus. In this lab setting, particle size and shape data were gathered using a combination of sieving and image analyses. Slot testing was completed using an automated plugging and permeability device, provided lost circulation materials, and a pre-designed fluid or “mud” system. Material testing successes were determined by measuring fluid loss at pressure, through standard slot sizes. Testing results were compared to the size and shape data previously gathered.

When comparing size and shape data to sealing pressures, common material characteristics were identified in their overall sealing effectiveness. Comparing materials physical properties and using our current understanding of fracture conductivity, it became apparent that a material blend's sealing effectiveness was directly related to its combined ability coarse materials to create a stable infrastructure fine fibrous material. The study results should supplement lost circulation materials design and engineering material blends in tailored applications.

TABLE OF CONTENTS

LIST OF FIGURES

LIST OF TABLES

LIST OF SYMBOLS

General Nomenclature

P_m .... Mud Pressure

P_t .... Pressure at fracture tip

P_p .... Pore Pressure

P_w .... Wellbore Pressure

S_H .... Maximum far-field horizontal stress

S_{hmin} .... Minimum far-field horizontal stress

E .... Elastic modulus

v .... Poisson's ratio

L .... Fracture Length

R.......... Wellbore Radius

x .... Distance from the center of the wellbore

R_{fluid} .... Fluid-filled fracture length

R_{cake} .... Length of mud cake

R_{tip} .... Length of fracture tip without mud invasion

M_{CSD} .... Cumulative measured material mass at a mesh size

M_{CS0} .... Cumulative measured material mass at a previous mesh size

M_S .... Measured material mass at a mesh size

M_T .... Total measured material mass

LIST OF ABBREVIATIONS

APPA .... Automated Plugging and Permeability Apparatus

CSDF........ Chemical Storage Distribution Facility

ECD .... Equivalent Circulating Density

EMW........ Equivalent Mud Weight

FCS .... Fracture Closure Stress

FIP........ Fracture Initiation Pressure

g .... Gram

HSE .... Health, Safety, and Environment

LCM........ Lost Circulation Materials

LOC .... Lost Circulation

mL........ Milliliter

mm .... Millimeter

MW .... Mud Weight

NFP .... Net Fracture Pressure

NPT........ Non-Productive Time

ppb .... Pounds per Barrel

PSD .... Particle Size Distribution

PS_hD........ Particle Shape Distribution

psi........ Pounds per Square Inch

SDS .... Safety Data Sheet

TOC .... Top of Cement

µm........ Micrometer

ACKNOWLEDGMENTS

I would like to acknowledge the support of my advisor Alfred William Eustes, Ph.D and committee members Jennifer L Miskimins, Ph.D and Jorge Sampaio, Ph.D. Funding and materials were provided by Apache Corporation. Lab facilities at Colorado School of Mines were used in the work described.

CHAPTER 1: INTRODUCTION

Considerable time, capital, and resources have been spent attempting to address and mitigate lost circulation events in oil and gas drilling operations. The unplanned loss of drilling fluids into a formation bears significant tangible and intangible costs. These time and material costs have grown with increased well depth, reservoir depletion, and the considerable costs of modern drilling fluid systems.

Using hydraulic fracturing, operators are exploring new vertical depths in pursuit of reserves in low permeable source rock. In seeking these deeper targets, operators face the challenge of drilling through previous conventional targets that are often depleted from historic production. Considering lost circulation (LOC) is a result of hydraulic overbalance in an open wellbore, in terms of reservoir pressure, these events are exacerbated by reservoir depletion. Consequently, as current conventional reservoirs continue to produce, and operators continue to seek deeper unconventional source rock, the scale and frequency of uncontrolled fluid loss events is expected to intensify.

The severity of LOC events varies in scale as a function of drilling fluid rheology, density, wellbore and pore pressure, and rock properties. Fluid loss may occur in pore space, fractures (occurring naturally or induced), or subsurface caverns. Losses into pore space are typically the least severe and are relatively straightforward to treat. Such losses, often referred to as *seepage,* have been successfully treated and mitigated using high compressive strength granular materials. These lost circulation materials (LCM) are chosen/engineered using average particle sizes that are matched to average pore-opening width. Pore opening sizes are estimated using either local core samples or empirical lithology correlations. Figure 1.1 illustrates standard expected pore size distributions based on lithology.

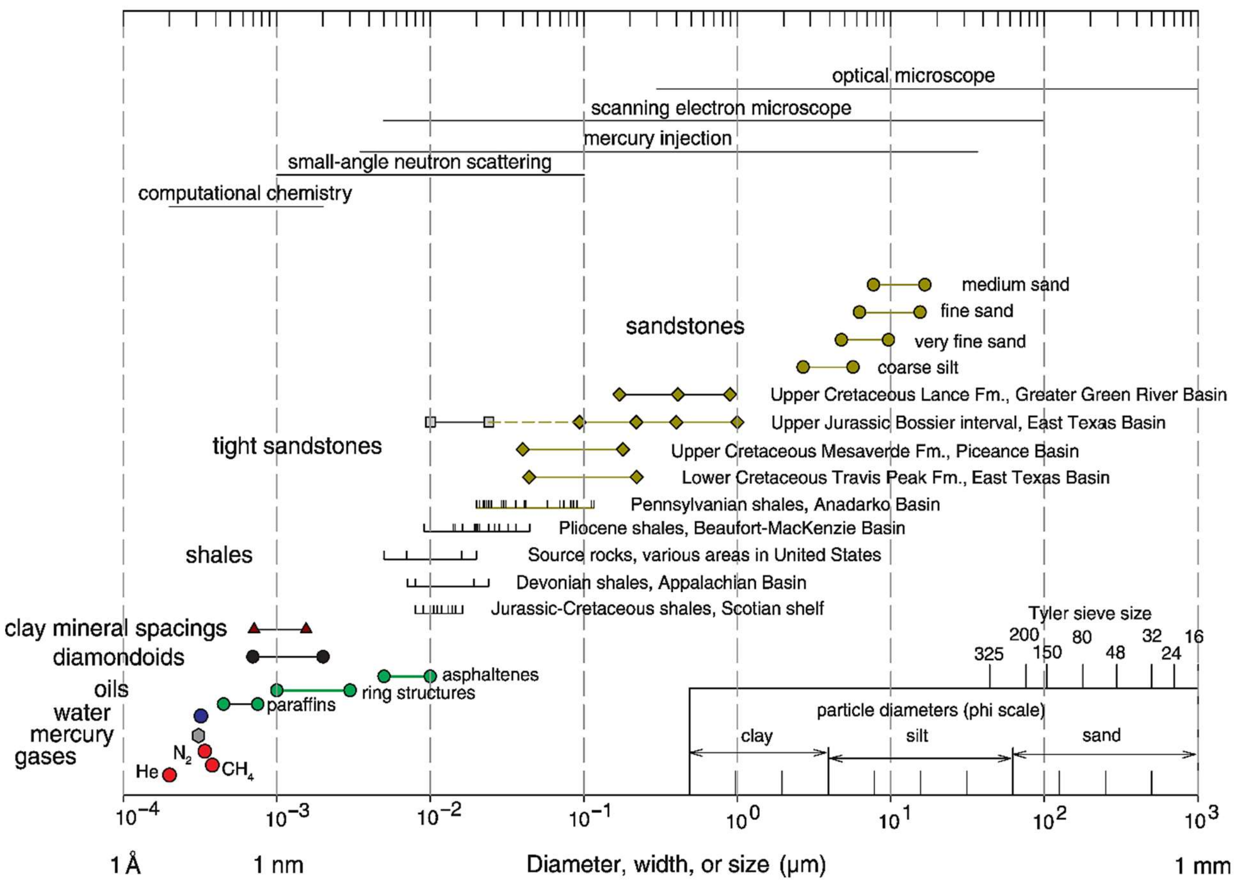

Figure 1.1 Measured and calculated pore size distributions found in conventional tight sandstones and shales. Source: Nelson (2009).

Losses into fractures are known to be severe and difficult to treat. To successfully mitigate fracture losses, materials and blends must be engineered to construct a high-pressure seal that prevents further pressure/fluid communication. Figure 1.2 depicts primary loss categories in the order of severity.

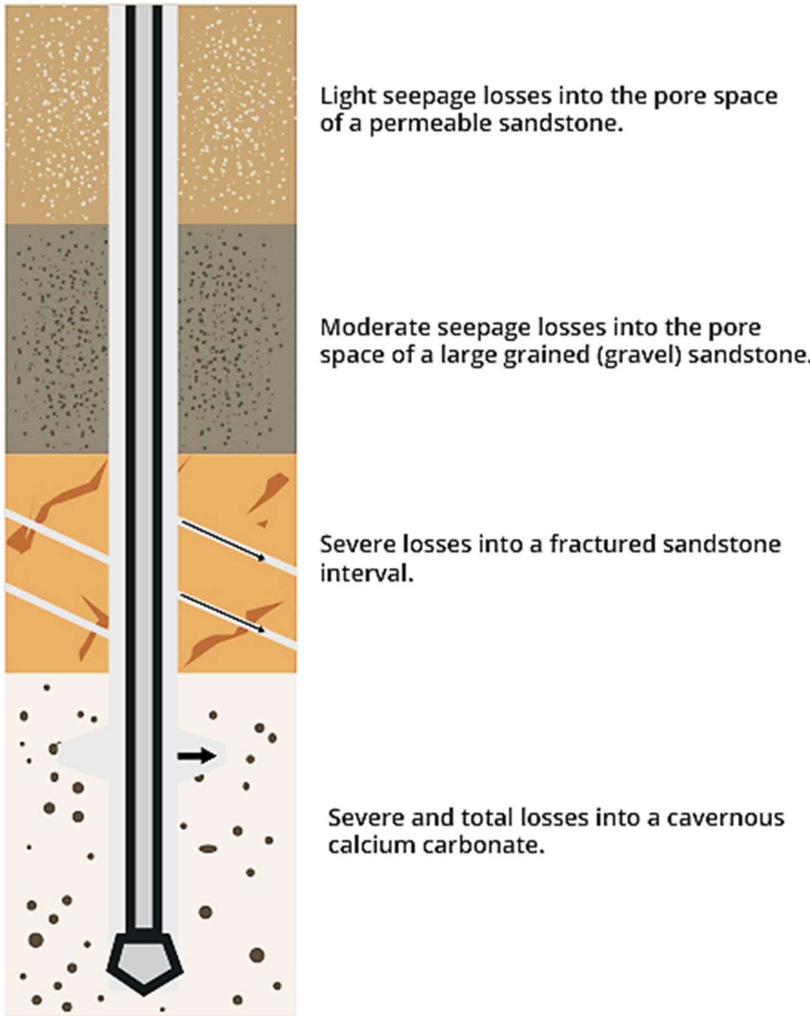

Figure 1.2 Primary loss categories in the order of severity encountered in different environments.

The aim of this study was to address drilling fluid losses in natural and induced fractures by documenting the physics observed during these events and analyzing the materials available to address them. To understand the current status of this problem in academia and industry, academic courses were taken and a relevant review of the literature was completed. To effectively provide a tangible, material solution to this studied issue, a particle analysis was completed on several industry-available LCM and the measurements were compared to sealing performance testing results conducted in the Colorado School of Mines Apache Drilling Research Laboratory.

1.1 Motivation: Industry Cost of Losses

Drilling costs remain a primary consideration in the economic evaluation of the single well to field development evaluations. These costs can be broken down into can be categorized by time-based or material (Rahil 2007). Unfortunately, LOC events have added billions to these drilling costs globally (Al Maskary et al. 2014). Tangible and intangible drilling costs associated with LOC are discussed further in this chapter.

1.1.1 Drilling Fluid

As previously discussed, fluid losses take place when fluid is effectively lost to a drilled formation. The material cost of a LOC event is a function of the cost to build the drilling fluid system. In this study, *drilling fluid* or “mud” describes the fluid used for cuttings transport, physicochemical functions, cooling and lubricating the bit, pressure control, drill string and casing weight support, optimize logging efforts and fluid-loss control (Mitchell and Miska 2011). Each fluid system varies in the chemistry of additives, continuous and discontinuous phases, level of sophistication, and price. Higher-performance–unconventional-fluid systems have been used successfully to treat a myriad of wellbore stability challenges ranging from shale reactivity to salt erosion. In areas with a high risk of fluid loss, these more complex systems can add significant costs or be avoided entirely. When drilling in a high-risk LOC area, a widespread practice is to use a cheaper sacrificial water-based fluid system or “junk mud”. The avoidance of using a more sophisticated oil-based system can have performance and well integrity consequences (Patel et al. 2021).

1.1.2 Well Design: Casing Points

Instead of using an engineered fluid system to address wellbore instability, losses, and improve drilling performance, intermediate casing strings are run to cover and isolate problematic intervals. Adding a casing string to a well design results in a multitude of costs. These costs are primarily a function of time needed to run casing, wellhead, and casing materials. Opportunity costs are accrued due to an effective reduction in final production casing size. (Wang et al. 2007)

1.1.3 Cement

Cement begins as a fluid or *slurry* before setting up. Unfortunately, like drilling fluids, it can be lost into highly fractured or cavernous formations. To alleviate that problem, operators may add LCM to the slurry. In exceptional conditions, operators will cement in multiple stages and/or complete a “top off” job. Multiple-stage cementing is significantly more expensive than traditional single-stage cementing, and unfortunately, it is often a last resort to effectively isolate a loss interval. Using downhole packers, a zone can be isolated to get a desired top of cement (TOC). A top-off job is completed in areas where severe losses occur, and it is necessary to have TOC at the surface. Top-off jobs require a small string to be run behind casing to the current TOC and pump cement to literally top-off the cement to surface. This procedure, like multi-stage cementing, is costly in time and materials (Vasquez et al. 2022).

1.1.4 Well Control and Integrity

In a LOC event, the loss of fluid in the wellbore will reduce the equivalent mud weight (EMW) acting on the wellbore. The reduction of EMW is a function of total volume lost and the mud weight (MW) of the system.

Losses taken in a permeable and depleted zone may effectively reduce the EMW below pore pressure in another over-pressured zone, which may cause the well to flow and create a well control event. Prevention of well control events has been a primary health, safety, and environment (HSE) concern when drilling productive over-pressured reservoirs. Mechanical borehole instability takes place when wellbore pressure is insufficient to maintain the structural integrity of the formation(s) drilled. Reduction of effective wellbore size caused by a collapse event may lead to packed off drilling assemblies or casing running issues. A failure to run casing to the pre-designed measured depth often occurs with an effective reduction of wellbore diameter.

1.2 Problem Statements

This study focuses on addressing the following two problems facing the oil and gas industry today.

1. Currently, industry lacks the ability to address severe losses reliably and consistently drilling across fractured rock.
2. There is a limited amount of data and information available to organizations experiencing LOC issues, concerning materials that can effectively mitigate and treat losses (i.e., LCM).

Throughout the industry, there appears to be a lack of guiding principles that could evolve into an engineered workflow and lead to successfully mitigating or sealing off severe losses while drilling. When severe losses are experienced, it has been common practice to produce solutions based on empirical evidence or on assumptions made from prior experience in other drilled wells. Unfortunately, the available empirical evidence is often anecdotal and not based on the physical mechanisms behind the losses. The vast multitude of LCM products available—each with its own marketable theory—is evidence the current unstandardized approach. A lack of determined principles based in physics and proven with performance data has left the field of LOC remediation ungrounded.

To begin to address LOC using engineered methods, operators need to have material data available. Current operators may query service companies for particle size distributions using their LCM products. Unfortunately, this information is gathered using non-standard methods that lead to inconsistencies. Particle shape data, when collected, often is considered proprietary and is not made available to the consumer. The lack of, and inconsistency in, currently available LCM data inhibit operators from implementing the optimal blends of LCM in an engineered response of dealing with loss events.

1.3 Study Objectives

The following primary objectives were developed to address the problem statements identified in this study.

- Create and maintain an evolving data set containing size, shape and performance measurements of LCM available in the drilling industry.
- Expand upon the current research of LCM effectiveness by correlating particle size and shape characteristics with aperture sealing performance in a lab setting.
- Using lessons learned in both the field of drilling and hydraulic fracturing, provide real solutions based on the physics of the problem.

CHAPTER 2: LITERATURE REVIEW AND BACKGROUND

This chapter gives a standard study definition to lost circulation, lost circulation material and provides a literature review of study and materials relevant to this thesis.

2.1 Lost Circulation

In this study, *lost circulation (LOC)* is defined as the unplanned loss of drilling fluid to the formation during the well creation process. Unexpected drilling fluid losses occur when drilling equivalent circulating density exceeds the current drilling window and fluid communication with the rock is present. From a fluid loss perspective, the safe drilling window (drilling margin) is limited by the pore pressure and current permeability (pre-fracturing) and the fracture gradient and future permeability (post-induced fracturing).

2.1.1 Lost Circulation Severity

LOC may be observed on a spectrum of severity that ranges from light seepage to total loss. It is the severity and loss behavior over time that provides the first clue into the cause and mechanisms behind the loss event, allowing an engineered response. The following are classifications of different severities of fluid loss based on rate of loss:

- *Seepage Loss (0.01- 0.2 bbl/min)*: Typically, losses take place at the pore and matrix level, occurring in high permeable and unconsolidated sands and/or depleted reservoirs. These losses can be considered a Darcy problem.
- *Partial Loss (0.2 - 1 bbl/min)*: These losses are observed typically in highly permeable formations or when small, natural, and induced fractures are present.

- *Severe Loss (1 - 10 bbl/min)*: Losses can occur where formations with permeable natural fractures present.
- *Total Loss (> 10 bbl/min)*: Massive or total losses can occur in cavernous formations or where deep wide, natural, fractures are present (Beda and Caruga 2001; Dyke et al. 1995).

To characterize target rock, Beda used an electromagnetic flowmeter installed on a standpipe to identify conductive intervals by observing loss behavior trends. Using Beda and Caruga's work, fluid loss behavior can be interpreted or predicted based on expected rock properties. In Figure 2.1 below, flow trend behavior is related to different LOC event causes.

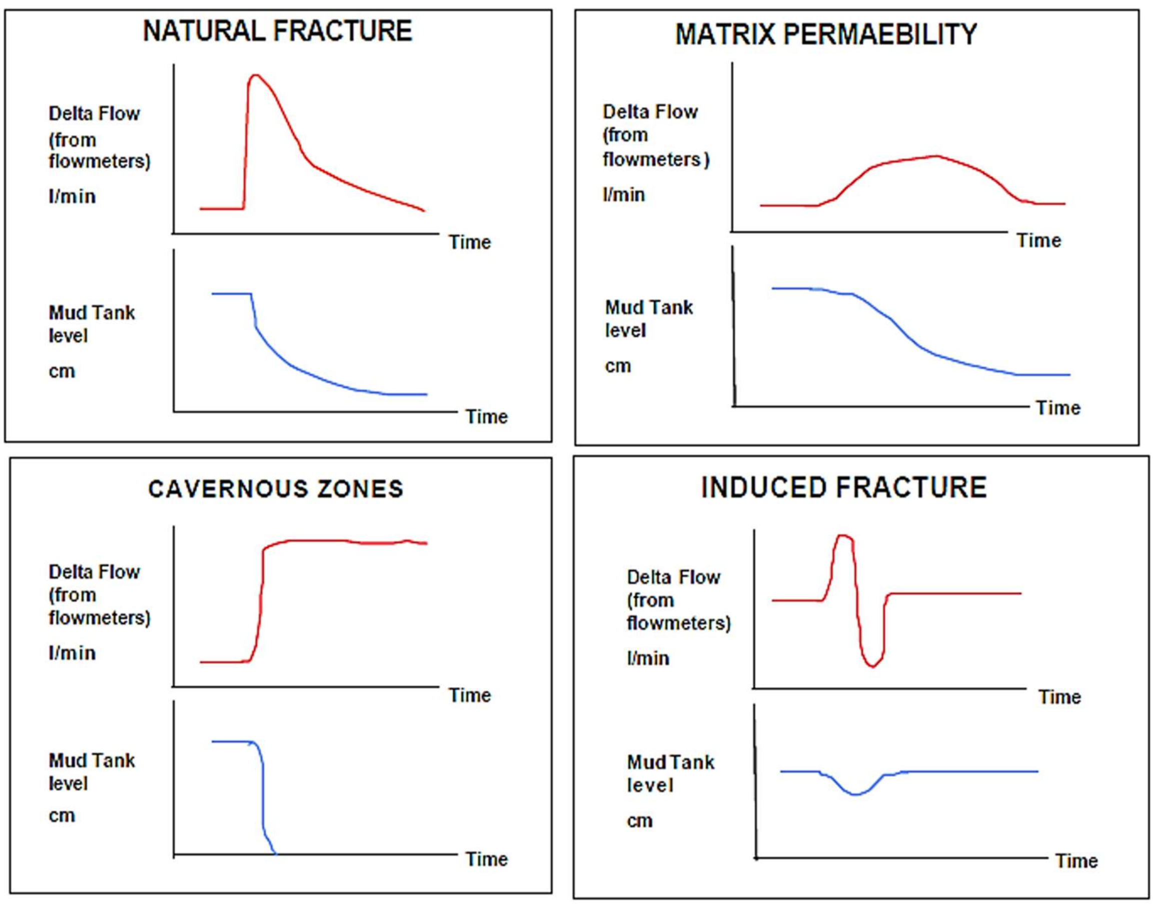

Figure 2.1 Shape of the Delta Flow Behavior different loss events (Beda and Caruga 2001).

Induced fracture losses, like natural fracture losses, are initially drastic. These losses take place when the equivalent circulating density (ECD) of the drilling fluid is higher than the fracture gradient of the formation. Losses tend to occur during downhole pressure surges, such as when mud pumps are turned on or off. However, when the ECD of the drilling fluid becomes lower than the fracture gradient, these fractures begin to close. The closing of the fractures pushes lost drilling fluid back into the wellbore. This phenomenon is known as wellbore breathing. Most reported significant losses tend to take place through existing open fractures (Beda and Caruga 2001). Thus, massive and total losses are a good indicator of permeable natural fractures (Dyke et al. 1995).

2.1.2 Naturally Fractured and Vugular Rock

Losses into natural fractures occur when the ECD is higher than pore pressure or the cementation strength of existing fracture networks. Losses come on suddenly and eventually begin to decline as the bit travels deeper and away while the frac fills with cuttings.

When treating faulted, naturally fractured, or cavernous intervals, the particle size and shape selection importance should be focused on the estimated fracture aperture and should account subsequent induced fracturing. Materials should be designed to seal off these open zones near the wellbore to mitigate risk in communicating with connective fracture or fault systems. The operator should also consider the adjustment to the overall wellbore hoop stresses post-treatment. In the event the losses are correctly sealed, depending on near well stress, induced fracturing may occur. The increase in hoop may induce fractures at tensile weak points at the wellbore, which is why a correct application of LCM should include a diverse material blend to correctly bridge initial frac widths and secondary fractures and fissures.

Unfortunately, naturally open fracture widths are difficult to approximate and are limited currently to offset well logging and core analysis. In the future, the combination of fracture modeling and drilling data may be used to approximate the geometry of natural fractures and caverns.

2.1.3 Drilling Induced Fractures

Drilling-induced fractures occur anytime the wellbore pressure exceeds the local fracture gradient. These fractures are created when the ECD of the drilling fluid increases the wellbore hoop stress to exceed the tensile strength of near wellbore. In this case, historically, the stress cage and fracture closure stress have been implemented successfully. Using sized bridging particulate, fracture tip isolation can occur to successfully screen out an induced fracture. With the fracture screened out, the resulting wellbore compressional forces, induced by width propagation of the original induced fracture, increase overall hoop stress and wellbore resistance to subsequent fracturing. Figure 2.2 shows another example of how stress cage theory works; specifically, it illustrates how fracture width propagation and hoop stress are directly and positively related.

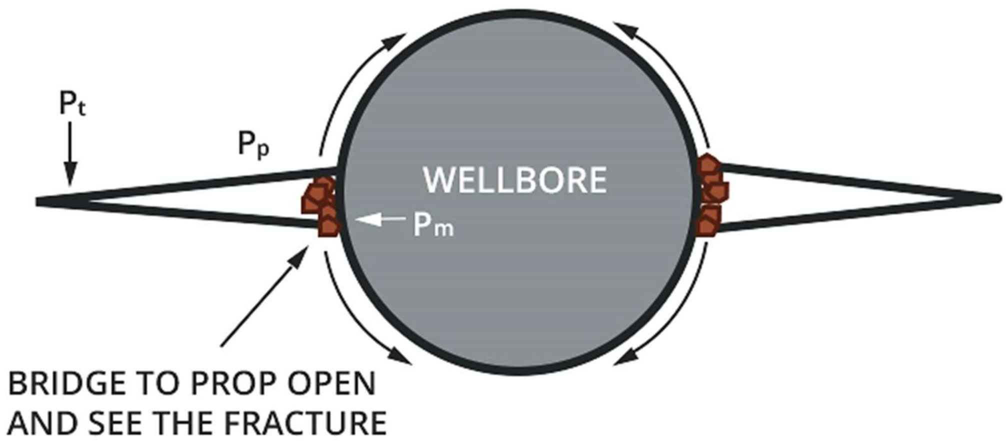

Figure 2.2 Illustration of how the near wellbore experiences compressional forces because of a propped fracture width. $P_m = Mud\ Pressure$; $P_t = Pressure\ at\ fracture\ tip$; $P_p = Pore\ Pressure$; $For\ Stability\ P_t - P_p < P_m$ (Fekete et al. 2013).

2.1.4 Drilling Induced Fractures in Permeable vs. Impermeable Rock

The difficulty with effectively isolating an induced fracture tip is heavily influenced by the permeability of the rock. Leak-off enables a fracture to bleed fluid and pressure to mitigate or halt propagation. This leak-off ability is a direct function of a rock's permeability. A higher fluid efficiency is observed in impermeable rock where leak-off can be negligible, which results in greater fracture propagation. In this environment, LCM should be designed to provide a resilient-close to wellbore pressure seal. A bridge or seal failure in an impermeable (nano-Darcy) interval will result in continuous fracture propagation until hoop stress restricts the growth fracture width and the frictional losses within the fracture reduce fluid pressure at the fracture tip below fracture closure pressure. These propagation limitations have been observed and measured in hydraulic fracturing of current shale plays.

In permeable rocks, bridging material size and characteristics are less important. Leak-off ability provides the necessary bleed off to avoid propagation. In this case, materials can be designed to either seal the aperture of an induced fracture near-wellbore, or to act proppant-like—filling in a fracture and eventually isolating its tip further away from the wellbore (i.e., more locally). This has been demonstrated using finer barite-sized materials in the wellbore strengthening methods practiced in the Gulf of Mexico. The average particle size these fine materials is often designed to match the pore throat of existing rock. The relationship between leak-off ability and sealing material supports both fracture propagation resistance (FPR) and fracture closure stress (FCS) theories (Luzardo et al. 2015).

2.2 Lost Circulation Material

Any solid materials intentionally pumped down a hole to seal and prevent an uncontrolled fluid loss is considered a *lost circulation material* (LCM). Fine materials used as mud cake additives to reduce seepage are also referred to as *filtrate control*. LCM can be divided into three primary shape categories:

1. *Fibrous*: Long and high aspect ratio materials that are often used bridging an aperture. Fibrous bridging materials provide a necessary framework to allow other materials (including smaller fibers and cuttings) to accumulate and eventually create a pressure seal. Some fibrous materials measured in this study were cedar, cottonseed hulls, and synthetic polypropylene.

2. *Granular*: Low aspect ratio and higher roundness materials currently are used to treat seepage. When used in combination with a bridging material, heavy losses can be treated. Granular materials can also be used to promote wellbore integrity/stability when pumped in preventative maintenance sweeps. This can be accomplished by settling in pore throats,

small fractures, and facilitating a screen out. Some granular materials measured in this study were calcium carbonate, graphite, and nutshells.

3. *Flake***:** Thin, flat, granular materials are primarily used as an additive to LCM blends, which already contain granular and fibrous-shaped materials. Flake materials are designed to add particulate shape diversity to inhibit permeability throughout an LCM-laden seal. These materials also can be useful when pumped in a sweep wellbore cleanup (e.g., cuttings). Flakey materials measured in this study were flaked calcium carbonate, mica, cellophane, and wood chips.

Examples of fibrous, granular, and flakey LCM can be observed in Figure 2.3. A second look at flaked calcium carbonate can be seen in Figure 2.4.

Figure 2.3 Depiction of Halliburton product samples. Left: The "Pluggit" sample contains cedar fibers used as a fibrous LCM. Center: The "Wall Nut Medium" sample contains ground nutshells used as a granular LCM. Right: The Baker Hughes "Soluflake" sample contains flaked calcium carbonate used as a flakey LCM.

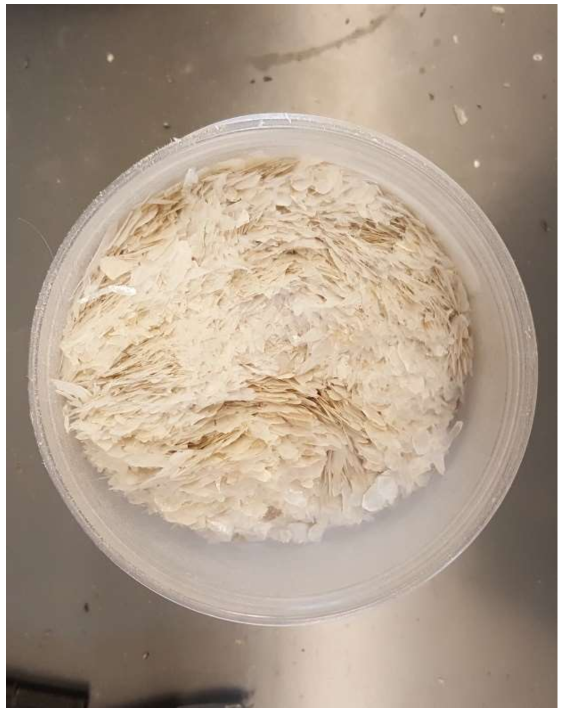

Figure 2.4 Photograph of Baker Hughes' Soluflake (flaked calcium carbonate).

2.2.1 Particle Size Distribution (PSD)

LCM is further categorized by PSD and a determined median size. Like with proppant, PSDs can be used to provide a quick description of an LCM product's material size—the statistical spread those sizes fit engineered applications. In this study, a *particle size distribution (PSD)* is defined as a statistical representation of a material with a known volume—measured particle sizes. PSDs in this study were determined by dry sieving. Specifics regarding the methods and errors associated with these methods are presented in later chapters.

A cumulative PSD can be subdivided into statistical distributions. These distributions represent a point at which a certain percentage of material is either larger or smaller than a specific size. example, in Figure 2.5 the D80 of Steel Seal appears to be approximately 600 µm. This means that 80% of the material's particles (measured by mass) are approximately 600 µm or less in size. As depicted in Figure 2.5, 50% of the particles are equal to or less than approximately 400 µm, giving this product a median (D50) particle size of 400 µm.

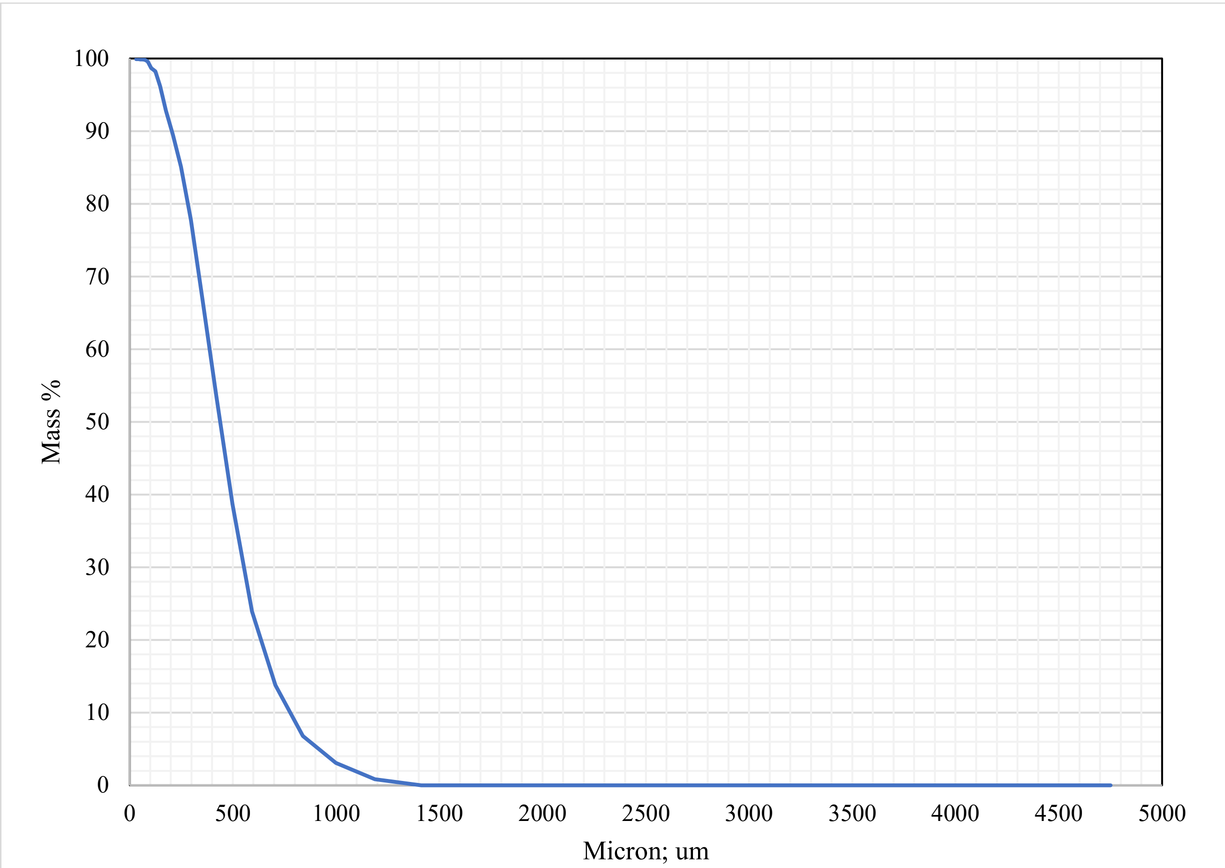

Figure 2.5 Example of a particle-size distribution determined Halliburton's Steel Seal 400 LCM using mass percentage.

Currently, particle-size distributions of LCM can be used to identify and tune material blends to treat particular applications. Specifically, the current customary practice is to attempt to find materials with a median (D50) particle size that are close to the believed aperture needed to be plugged. More advanced theories and models have been created to consider more optimal distributions necessary to seal a known aperture width. Within this study, determined PSDs provide a necessary framework to communicate a more comprehensive particle explanation of each of the studied LCM, including size and shape.

2.3 Wellbore Strengthening

Wellbore strengthening is the attempt to improve drilling windows/margin by using stress modification to enhance the local fracture gradient. Specifically, by altering near-wellbore (hoop) stress, operators can avoid severe losses by mitigating or halting induced fracture growth. The following are related theories and practices currently used and studied in the field. (Mirabbasi 2022)

2.3.1 Stress Cage Theory

Stress cage theory was developed as an attempt to account the successes in the application of fine granular LCM used to widen safe MW windows in the Gulf of Mexico. The basis of the theory is that the implementation of well-sized high strength materials may enable particulates to act as impermeable proppants or seals. Sealing of fractures requires LCM to successfully bridge and plug the fracture opening while net fracture pressure can leak off. The ability of particulate to plug the opening of a fracture requires knowledge of the fracture width and a pre-designed–particle-size distribution of the treatment. With knowledge of fracture width, LCM PSDs can be designed to bridge and plug the multiple scales of permeability within a fracture opening. Figure 2.6 provides a visual of how particulates can begin to bridge and plug a fracture with the correct particle size.

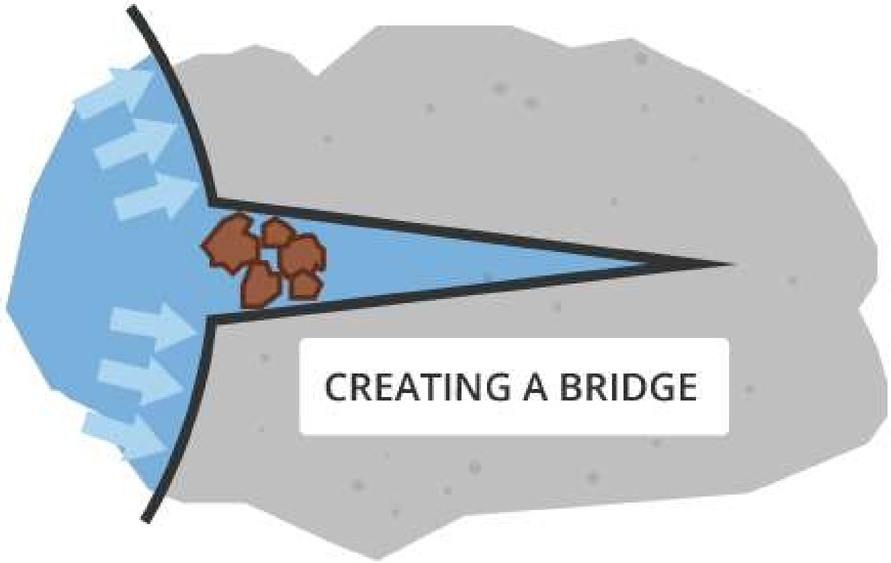

Figure 2.6 Illustration of how sized particles can begin to bridge and plug a fracture opening (Alberty and McLean 2004).

The leak-off ability of the treatment is critical to applying the stress cage theory. Fracture leak off allows two outcomes to take place. The first is the immobilization of the LCM material within the fracture. If the LCM delivery fluid leaks off, it can remain stationary. The second outcome is the depressurization of the fracture past the LCM seal. If the fracture pressure is able to leak off, a successful tip screen-out can take place. If leak-off fails to take place, the fracture may continue to grow or at least stay communicable/open to the reservoir. The compressional stress at the fracture closure is supported by correctly-sized LCM, resulting in higher fracture initiation pressure (FIP). A visualization of how leak-off is related to the successful closing of a fracture is illustrated in Figure 2.7.

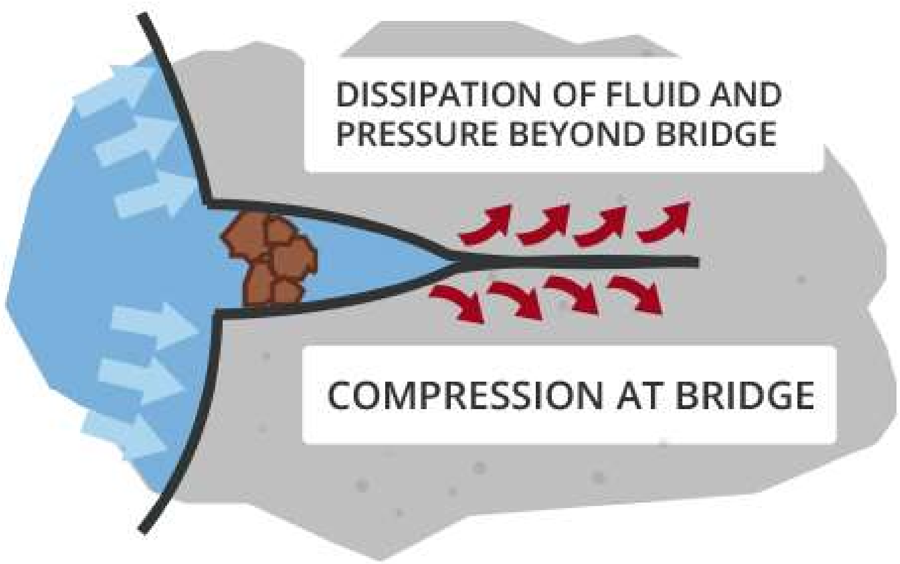

Figure 2.7 Portrayal of the depressurization of the fracture tip due to leak-off, which permits fracture closure and compressional forces at the opening (Alberty and McLean 2004).

The effectiveness of particulate acting as a proppant and seal to bolster wellbore strength is contingent on the inter-angular stresses within the wellbore. The model relies on the presence of new LCM inside the fracture opening, which props and maintains formation load. This new volume of solids is what creates compressional forces near the fracture opening. Changes in the near-wellbore forces is transmitted around the wellbore, which creates hoop stress. Considering rock strength is exponentially higher in compression, the increased compressional load via hoop stress, gives the wellbore strength. Thus, a propped and plugged fracture may increase the local frac gradient or FIP.

Fracture gradients have traditionally been estimated using the Kirsch equations (Scheldt et al. 2020). Typically, because of significantly longer designed fracture lengths and high treatment pressures, fracture models do not consider the wellbore and its hoop stresses. However, the stress cage model developed by Alberty and McLean, uses a variation of a 2D crack equation to calculate fracture width (w) as a function of distance from the center of the wellbore (x)as depicted in Equation 2.1:

Equation 2.1:

$$\frac{4(1-v^2)}{E}(P_w - S_H)\sqrt{(L+R)^2 - x^2} = w(x) \tag{2.1}$$

P_w is wellbore pressure, psi; S_H is the estimated (max) horizontal stress, psi; E is elastic modulus, psi; v is Poisson's ratio; L is the estimated fracture length, ft; R is wellbore radius, ft; and x is the distance from the wellbore center, ft.

The distance from wellbore x can be set to be equal to the wellbore radius (R) to address the fracture width at the wellbore wall. The above crack equation may be suitable induced for fractures given a very small, induced fracture length; however, because the model doesn't account fracture geometries with significant fracture lengths, it appears it will fail in addressing the widths of enhanced naturally occurring fractures.

Stress cage theory does show promise treating losses through fractured rock. Currently materials can be deployed successfully to treat drilling induced fractures by applying bridging material to the estimated fracture width. Further study is needed to model the potential widths of naturally occurring fractures and the ability to screen them out with pre-designed LCM. (Jinsheng et al. 2021)

2.3.2 Fracture Closure Stress

This approach is focused on determining and optimizing *Fracture Closure Stress (FCS)* by using the least pressure required to open a fracture (Nolte and Smith 1981). As with stress cage theory, the primary goal of this method is to successfully improve wellbore integrity by increasing FCS higher than the desired ECDs. To achieve improvements in wellbore integrity, this method often requires pumping of high-solids content pills to successfully halt fracture length propagation and initiate width growth. Through frac leak-off, the solids will eventually need to become an "immobile" mass to seal off pressure communication to the frac tip. Frac width growth results in wellbore hoop stress (compressive) which leads to an increase in FCS. This can be related to stress cage theory in that its compressive forces, acting on the opening of the newly propped fracture, will provide an increase in hoop stress and wellbore strength. The difference is that FCS requires the LCM to propagate fracture width instead of maintaining its width from initial propagation. In this study, this is achieved by increasing the *Net Fracture Pressure (NFP)*. NFP is defined as the degree to which the fracture pressure exceeds the minimum far-field stress (Sh_{min}). The greater the NFP, the wider the fracture is expected to become. Figure 2.8 depicts the relationship between fracture width propagation and FCS.

Figure 2.8 FCS increases with fracture width (Dupriest 2005).

Unlike Alberty and McLean, Dupriest (2005) made the argument that a successful LCM fracture seal can occur inside the fracture beyond the entrance. He further asserted that an LCM treatment's ability to isolate a fracture's tip is less dependent on its PSD than its solids content per volume and its ability to support leak-off into the fracture walls. Dupriest also noted that the presence of fines within the treatment slurry can drastically inhibit its ability to leak off into the fracture causing the treatment to fail.

Finally, the FCS method recommends three criteria in the selection of LCM.

1. The material must achieve and maintain fracture tip isolation even during fracture widening.
2. The final fracture width must be sufficient to create a FCS greater than ECD.
3. The materials need to be designed to create a seal that can release pressure or de-hydrate (i.e., using similar-sized materials).

Given that both the stress cage theory and the FCS method are dependent on leak-off and weak wellbores, it can be postulated that the depleted nature and permeability of a reservoir aids the mechanisms behind the success of the two (Dupriest 2005).

2.3.3 Fracture Propagation Resistance

Fracture propagation resistance (FPR) method (van Oort et al. 2011) is the practice of using selected size materials of desired strength to inhibit fracture propagation by sealing/blocking wellbore pressure from the fracture tip (i.e., tip screen-out). This is accomplished by using a robust materials–laden filter cake to act as a barrier between wellbore pressure and a fracture tip. The barrier, unlike the previous methods, does not act as a single immobile mass/plug but is comprised of fracture walls designed to resist propagation. The resistance in propagation occurs as a function of the fracture's inability to create new void space through rapid spurt loss. The magnitude of resistance to propagation correlates with the strength of mud cake formed by the fluid system. Unlike the previous methods, when combined with high-strength gels, FPR can potentially address losses in impermeable formations that allow little to no leak-off. Figure 2.9 shows how filter cake can be used to successfully isolate a fracture tip.

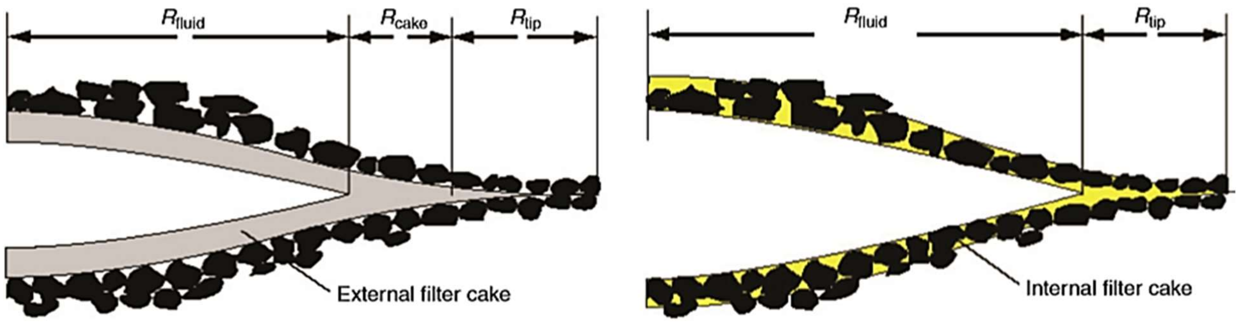

Figure 2.9 Left: A fracture is seen successfully screened out using mud filtrate. Right: The filter cake is insufficient to fully isolate the tip of the fracture (van Oort et al. 2011).

Because FPR doesn't rely on near-wellbore stress changes, when comparing theoretical pressure and rate plots (i.e., post stress cage method and FPR), one would expect the fracture initiation pressure to be adjusted upward. This would occur as a function of a near-well stress change. Compared to FPR (where initiation pressure remains constant), the pressure vs propagation trend moves upward as a function of fracture growth resistance (see Figure 2.10).

To apply the FPR method, the LCM size distribution should be fine-tuned with the estimated rock properties and the desired fracture geometry. example, in a tighter rock with a higher young's modulus, the operator may use small material to account a narrower fracture. Fluid rheological properties (i.e., gel strength and ability to create a mud cake) should also be considered, such as chemical and mechanical abilities to control filtrate losses at the near wellbore or within a fracture. Small filtrate additives have been used successfully with graphite being a more recent and resilient solution (van Oort et al. 2011).

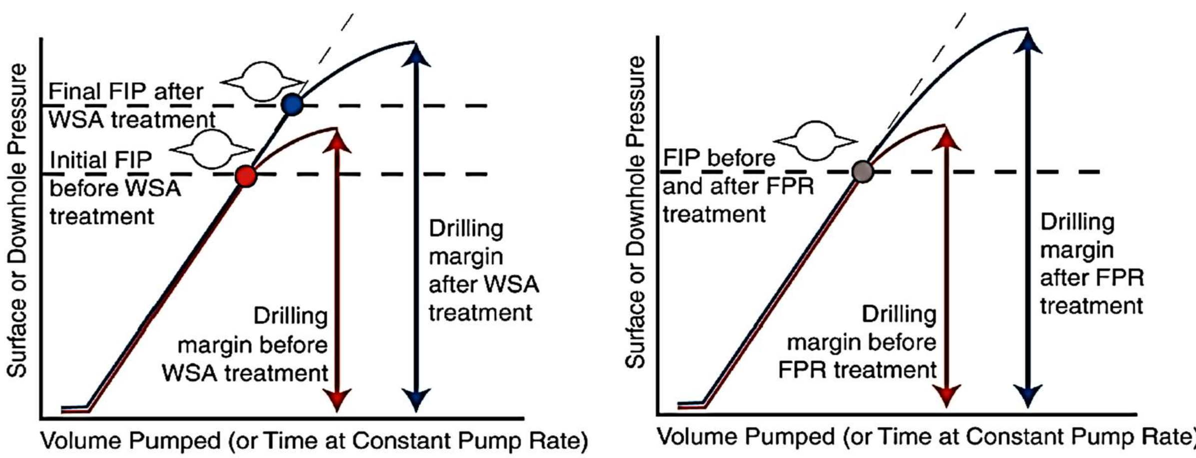

Figure 2.10 On the left, the LOT response is depicted before (red) and after (blue) stress cage treatment. On the right, the LOR response is depicted before (red) and after (blue) FPR treatment (van Oort et al. 2011).

CHAPTER 3: METHODS

This chapter discusses the work and methods of this investigation, including the order of completion, necessary measurements, calculations, and observations utilized to complete this study.

3.1 Receive Study-LCM

To obtain materials this study, LCM samples were ordered by the Apache Corporation and sent to the campus Chemistry Hygiene Officer at Colorado School of Mines. The materials and their safety data sheet (SDS) were documented and inventoried. Each SDS was read, and the identified hazards and ingredients of each material was studied and noted. Due to safety concerns and the lack of sufficient lab space, the materials were initially and temporarily stored in the Colorado School of Mines Campus Chemical Storage Distribution Facility (CSDF).

3.2 Lost Circulation Laboratory

To facilitate this study, a lab space was created on the Colorado School of Mines campus. This lab needed to provide enough space to (a) safely analyze materials, (b) properly and permanently store materials temporarily housed at the CSDF, and (c) provide storage future materials. Due to the wide range of chemistries and variations of LCM, substantial preliminary research was completed. This research was focused on potential hazards, safe handling practices, and proper storing procedures of incoming LCM. On-campus research was completed by communicating with lab coordinators in the Metallurgical and Materials, Mining, Petroleum Engineering Departments and the Environmental Health and Services at Colorado School of Mines. Off-campus research was completed by consulting lab technicians and research engineers actively working with two LCM manufacturers: Mi-Swaco and NewPark. Because of this initial study and the lessons learned, the following precautions were taken in developing a working lab space:

1) LCM particulate may cause irritation and damage to the eyes. Particulates of all sizes may be blown or accidentally rubbed into the eyes causing injury. This damage may result in temporary or permanent vision impairment.

    a) OSHA-compliant safety glasses were made readily available and utilized at all times while inside the lab space.

    b) An eyewash station is located at the entrance of the lab space.

2) LCM particulates, if left on the skin, may cause irritation and dryness.

    a) Protective lab gloves were made available and used while inside the lab space.

    b) Protective lab coats were also made available use inside the lab space.

3) LCM is consisted of fine granular particulates containing quartz or synthetic fibers that may pose a risk to the upper respiratory system. Due to their size, shape, and chemistry, these materials can become hazardous when airborne. If inhaled, these materials can damage soft tissue and cause cancer within the respiratory system.

    a) To mitigate the risk of accidental inhalation of potentially harmful and/or cacogenic materials, a ventilation and snorkel system were installed.

    b) Snorkels were connected to a filtered ventilation system within the space where LCM was analyzed openly. The vacuum created by a localized snorkel formed a path of least resistance airborne particulate to prevent accidental inhalation (Figure 3.1).

4) Large granular or fibrous LCM and testing fluids containing bentonite may cause damage to conventional plumbing if rinsed into a traditional drain. LCM or concentrated Bentonite may plug or damage a line. Due to its chemistry, certain LCM (e.g., carbon-based materials) may pose a health and environmental risk if pumped into a public sewer system.

   a) A fluid-waste barrel was secured disposal of testing fluids and LCM.

   b) The fluid-waste barrel was utilized throughout the study to ensure proper and safe disposal practices.

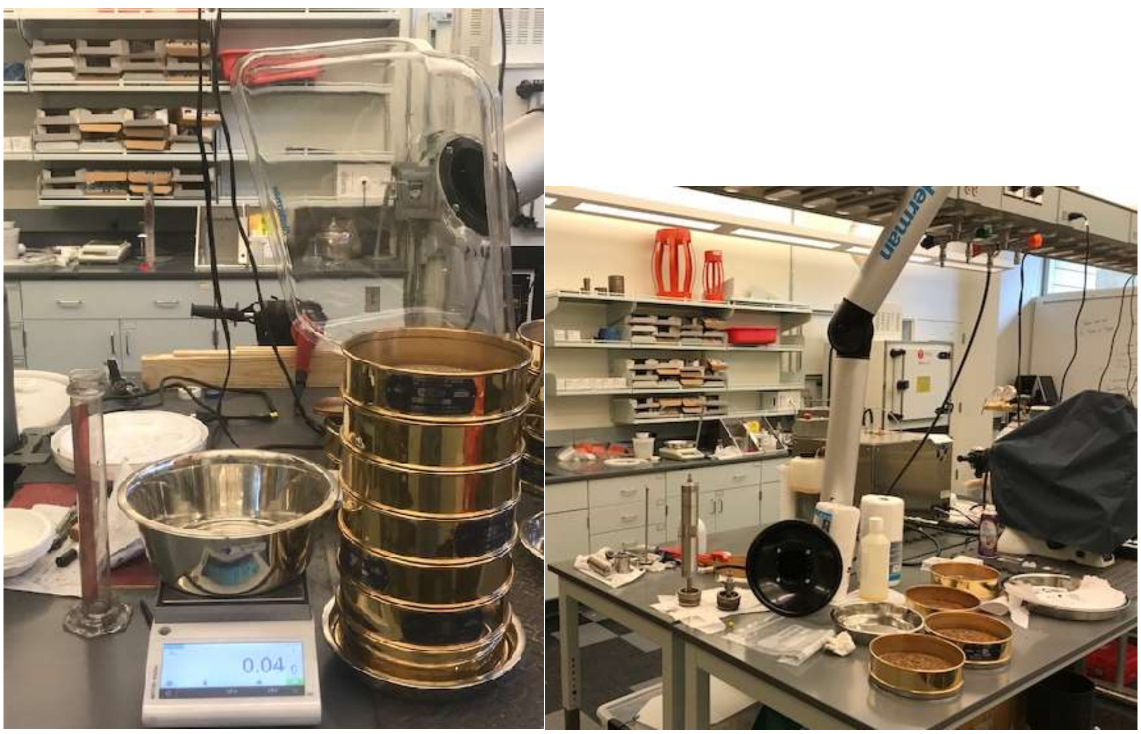

Figure 3.1 Dry-Sieve weigh station (left) and image scanning sample preparation station (right) both with snorkel systems installed to prevent accidental inhalation of particulate.

3.3 Dry Sieve Analysis

To begin a particle analysis, dry sieving was completed to obtain initial PSDs inventoried LCM (Figure 3.1). PSDs each product provided the means to categorize products throughout scanning and testing measures. PSDs delivered the necessary format reduction, normalization, and observation of particle shape data gathered in future scanning procedures. This format is further discussed in the construction of Particle Shape Distributions (PS_hD) section.

Each material was sieved through a standardized stack consisting of 8-inch diameter sieves with mesh sizes ranging from 4 um to 450 um. A volume of inventoried LCM (typically +500 mL) was measured and weighed using a mass balance. The weighed volume was placed at the top of the sieve stack. The stack containing the materials was placed in a Tyler RX-29 Model Ro-Tap sieve shaker and agitation apparatus (Figure 3.2). The shaker was set to agitate the stack 20 minutes.

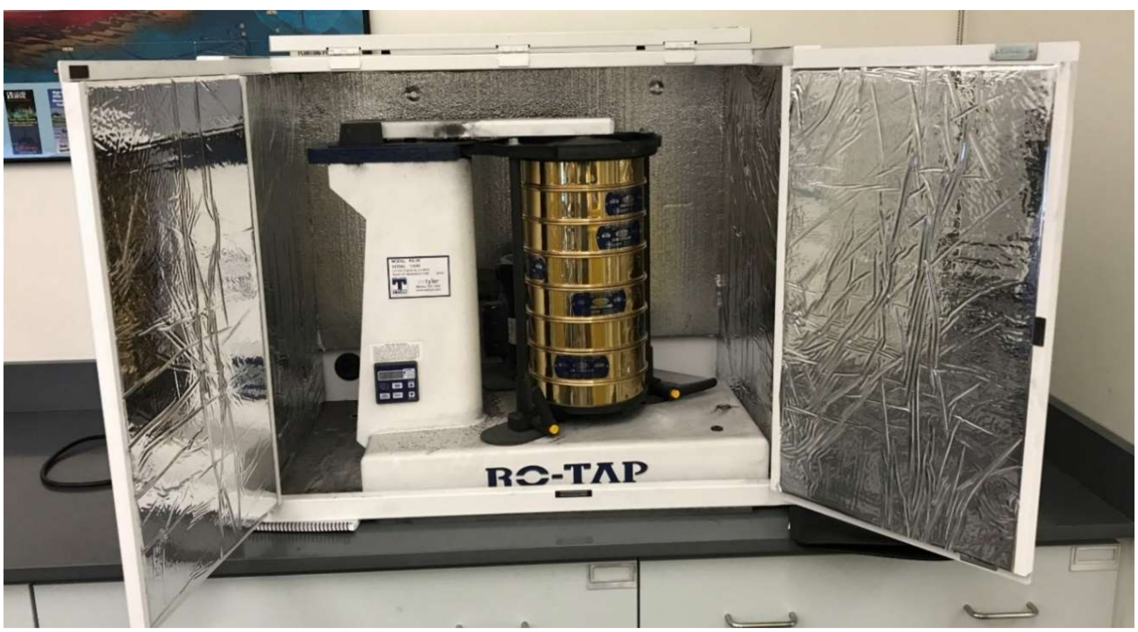

Figure 3.2 Tyler RX-29 Model Ro-Tap sieve shaker and agitation apparatus.

After 20 minutes of agitation, the sieve stack was removed from the shaker and taken to a weighing station under a working ventilation snorkel (Figure 3.3). The materials contained in each sieve were upended, shaken, and brushed into a weighing dish.

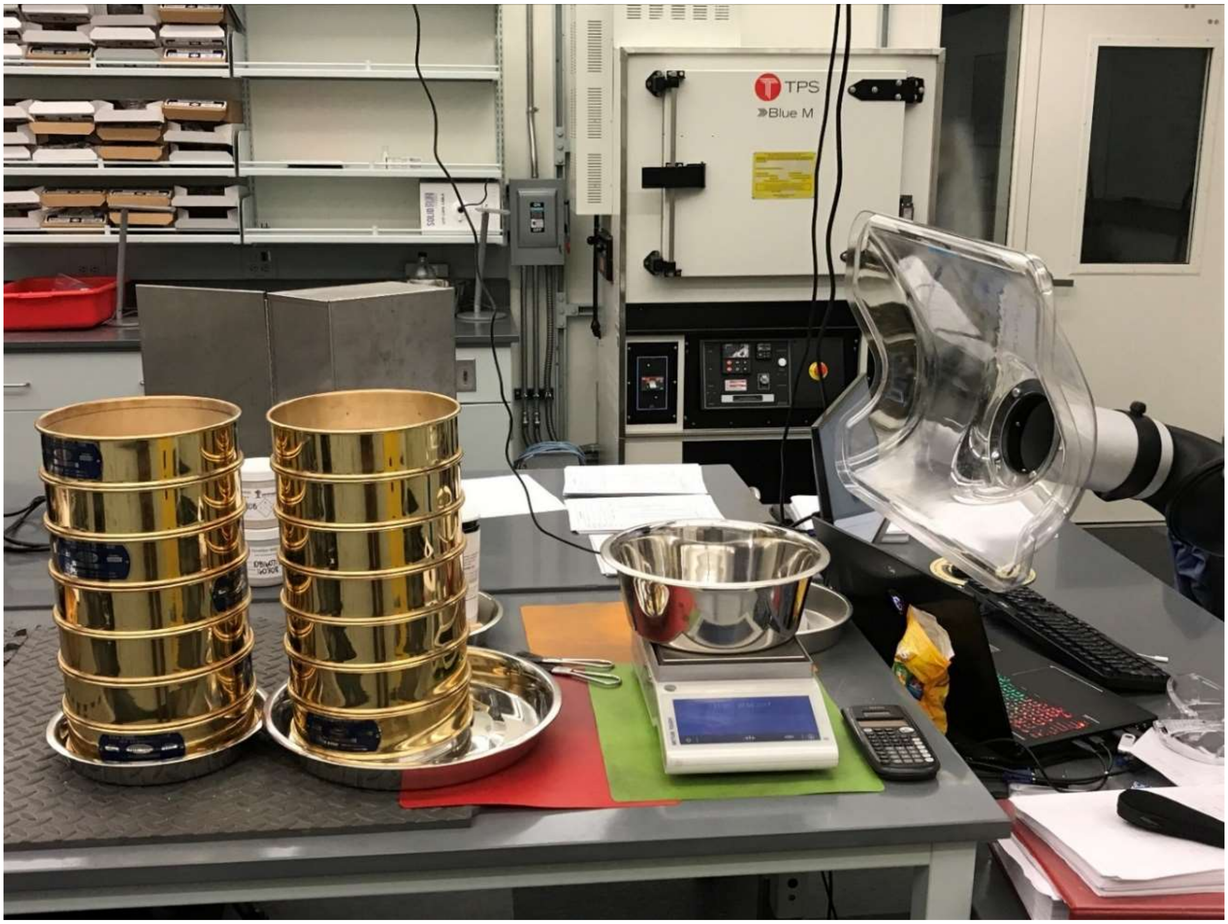

Figure 3.3 Weighing station containing weight dish and ventilation snorkel.

The resulting weight from each sieve was cumulatively measured and recorded on a sieve worksheet (see Figure 3.4). If the final cumulative weight was less than 98% of the original weight, the sample was sieved again. The purpose of repeating sieving procedures when a final mass discrepancy occurred was to mitigate errors in the sieving process. Error and error mitigation throughout the sieving process is discussed further in Chapter 4.

Apache - Sieve Worksheet			
Product Name	Baracarb 600		
Product mfr/vendor	Halliburton		
Sieve/Shake Time	**min**	20min/stack*3stacks = 60min	
Sample Wt.	**g**	780.58	
Sample Vol.	**mL**	500	
Sieve #	**Sieve Standard Size**	**Opening Size**	**Cum. Wt. (Total - Pan)**
unitless	**no.**	**um**	**g**
1	4	4750	0
2	5	3994	0
3	6	3359	0
4	7	2824	0
5	8	2375	0
6	10	1997	0
7	12	1679	0
8	14	1412	0
9	16	1188	0
10	18	999	28.65
11	20	840	260.76
12	25	706	499.54
13	30	594	640.86
14	35	499	745.68
15	40	420	772.94
16	45	353	777.06
17	50	297	777.71
18	60	250	777.96
19	70	210	778.15
20	80	177	778.24
21	100	148	778.37
22	120	125	780.09
23	140	105	780.09
24	170	88	780.09
25	200	74	780.09
26	230	62	780.09
27	270	52	780.09
28	325	44	780.09
29	400	37	780.09
Pan	**>400**	**<37**	780.09
Total Cum. Wt. Should be within 2% of original sample (Total (g) >98% of Sample (g))		**Total; g**	780.09

Figure 3.4 Example worksheet used to record data gathered during the dry sieve analysis of each material. The worksheet was completed using data gathered from sieving BARACARB® 600.

3.3.1 Dry Sieve Data Reduction

To successfully derive cumulative and normal PSDs from sieving, the accumulated mass of sieved materials was measured and recorded. Normal and cumulative distributions were created using percent by mass values. This was accomplished using the following equations:

$$M_{CSD} - M_{CS0} = M_S \tag{3.1}$$

$$\frac{M_S}{M_T} * 100\% = Material\ Mass\ \% \tag{3.2}$$

$$\frac{M_{CS}}{M_T} * 100\% = Cumulative\ Material\ Mass\ \% \tag{3.3}$$

where M_{CSD} is cumulatively measured mass at mesh size (g); M_{CS0} is cumulatively measured mass at previous mesh size(g); M_S is material mass at mesh size(g); and M_T is total material mass (g).

The determined mass and cumulative mass percentages were plotted as a function of mesh size. Mesh size was determined using U.S. Sieve Number and the fourth root of two methods per the following equations.

$$U.S\ Sieve\ Number\ 4 = 4750\ \mu m\ mesh\ size\ opening \tag{3.4}$$

$$U.S\ Sieve\ Number\ 5 = \frac{4750\ \mu m}{2^{\frac{1}{4}}} = 3994\ \mu m\ mesh\ size\ opening \tag{3.5}$$

Figure 3.5 displays an example of a plotted standard and cumulative PSD the Baracarb 600.

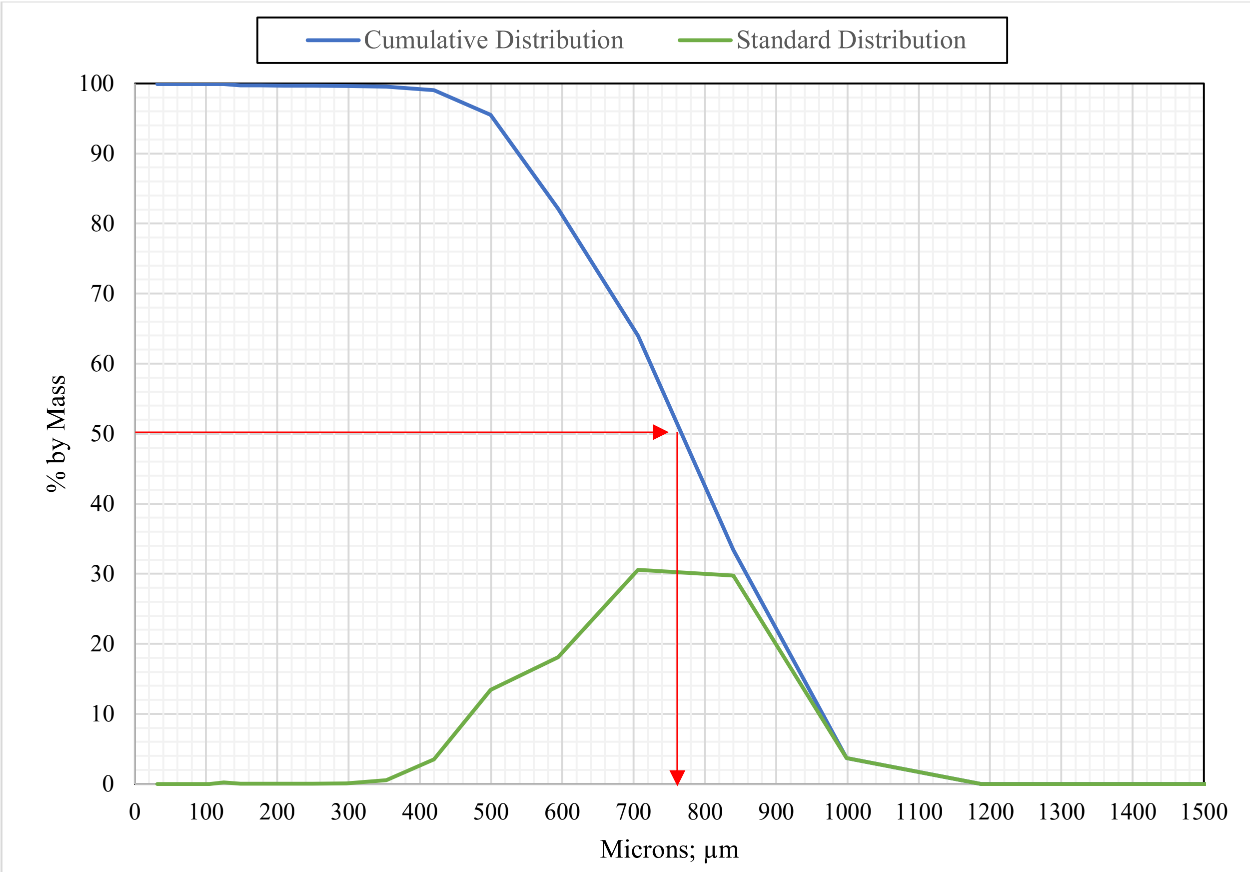

Figure 3.5 Standard and cumulative particle distributions determined "Baracarb 600." The D50 or mean particle size is approximately 760 µm.

3.3.2 Standard Coarseness Determination

Using the PSDs gathered in the dry sieve analysis, materials were organized by their measured coarseness. Overall coarseness was determined by examining plotted cumulative distributions and organizing materials based on their statistical Median or D50. The median was chosen over the Mean or Mode due to its straightforward and simple determination. Unlike mean and mode, a median can be determined by observing a common cumulative distribution plot without requiring numerical calculations and access to raw numerical data. The plotted cumulative distributions used to determine the level of coarseness studied Halliburton products is displayed in Figure 3.6.

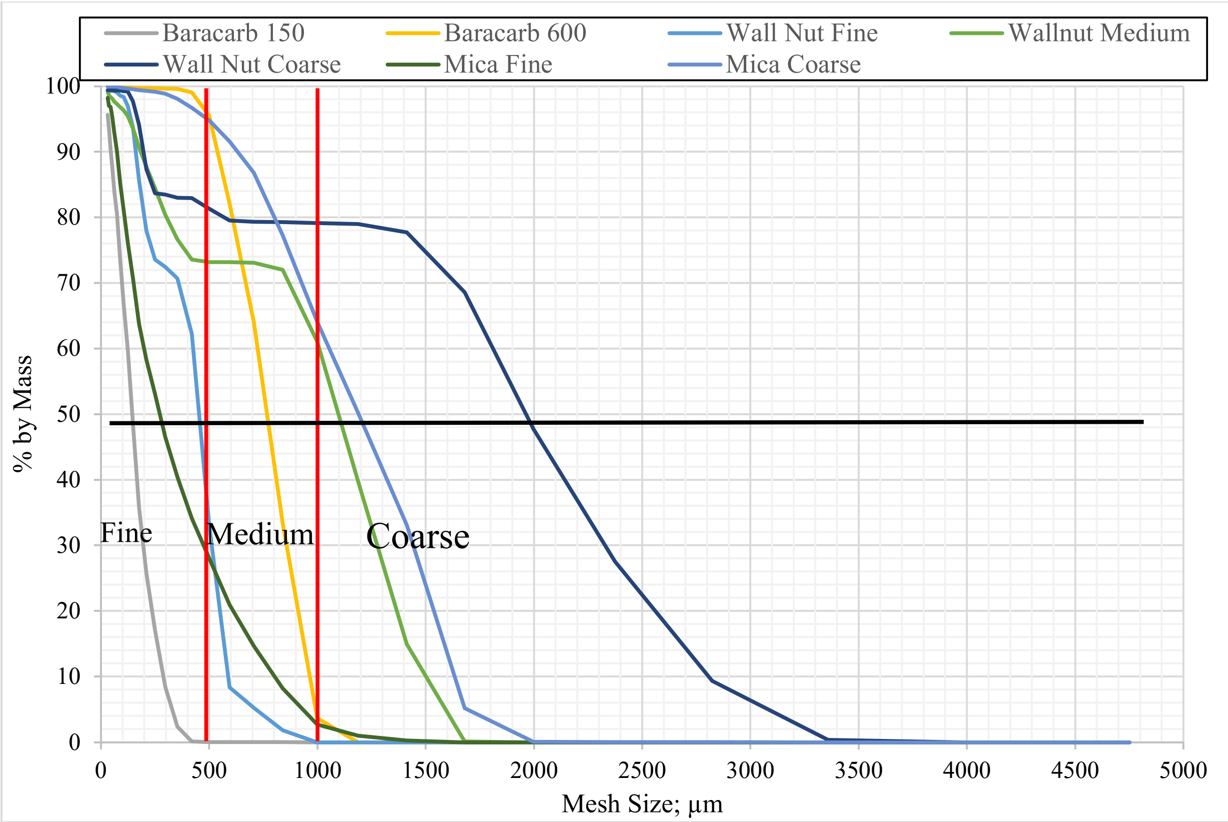

Figure 3.6 Cumulative distributions used to determine a standard level of coarseness Halliburton products studied.

A standard evaluating the overall coarseness of a product was established and served two purposes. First, it enabled me to work more efficiently within the bounds of the image scanning software and to mitigate error (further explained in Section 3.4 of this chapter). Secondly, it provided a quick reference in which to categorically organize and implement products in the testing phase. The following D50 ranges correspond to each level of coarseness standard utilized in this study:

- *Coarse*: D50 > 1000 µm
- *Medium*: 500 µm < D50 < 1000 µm
- *Fine*: 500 µm > D50

Standard coarseness and its impact in the testing phase are further explained in Section 3.6 of this Chapter.

3.3.3 Dry Sieve Error Analysis and Mitigation

Error mitigation was made by ensuring the cumulative mass measured was within ±2% of the original sample weight. Considering the standard stack was 30 sieves, the stack was broken into five separate series to fit into the Ro-tap agitator. Each of the six-stack series was agitated twenty minutes. The agitation time was determined after running various products through the sieving process at different times. The final data were plotted, and the precision was compared.

It was determined that twenty minutes of agitation was a reasonable standard to properly sieve the various LCM studied and retrieve repeatable results. The mass balance used in measuring the mass contained in each sieve was designed and calibrated to be accurate within ±0.01 g. How materials were passed into separate stack series and sizes is depicted in Figure 3.7.

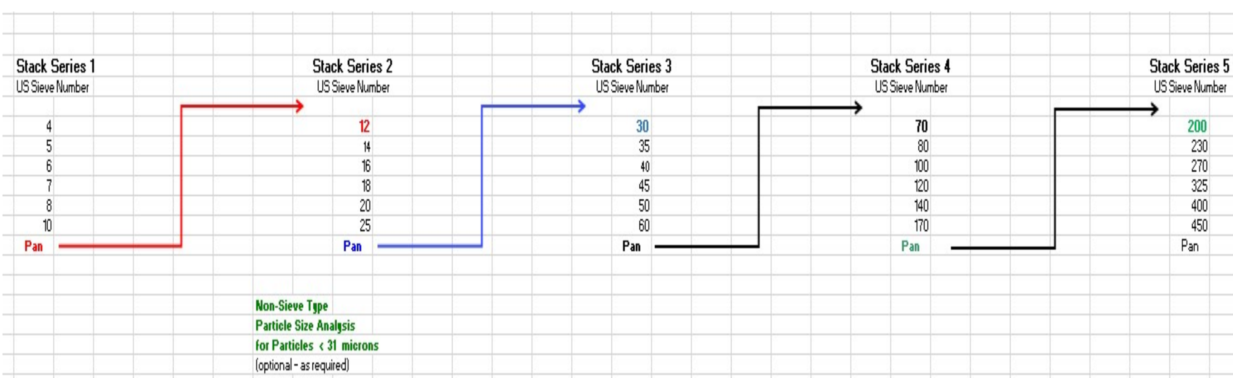

Figure 3.7 Sieving order example using a multiple sieve stack series to accomplish a larger standard sieve distribution.

3.4 Image Scanning Analysis

Shape and size measurements were gathered using image scanning hardware and software. Image scanning is the process in which high-resolution pictures are taken of sample material at pre-determined and specific magnifications. The image is then uploaded and analyzed by image scanning software. In this study, a Clemex Vision Lite and PE image scanning system was used (Figure 3.8). To successfully operate the Clemex Image Scanner efficiently, routines were written within the software package to communicate instructions to the system. These routines/instructions were designed and tailored to the average size of material being analyzed.

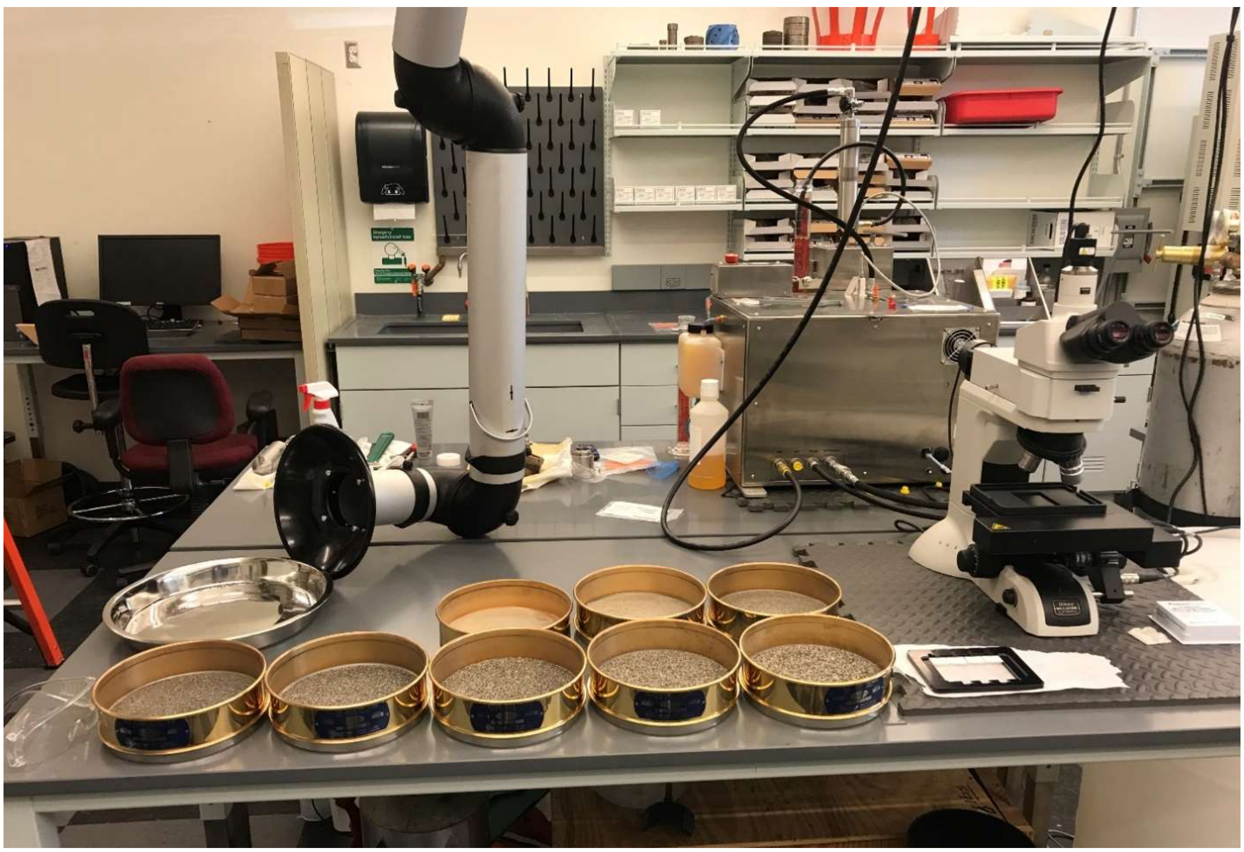

Figure 3.8 Clemex Vision Lite and PE image scanning system.

3.4.1 Slide Evaluation and Routine Design

A stage pattern was created to evaluate and measure the desired LCM sample and build the initial photo mosaic evaluation (Figure 3.9). The stage pattern defined the bounds and points at which the camera moved and took pictures. It provided the framework the desired mosaic. The stage pattern size and shape were created with the dimensions and position of the sample slide and the lens magnification used.

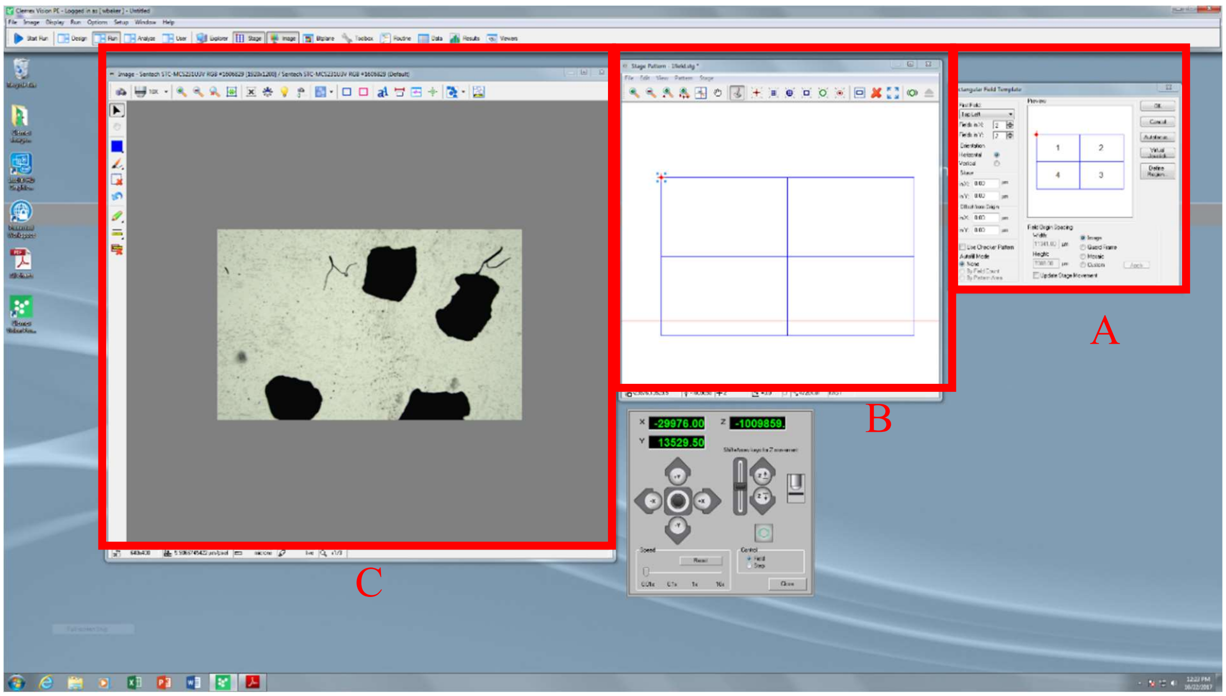

Figure 3.9 Clemex desktop view while creating a stage pattern to complete a particle analysis using a scanned image. From right to left: A = Stage template creator; B = Stage pattern; and C = Image.

Two types of routines were written to evaluate a single sample. The first routine was designed to build an image mosaic (with the dimensions of a manually-created stage pattern) and to automatically start the second routine. The second routine was created to effectively analyze and measure the sample using the photo mosaic created in the first routine. Essentially, the system takes several pictures, puts them together to create the entire sample, and then takes measurements from the picture using scanning and measurement algorithms (see Figure 3.10). At the end of the second routine, a data set in Excel format was created and saved in a data folder.

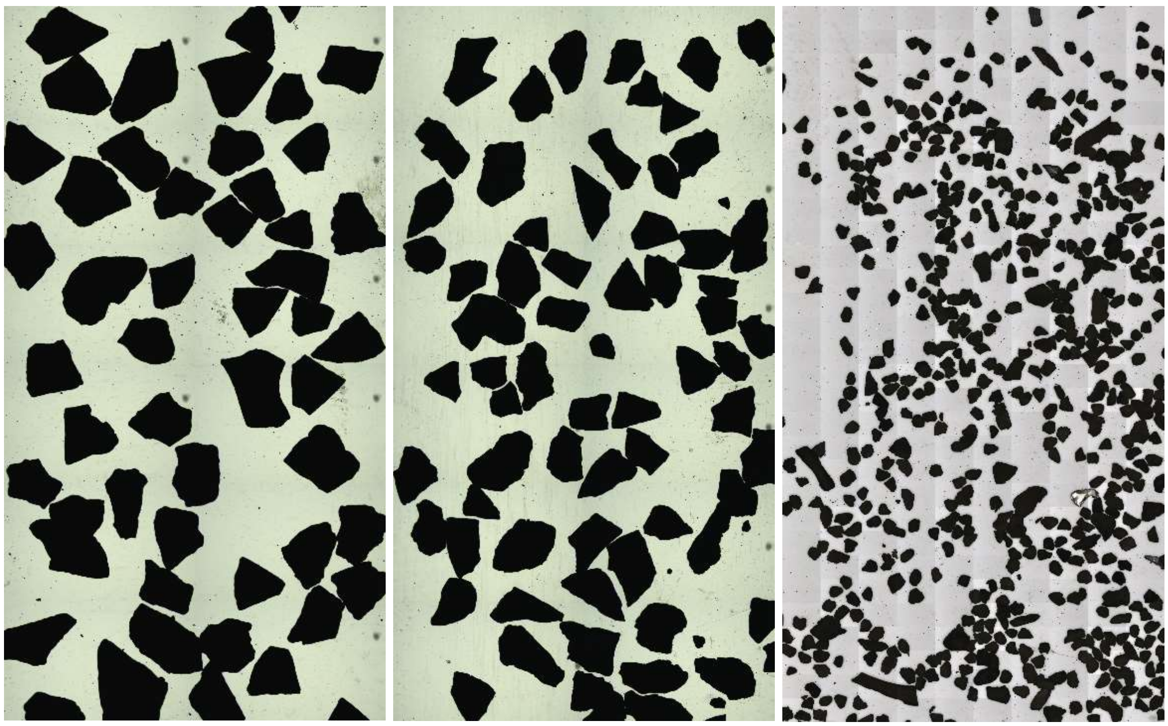

Figure 3.10 Created image mosaics of Halliburton walnut coarse samples. The left and center mosaics are of the coarser particles at a magnification of 10X. The right mosaic represents the finer material in walnut coarse samples and was created at a 50X magnification.

To ensure that a representative sample was analyzed, the material was organized and studied using routines designed and tailored to the product's standard coarseness, which was established in the dry sieving analysis (Figure 3.11). Standard sieve stacks were developed based on the standard coarseness of product materials analyzed in the image scanner. Samples were taken from each of the sieves and analyzed in the Clemex Image Scanner.

Sieve Worksheet: Pre-Image Analysis			
Product Name			
Product Mfr/Vendor			
Sieve/Shake Time	min		
Sample Wt.	g		
Sample Vol.	mL		
Size (Circle One)	Fine	Medium	Coarse
Fine			
Sieve #	Standard Size	Opening Size	Material Weight
No.	No.	mm	g
1	60	0.25	
2	120	0.125	
3	200	0.075	
Pan	>200	<0.075	
Medium			
Sieve #	Standard Size	Opening Size	Material Weight
No.	No.	mm	g
1	18	1	
2	35	0.5	
3	60	0.25	
Pan	>60	<0.25	
Coarse			
Sieve #	Standard Size	Opening Size	Material Weight
No.	No.	mm	g
1	10	2	
2	18	1	
3	35	0.5	
Pan	>35	<.5	
Notes:			

Figure 3.11 Example of pre-image scanning sieving worksheet. This worksheet is used to create slide samples and is organized by overall particle shape.

3.4.2 Shape Measurements

The Clemex system was used to measure and calculate the following:

- *Length*: Longest measured distance (Feret) between two points on an object.
- *Main Length*: Highest length measured (Feret) perpendicular to the shortest measured length (smallest Feret).

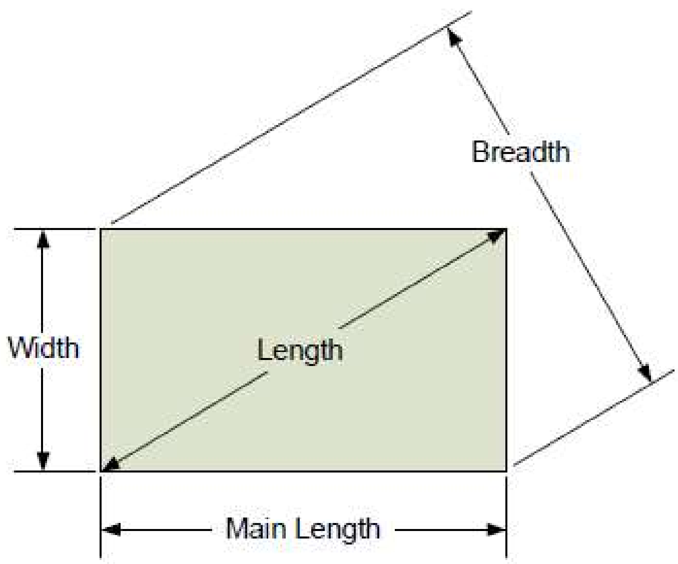

Figure 3.12 Measurement labels on a rectangle demonstrating the difference between length and main length (Clemex Vision User's Guide).

- *Breadth*: Length of the feret that is perpendicular to the longest feret.
- *Width*: Shortest distance between two points on an object (smallest Feret).
- *Sphericity*: Estimated determination of how close an object approaches a mathematically perfect sphere. Determined index ranging from near zero to near one with one being a mathematically perfect sphere.

$$\frac{4\,\pi\,Area}{Perimeter^2} = Sphericity \tag{3.6}$$

- Aspect Ratio: Calculated ratio of length over width.

$$\frac{Measured\ Length}{Measured\ Width} = Aspect\ Ratio \tag{3.7}$$

- Roundness: Estimated determination of how close an object's two-dimensional image approaches a mathematically perfect circle. Determined index ranging from near 0 to near one with one being a mathematically perfect circle.

$$\frac{4\ \ Area}{\pi\ Length^2} = Roundness \tag{3.8}$$

- Compactness: Ratio of area over a convex perimeter.

$$\frac{4\pi\ Area}{Convex\ Perimete\ \ ^2} = Compactness \tag{3.9}$$

- Area: Sum of pixels in an object.

- Perimeter: Average distance interpolated using three points on an object.

- Convex Perimeter: Sum of the line segment lengths joining tangent points on a curve.

$$\sum \text{ferets2}\tan\left(\frac{\pi}{2(number\ of\ ferets)}\right) = \text{Convex Perimeter} \tag{3.10}$$

- Feret: Distance between two parallel tangents on each side of an object (analogous to using a caliper).

Upon the completion of the scanning and measurement process, a data set was generated by the Clemex software each particle present in the sample. A sample of the raw measurement data generated is displayed in Appendix A.

3.4.3 Image Scanning Data Reduction and Error Sources

To normalize data exported from the imaging software, the statistical measurement data were normalized with the sieving data assuming width is equal to sieve size. This assumption was made after observing a direct correlation of particle width measured by image scanning and the known mesh size range of the sample. Compare the statistical width data obtained from the imaging software (Figure 3.13) to the PSD data gathered during sieving Figure (3.14).

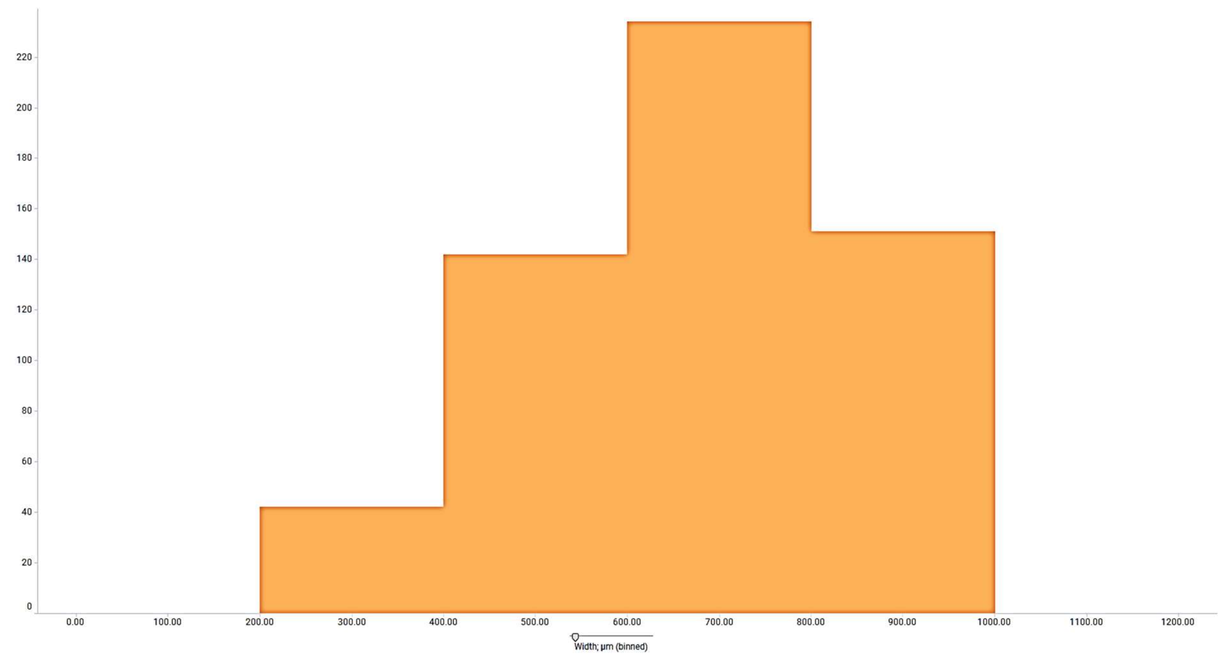

Figure 3.13 Histogram plot of Nut Plug Fine particle width measurement data obtained using the imaging technique.

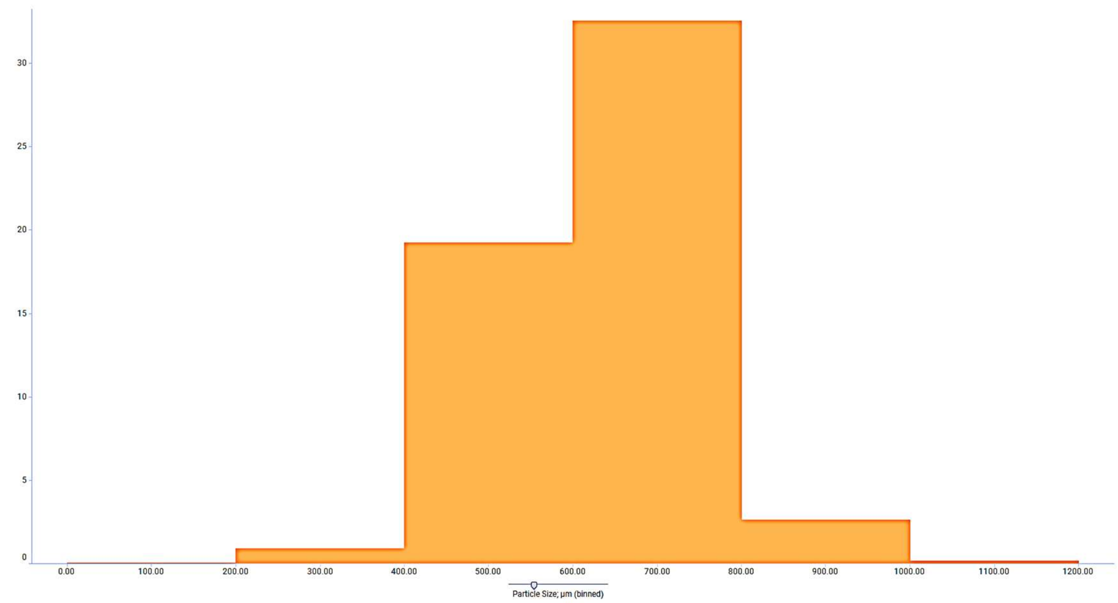

Figure 3.14 Bar plot of Nut Plug Fine PSD obtained from sieving.

The normalizing process provided an opportunity to observe the acquired shape data on the standard PSD model. To accomplish this, exported measurement data (see Appendix B) from the Clemex software was sorted by particle width. The sorted shape measurements were then averaged over the mesh sizes used in the sieving process. This averaging process allowed standard plotting providing a data point at each common mesh size. Plotted averaged measurements are compared to the overall sieved particle distribution (see Figure 3.15).

Particle width was used because it was observed to be the measurement that most correlated with mesh size from the sample taken from during the analysis. After it was determined that a particle's width was the leading characteristic that prevented it from passing into the next sieve or mesh size, routines were tuned to account anticipated particle size.

Specifically, within each routine, data were only taken from particulates with widths that fell in the expected range (based on the Ro-Tap sieving). This was a leading source of error in image scanning by the user and the software separating particulates, resulting in clumped particulates counted as one particle.

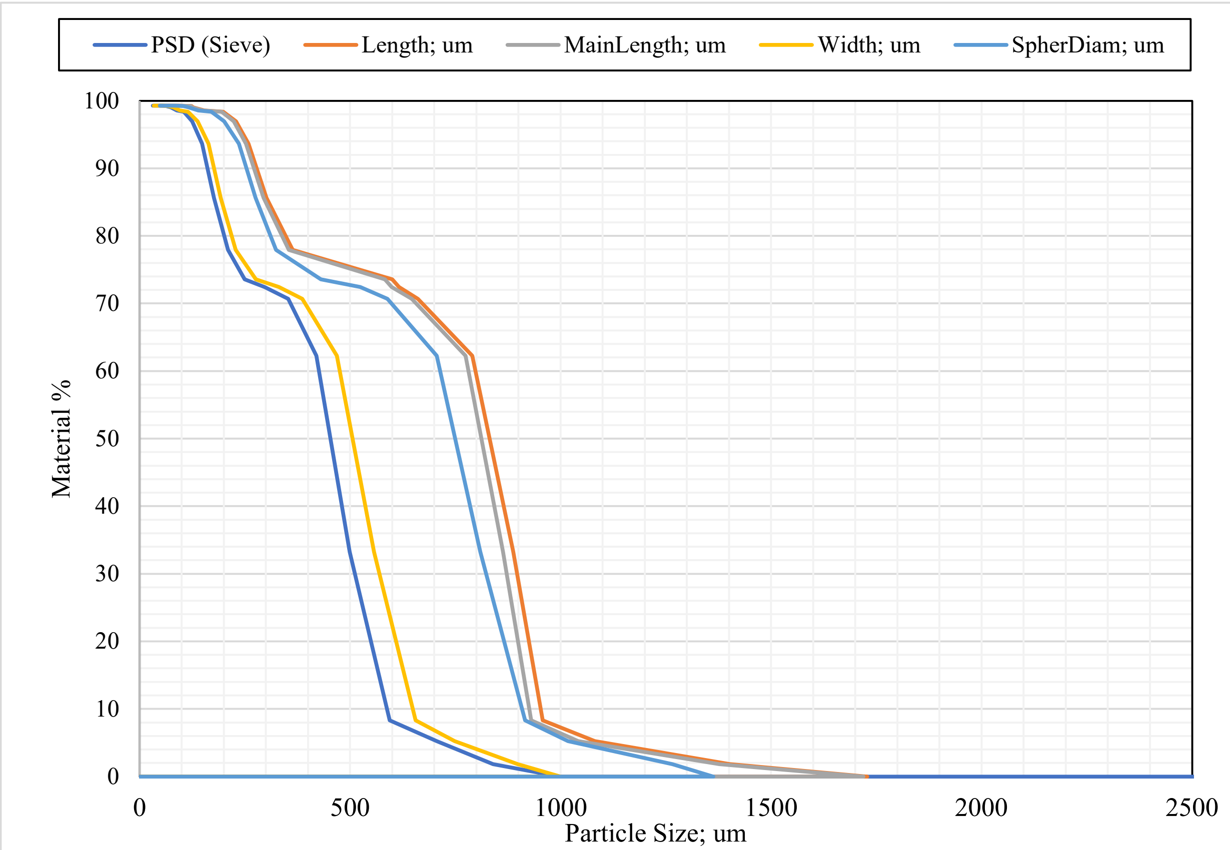

Figure 3.15 Plotted cumulative shape and size distributions of Halliburton's Wall-Nut Fine®. PSD data gathered in the dry sieving process was plotted with averaged measurements produced in the image scanning process.

To mitigate random error caused by particle clumping, each sample was prepared carefully, particulates were spread evenly on the slide, and data were taken from particulates within an expected size range. A well-prepared sample is compared to an unsatisfactory sample below in Figure 3.16.

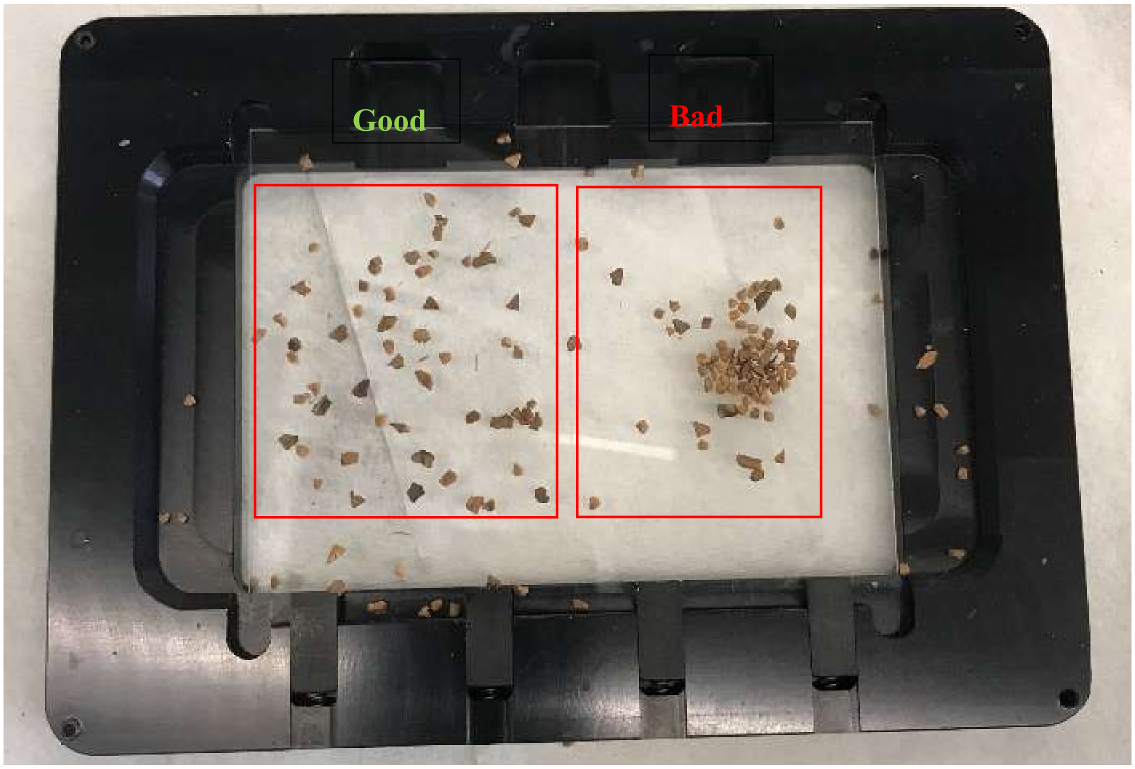

Figure 3.16 Well-prepared sample material is depicted on the left of the sample slide. Unsatisfactory and clumped sample material is portrayed on the right of the sample slide.

Each lens used in the image scanning process was calibrated and tested before use. Clemex image scanning software calculated calibration factors each lens magnification based on the success of calibration and lens magnification. The success of each calibration was determined using the calculated error of the smallest successful measurement made on a standard calibration slide. The calibration factor represented the smallest distance that could be successfully measured by the system. The creation and scanning of image mosaics increased the effective calibration factor or error. This is because measurements were affected by the magnification of the microscope, the resolution of the camera, and the system's ability to successfully and accurately align each image in a mosaic pattern measurement (see Figure 3.17). A final software-calculated calibration factor was exported with each data set.

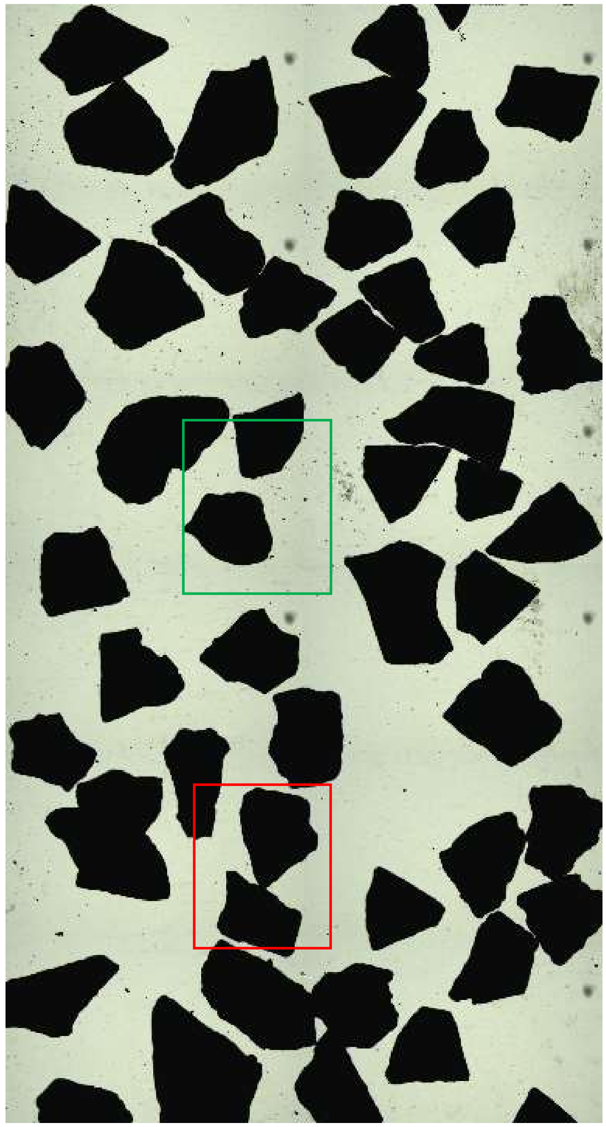

Figure 3.17 Created image mosaics of Halliburton walnut coarse samples. Red Box is an example of two particles touching, which would be counted as a single particle. Green Box is the desired multiple particles not touching (light in between) which would allow the software to count and measure each individually

In this study, the final calculated calibration factor represented measurement error. Since a standard magnification was used at specific size ranges, average calibration factors over particle sizes analyzed were able to be plotted and are displayed in Figure 3.18.

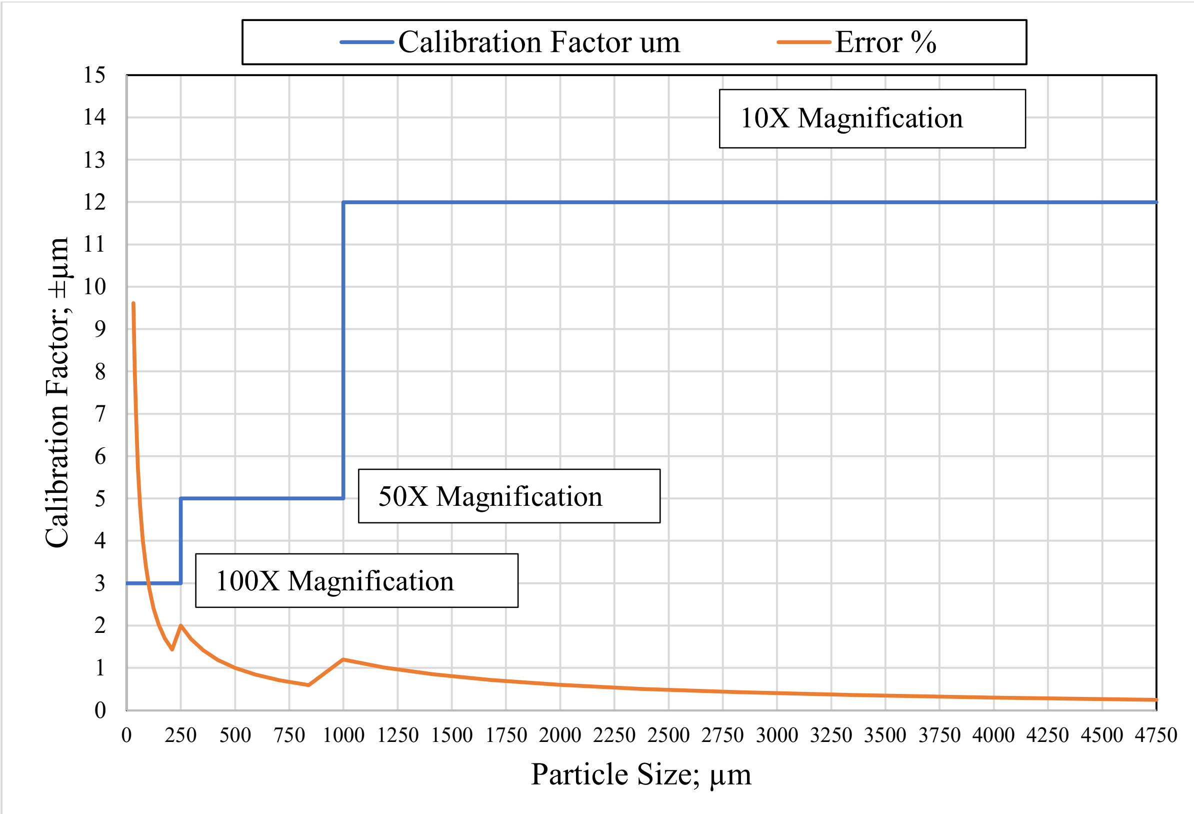

Figure 3.18 Plotted averaged calibration factors and calculated error percentage corresponding to the average-sized particles measured. The magnifications used to capture particle images are labeled.

Higher calibration factors were observed when measuring larger particulates under lower magnifications; however, a higher calculated error percentages was observed with finer materials. The highest calculated error (9.6%) was observed with sieved particle sizes of 31 µm and below.

$$\frac{Calibration\ Factor}{Particle\ Mesh\ Size} * \%100 = \%\ Error \quad (0.11)$$

3.5 Test Fluid

At the end of the particle analysis, testing fluid was created to facilitate standardized LCM testing procedures and methods. To successfully test the sealing ability of the lab LCM in a slot test, a uniform testing fluid was built. The testing fluid was designed using a consistent method to achieve standard and desired rheological properties. The desired rheological properties the testing fluid were the following:

1. *Plastic viscosity of the base fluid in the range of 15-25cp*: This plastic viscosity range is high enough to deliver LCM particulates to the testing slot and low enough to avoid significant viscosity fluctuations as a function of testing LCM concentrations. Fluctuations in viscosity as a result of LCM concentrations could affect the bridging abilities of the testing fluid. This would be counter-productive to the study considering its focus on particle shape and size as opposed to overall slurry concentrations.
2. *Yield point of the base fluid in the range of 10 to 20* $lb/100ft^2$: This yield point range was determined as sufficient to suspend the larger, heavier granular materials measured in the studied LCM.

To achieve and maintain the standard rheological fluid properties discussed, a freshwater system was designed using pre-hydrated bentonite. Bentonite was chosen its solids suspension properties and resistance to rheological degradation. Bentonite—unlike Xantham gum, starch, and other organic polymers—is not susceptible to bacterial degradation. This allows large volumes of testing fluid to be stored extended periods without risk of significant rheological fluctuation from biological deterioration. Testing fluid was prepared and organized in batches. Each batch consisted of four gallons of fresh water and 25 ppb of dehydrated bentonite. The mixture was sheared eight hours followed by a 12-hour resting period. Fluid rheological properties were tested after the resting period, and the batch was labeled. Rheological properties were measured using an OFITE Rheometer: Model 900 (see Figure 3.19).

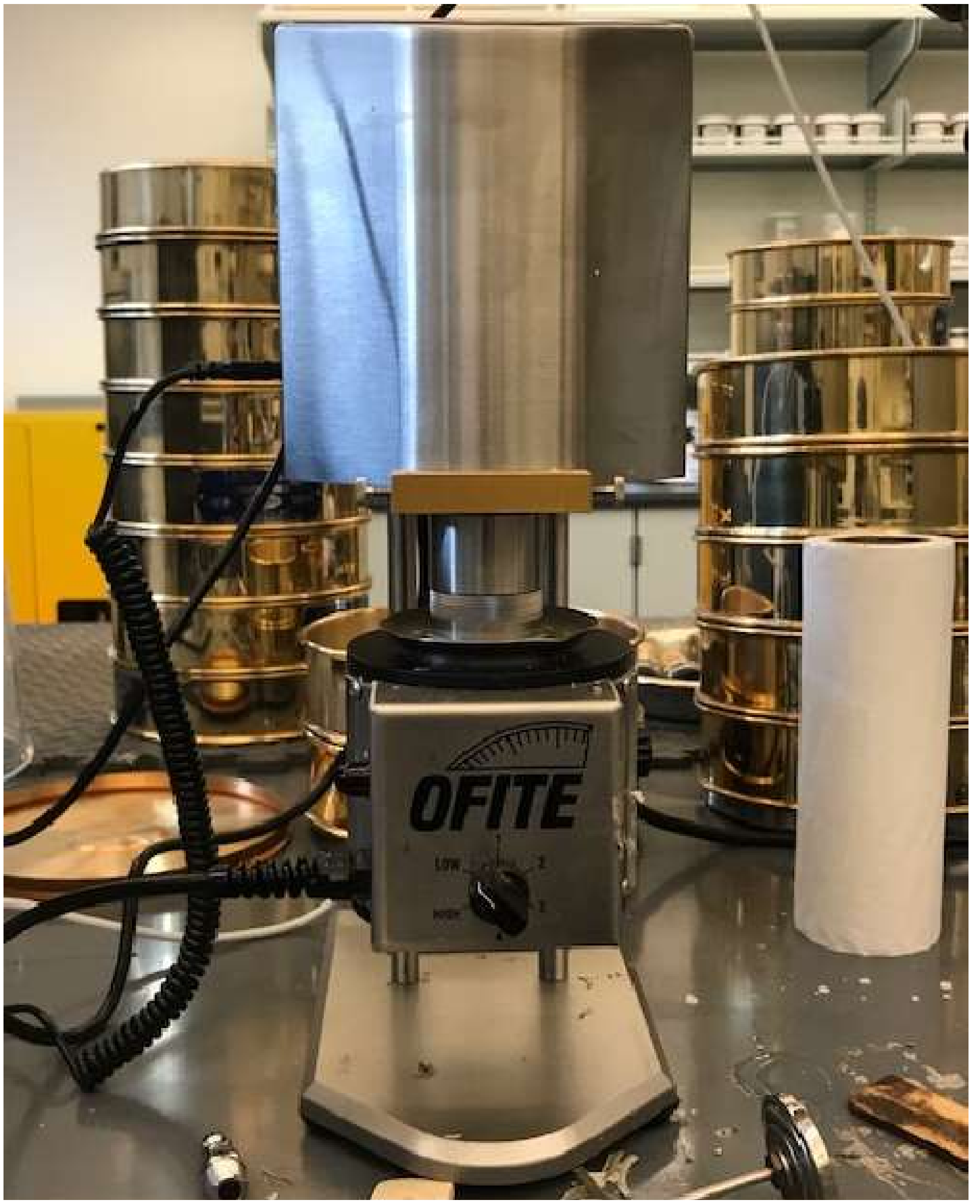

Figure 3.19 Photograph of the lab rheometer measuring rheological properties of a test fluid sample.

3.5.1 Testing Fluid Preparation Error Sources

The rheological properties of the testing fluid were not assumed or observed to be static throughout the testing process. Specifically, the test fluid's viscosity consistently increased as a function of settling time and volume used/taken from each batch (see Figure 3.20).

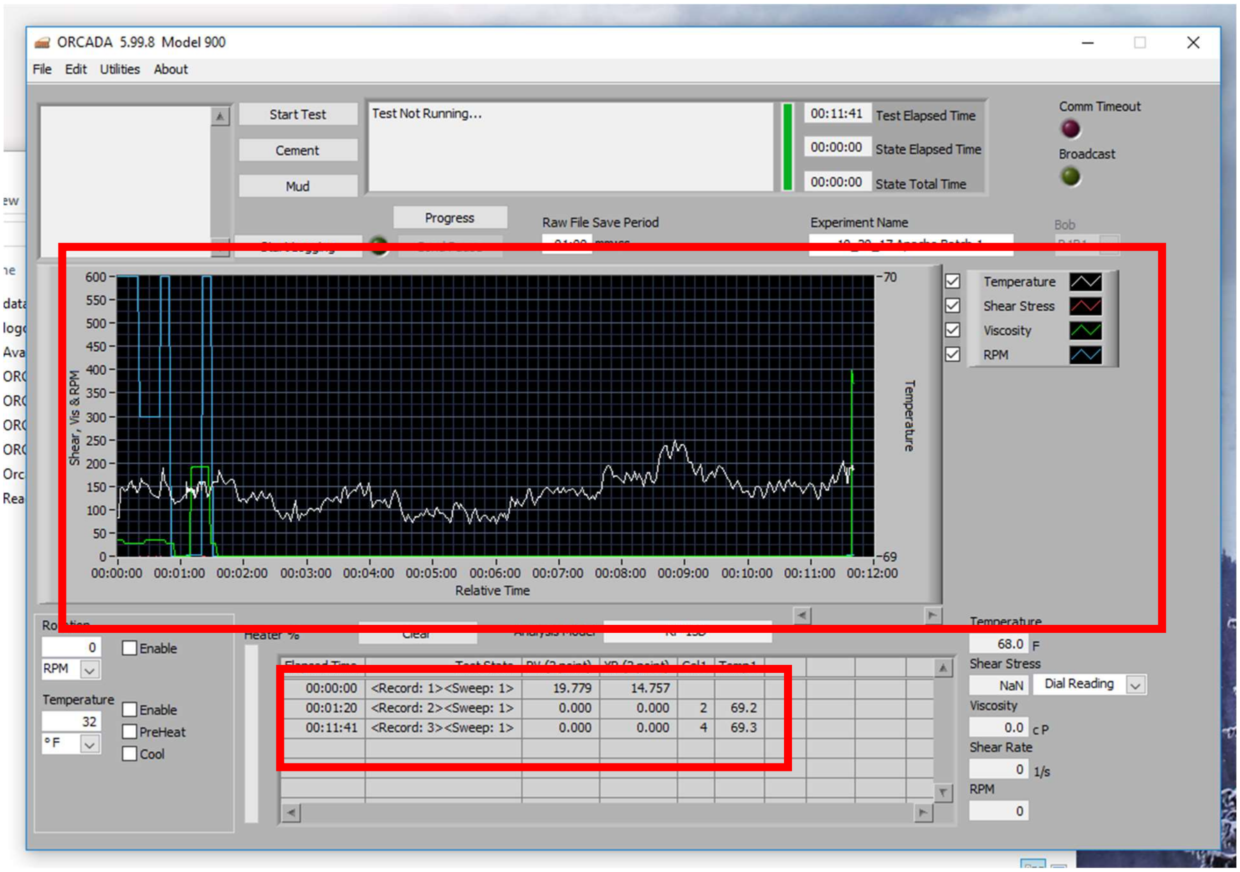

Figure 3.20 Rheological test results from a sample taken from the “Apache Batch 1” test fluid.

To mitigate errors associated with fluctuating test fluid properties, samples from each test batch were sheared one hour and then tested at the beginning of each day and/or when batch volume reached half of its original.

Test fluid was sheared when the rheological properties were visually observed to be abnormal. Figure 3.21 illustrates an example of a failed rheological test that was completed on a test fluid after the rheological properties were visually observed to be different than the original. At the end of the failed test, the original test fluid sample was sheared one hour and retested. In the event that the test fluid failed a second test, the batch was taken out of service and disposed of responsibly.

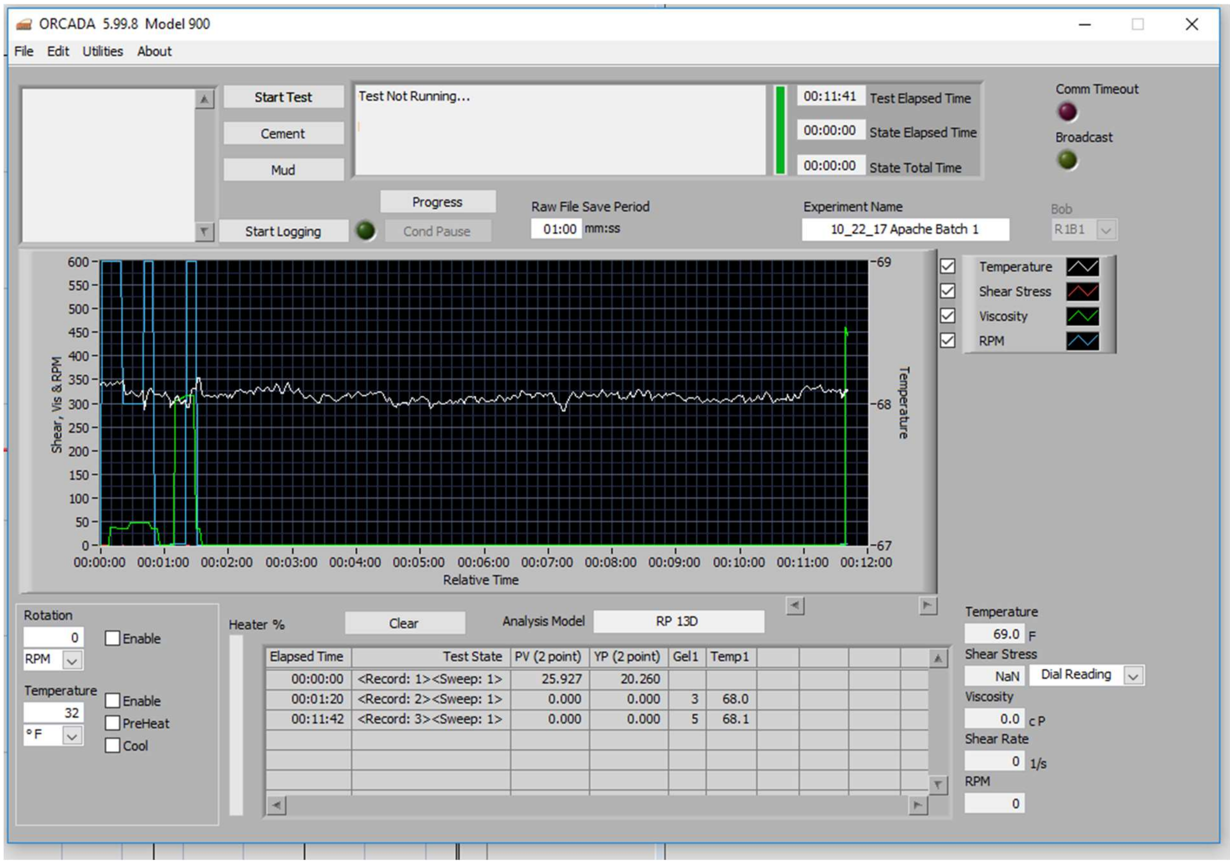

Figure 3.21 Example of results from a failed measured sample. PV was determined to be above 25cp & YP above 20 $lb/100\text{ft}^2$

3.6 LCM Performance Testing

With a particle size and shape data set and a standardized testing fluid in place, LCM was evaluated with the anticipation and hope of identifying common physical characteristics with successful LCM blends.

3.6.1 Sample Preparation

Considering the variance in particle size and shape distributions, testing materials were separated by mesh size, which was determined by means of the standard sieve stack used in the particle distribution analysis phase of this study. After sieving, material left in each sieve was transferred to a container and labeled individually with the corresponding sieve number it was taken from. As illustrated in Figure 3.24, Halliburton's Baracarb 600 is shown separated by its mesh size.

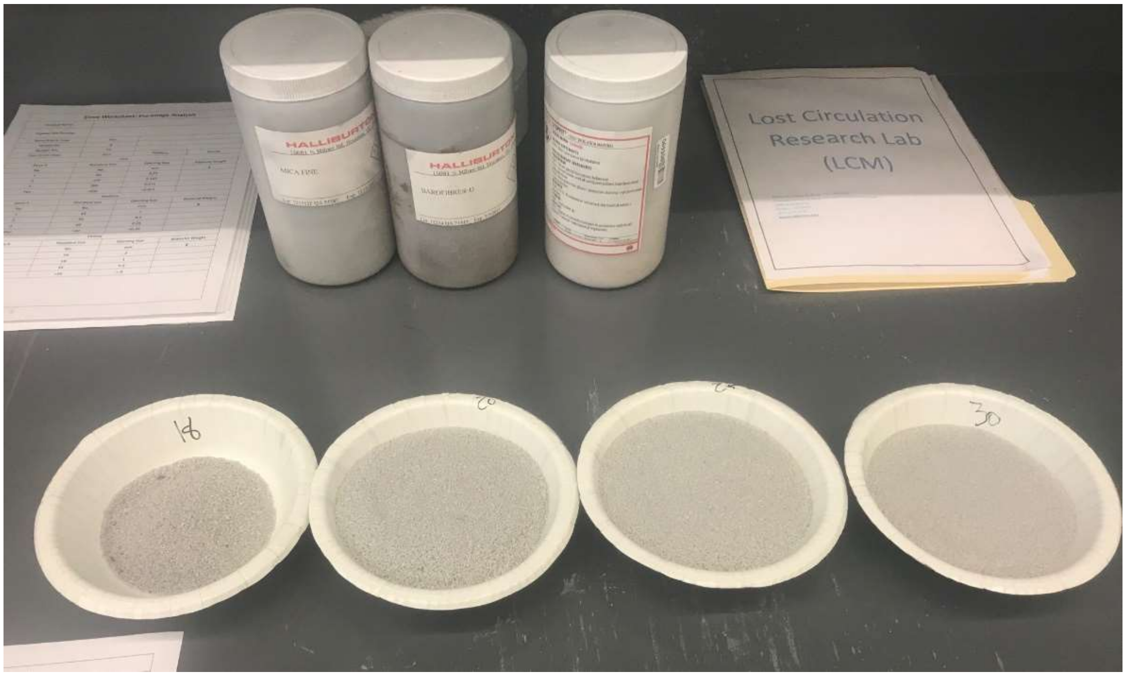

Figure 3.22 Baracarb 600 testing material organized by standard sieve size.

Materials were organized by size to allow better control in developing LCM testing blends. Thus, instead of building an LCM blend with an undivided product sample (e.g., 25 ppb of Baracarb 600), an LCM testing blend could be *10 ppb* of Baracarb (sieve-30) or Baracarb 600 (30) and *15 ppb* of Baracarb (18). This control was assumed to aid in the discovery of particle size, shape, and sealing performance correlations.

Material of a known LCM product and particle size range were weighed, then mixed/sheared 20 minutes into a lab barrel (*350 mL*) of test base fluid using a Hamilton Beach mixer (see Figure 3.23).

Figure 3.23 Hamilton Beach mixer shearing an LCM blend performance testing.

3.6.2 Sample Testing

To evaluate a material's aperture sealing ability, slot tests were completed using the Automated Plugging and Permeability Apparatus (APPA) as displayed in Figure 3.24.

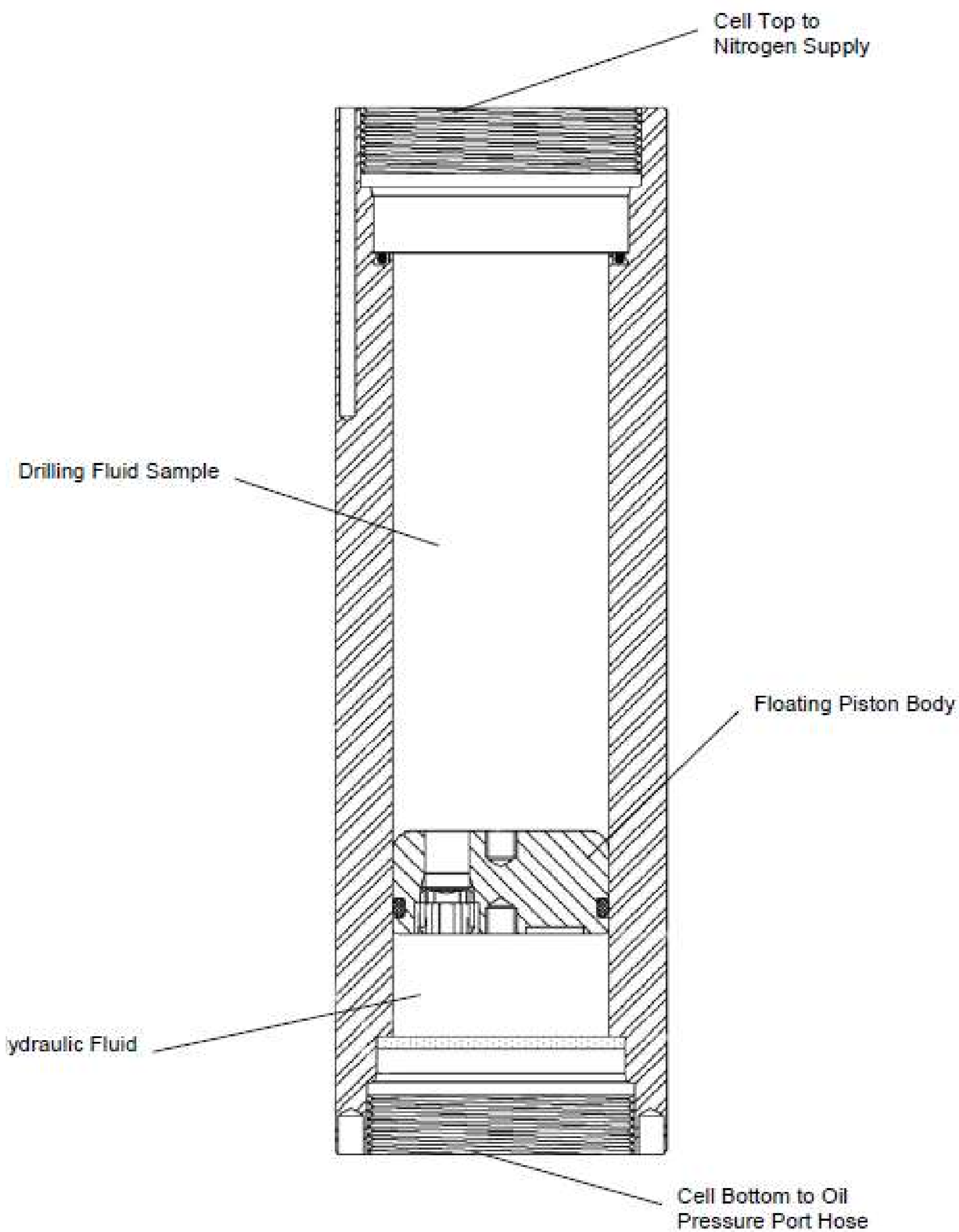

Figure 3.24 APPA Testing Cell Arrangement.

Materials and fluids were slot tested at room temperature. The mixed-sample LCM-laden fluid was transferred to the APPA testing cell, which was mounted inside the APPA heat chamber. A steel disc with a defined-sized slotted aperture was installed at the top of the cell above the fluid (Figures 3.25).

Figure 3.25 Photo of a slotted disc with three 3 mm wide apertures.

A vug adapter and LCM evaluation receiver were installed on the top of the testing cell. A hydraulic pressure hose was inserted and connected to the bottom of the testing cell (Figure 3.26).

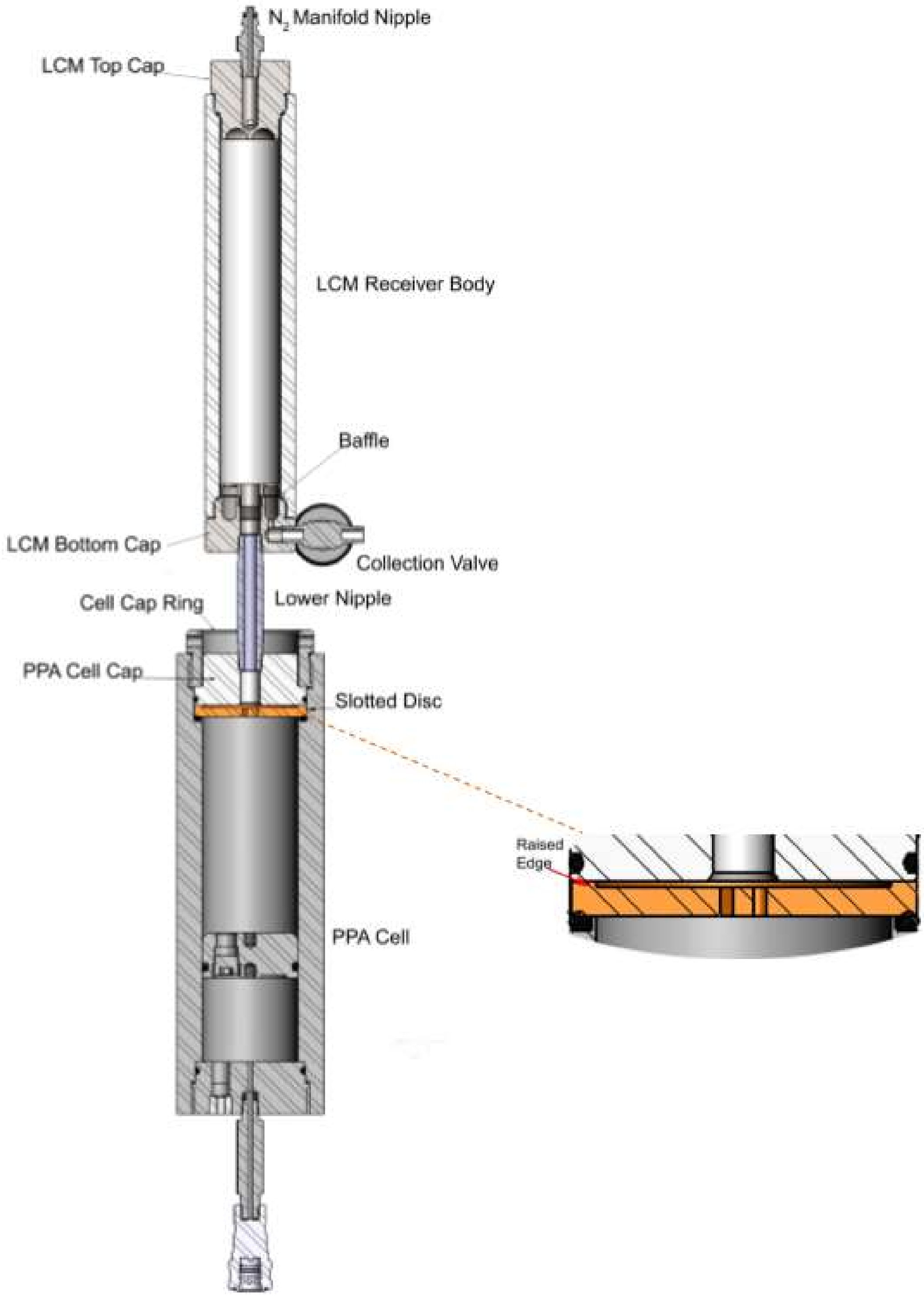

Figure 3.26 APPA testing cell with slotted disc installed and LCM evaluation receiver connected.

From a computer workstation and using the Fann APPA software, a pressure step test was created. The test was designed to pressure-up the system in 500 psi increments from atmospheric to 2500 psi, with 5-minute intervals between each step to allow pressure settling (see Table 3.1).

Table 3.1 Standard staged LCM pressure test schedule

Cumulative Test Time; min	Stage Time; min	Test Cell and Seal Pressure; psi
0	0	0
5	5	500
10	5	1000
15	5	1500
20	5	2000
25	5	2500

The system used a floating piston inside the test cell, which moved because of pressurized hydraulic fluid pumped behind it. The system only became pressurized as a function of the LCM's ability to seal the slotted apertures within the test cell. If the LCM failed to create a pressure seal within the cell, the system did not pressure-up, and the testing fluid continued to pump into the open-topped LCM receiver.

LCM tests that failed to noticeably pressure-up the test cell within 30 seconds of hydraulic pumping were deemed failures. Proactively shutting down failing tests prevented the floating piston from topping out. If the floating piston topped out, and differential pressure was seen across it, a disc located inside of the piston would rupture and result in instant communication with the hydraulic system. This type of failure leads to costly repairs of the APPA. Data from tests that could continue in their entirety were recorded within the APPA software and downloaded into an Excel data set.

To ensure the correct particle shape and size characteristics were compared to their performance, LCM slurry additives were recorded with each test using the APPA software's test profile. An example is shown in Figure 3.27.

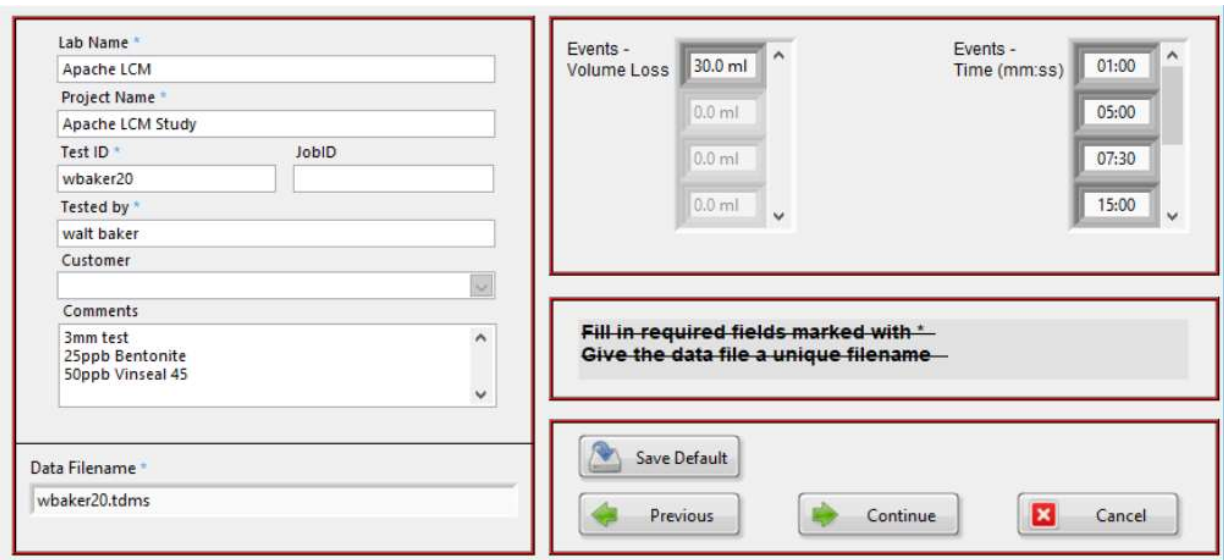

Figure 3.27 Image capture of an inputted testing profile used when testing M-I Swaco's VinSeal, sized approximately mesh #45.

3.7 CM Performance Testing Data Reduction and Error Sources

3.7.1 Test Sample Preparation

A lab "barrel" (*350 mL*) of test fluid was measured using a graduated cylinder with an observed measurement error of ±*5 ml*. LCM was added to the test fluid and was weighed using a mass balance calibrated to an error of ±*0.01 g*. LCM and test fluid were mixed into a slurry using a standard 20-minute shearing time. A standard shear time was used to mitigate random error associated with fluctuation in rheological properties and uneven particle suspension between tests.

3.7.2 Slot Testing

Pressure (in psi) and time (in seconds) were automatically recorded by the Fann APPA software. The data were then exported into an Excel dataset. Maximum sealing pressure was determined by taking the maximum pressure measurement in the pressure transient data sets. The maximum sealing pressure observed in Figure 3.28 is 2445 psi.

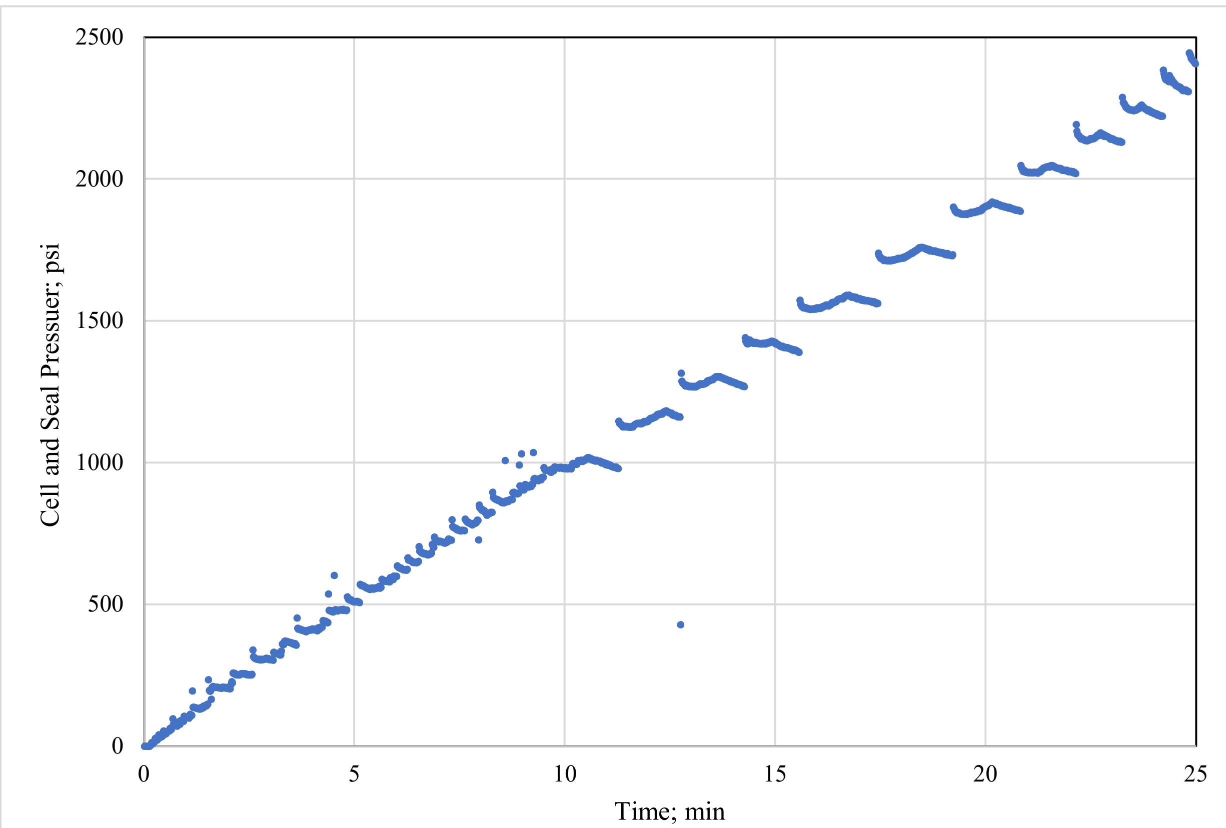

Figure 3.28 Pressure transient plot produced of data recorded by the APPA software. This figure shows a successful test of 10 ppb Wall Nut (18), *10 ppb* Wall Nut (60), and *30 ppb* VinSeal (120).

The approximate fluid lost during the test was determined by measuring the testing cell volume before and after the testing. The floating piston only moves as a result of the delta pressure created when a seal isn't formed and leakage occurs. When a seal is successfully formed, pressure builds inside the system while the floating piston remains relatively stationary. At the end of a successful test, it was assumed that the final position of the floating piston was the sole function of the reduction of fluid volume lost through the slotted disc and into the LCM receiver. After each successful test, the tested LCM slurry left behind in the testing cell was measured and compared to its original volume. This final slurry volume was measured using a graduated cylinder with a ±*5 mL* accuracy. Random error may have also been introduced into the final slurry volume by inconsistency in the slurry removal process.

Testing was completed with slotted discs of varied sizes (1000 µm, 2000 µm, and 3000 µm aperture width slots) using similar LCM concentrations and fluid properties. Successful testing using the smaller 1000 µm aperture may have had less to do with particle size and shape and more to do with an overwhelming concentration of solids. To mitigate this error, testing was predominantly completed using the larger 3000 and 2000 µm slotted discs.

3.7.3 LCM Sealing Performance and Particle Shape and Size Correlations

To successfully compare particle size and shape measurements to sealing performance, the average measured size and shape data corresponding with the LCM additives in each slurry were plotted (Figure 3.29) along with the LCM slurry's maximum sealing pressure (Figure 3.30).

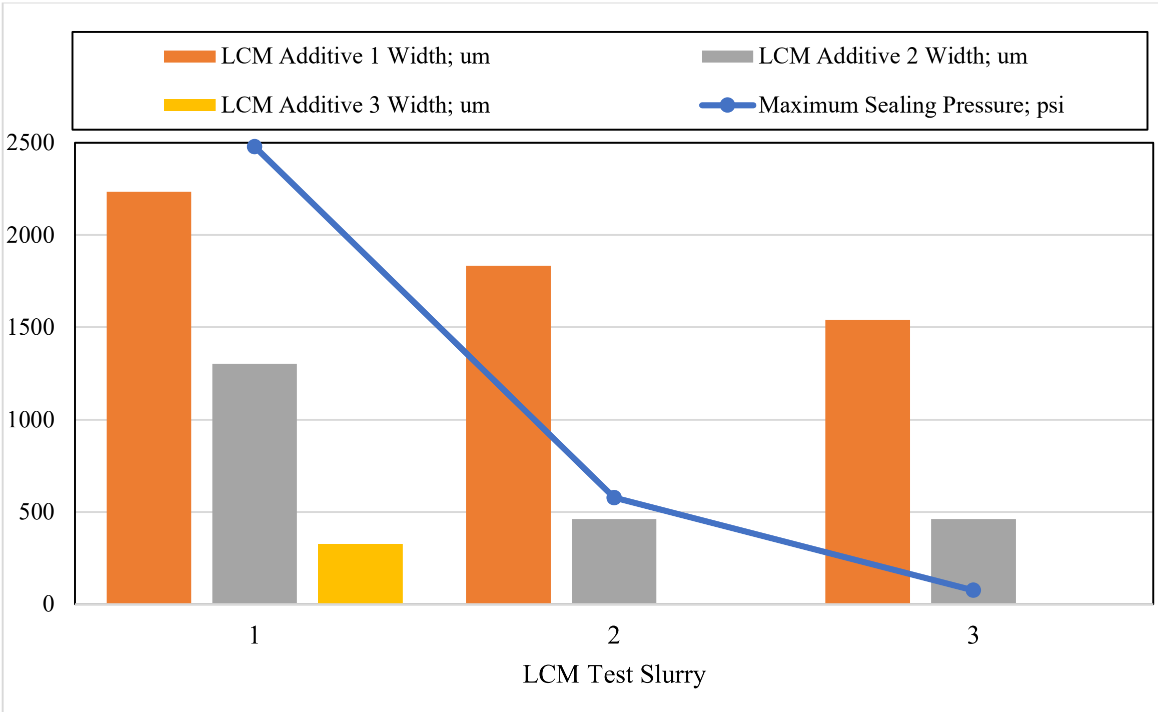

Figure 3.29 LCM slurry maximum sealing pressures plotted with averaged measured width of each testing slurry LCM additive.

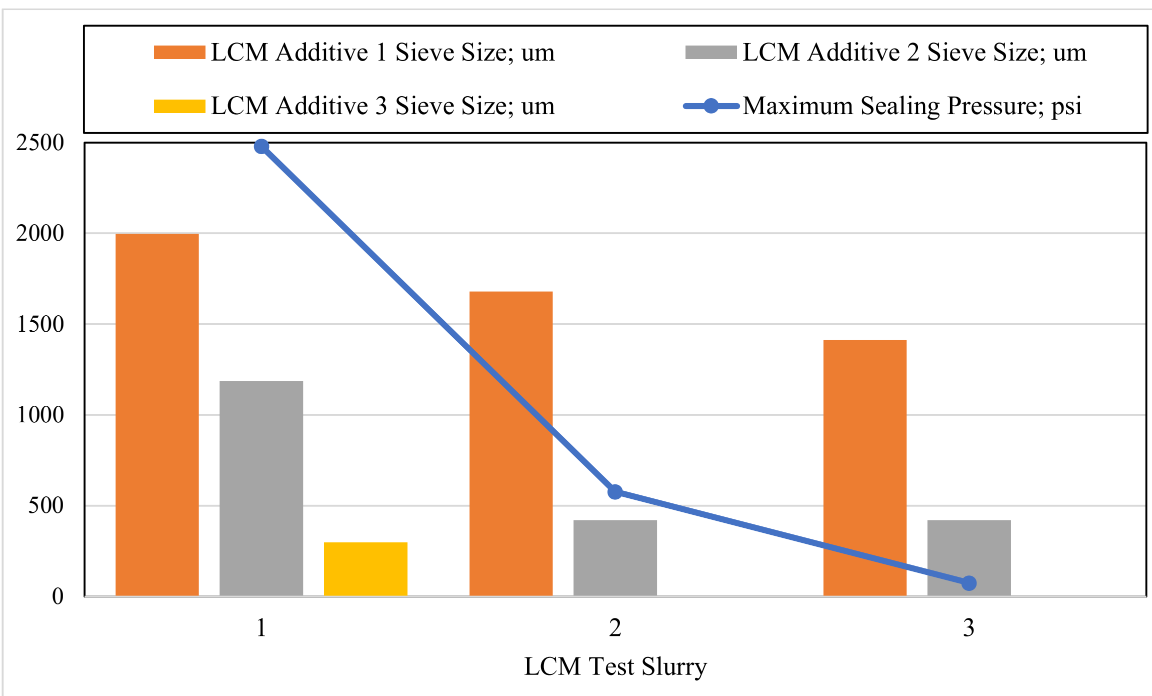

Figure 3.30 LCM slurry maximum sealing pressures plotted with sieve mesh sizes of each testing slurry LCM additive.

CHAPTER 4: RESULTS AND DISCUSSION

The following chapter discusses the experimental and calculated results of this study, organized by the slotted disc size used in the testing process. Each slurry was ranked by its sealing performance. Blend performance was determined by its calculated fluid loss percentage. Fluid loss percentage was deemed the performance indicator due to the physical principles of practice during testing. Specifically, if a blend's seal failed or leaked, the cell pressure would fail to obtain the desired maximum pressure value. This fluid loss percentage and sealing pressure relationship was observed in the testing data that is plotted and presented in this section.

4.1 3000 µm Aperture Width Slotted Disc Testing

Using a pre-designed pressure test, ten different LCM configurations were tested to 2500 psi with a 3000 µm aperture width slotted disc. Slurry additives and concentrations are listed in Table 4.1.

Table 4.1 Contents of tested LCM blends using a 3000 µm slotted disc

Test	Total Test LCM Blend Concentration	LCM Add #1	LCM Add #2	LCM Add #3	LCM Add #4
1	50ppb	10ppb - (10) Sieve Baroid Wallnut Coarse	10ppb - (14) Sieve Baroid Wallnut Coarse	30ppb - (60) Sieve Mi Swaco VinSeal Medium	-
2	50ppb	10ppb - (7) Sieve Baroid Wallnut Coarse	10ppb - (12) Sieve Baroid Wallnut Coarse	30ppb - (45) Sieve Mi Swaco VinSeal Medium	-
3	50ppb	10ppb - (7) Sieve Baroid Wallnut Coarse	20ppb - (12) Baroid Wallnut Coarse	20ppb - (40) Sieve Mi Swaco VinSeal Medium	-
4	50ppb	10ppb - (7) Sieve Baroid Wallnut Coarse	25ppb - (40) Sieve Mi Swaco VinSeal Coarse	15ppb (50) Sieve Mi Swaco VinSeal Coarse	-
5	50ppb	10ppb - (10) Sieve Baroid Wallnut Coarse	40ppb - (60) Sieve Mi Swaco VinSeal Medium	-	-
6	50ppb	10ppb - (10) Sieve Baroid Wallnut Coarse	10ppb - (18) Sieve Baroid Wallnut Medium	30ppb - (70) Sieve Mi Swaco VinSeal Medium	-
7	45ppb	5ppb - (6) Sieve Mi Swaco Nut Plug Coarse	10ppb - (7) Sieve Mi Swaco Nut Plug Coarse	10ppb - (8) Sieve Baroid Wallnut Coarse	20ppb - (40) Sieve Mi Swaco VinSeal Medium
8	50ppb	10ppb - (8) Sieve Baroid Wallnut Coarse	10ppb - (50) Sieve Mi Swaco VinSeal Medium	30ppb - (45) Sieve Mi Swaco VinSeal Medium	-
9	50ppb	50ppb - (45) Sieve Mi Swaco VinSeal Medium	-	-	-
10	50ppb	10ppb - (6) Sieve Mi Swaco Nut Plug Coarse	20ppb - (8) Baroid Wallnut Coarse	20ppb - (25) Sieve Mi Swaco VinSeal Coarse	-

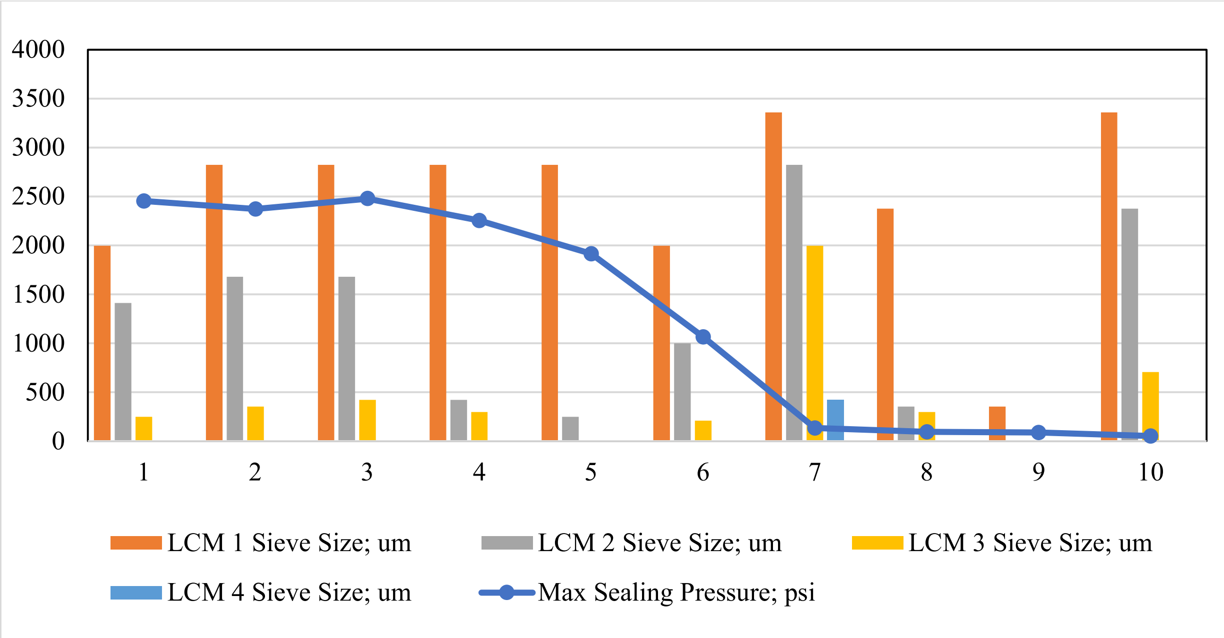

Figure 4.1 Particle mesh size plotted with LCM slurry maximum sealing pressures obtained using a 3000 µm aperture width slotted disc.

The slurries that ranked the highest consisted of three LCM additives. Surprisingly, these additives all had a smaller mesh size than the testing aperture, which is inconsistent with the current and customary practice of matching average particulate size with aperture width. In fact, if average particle size were needed to match the aperture, slurry 7 would have ranked the highest. Further examination suggested that the particles may have bridged the aperture width as a function of particle length (see Figure 4.2). Figures 4.2 and 4.3 offer evidence that suggests that LCM additives 1 and 2 may have acted as the primary bridging mechanism within the seals of the successful slurries (1, 2, and 3). The average lengths additives 1 and 2 (Figure 4.2) are both greater than the aperture width (Figure 4.3).

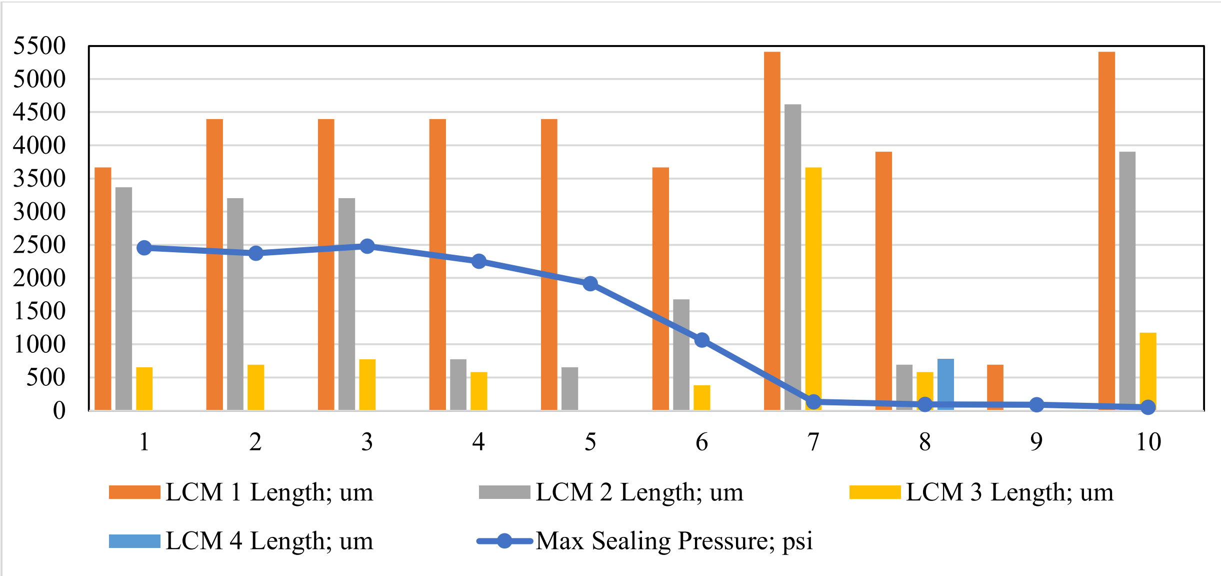

Figure 4.2 Averaged length measurements plotted with LCM slurry maximum sealing pressures obtained using a 3000 µm aperture width slotted disc.

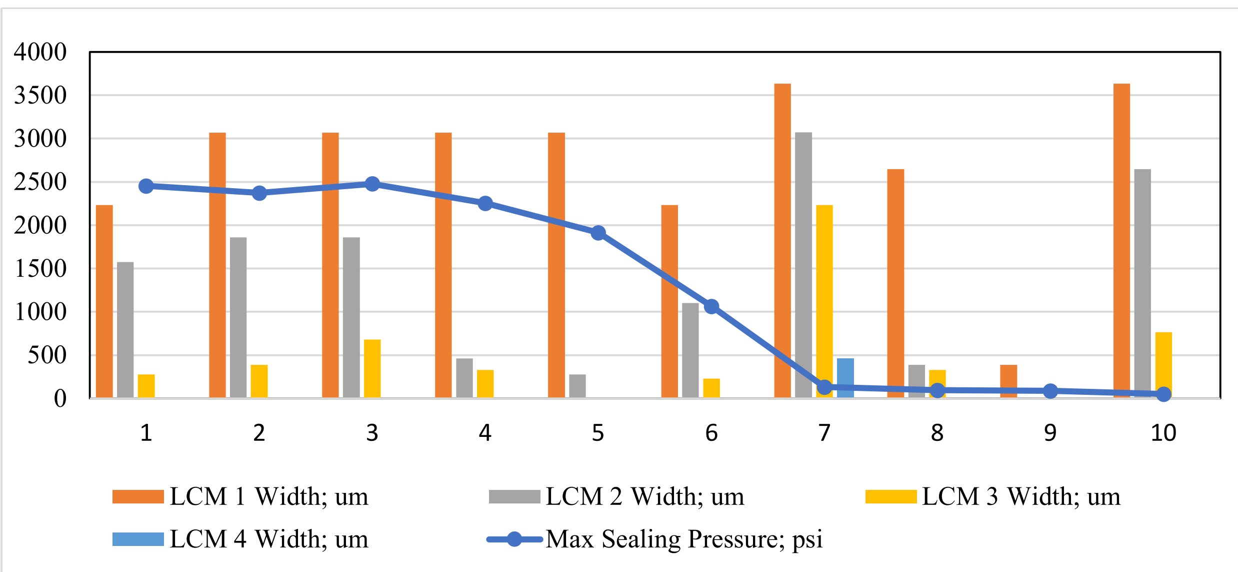

Figure 4.3 Averaged width measurements plotted with LCM slurry maximum sealing pressures obtained using a 3000 µm aperture width slotted disc.

Observing the averaged calculated aspect ratio of each additive, the most successful slurry's third additive was considerably the highest (Figure 4.4). Keeping in mind its fine length and width, it appears that this additive may have acted as a necessary binding agent.

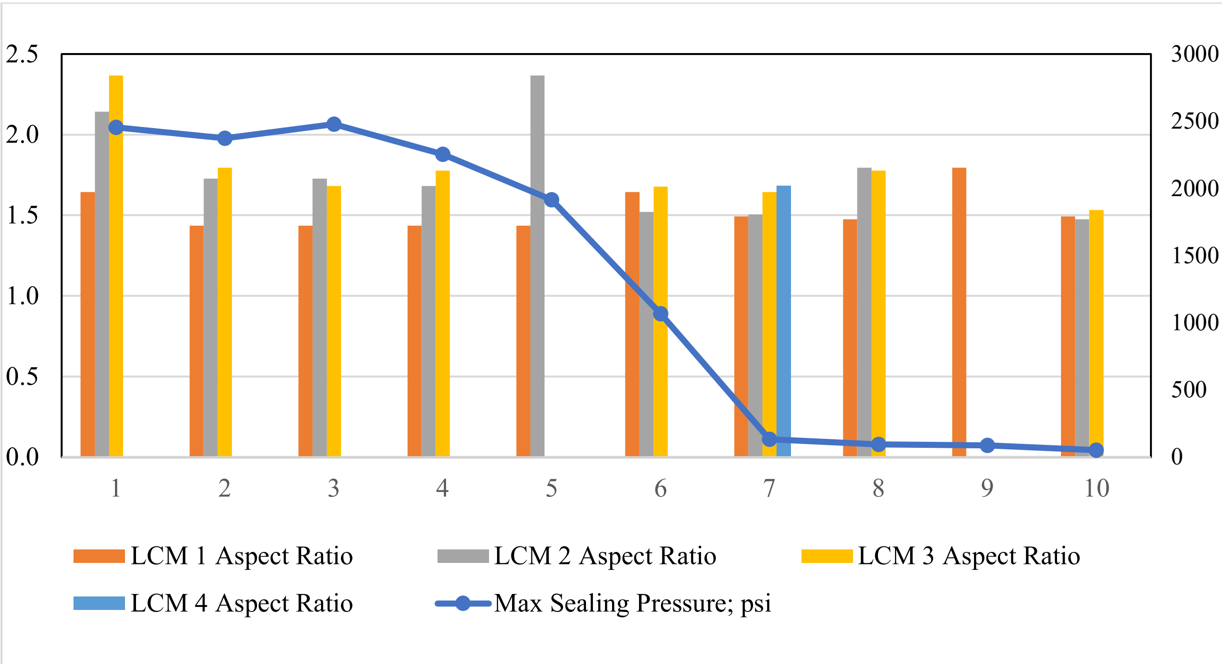

Figure 4.4 Averaged aspect ratio calculations plotted with LCM slurry maximum sealing pressures obtained using a 3000 µm aperture width slotted disc.

Further evidence was found when comparing the fluid loss percentage of the slurries (i.e., the difference in slurries 2 and 3). Slurries 2 and 3 had almost identical additive sizes; however, slurry 2's third additive had a higher aspect ratio. Another difference between the two blends was the concentration of additives. Slurry 2 had a concentration of 20 ppb of its perceived bridging agent and 30 ppb of its perceived binding material. Conversely, slurry 3 consisted of 30 ppb of bridging agent and only 20 ppb of what could be considered its finer binding material.

The bridging and binding theory—or brick & mortar—is further explored by examining the removed seal itself (Figure 4.5). After examining the seal, it was assumed that the larger grains in additives 1 and 2 acted as the primary bridging agent and seal infrastructure. Likewise, the finer and more fibrous additive 3 acted as the necessary filler, or mortar, to create a pressure seal across the testing apertures. Further testing was completed on different sized apertures to test particle sealing roles.

Figure 4.5 Photographs of the seal taken out of the testing cell after slurry 1 was tested.

4.2 2000 µm Aperture Width Slotted Disc Testing

Nine different LCM configurations were evaluated using a pressure step test to 2000 psi, with a 2000 µm slotted disc. Slurry additives and concentrations are noted in Table 4.2.

Table 4.2 Contents of tested LCM blend using a 2000 µm slotted disc

Test	Total Test LCM Blend Concentration	LCM Add #1	LCM Add #2	LCM Add #3	LCM Add #4	LCM Add #5	LCM Add #6
1	50ppb	10ppb - (7) Sieve Mi Swaco Nut Plug Coarse	20ppb - (12) Sieve Mi Swaco Nut Plug Coarse	20ppb - (40) Sieve Mi Swaco VinSeal Medium	-	-	-
2	50ppb	30ppb - (12) Sieve Mi Swaco Nut Plug Coarse	20ppb - (40) Sieve Mi Swaco VinSeal Medium	-	-	-	-
3	40ppb	20ppb - (8) Sieve Mi Swaco Nut Plug Coarse	20ppb - (10) Sieve Mi Swaco Nut Plug Coarse	-	-	-	-
4	60ppb	15ppb - (8) Sieve Mi Swaco Nut Plug Coarse	15ppb - (10) Sieve Mi Swaco Nut Plug Coarse	20ppb - (40) Sieve Mi Swaco Nut Plug Fine	10ppb - (pan) Mi Swaco Mica Fine	-	-
5	52.5ppb	2.5ppb - (6) Sieve Mi Swaco Nut Plug Coarse	20ppb - (12) Sieve Mi Swaco Nut Plug Coarse	20ppb - (140) Sieve Mi Swaco Mica Medium	10ppb - (270) Sieve Mi Swaco Mica Medium	-	-
6	40ppb	20ppb - (10) Sieve Mi Swaco Nut Plug Coarse	20ppb - (40) Sieve Mi Swaco Nut Plug Fine	-	-	-	-
7	65ppb	5ppb - (8) Sieve Mi Swaco Nut Plug Coarse	20ppb - (12) Sieve Mi Swaco Nut Plug Coarse	10ppb - (40) Sieve Mi Swaco Nut Plug Fine	10ppb - (80) Sieve Baroid Wallnut Fine	10ppb - (120) Sieve Mi Swaco Nut Plug Fine	10ppb - (270) Sieve Baroid's Wall Nut Fine
8	50ppb	30ppb - (14) Mi Swaco Mica Coarse	20ppb - (40) Sieve Mi Swaco VinSeal Medium	-	-	-	-
9	40ppb	20ppb - (16) Sieve Mi Swaco Nut Plug Medium	20ppb - (35) Sieve Mi Swaco Nut Plug Fine	-	-	-	-
10	52.5ppb	2.5ppb - (7) Mi Swaco Mica Coarse	10ppb - (10) Mi Swaco Mica Medium	10ppb - (40) Mi Swaco Mica Medium	10ppb - (80) Mi Swaco Mica Fine	10ppb - (120) Mi Swaco Mica Fine	10ppb - (270) Mi Swaco Mica Fine

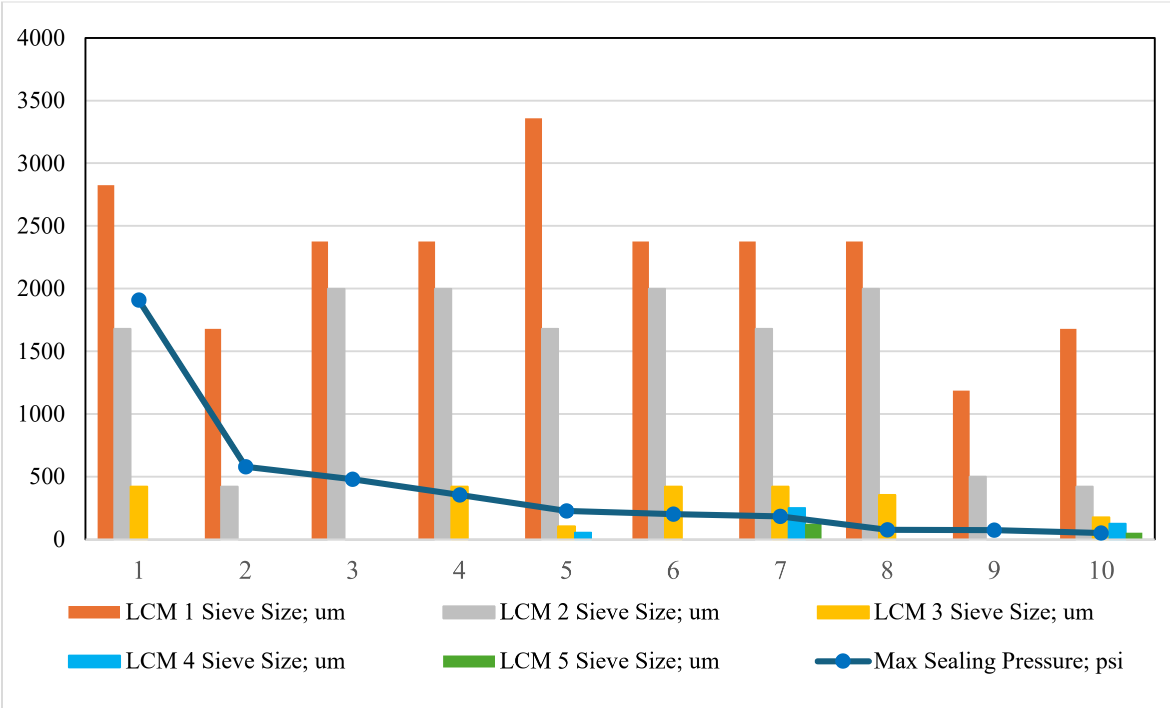

Figure 4.6 Particle mesh size plotted with LCM slurry maximum sealing pressures obtained using a 2000 µm aperture width slotted disc.

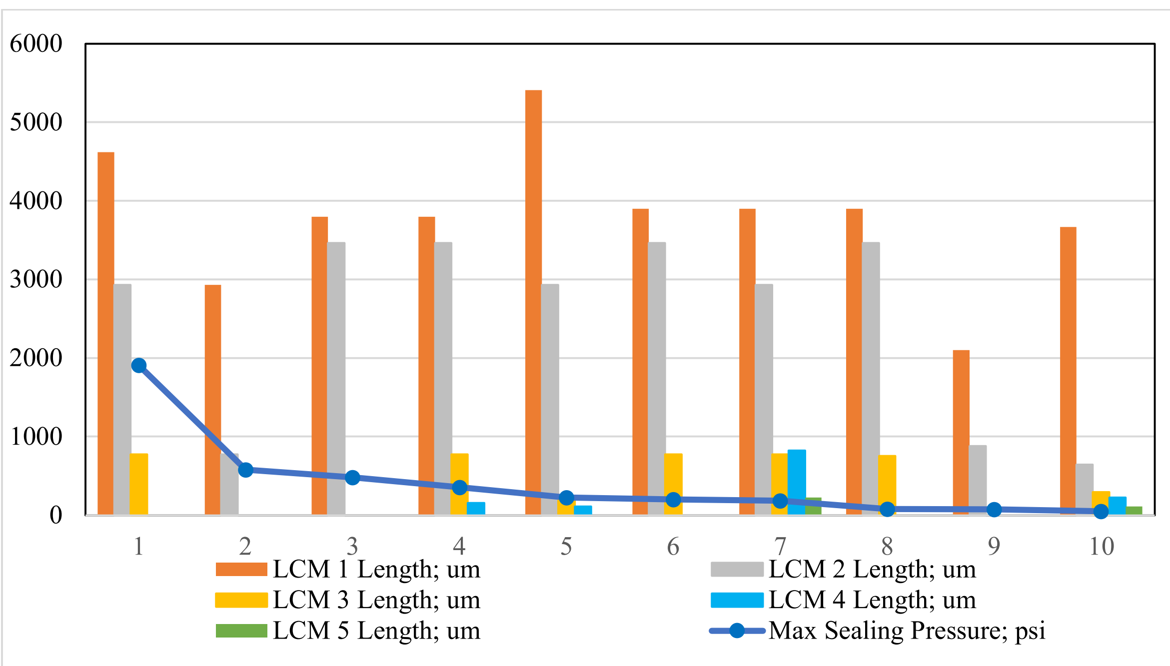

Figure 4.7 Averaged length measurements plotted with LCM blend maximum sealing pressures obtained using a 2000 µm aperture width slotted disc.

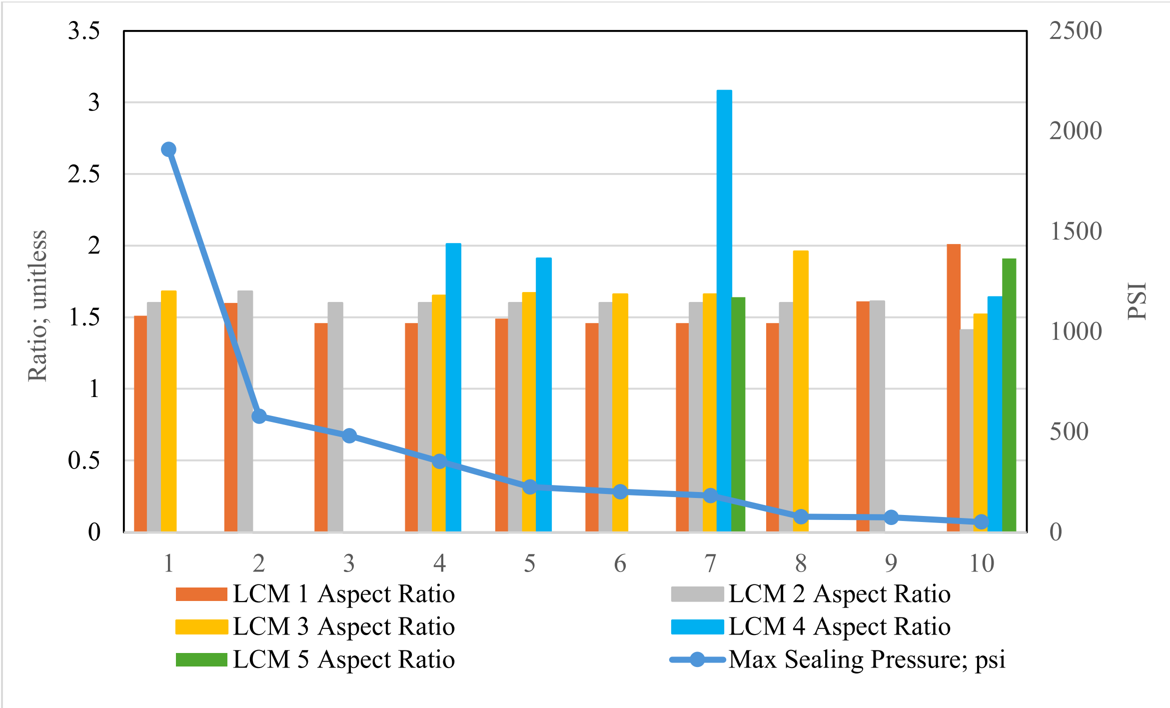

Figure 4.8 Aspect ratio calculations plotted with LCM blend maximum sealing pressures obtained using a 2000 µm aperture width slotted disc.

4.3 1000 µm Aperture Width Slotted Disc Testing

Using the previous success and failure data from the larger aperture testing, a single blend was successfully tested using a 1000 µm width aperture slotted disc. A pre-designed step test to 2500 psi was successfully evaluated with less than 5% fluid loss observed.

Table 4.3 Contents of tested LCM blend using a 1000 µm slotted disc

LCM Additive ppb	LCM Additive	Additive
10	Wall Nut (18)	LCM 1 Additive
10	Wall Nut (60)	LCM 2 Additive
30	VinSeal (120)	LCM 3 Additive
50	*Total LCM ppb*	

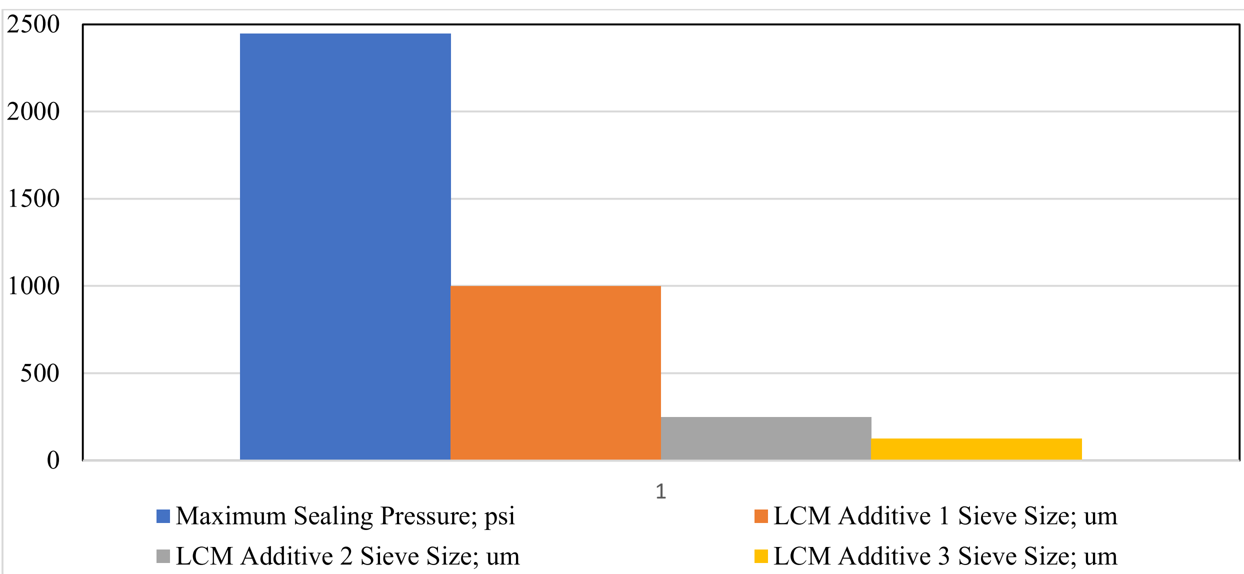

Figure 4.9 Particle mesh size plotted with LCM slurry maximum sealing pressures obtained using a 1000 µm aperture width slotted disc.

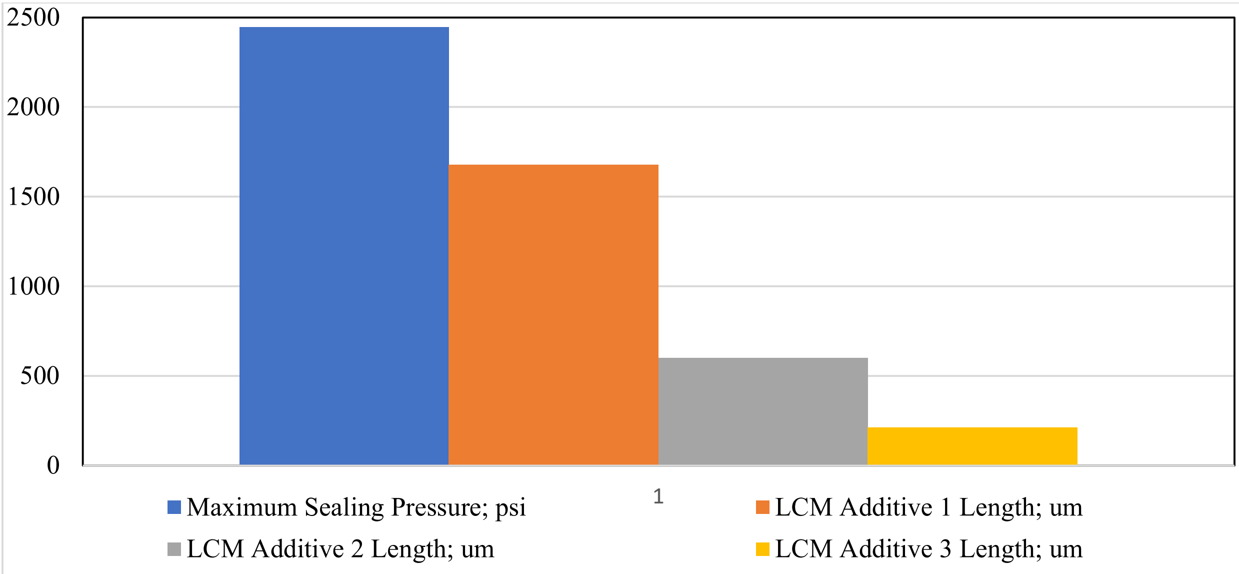

Figure 4.10 Averaged length plotted with LCM blend maximum sealing pressures obtained using a 1000 µm aperture width slotted disc.

LCM additive 1 is assumed to act as the primary bridging agent using either particle width or length. Additive 2 is assumed to be serving as a lower-scale bridging agent—not actually bridging the width of the aperture but creating a smaller matrix by bridging points of contact on additive 1. Additives 1 and 2, given their granular and larger measured traits, are assumed to have created the necessary framework or matrix the created seal.

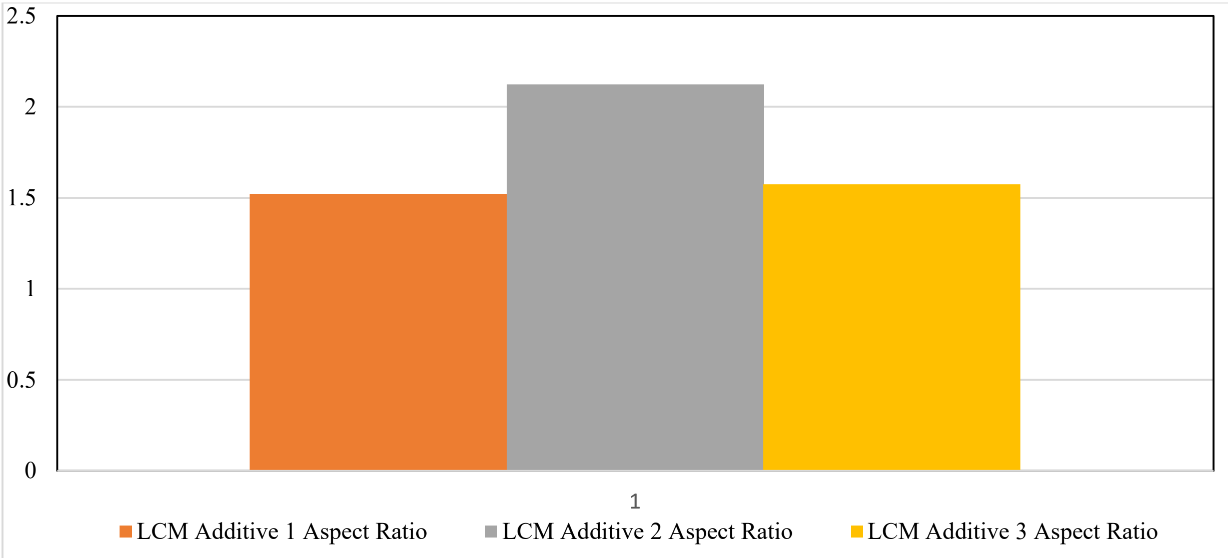

Figure 4.11 Averaged aspect ratio calculations of LCM Blend successfully tested using a 1000 µm aperture width slotted disc

The overall size and lengths of additives 1 and 2 were significantly larger, relative to the aperture width, than the successful blends tested in the previous rounds. The aspect ratio of the binding agent was also significantly less than that found in the previous successful blends. Since the aperture size used in this testing was significantly smaller, the results from this round were secondary. As explained previously, a higher amount of error is believed to exist when testing using a smaller aperture.

CHAPTER 5: CONCLUSIONS

Using dry sieve analysis, a standard PSD was created for each inventoried LCM. This PSD served as the backbone all other measurements and testing data. The PSD allowed the products to be categorized by level of coarseness leading to more efficient methods and error mitigation in the image scanning process. In the image scanning process, materials organized by their coarseness were analyzed and measured. Measurements were taken over their corresponding width ranges to create measured shape distributions.

Each product, separated by a standard mesh size, was used to make tailored LCM test blends that were mixed with a standard test fluid to create a blend slurry. To mitigate error and provide standardization, the fluid was routinely tested to ensure its desired rheological properties. The tailored LCM blend slurry was tested using an APPA. Using pressure step testing, the LCM slurries were evaluated based on their ability to achieve a maximum sealing pressure with minimal losses.

Testing was completed on three separate slotted disc apertures that measured 1000 µm, 2000 µm, and 3000 µm in width. Data gathered from the largest testing aperture was deemed to be the most useful based on slurry concentration versus aperture width. Analyzing the performance data from each round of testing, the following conclusions serve as rules of thumb.

An LCM blend should be filled with three separate material sizes to successfully fill the following roles:

1. *Primary Bridge*: The primary bridging particulate should be approximately 75% of dry-sieved mesh size of the aperture width, while the length should be approximately 120% of the aperture size.
2. *Secondary Bridge or Matrix Building*: The secondary or matrix building particulate should be approximately 75% of dry-sieved mesh size and the length of the primary bridging particulate's mesh size.
3. *Binding or Mortar Material*: The binding or mortar material should be approximately 1/8 or 12.5% of dry-sieved mesh size of the primary bridging particulate and its average aspect ratio should be at least 120% of the bridging particulates.

It was determined by observing and analyzing testing data, and conducting post-test seal analysis, that the properties listed above can be used to create a strong impermeable seal across apertures of *known* widths. The best type of inventoried LCM was ground nutshells and cellulose fibers. The larger granular ground nutshells facilitated the creation of a seal framework and created a matrix. The finely ground, more-fibrous cellulose fibers, gave the seal its impermeable nature to close the seal at a finer level.

This study also resulted in a substantial data set with shape, size, and performance data of known LCM available throughout the industry. This data can be used, moving forward to further engineer LCM blends various applications.

CHAPTER 6: RECOMMENDED FUTURE WORKS

Recommendations in future studies to build on this research and provide further supporting evidence and material related to LOC prevention and remediation are presented in the sections that follow.

6.1 Seek Out Further Test LCM

With a working LOC Laboratory located at the Colorado School of Mines, the effort should be made to further expand the lab's testing portfolio and data set. Measuring and testing of a higher range of product characteristics will bring about further understanding of aperture sealing physics. The result may produce new standards and rules that could further build on a comprehensive engineered workflow to study LCM in a lab setting or various field conditions.

6.2 Slot Testing and Procedures

To complete this study, slot testing was conducted using a stepped-up pressure approach, building pressure in 500 psi increment to a maximum desired sealing pressure. It was concluded that a step test was necessary in this study the initial evaluation of principles and tailored LCM blends. However, moving forward, these principles and tested blends should be tested by attempting to build sealing pressure more quickly. An immediate or quick pressure build rate would provide more representative wellbore conditions given that wellbore fluid pressure is not typically stepped up when entering a loss zone. These tests should be completed with constant vigilance and with LCM blends proven during step testing avoid exceeding the rated differential pressure across the APPA floating piston's rupture disc, which could cause a mechanical failure.

6.3 Fine Materials Analysis

This study, due to the large apertures being used in testing, focused on medium and coarse material analysis. Further research should be conducted on the finer materials that could aid in seepage-loss mitigation or help design a better binding particulate larger LCM blends. To successfully measure the PSDs of these fines, a laser particle analyzer should be used. Fines could be tested to address seepage by using filtrate discs of pre-designed grain size and permeability in lieu of the steel slotted discs used in this study.

6.4 Pump-Ability Experiment Design

Materials evaluated in this study were tested under lab conditions, specifically using an APPA. Any inability to pump LCM-laden fluid was assumed to be due to a seal forming at the desired test aperture. In practical field application, these slurries will have to successfully pass through a myriad of lines, valves, pumps, downhole tools, and bit nozzles to eventually reach the rock. A series of experiments should be designed to evaluate a designed LCM-laden fluid's ability to pass through a series of obstacles not related to its intended target. These experiments could include a flow loop in line with a progressive cavity pump and a series of pulsers and nozzles to simulate pumping through a drilling bottom hole assembly.

6.5 LCM with Cuttings Analysis and Testing

In this study, LCM was mixed in a 25-ppb bentonite and freshwater mud. The only desired solids within each tested slurry were LCM and bentonite. Adding cuttings of different lithology, sizes, and shapes may provide insight into how these materials interact and potentially seal with solids found in the wellbore. Cuttings could be pulled from known problematic areas and intervals and mixed with LCM blends at different concentrations. This study may lead to "While-Drilling" LCM materials and blends.

REFERENCES

Al Maskary, S., Halim, A. A., and Al Menhali, S. 2014. Curing Losses While Drilling & Cementing. Paper presented at the Abu Dhabi International Petroleum Exhibition and Conference, Abu Dhabi, UAE, 10-13 November. SPE-171910-MS. https://doi.org/10.2118/171910-MS

Alberty, M. W. and McLean, M. R. 2004. A Physical Model for Stress Cages. Paper presented at the SPE Annual Technical Conference and Exhibition, Houston, Texas, 26-29 September. SPE-90493-MS. https://doi.org/10.2118/90493-MS

Dupriest, F. E. Fracture Closure Stress (FCS) and Lost Returns Practices. 2005. Paper presented at the SPE/IADC Drilling Conference, Amsterdam, Netherlands, 23-25 February. SPE-92192-MS. https://doi.org/10.2118/92192-MS

Dyke, C. G., Wu, B., and Milton-Tayler, D. 1995. Advances in Characterizing Natural-Fracture Permeability From Mud-Log Data. *SPE Form Eval* (10): 160–166. SPE-25022-PA. https://doi.org/10.2118/25022-PA

Fekete, P. O., Adewale, D., Kuerunwa, A., Ekeinde, E. B., Chimaroke, A., and Baridor S. O. 2013. Wellbore Stability Management In Depleted And Low Pressure Reservoirs. Paper presented at the SPE Nigeria Annual International Conference and Exhibition, Lagos, Nigeria, 30 July – 1 August. SPE-167543-MS. https://doi.org/10.2118/167543-MS

Kumar, A., Chellappah, K., Aston, M., and Bulgachev, R. 2013. Quality Control of Particle Size Distributions. Paper presented at the SPE European Formation Damage Conference & Exhibition, Noordwijk, The Netherlands, 5-7 June. SPE-165150-MS. https://doi.org/10.2118/165150-MS

Luzardo, J., Oliveira, E. P., Derks, P. W. J., Nascimento, R. V., Gramatges, A. P., Valle, R., Pantano, I. G., Sbaglia, F., and Inderberg, K. 2015. Alternative Lost Circulation Material for Depleted Reservoirs. Paper presented at the OTC Brasil, Rio de Janeiro, Brazil, 27-29 October. OTC-26188-MS. https://doi.org/10.4043/26188-MS

Mitchell, R. F., Miska, S. Z. 2011. *Fundamentals of Drilling Engineering,* Vol. 12, Chap. 3 & 10. Richardson, Texas: Society of Petroleum Engineers.

Nelson, P. H. 2009. Pore-throat Sizes in Sandstones, Tight Sandstones, and Shales. *AAPG* 93 (3): 329–340. https://doi.org/10.1306/10240808059

Nolte, K. G., and Smith, M.B. 1981. Interpretation of Fracturing Pressures. Lessons Learned (contains highlights of paper SPE 8297 prepared for the 1979 SPE Annual Technical Conference and Exhibition by K.G. Nolte and M.B. Smith). *J Pet Technol* (33): 1767–1775. https://doi.org/10.2118/8297-PA

Patel, A., Singh, A. K., Bidwai, N., Indulkar, S., and Gupta, V. 2021. Innovative Surfactant Chemistry Offers the Performance Advantages to Invert Emulsion Drilling Fluids While Drilling Under Challenging Environments. Paper presented at the SPE International Conference on Oilfield Chemistry, The Woodlands, Texas, USA, 6-7 December. SPE-204362-MS. https://doi.org/10.2118/204362-MS

Rahil, A. 2007. Drilling Performance Management System. Paper presented at the International Petroleum Technology Conference, Dubai, U.A.E, 4-6 December. IPTC-11099. https://doi.org/10.2523/IPTC-11099-MS

Scheldt, T., Andrews, J.S., and Lavrov, A. 2020. Understanding Loss Mechanisms: The Key to Successful Drilling in Depleted Reservoirs?. *SPE Drill & Compl* 35: 180–190. SPE-195605-PA. https://doi.org/10.2118/195605-PA

Sun, J., Bai, Y., Cheng, R., Lyu, K., Liu, F., Feng, J., Lei, S., Zhang, J., Hao, H. 2021. Research progress and prospect of plugging technologies for fractured formation with severe lost circulation. *Petroleum Exploration and Development* 48 (3), 732-743, https://doi.org/10.1016/S1876-3804(21)60059-9

van Oort, E., Friedheim, J., Pierce, T., and Lee, J. 2011. Avoiding Losses in Depleted and Weak Zones by Constantly Strengthening Wellbores. *SPE Drill & Compl* 26: 519–530. SPE-125093-PA. https://doi.org/10.2118/125093-PA

Vasquez, J., Flores, A., Anggarawinata, R., Thien, V. H. J., Chan, L., and Yaakub, N. I. H. 2022. Innovative Spacer Solution to Control Losses While Cementing in Permeable and Depleted Formations. Paper presented at the International Petroleum Technology Conference, Riyadh, Saudi Arabia, 21-23 February. IPTC-22630-MS. https://doi.org/10.2523/IPTC-22630-MS

Wang, H., Towler, B. F., and Soliman, M. 2007. Fractured Wellbore Stress Analysis: Sealing Cracks To Strengthen a Wellbore. Paper presented at the SPE/IADC Drilling Conference, Amsterdam, The Netherlands, 20-22 February. SPE-104947-MS. https://doi.org/10.2118/104947-MS

APPENDIX A

DATA SET OF SAMPLE PARTICLES

Table A.1 illustrates example output from the Clemex Image Scanner.

Table A.1 Data set generated by Clemex software for particles in a sample.

Asp Ratio	Compact-ness	Round-ness	Sphericity	Length (µm)	Main Length (µm)	Width (µm)	Sphere Diam (µm)
1.17016	0.87821	0.79578	0.88231	785.47034	768.25885	671.24860	858.16846
1.39939	0.73227	0.57824	0.73746	718.18903	713.49500	513.21570	668.86328
1.37795	0.87912	0.68028	0.88211	821.45807	816.76398	596.14386	829.80310
1.69024	0.78799	0.52821	0.78407	1084.32458	1074.93652	641.51959	965.17560
1.45701	0.84996	0.60614	0.84643	1007.65521	976.36157	691.58942	960.82507
1.10794	0.81142	0.73685	0.74961	851.18701	810.50525	768.25885	894.86975
1.12000	0.85174	0.76368	0.83950	876.22192	832.41083	782.34100	937.81366
2.12748	0.69962	0.42290	0.68543	1175.07617	1129.70044	552.33276	935.89716
1.31938	0.87122	0.68315	0.86572	937.24451	905.95087	710.36560	948.75848
1.33484	0.90653	0.70438	0.90320	923.16235	920.03302	691.58942	948.91620
1.57764	0.72379	0.47154	0.69955	1192.28772	1114.05359	755.74139	1002.73553
1.30602	0.87618	0.68737	0.85789	848.05762	815.19934	649.34302	861.12744
1.88426	0.75144	0.47422	0.73570	1273.65112	1268.95715	675.94263	1074.20032
2.19624	0.71930	0.40775	0.69288	1278.34521	1256.43970	582.06171	999.74677
1.35321	0.89992	0.66763	0.90995	923.16235	901.25684	682.20135	923.82886
1.20082	0.85105	0.69505	0.84174	916.90363	913.77429	763.56482	936.21680
1.54526	0.79243	0.52514	0.72855	1121.87695	1098.40674	726.01245	995.69763
1.23091	0.78789	0.64064	0.76563	1034.25476	1034.25476	840.23425	1013.86499
1.35729	0.87428	0.62218	0.86244	1034.25476	1010.78455	762.00012	999.14789
2.28608	0.71596	0.42072	0.68980	1412.90784	1406.64917	618.04938	1122.42627
1.34000	0.85272	0.68101	0.82784	838.66956	821.45807	625.87280	847.64276
1.86280	0.76992	0.51928	0.75267	956.02069	954.45599	513.21570	843.75037
1.45796	0.85519	0.63872	0.80791	1031.12549	1029.56079	707.23627	1009.27972

APPENDIX B

RAW SIEVE AND IMAGE DATA

Table B.1 illustrates an example of manually gathered sieving measurements and an output from the Clemex Image Scanner.

Table B.1 Raw sieve data compared to raw image data

Raw Sieve Data						Raw Image Data							
Sieve Size #	Part Sz (mm)	Cum Wt (g)	Weight (g)	Volume (mL)	% Parti-culates	Asp Ratio	Compact-ness	Round-ness	Spheri-city	Length (µm)	MainLen (µm)	Width (µm)	SpherDiam (µm)
4	4750	0.00	0.00	0.00	0.00	1.7294	0.6251	0.4140	0.4525	1728.4790	1719.1530	999.4715	1362.1774
5	3994	0.00	0.00	0.00	0.00	1.4488	0.8415	0.6362	0.8159	1430.0370	1419.1560	987.0364	1396.9638
6	3359	0.00	0.00	0.00	0.00	1.2995	0.9029	0.7177	0.8668	1274.5980	1158.0190	980.8188	1322.4655
7	2824	0.00	0.00	0.00	0.00	1.1984	0.7674	0.6799	0.6696	1162.5590	1123.4420	970.1028	1174.0287
8	2375	0.00	0.00	0.00	0.00	1.2864	0.9012	0.7157	0.8678	1221.7490	1220.1950	949.7311	1265.8727
10	1997	0.00	0.00	0.00	0.00	1.6327	0.6838	0.4845	0.5079	1520.1920	1517.0830	931.0784	1295.9605
12	1679	0.00	0.00	0.00	0.00	1.5815	0.8189	0.5784	0.7733	1472.3660	1469.2360	930.9858	1371.4166
14	1412	0.00	0.00	0.00	0.00	2.1587	0.6336	0.3924	0.5042	1979.3230	1952.7230	916.9036	1518.5576
16	1188	0.00	0.00	0.00	0.00	1.4154	0.8530	0.6757	0.8255	1295.5570	1276.7810	915.3390	1304.3135
18	999	0.00	0.00	0.00	0.00	1.6856	0.7549	0.4971	0.6530	1534.9530	1486.4480	910.6449	1325.4789
20	840	5.15	5.15	9.16	1.83	1.9640	0.6616	0.4038	0.6049	1779.7740	1758.0130	906.2083	1385.1812
25	706	14.65	9.50	16.90	3.38	1.7057	0.7283	0.5065	0.6390	1540.3990	1529.5180	903.0994	1342.6332
30	594	23.41	8.76	15.58	3.12	1.5269	0.7593	0.5285	0.6504	1378.4850	1378.4850	902.8215	1227.3640
35	499	93.39	69.98	124.50	24.90	1.5810	0.7664	0.5448	0.6486	1425.3740	1417.6020	901.5450	1288.5330
40	420	174.94	81.55	145.08	29.02	1.7344	0.6736	0.4319	0.5401	1552.8340	1551.2790	895.3275	1249.7896
45	353	198.65	23.71	42.18	8.44	1.8947	0.6532	0.4213	0.4886	1689.8570	1635.0930	891.8687	1343.4188
50	297	203.59	4.94	8.79	1.76	1.2616	0.8794	0.7133	0.8530	1102.0610	1097.3980	873.5661	1139.9254
60	250	206.75	3.16	5.62	1.12	1.7110	0.7045	0.5164	0.6306	1491.1420	1489.5770	871.5279	1312.4331
70	210	219.06	12.31	21.90	4.38	1.6475	0.8188	0.5622	0.7877	1433.2490	1392.5670	869.9632	1316.1898
80	177	240.70	21.64	38.50	7.70	1.2581	0.8980	0.7318	0.8752	1090.5830	1060.8540	866.8338	1142.6398
100	148	263.18	22.48	39.99	8.00	1.7604	0.8093	0.4978	0.7825	1507.7560	1422.2650	856.4678	1302.8922
120	125	272.45	9.27	16.49	3.30	1.3400	0.8309	0.6484	0.7246	1145.5840	1123.8230	854.9134	1129.7765

APPENDIX C

PRODUCT PARTICLE SIZE DISTRIBUTIONS

These particle size distributions were created using measurements obtained through sieving each lost circulation material in a lab setting.

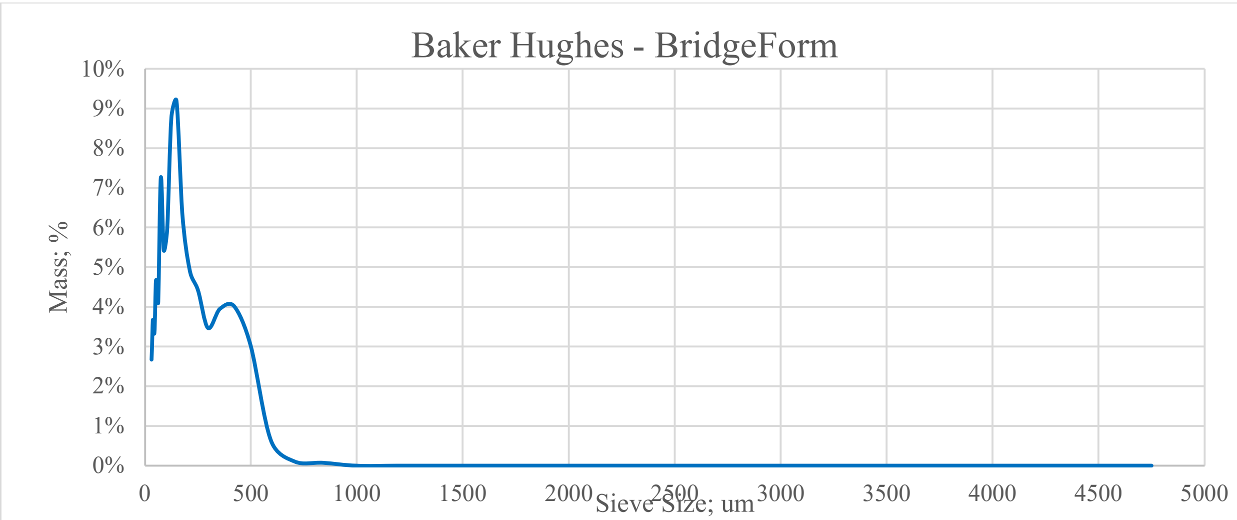

Figure C.1 Particle-size distribution determined by sieving Baker Hughes' BridgeForm

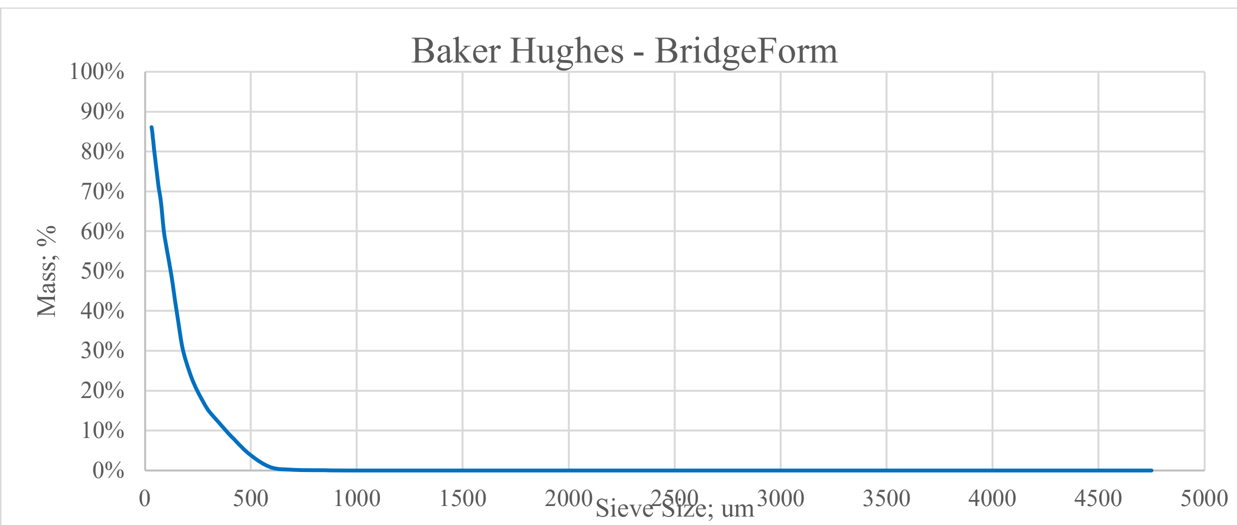

Figure C.2 Cumulative particle-size distribution determined by sieving Baker Hughes' BridgeForm

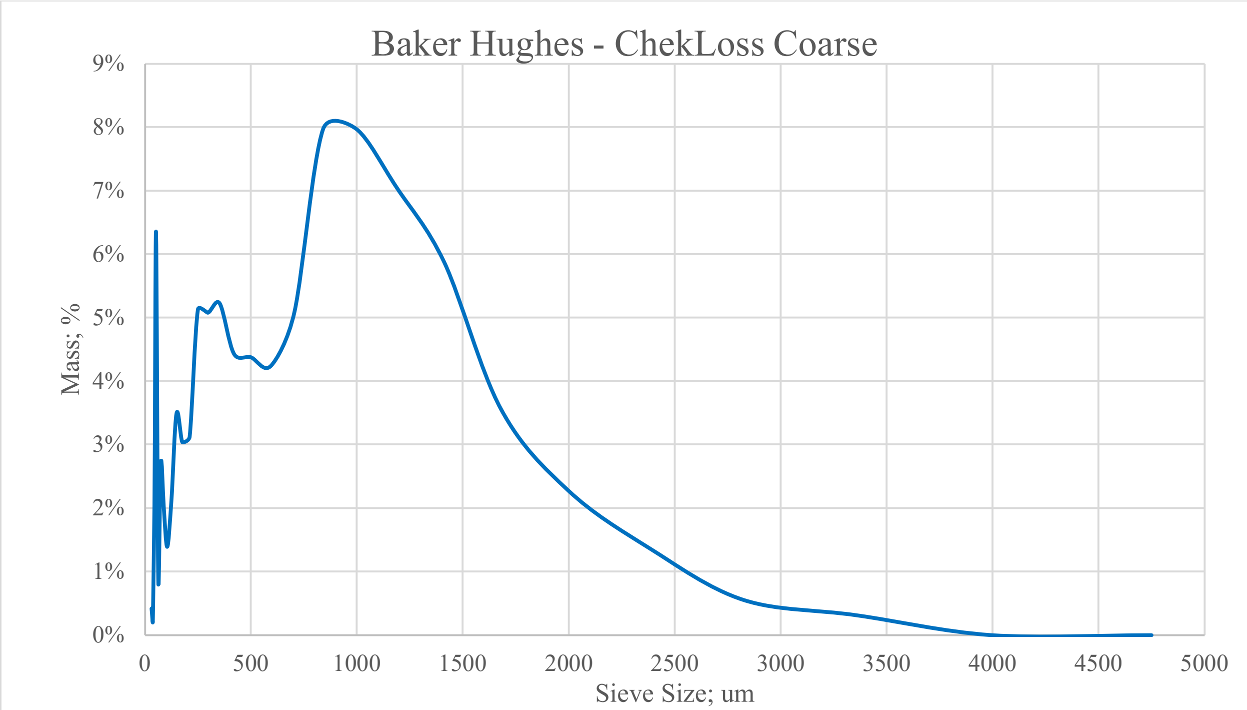

Figure C.3 Particle-size distribution determined by sieving Baker Hughes' ChekLoss

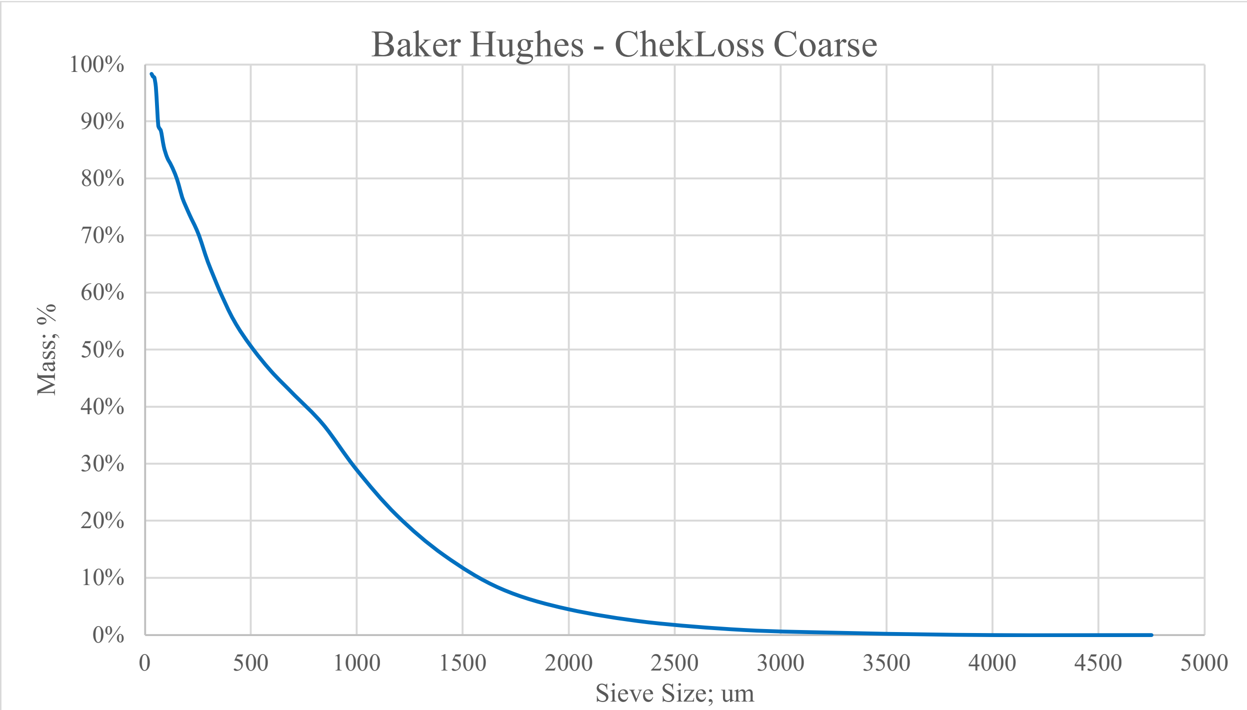

Figure C.4 Cumulative particle-size distribution determined by sieving Baker Hughes' ChekLoss

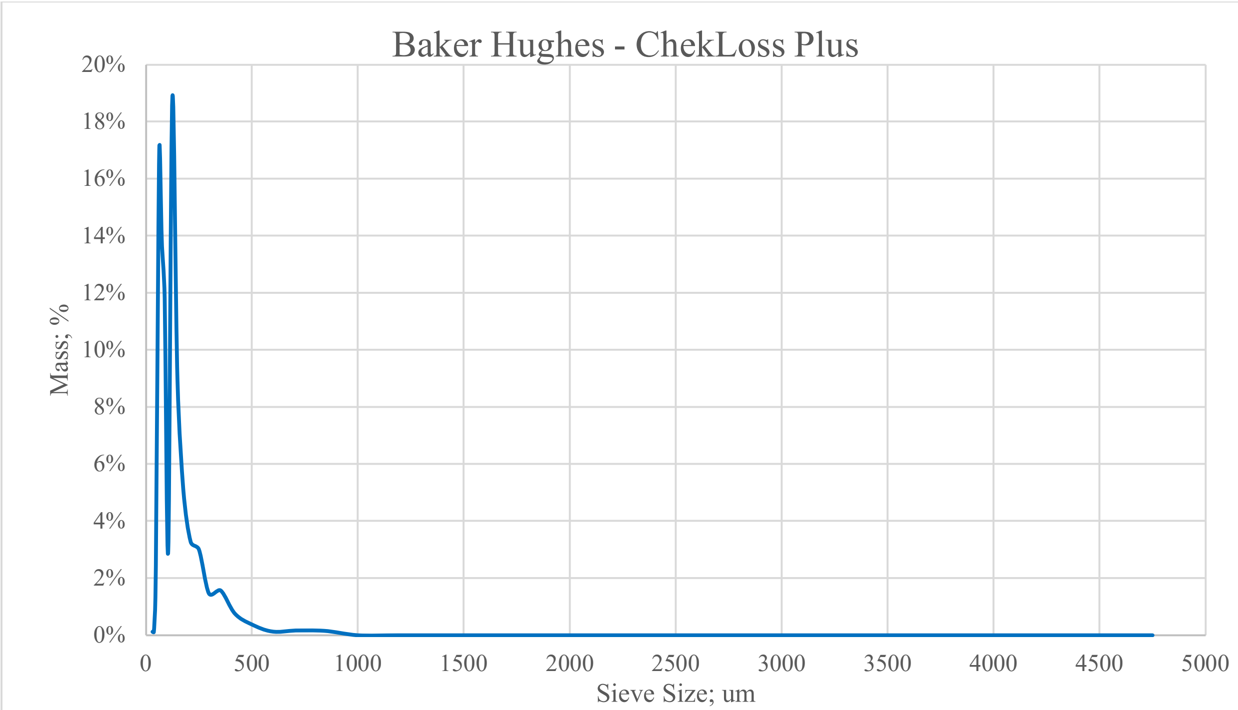

Figure C.5 Particle-size distribution determined by sieving Baker Hughes' ChekLoss Plus

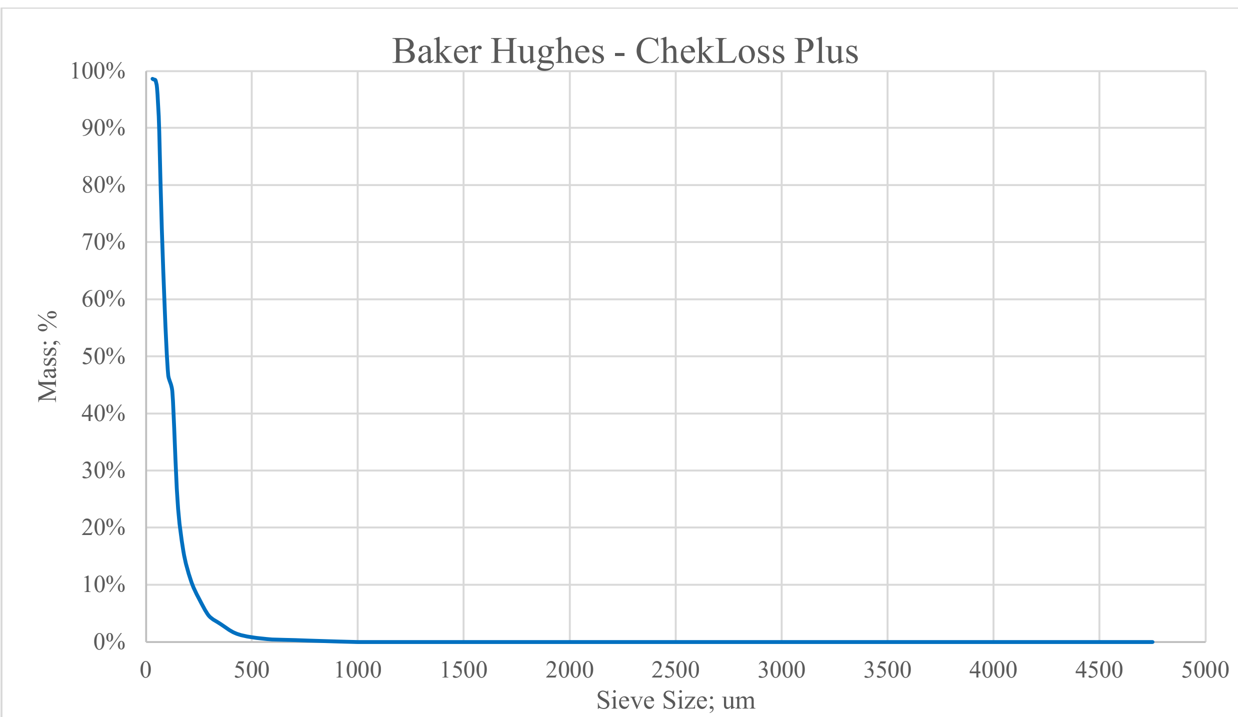

Figure C.6 Cumulative particle-size distribution determined by sieving Baker Hughes' ChekLoss Plus

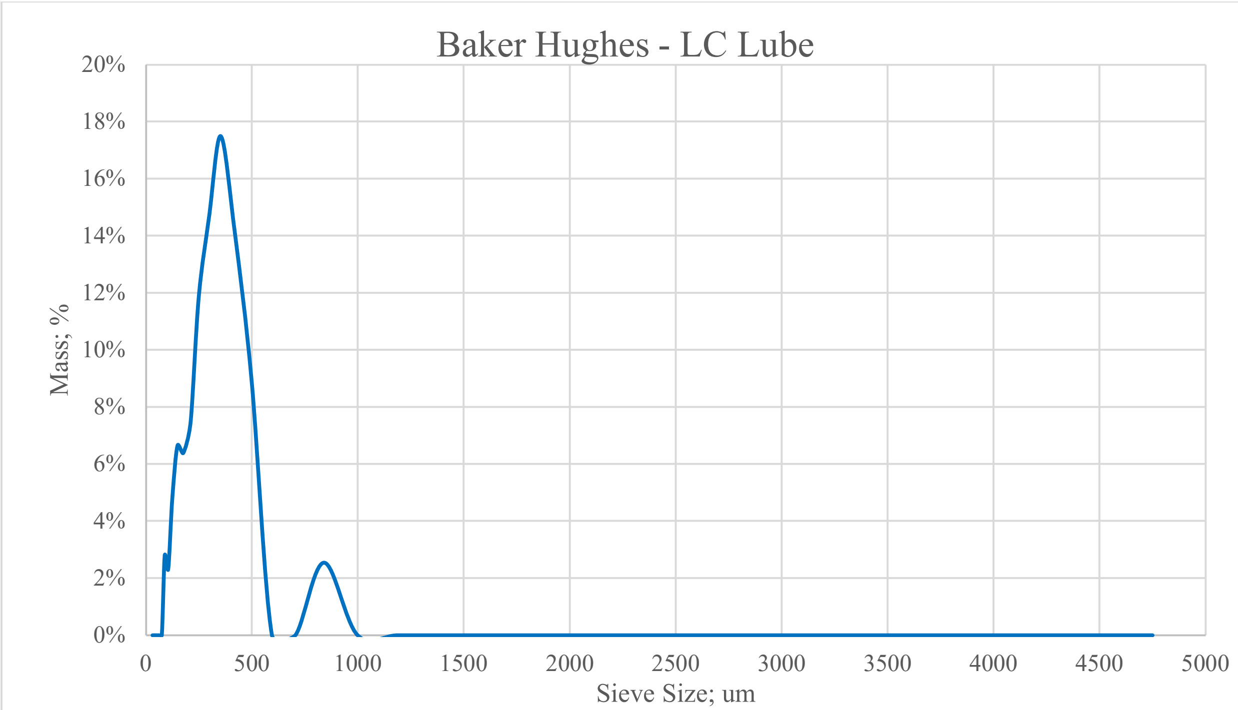

Figure C.7 Particle-size distribution determined by sieving Baker Hughes' LC Lube

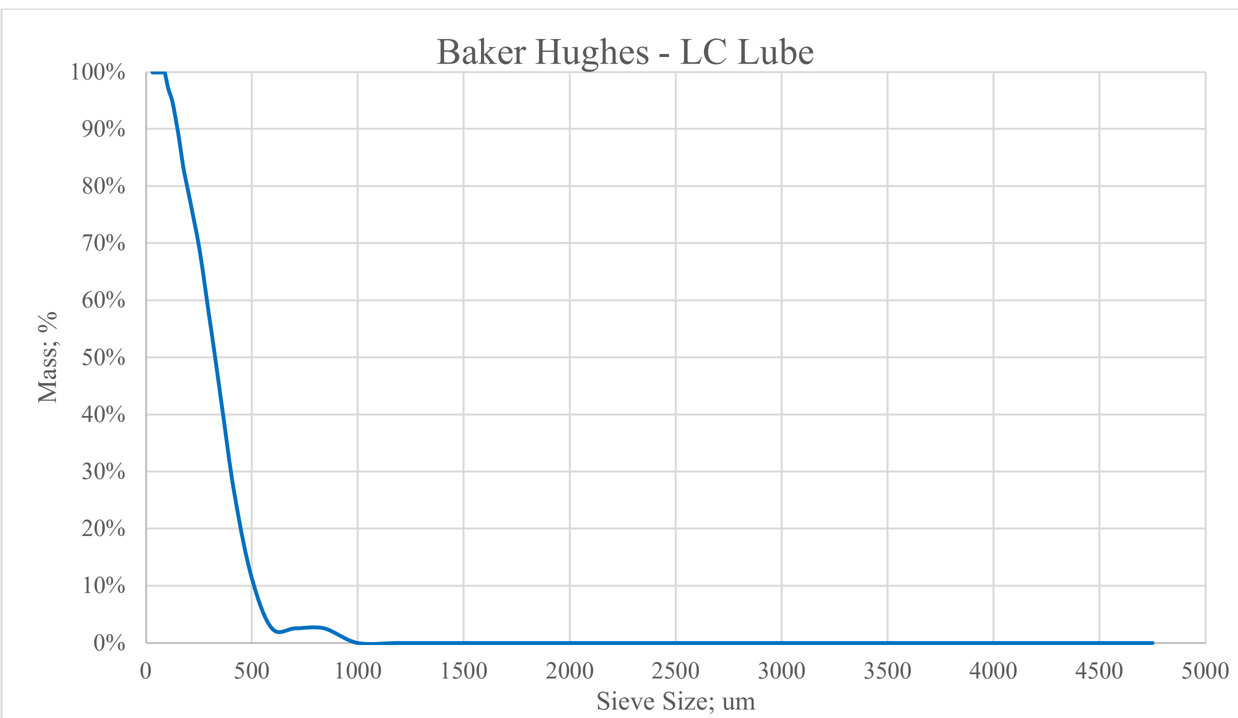

Figure C.8 Cumulative particle-size distribution determined by sieving Baker Hughes' LC Lube

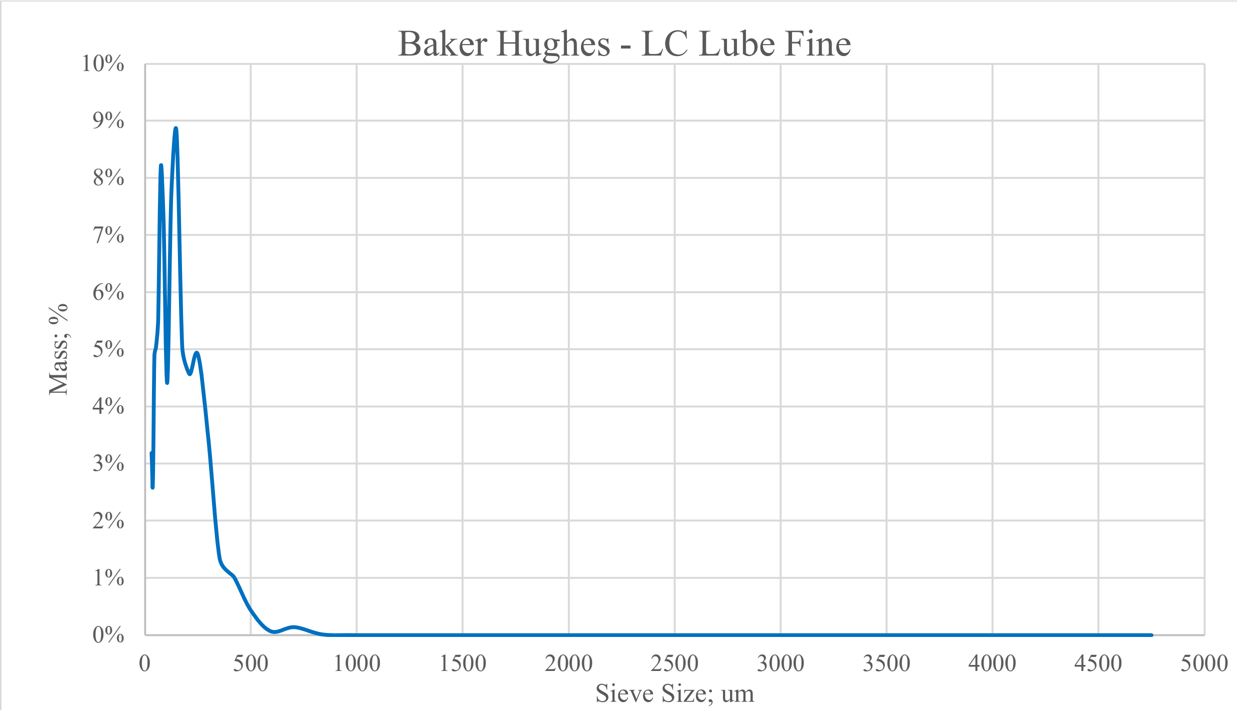

Figure C.9 Particle-size distribution determined by sieving Baker Hughes' LC Lube Fine

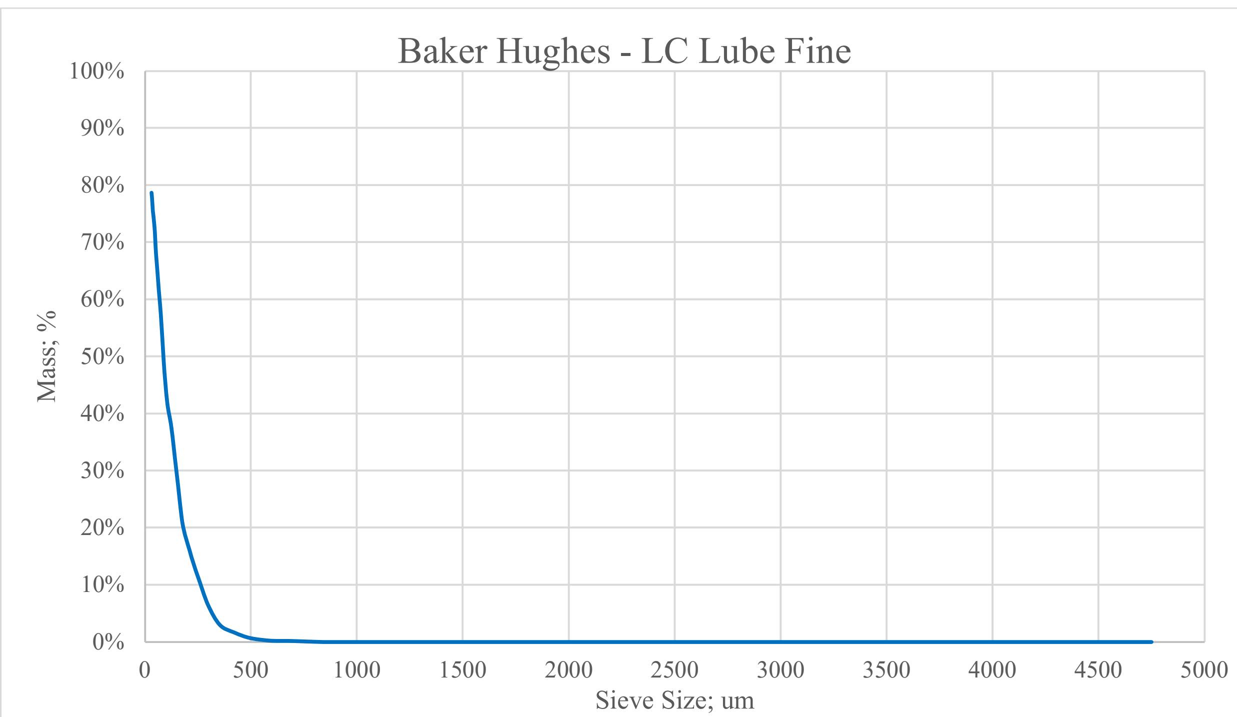

Figure C.10 Cumulative particle-size distribution determined by sieving Baker Hughes' LC Lube Fine

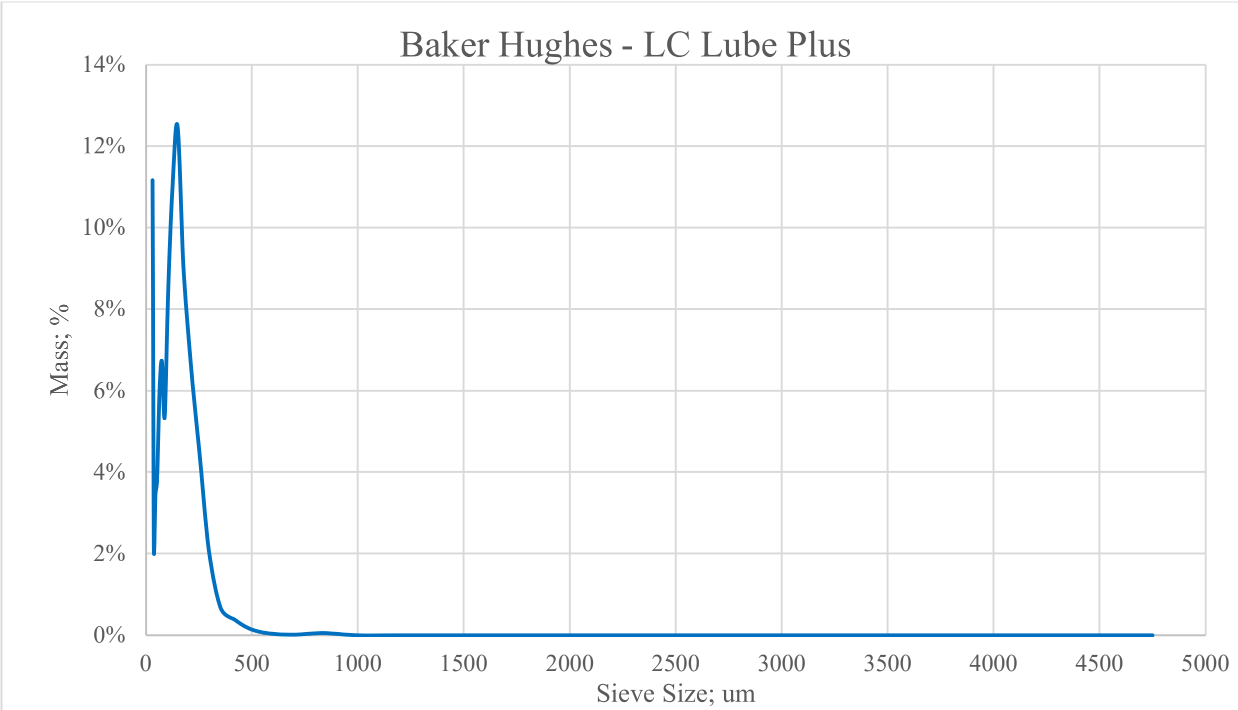

Figure C.11 Particle-size distribution determined by sieving Baker Hughes' LC Lube Plus

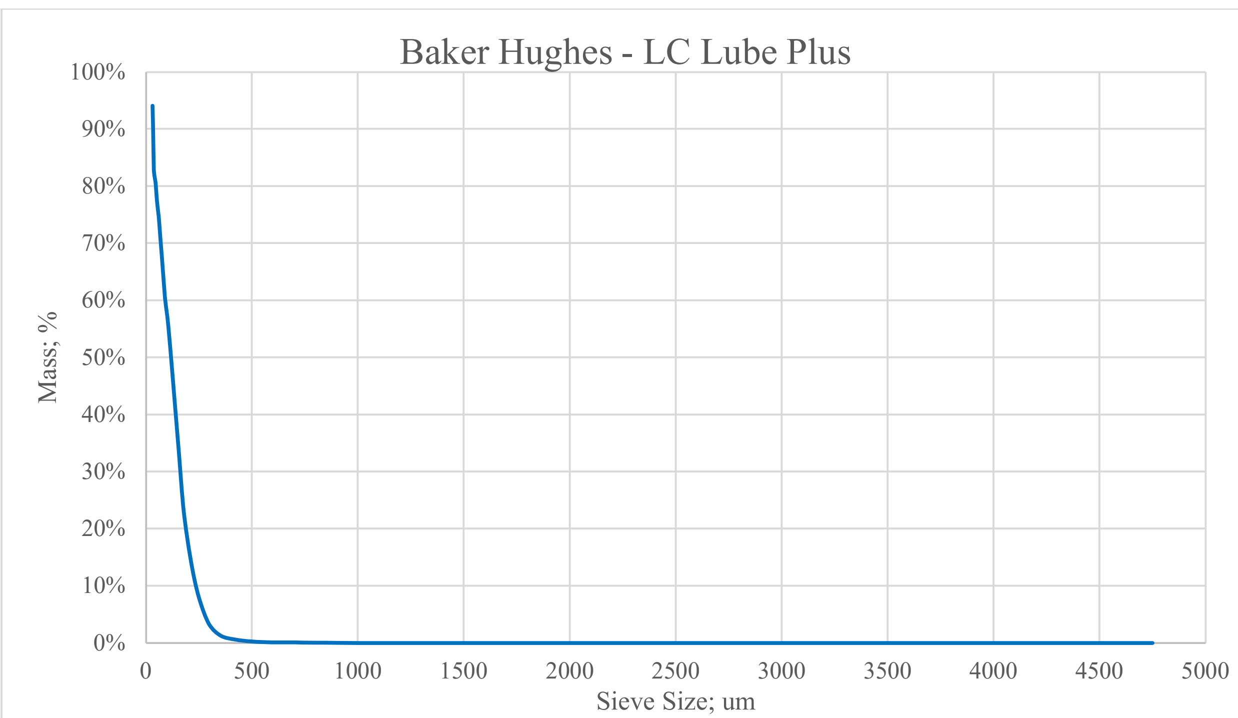

Figure C.12 Cumulative particle-size distribution determined by sieving Baker Hughes' LC Lube Plus

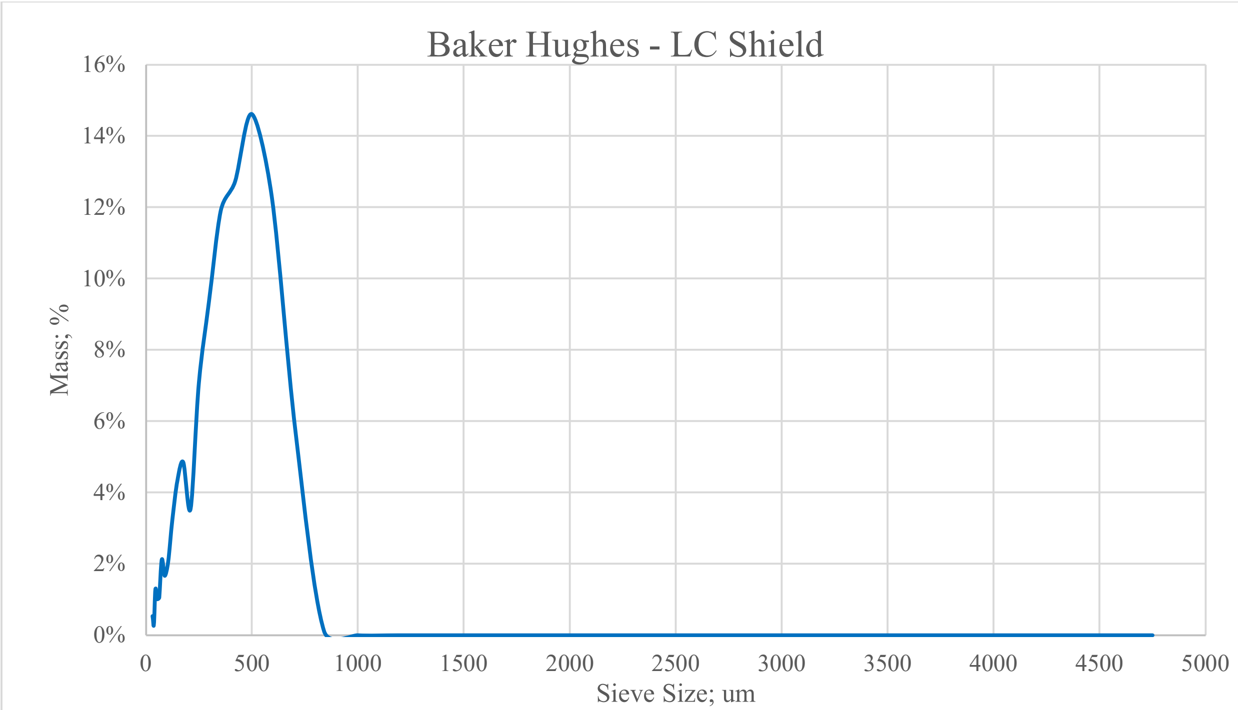

Figure C.13 Particle-size distribution determined by sieving Baker Hughes' LC Shield

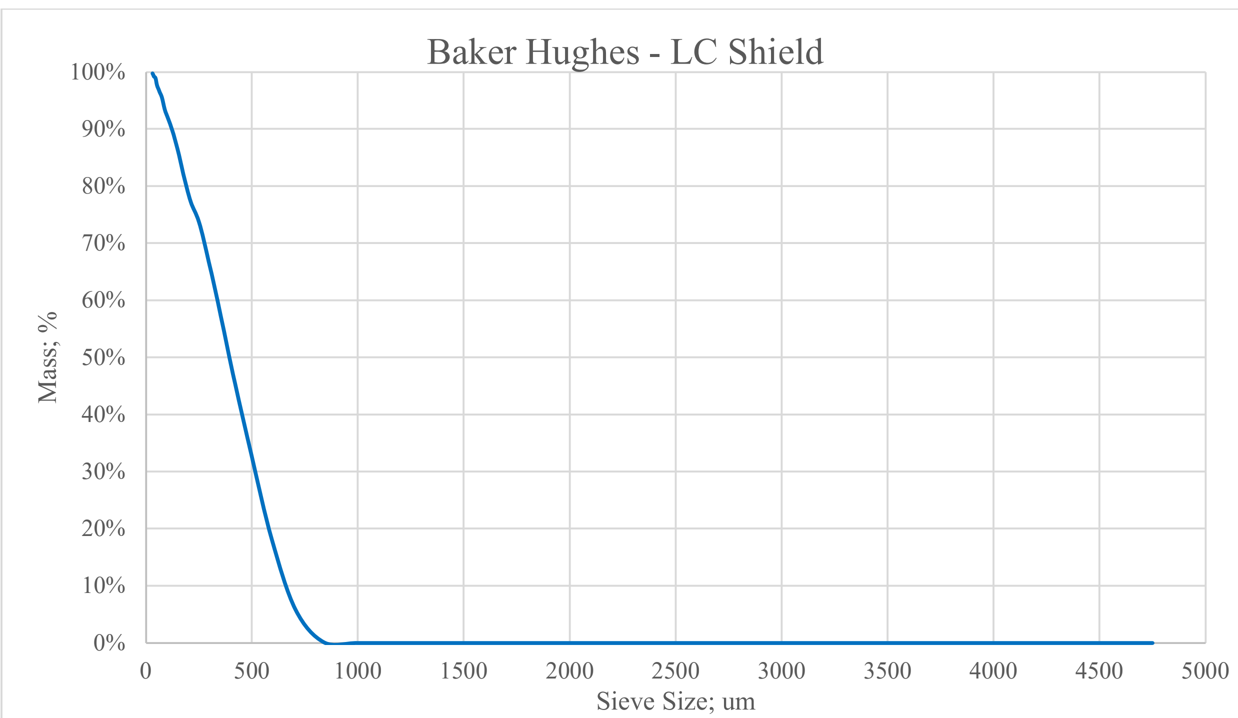

Figure C.14 Cumulative particle-size distribution determined by sieving Baker Hughes' LC Shield

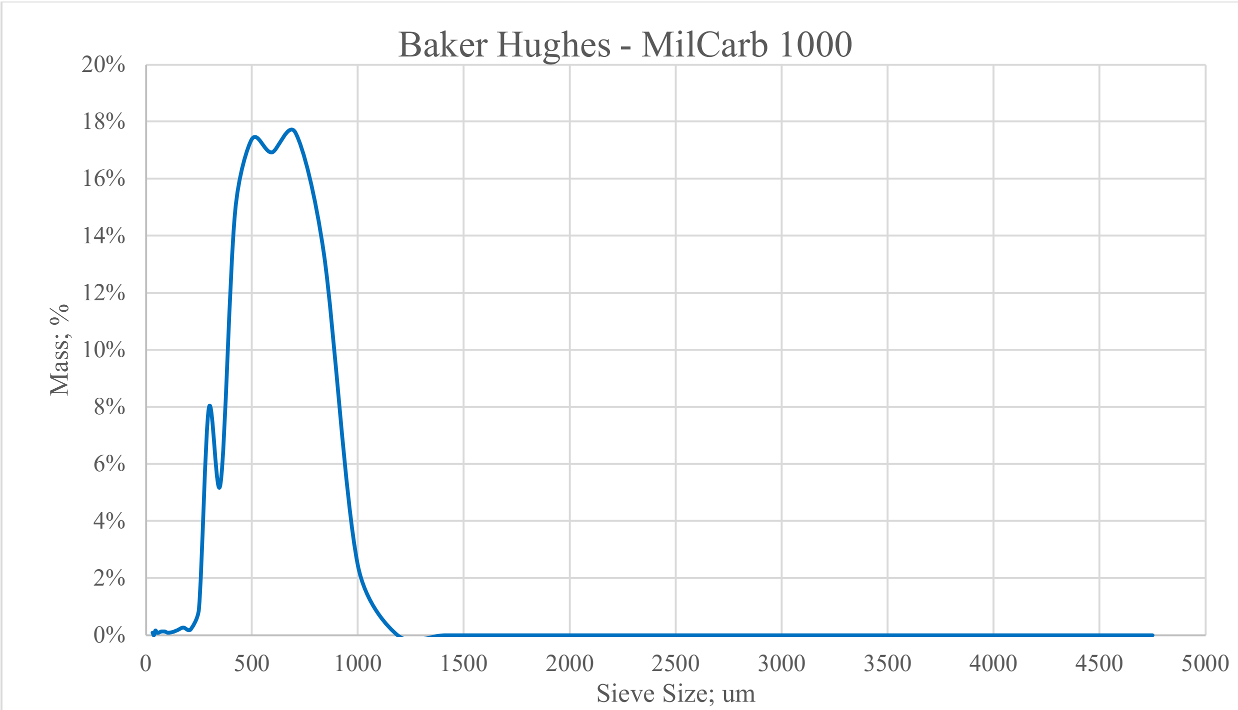

Figure C.15 Particle-size distribution determined by sieving Baker Hughes' MilCarb 1000

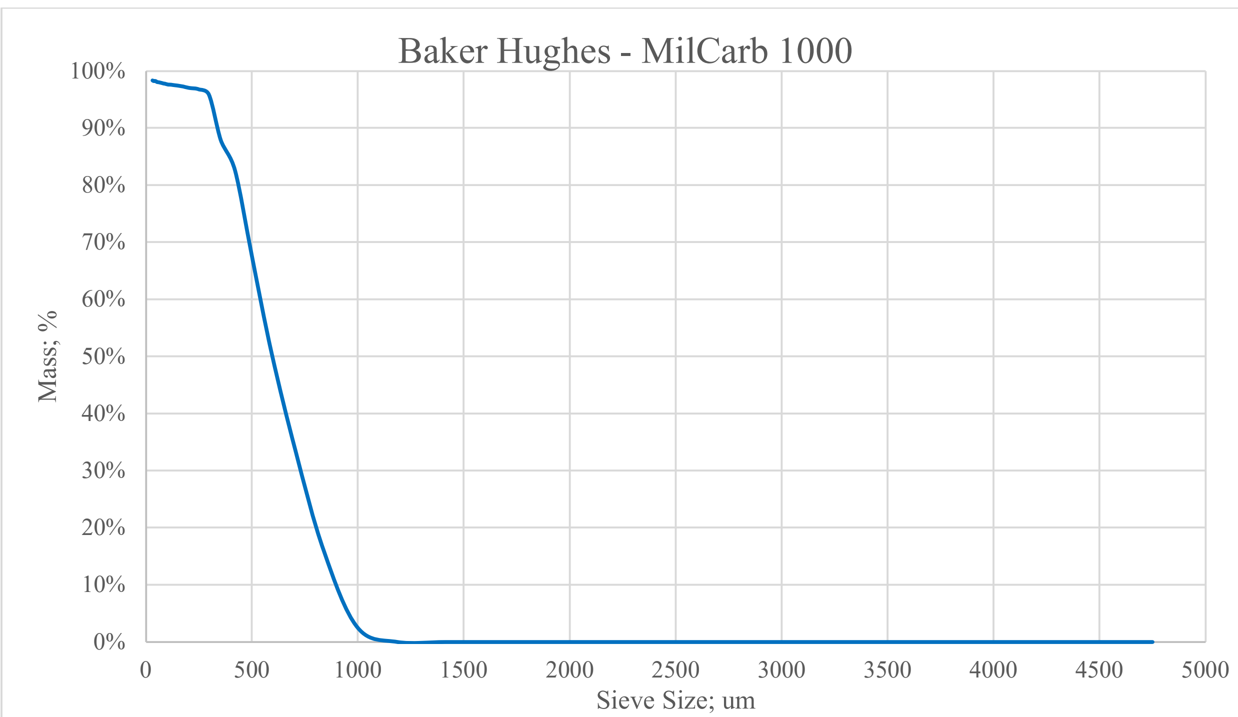

Figure C.16 Cumulative particle-size distribution determined by sieving Baker Hughes' MilCarb 1000

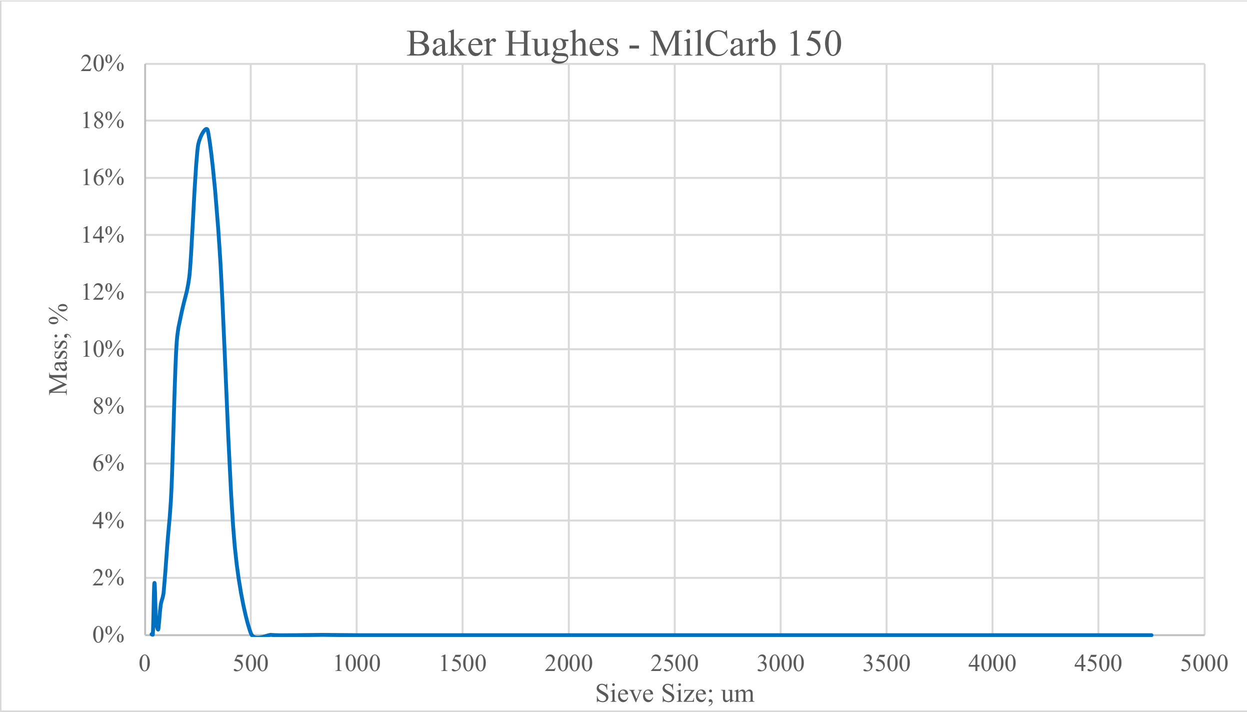

Figure C.17 Particle-size distribution determined by sieving Baker Hughes' MilCarb 150

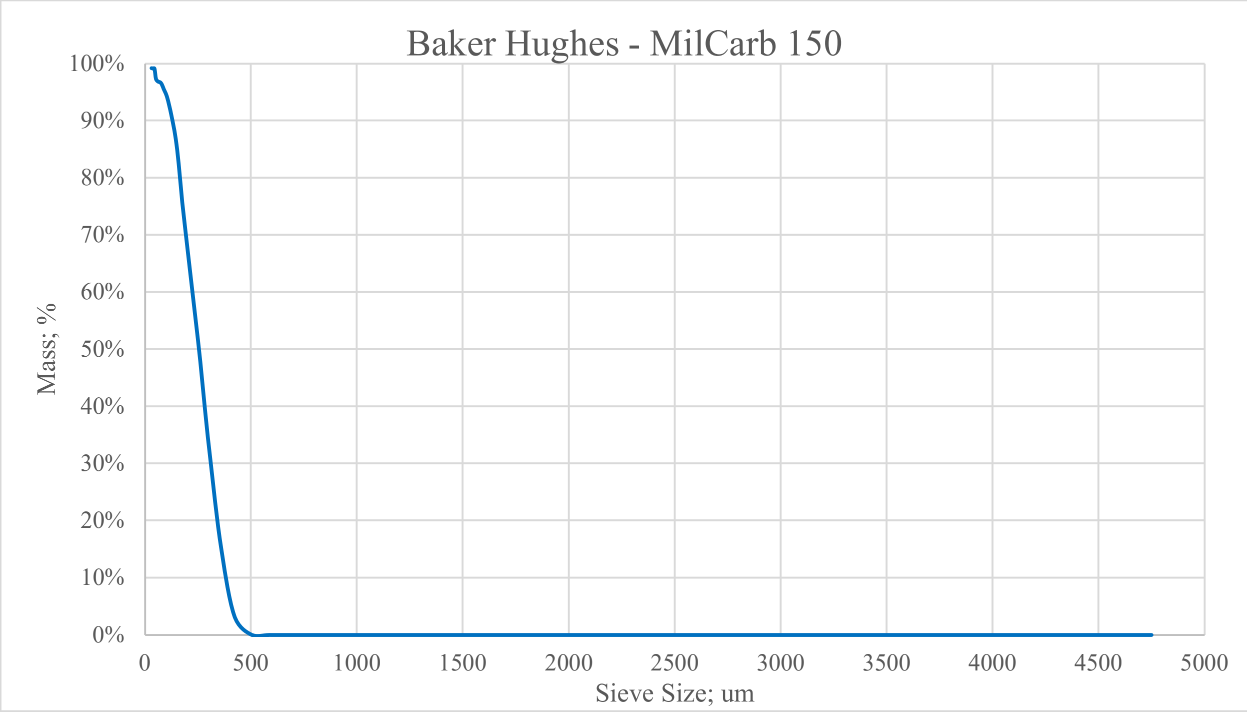

Figure C.18 Cumulative particle-size distribution determined by sieving Baker Hughes' MilCarb 150

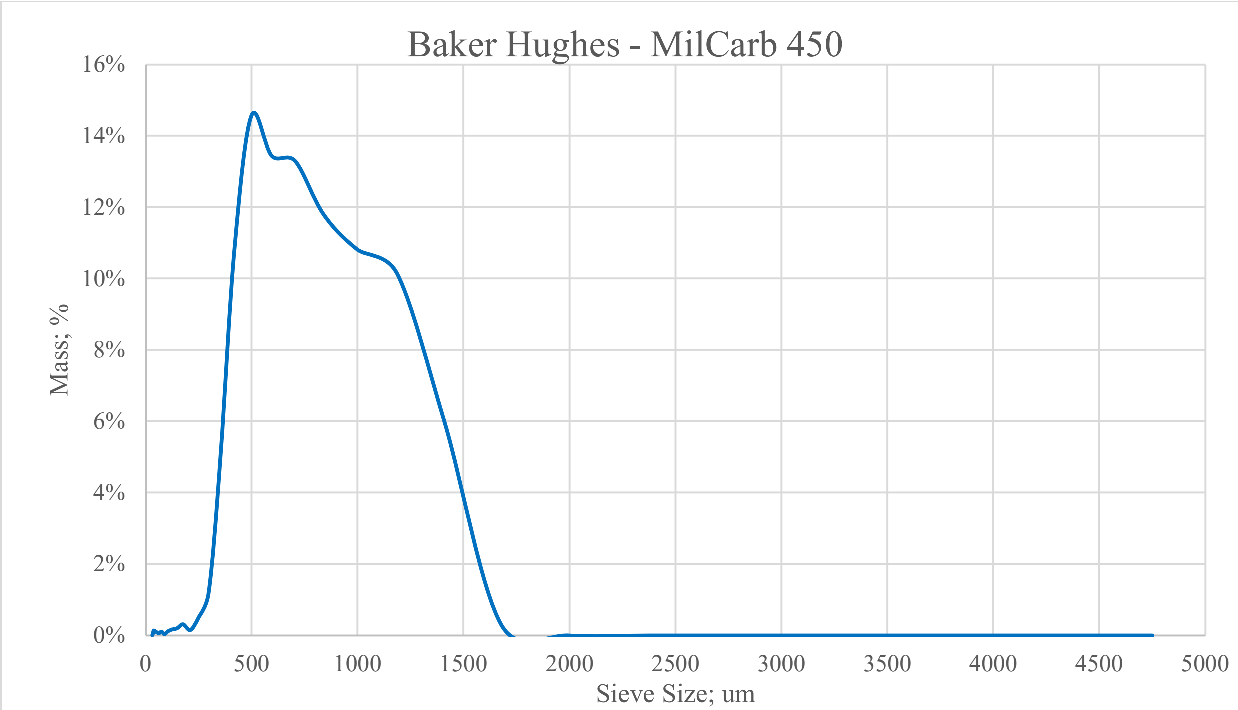

Figure C.19 Particle-size distribution determined by sieving Baker Hughes' MilCarb 450

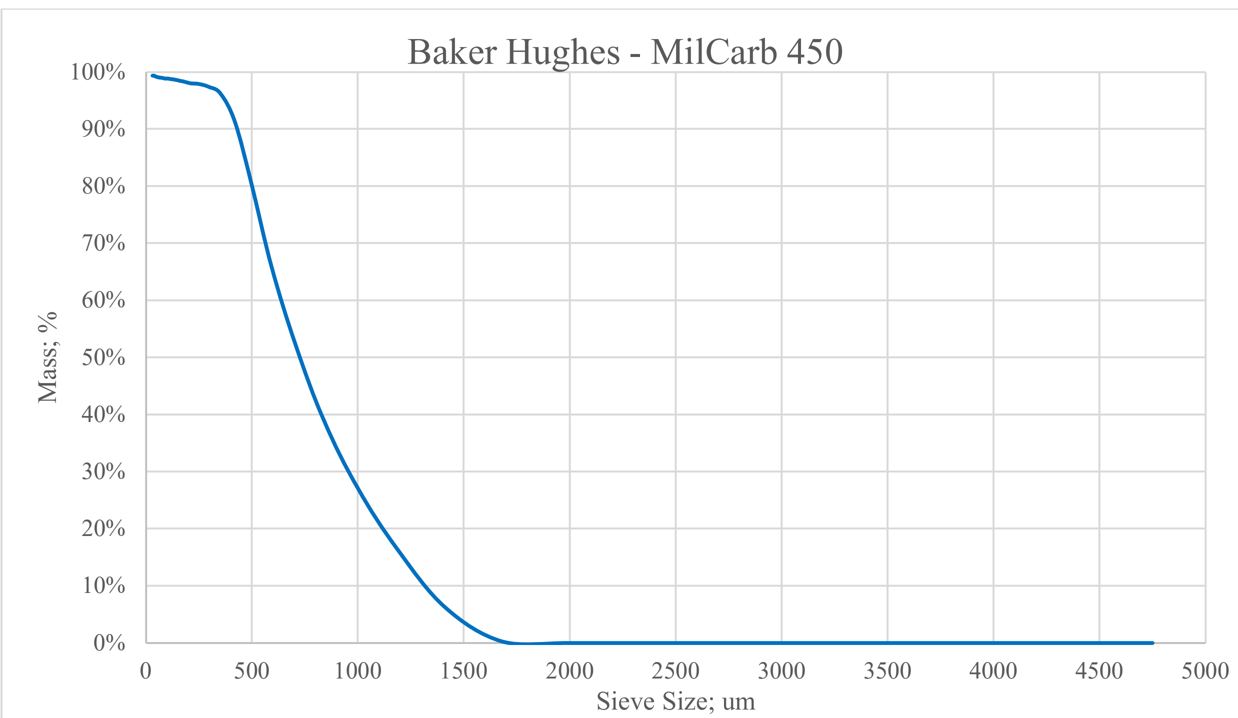

Figure C.20 Cumulative particle-size distribution determined by sieving Baker Hughes' MilCarb 450

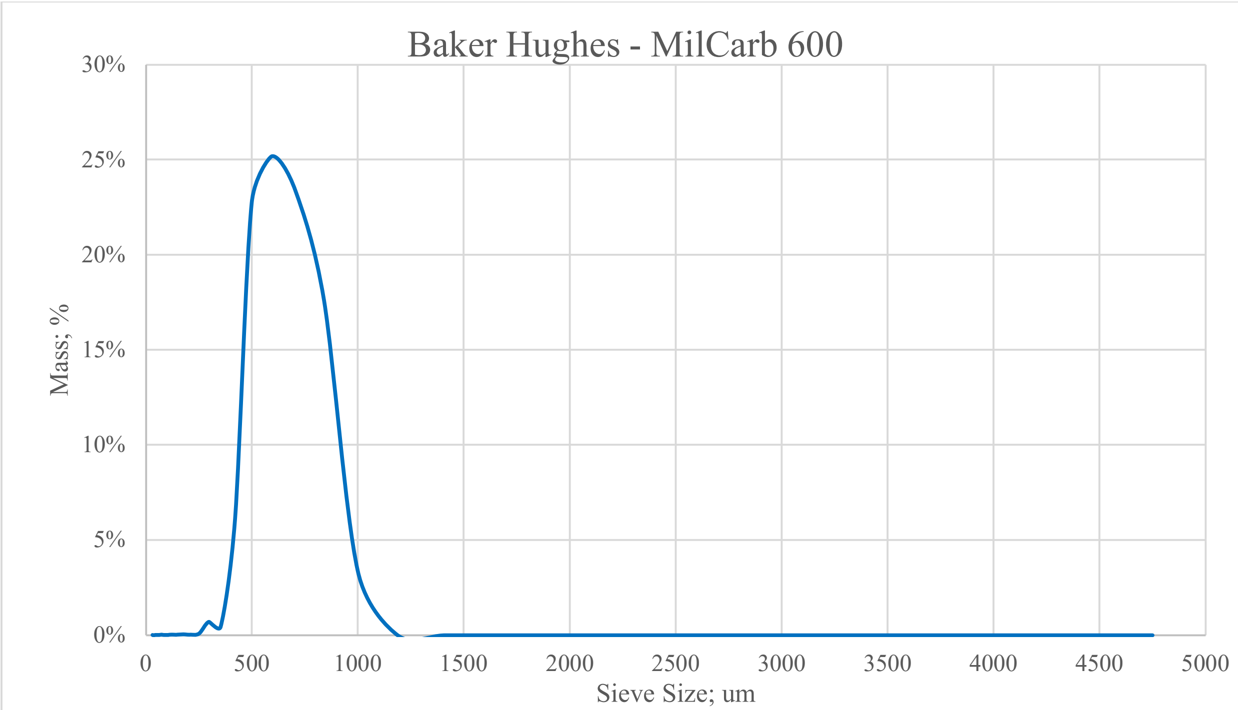

Figure C.21 Particle-size distribution determined by sieving Baker Hughes' MilCarb 600

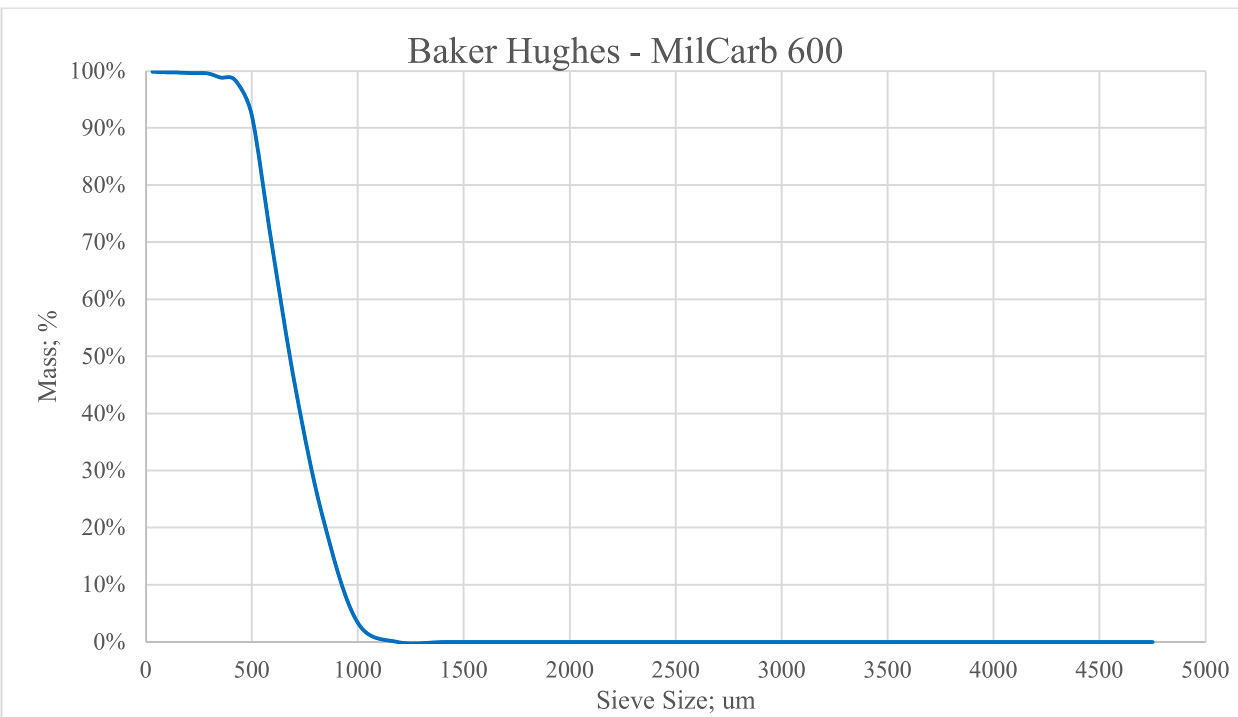

Figure C.22 Cumulative particle-size distribution determined by sieving Baker Hughes' MilCarb 600

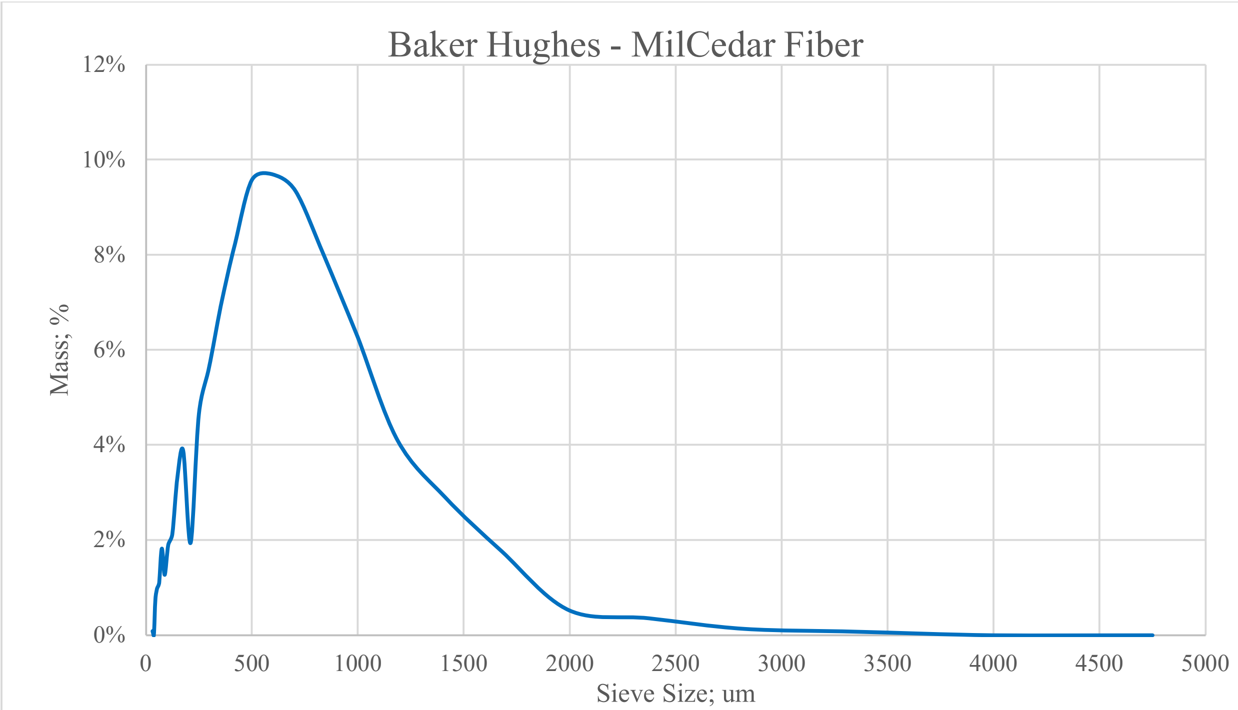

Figure C.23 Particle-size distribution determined by sieving Baker Hughes' MilCedar Fiber

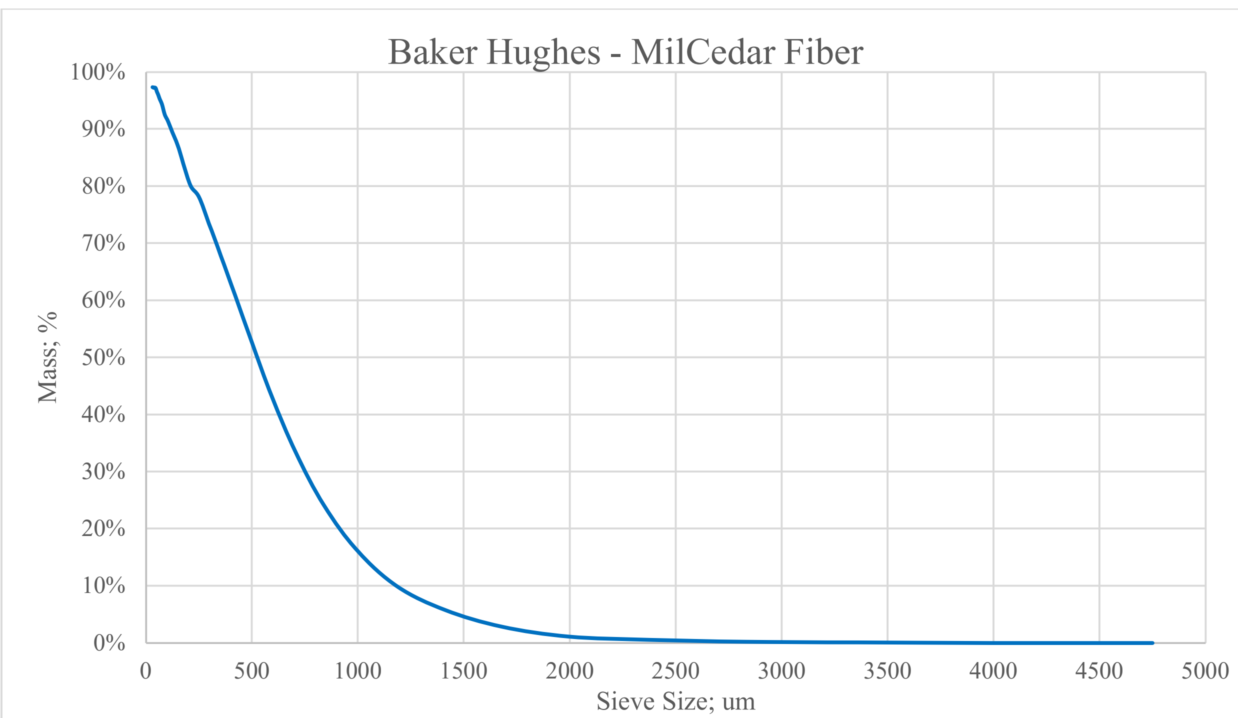

Figure C.24 Cumulative particle-size distribution determined by sieving Baker Hughes' MilCedar Fiber

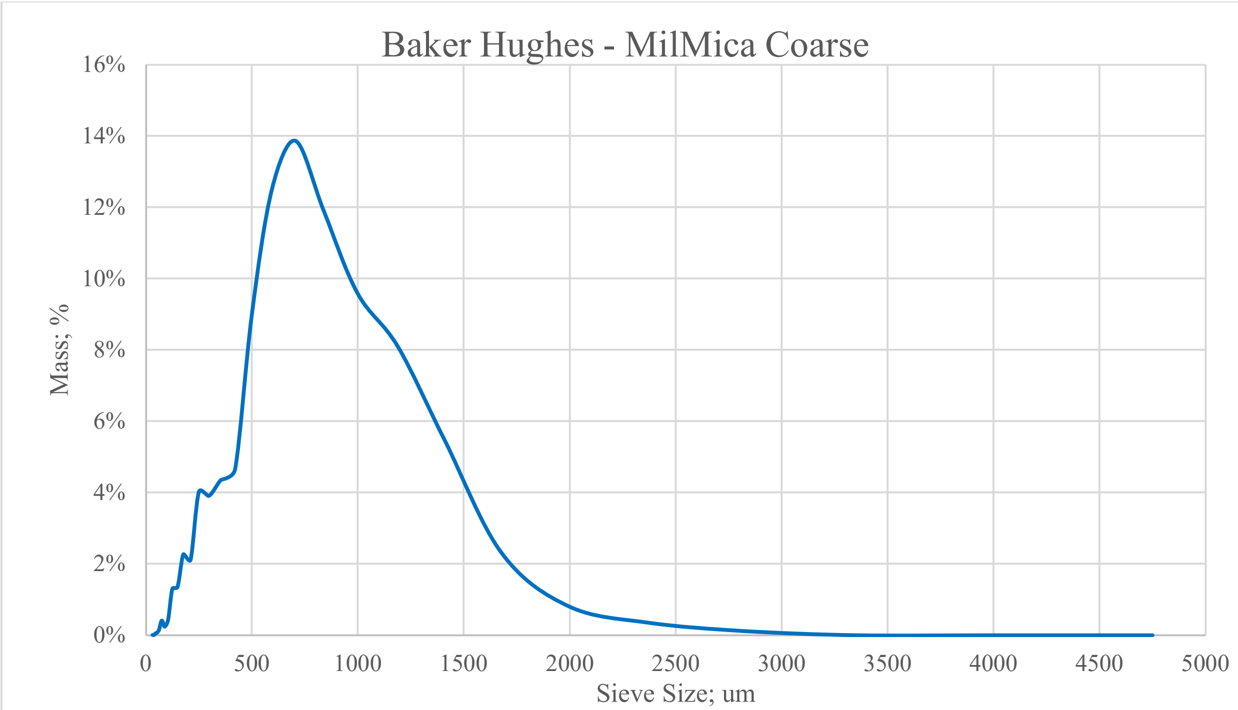

Figure C.25 Particle-size distribution determined by sieving Baker Hughes' MilMica Coarse

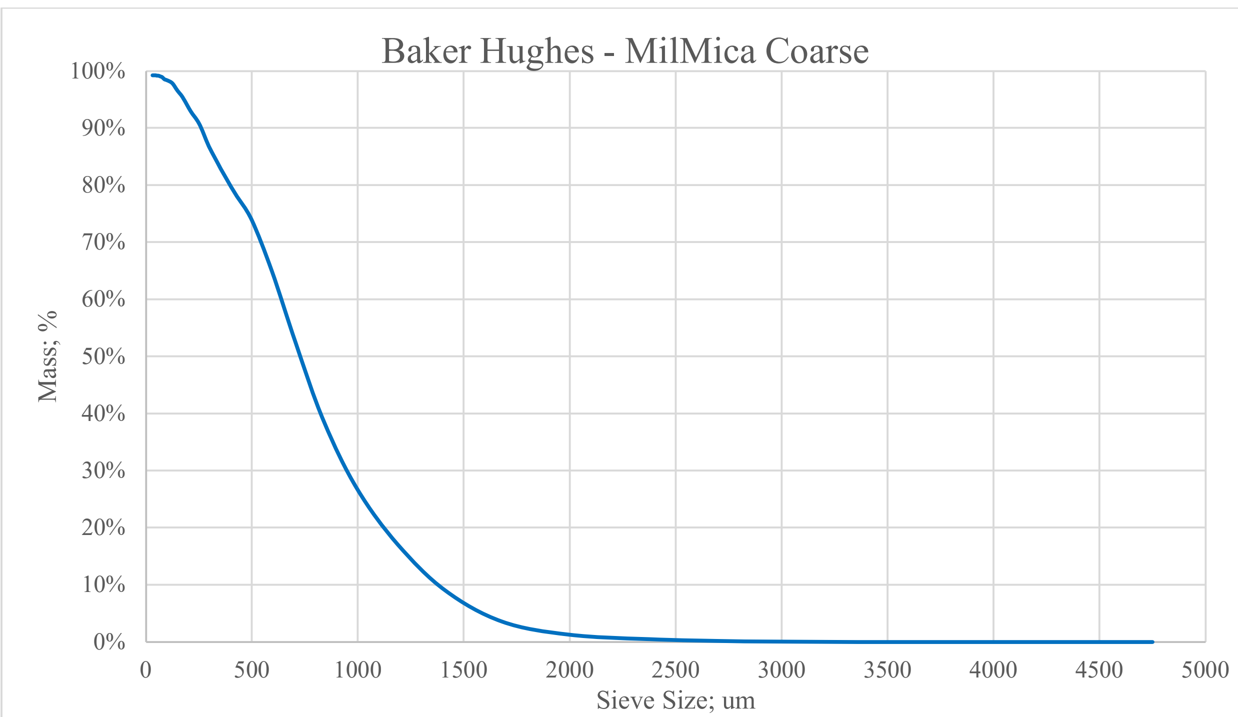

Figure C.26 Cumulative particle-size distribution determined by sieving Baker Hughes' MilMica Coarse

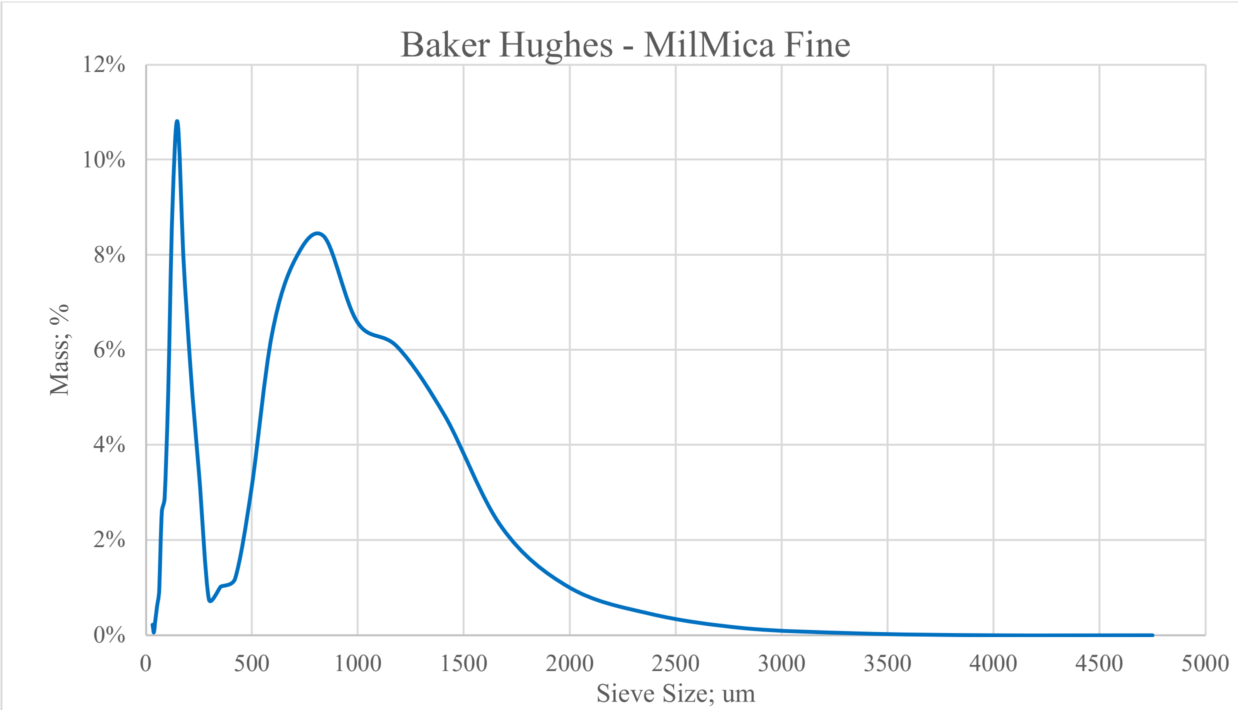

Figure C.27 Particle-size distribution determined by sieving Baker Hughes' MilMica Fine

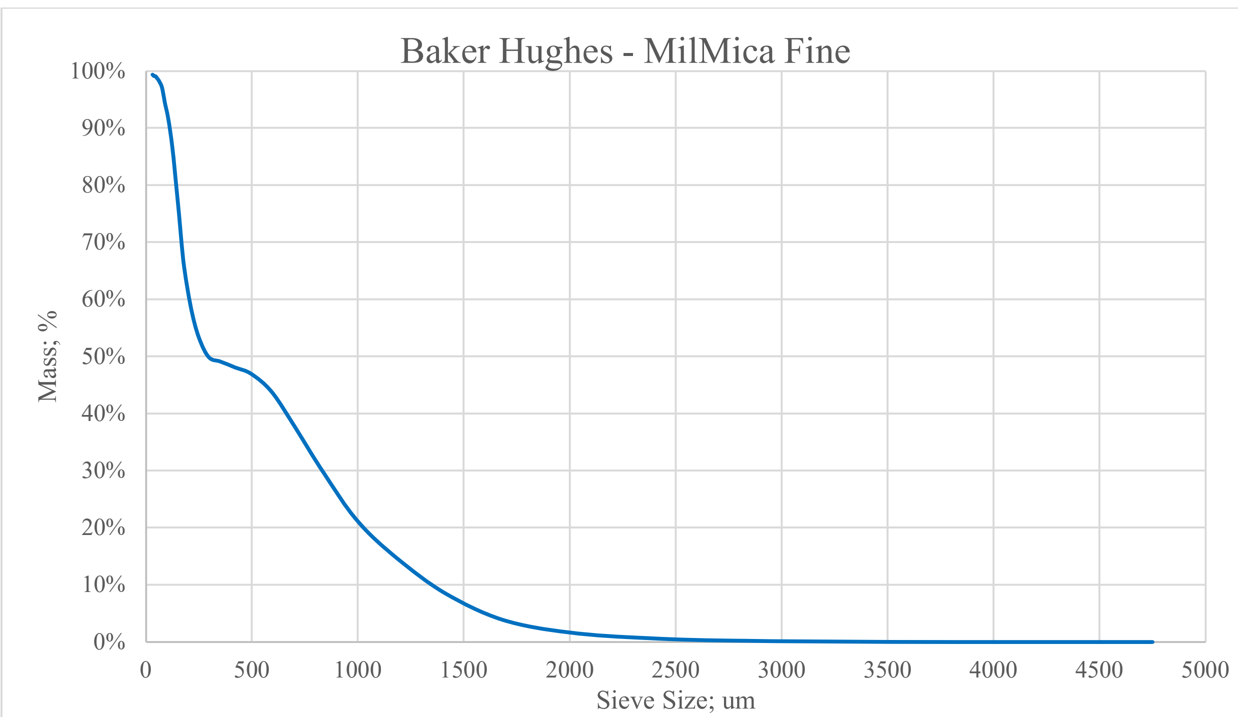

Figure C.28 Cumulative particle-size distribution determined by sieving Baker Hughes' MilMica Fine

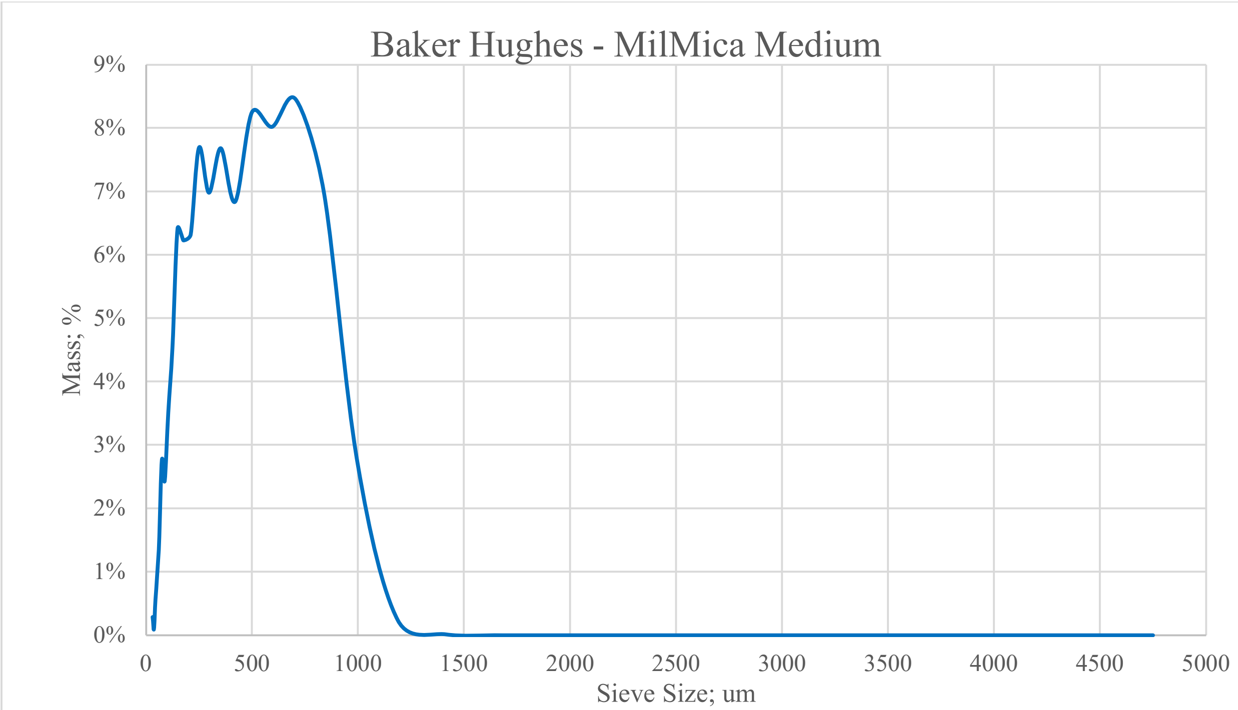

Figure C.29 Particle-size distribution determined by sieving Baker Hughes' MilMica Medium

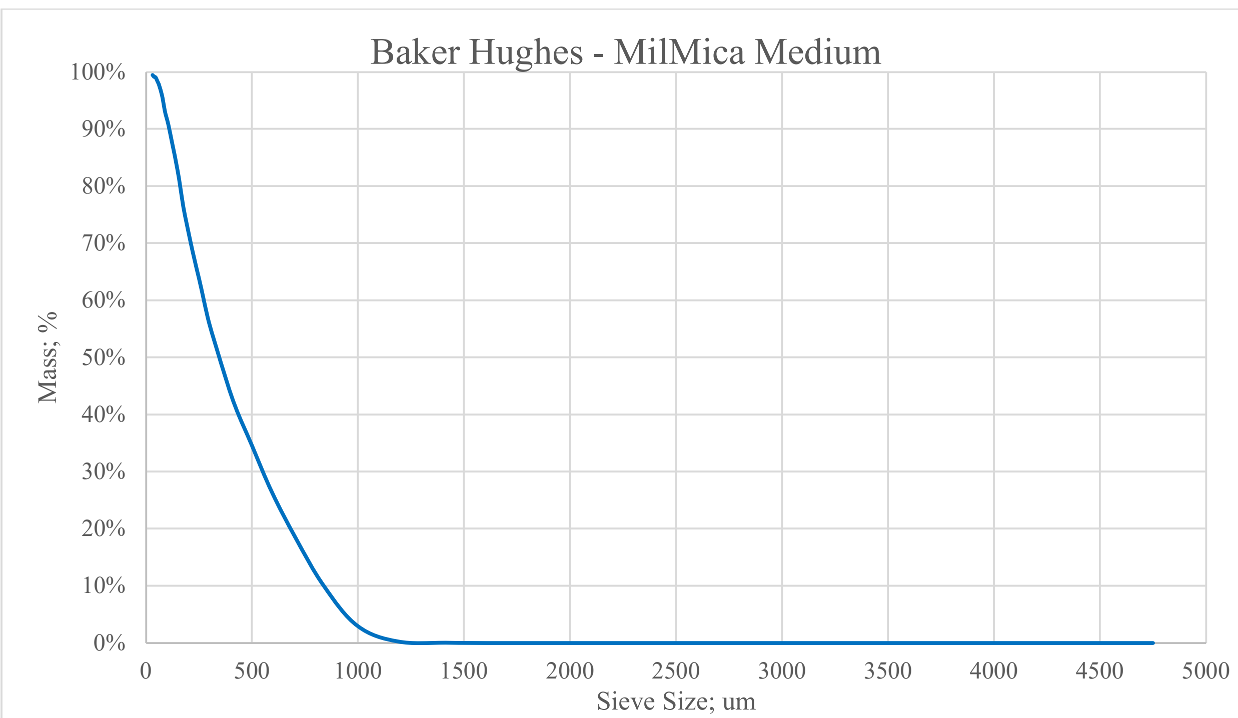

Figure C.30 Cumulative particle-size distribution determined by sieving Baker Hughes' MilMica Medium

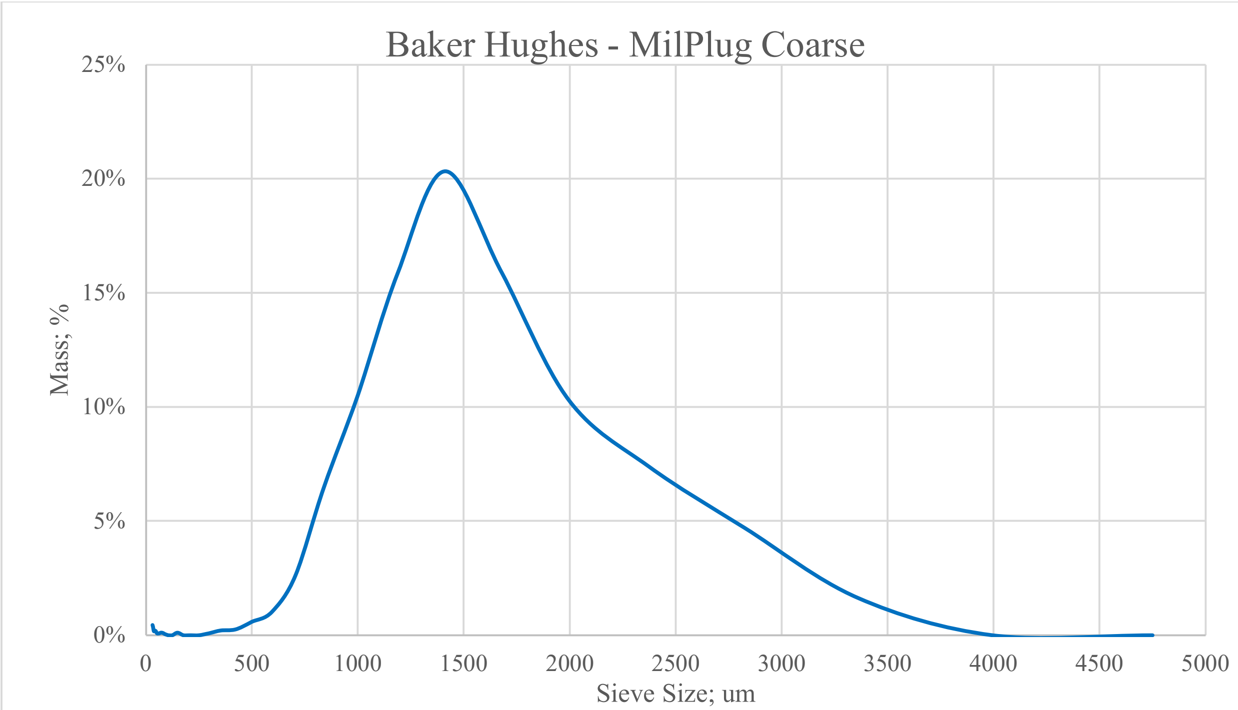

Figure C.31 Particle-size distribution determined by sieving Baker Hughes' MilPlug Coarse

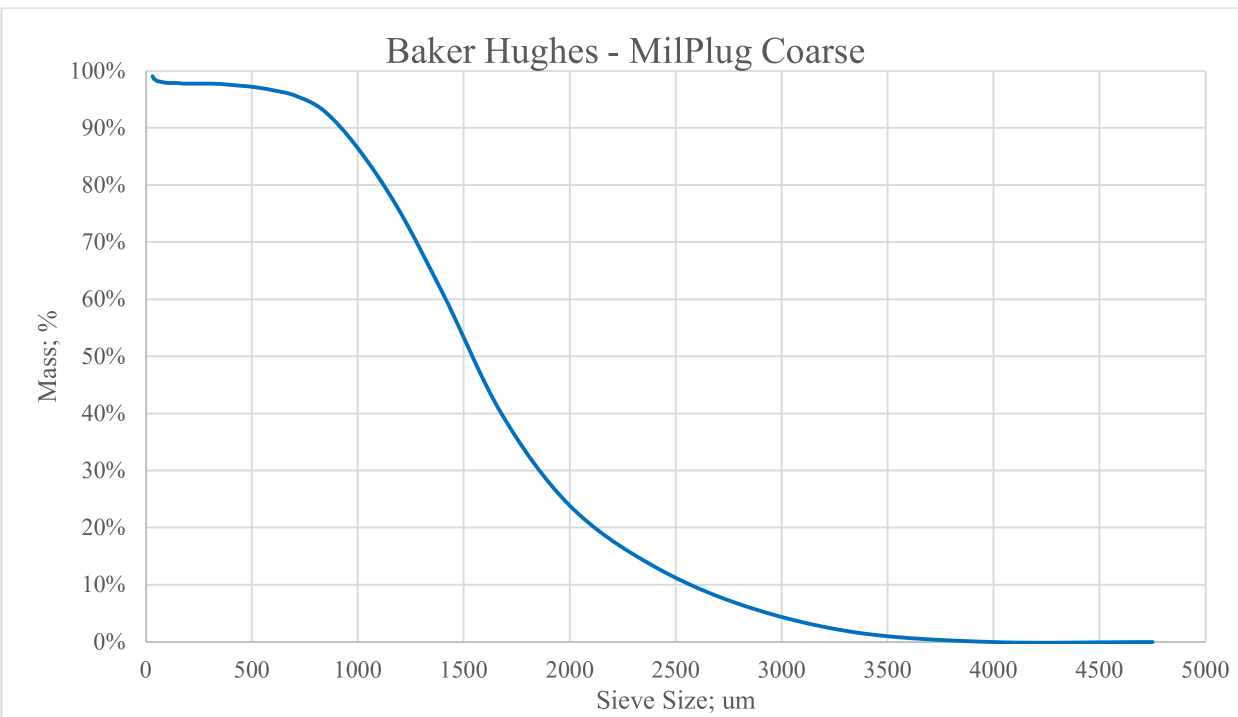

Figure C.32 Cumulative particle-size distribution determined by sieving Baker Hughes' MilPlug Coarse

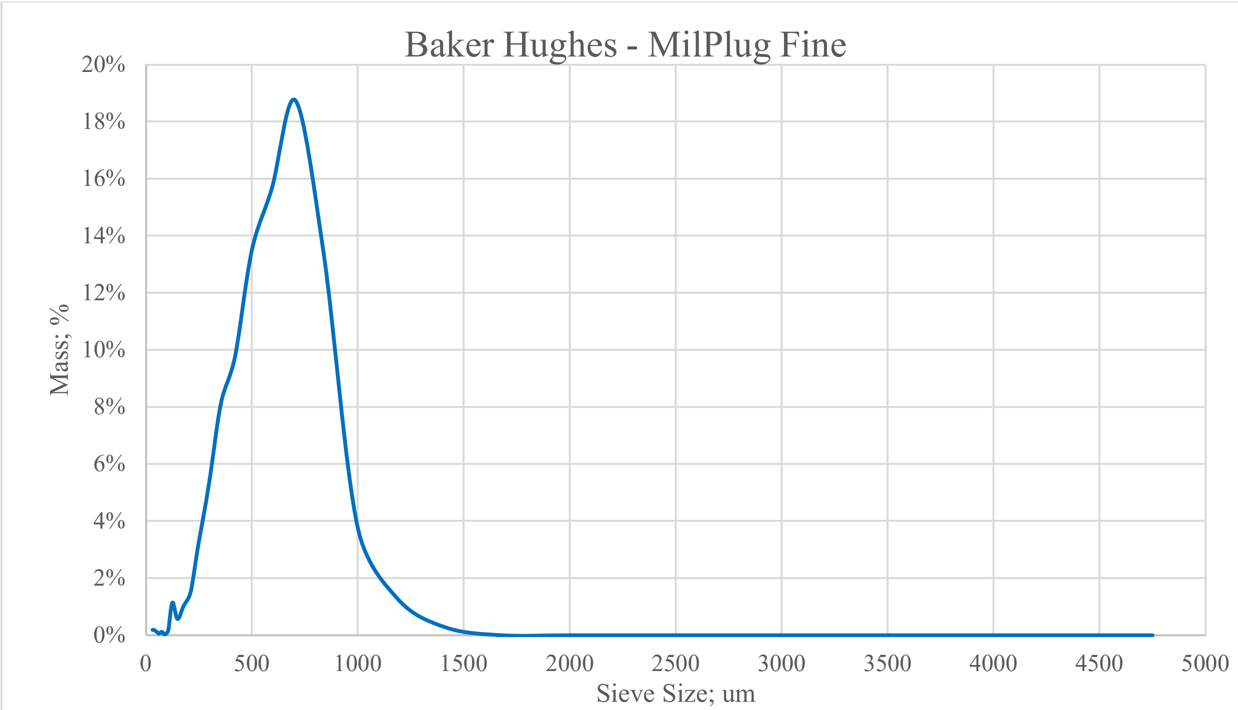

Figure C.33 Particle-size distribution determined by sieving Baker Hughes' MilPlug Fine

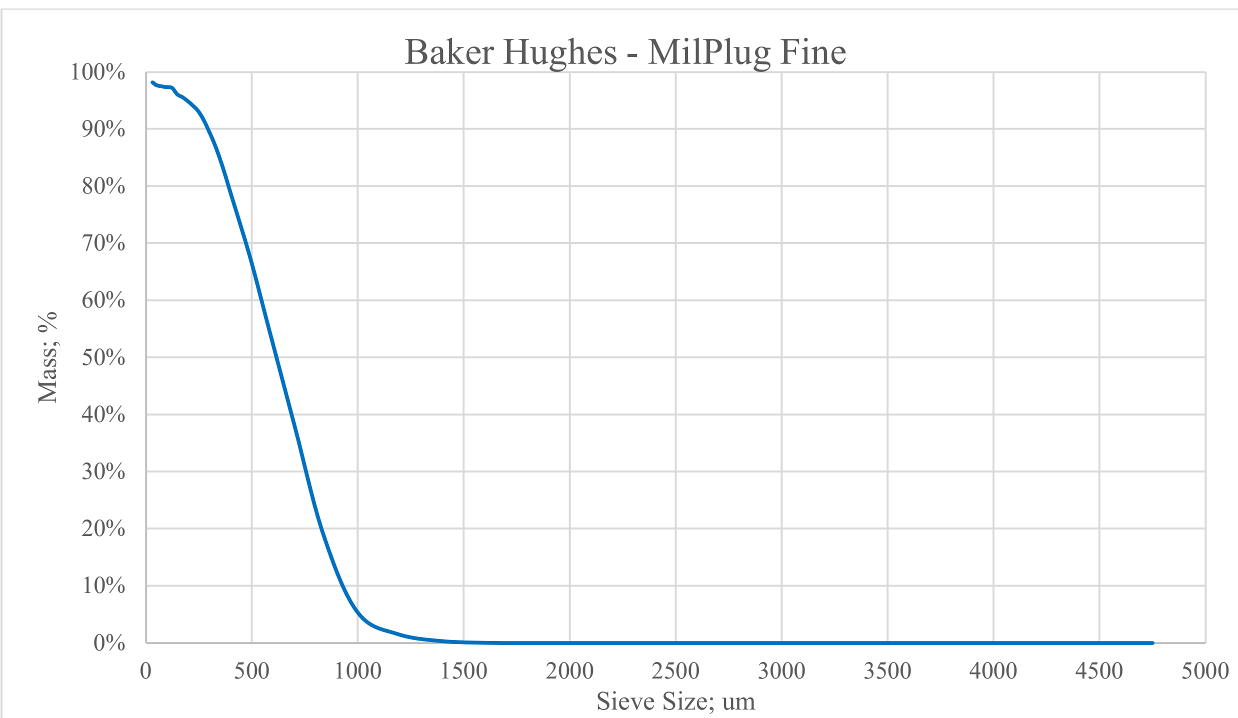

Figure C.34 Cumulative particle-size distribution determined by sieving Baker Hughes' MilPlug Fine

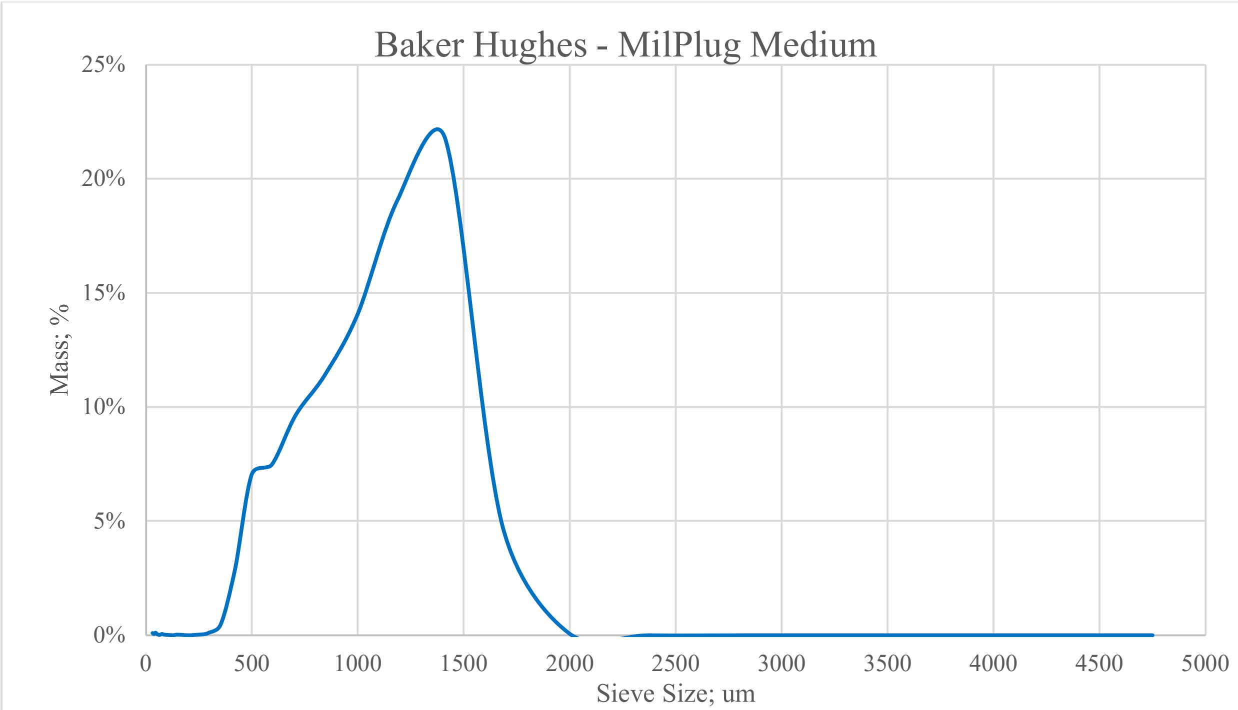

Figure C.35 Particle-size distribution determined by sieving Baker Hughes' MilPlug Medium

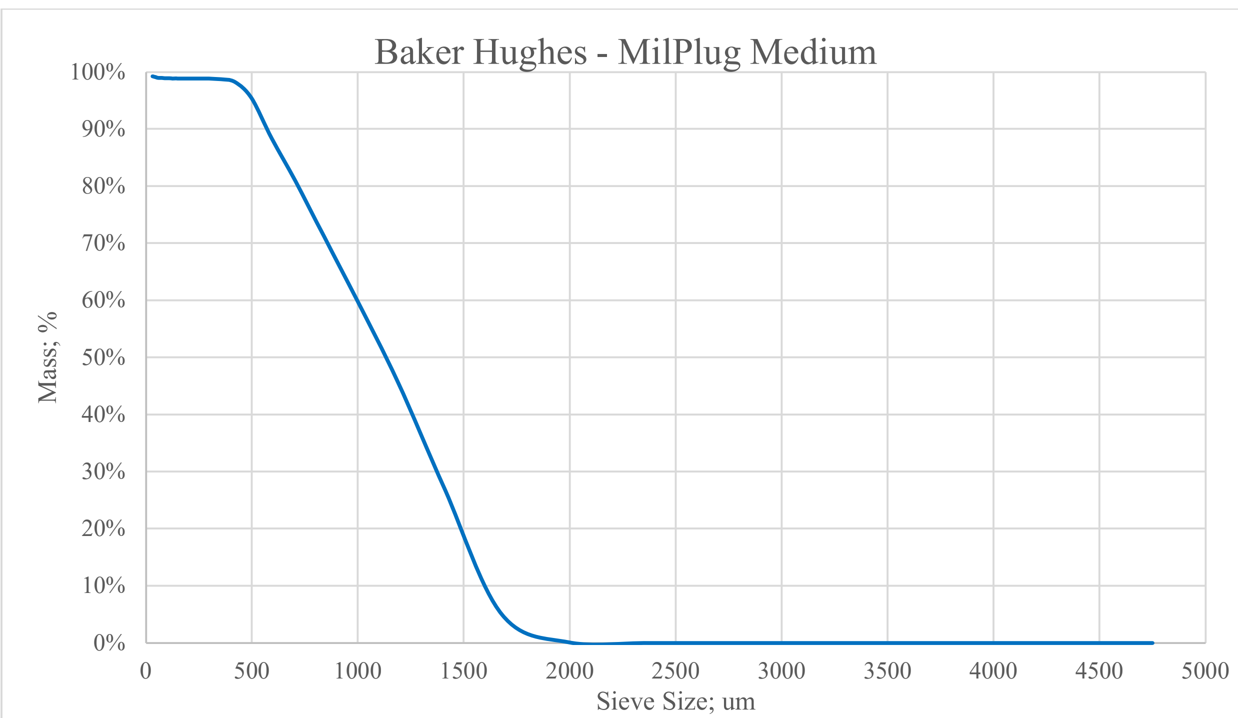

Figure C.36 Cumulative particle-size distribution determined by sieving Baker Hughes' MilPlug Medium

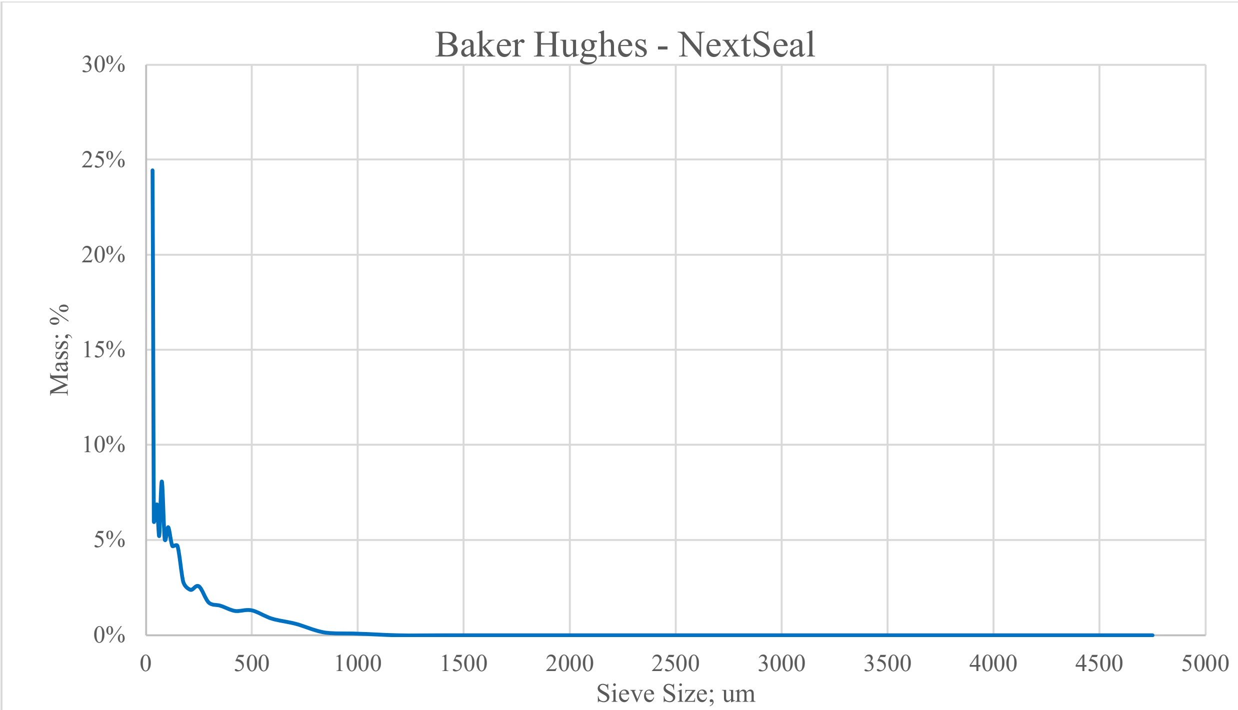

Figure C.37 Particle-size distribution determined by sieving Baker Hughes' NextSeal

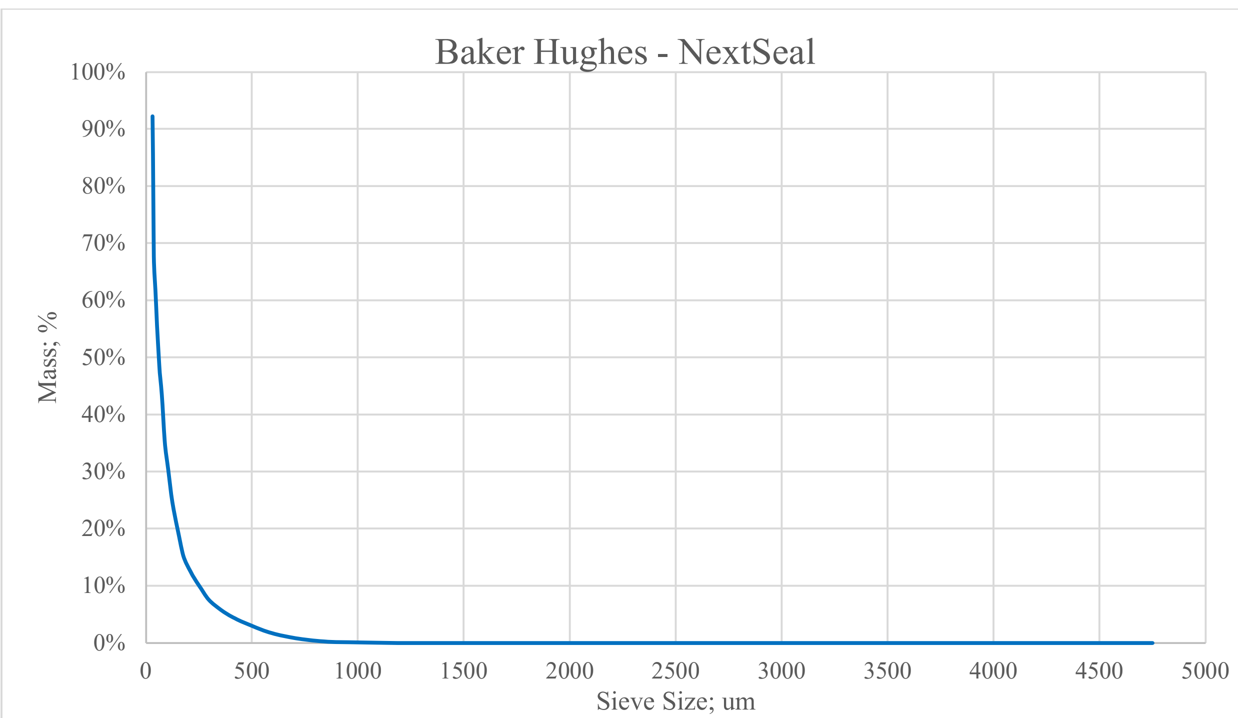

Figure C.38 Cumulative particle-size distribution determined by sieving Baker Hughes' NextSeal

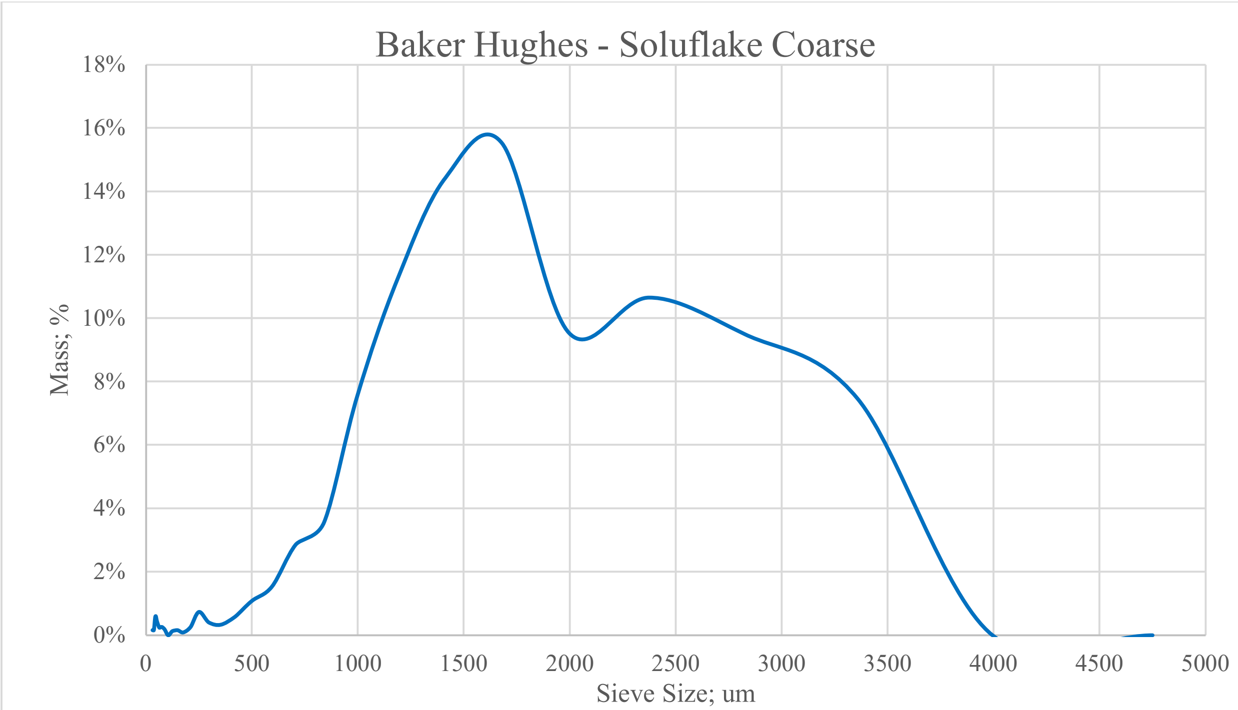

Figure C.39 Particle-size distribution determined by sieving Baker Hughes' Soluflake Coarse

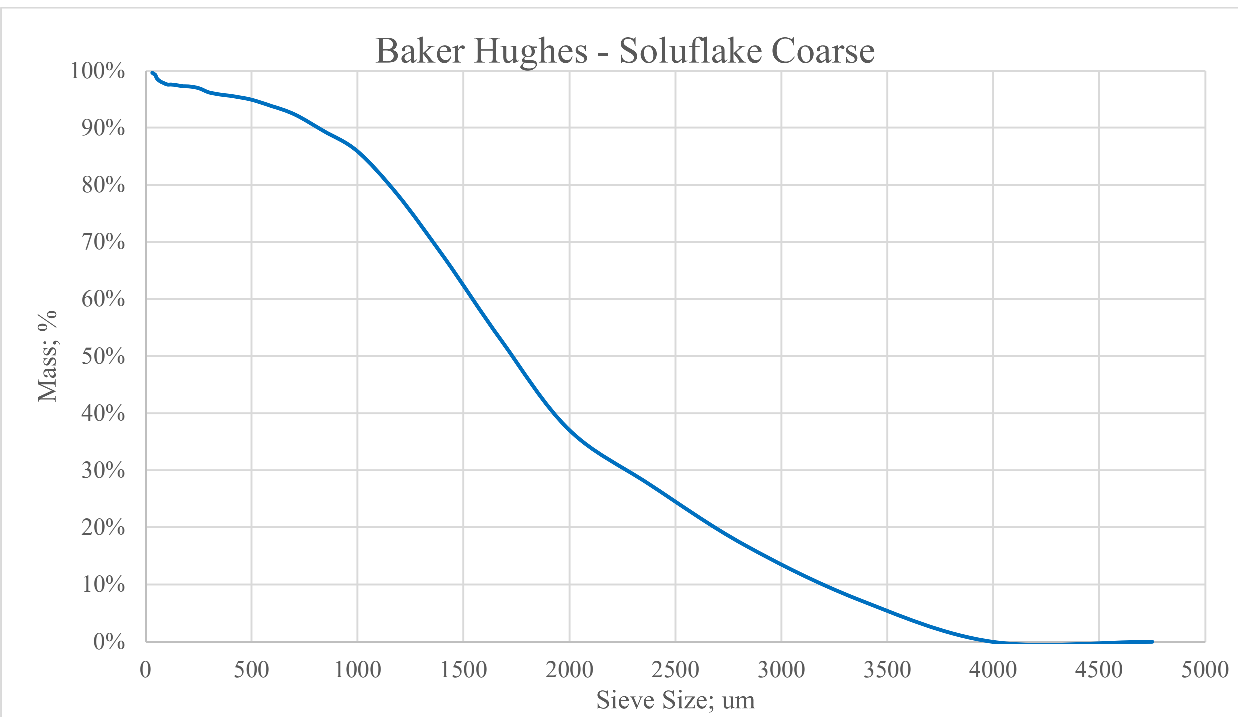

Figure C.40 Cumulative particle-size distribution determined by sieving Baker Hughes' Soluflake Coarse

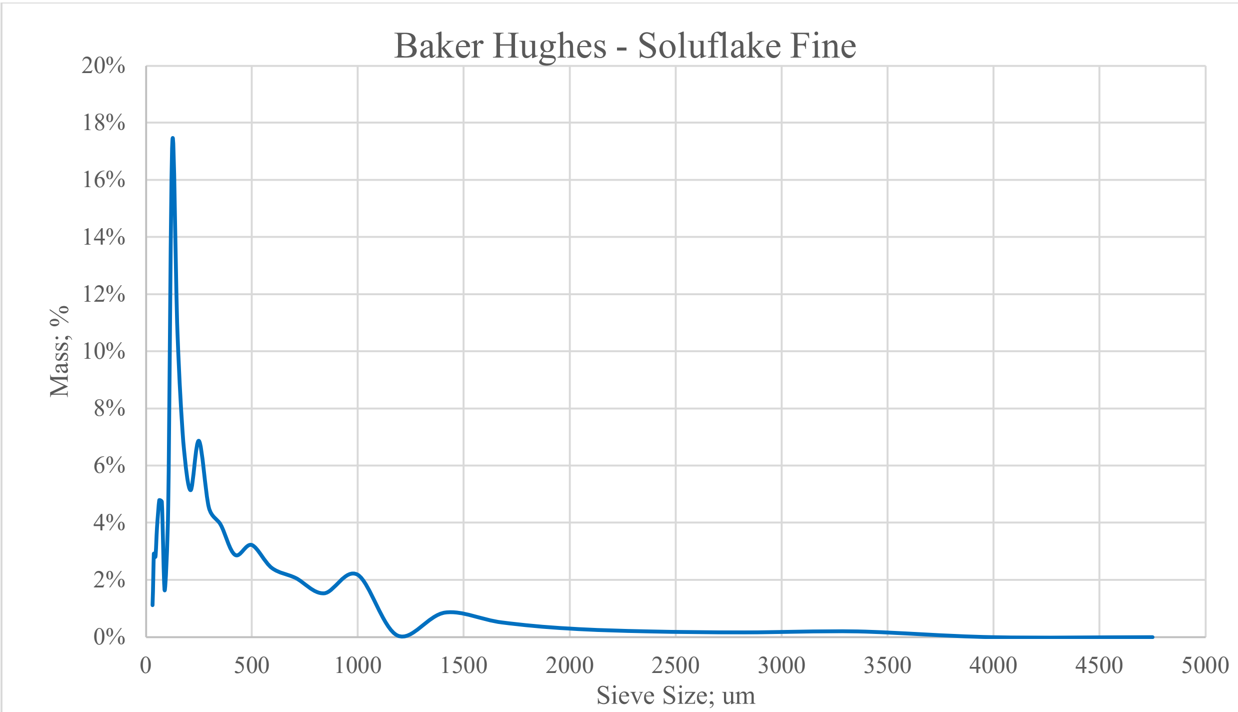

Figure C.41 Particle-size distribution determined by sieving Baker Hughes' Soluflake Fine

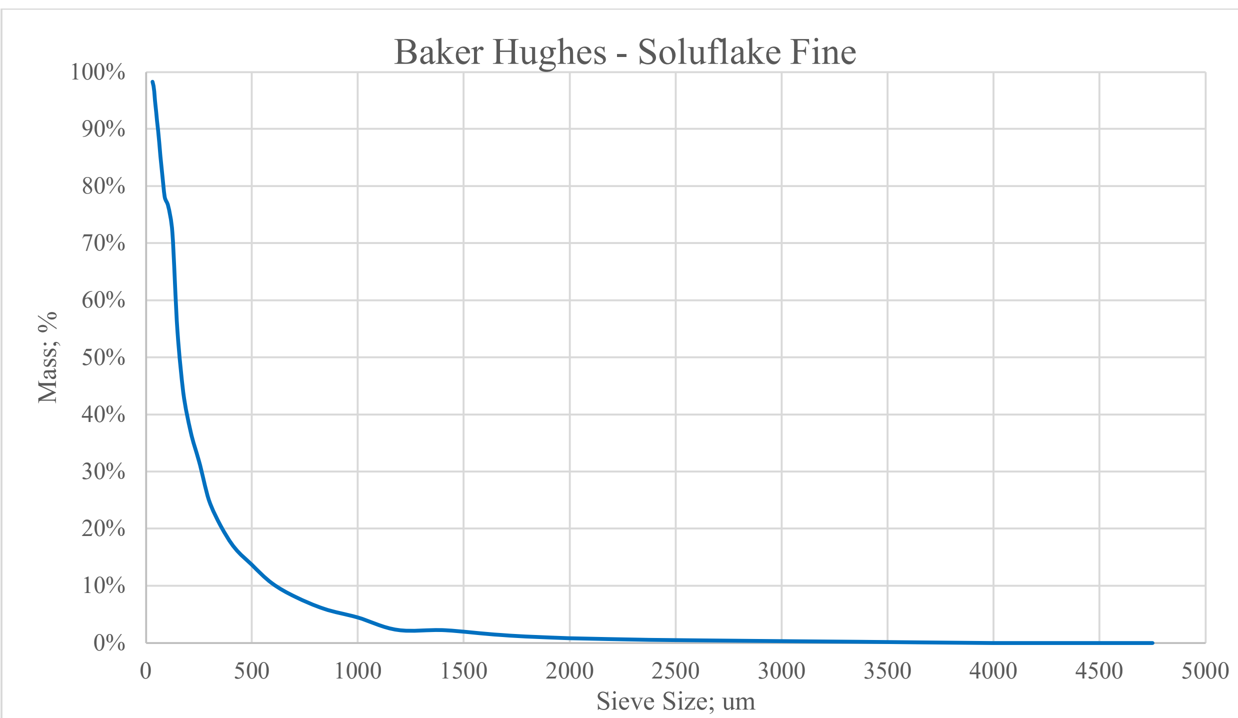

Figure C.42 Cumulative particle-size distribution determined by sieving Baker Hughes' Soluflake Fine

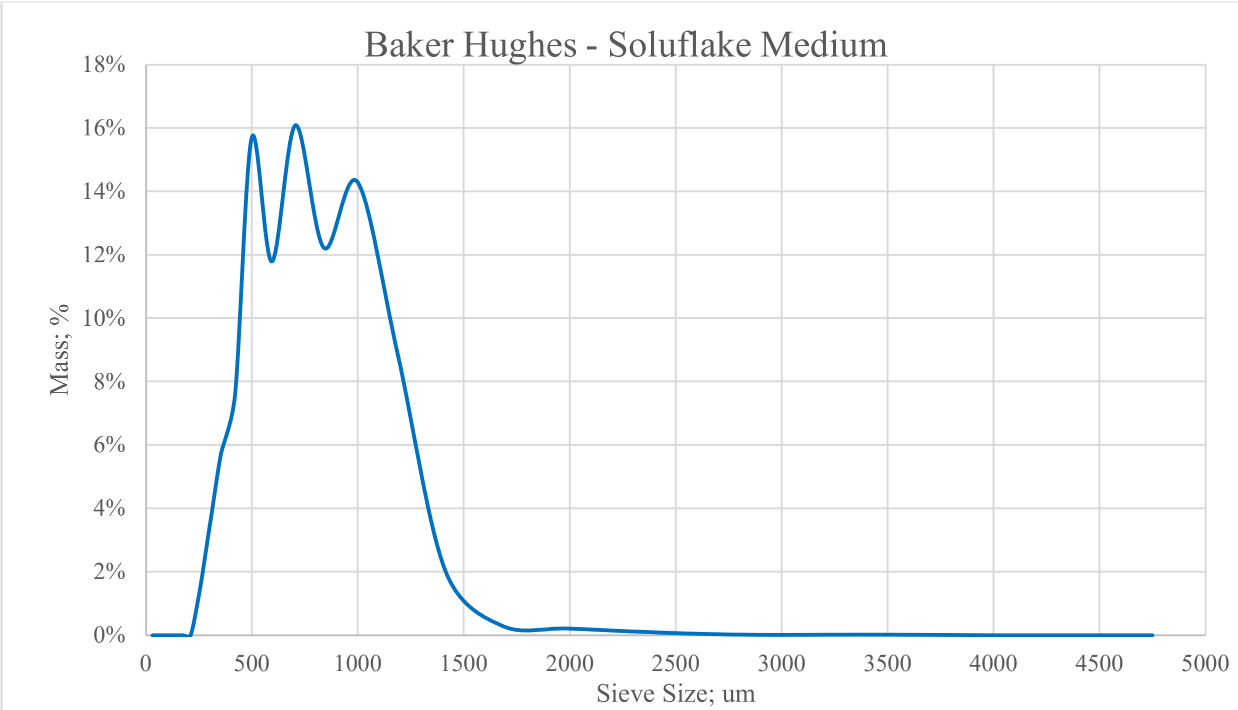

Figure C.43 Particle-size distribution determined by sieving Baker Hughes' Soluflake Medium

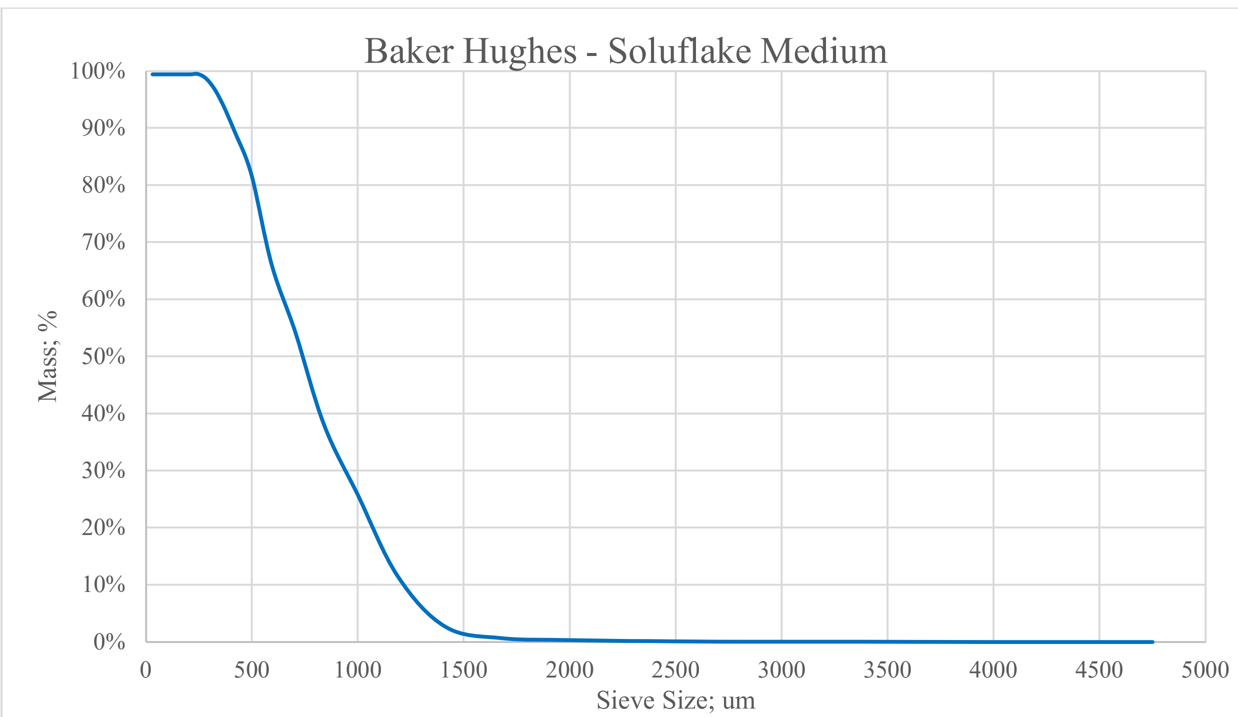

Figure C.44 Cumulative particle-size distribution determined by sieving Baker Hughes' Soluflake Medium

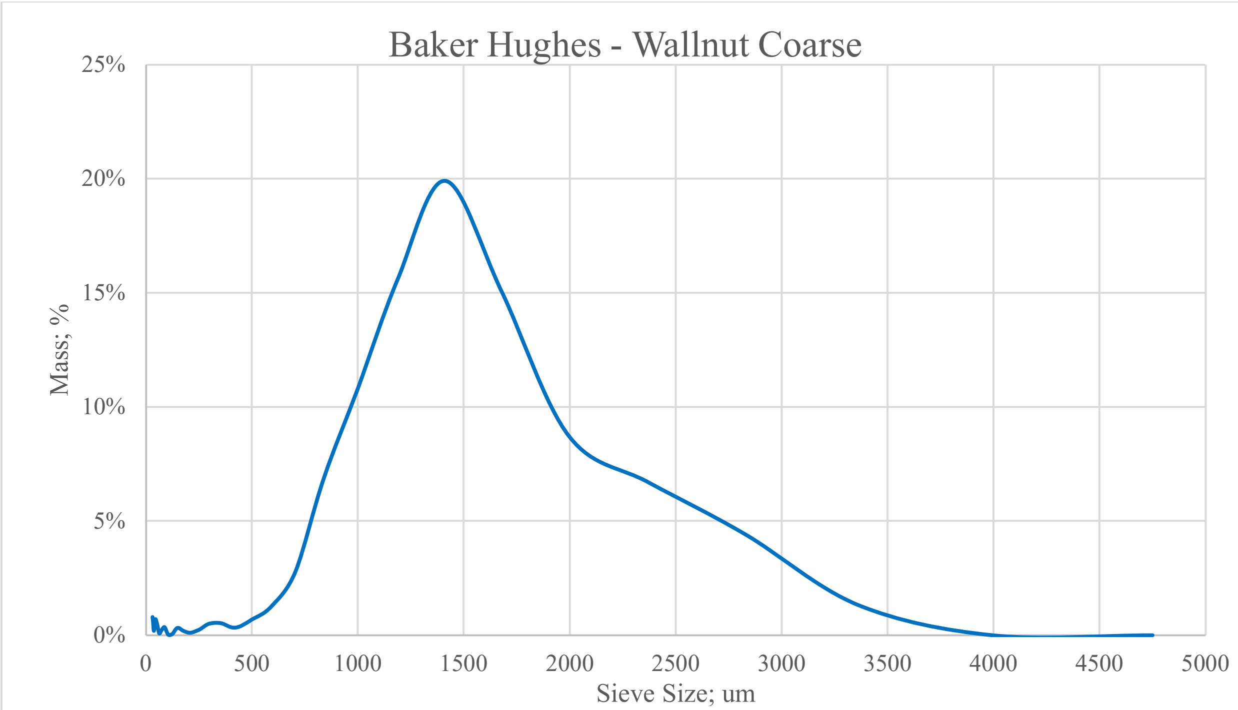

Figure C.45 Particle-size distribution determined by sieving Baker Hughes' Wallnut Coarse

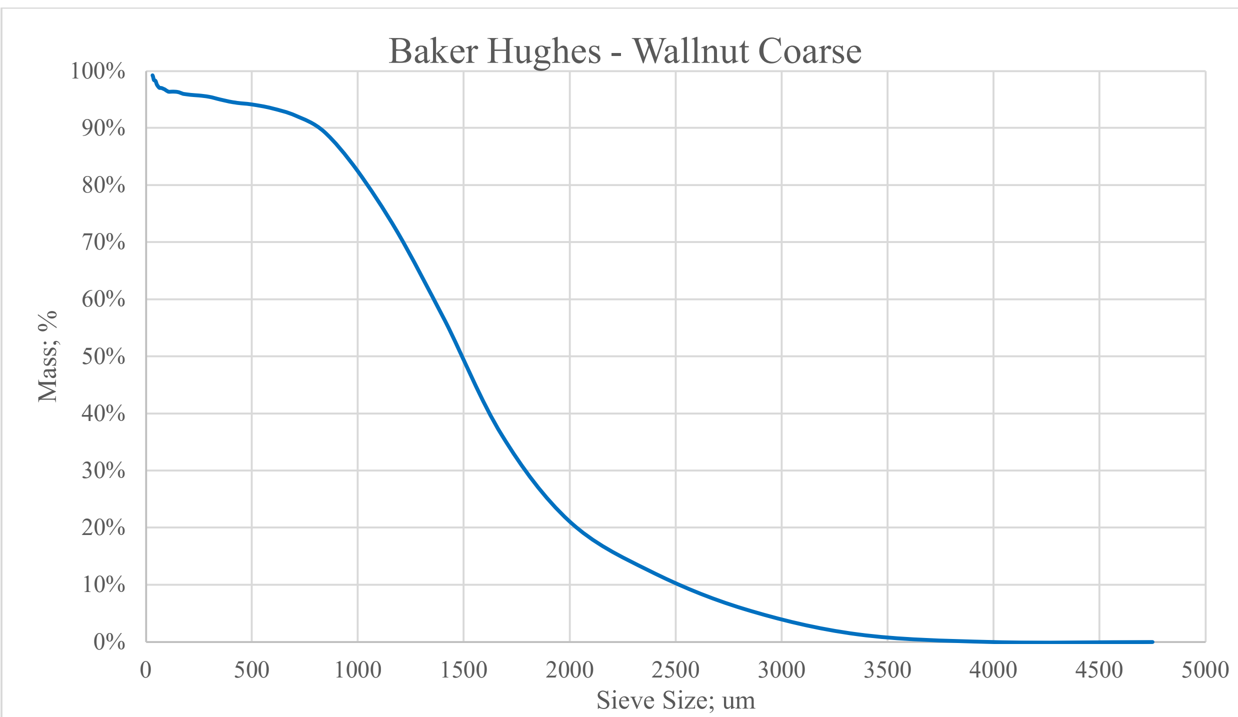

Figure C.46 Cumulative particle-size distribution determined by sieving Baker Hughes' Wallnut Coarse

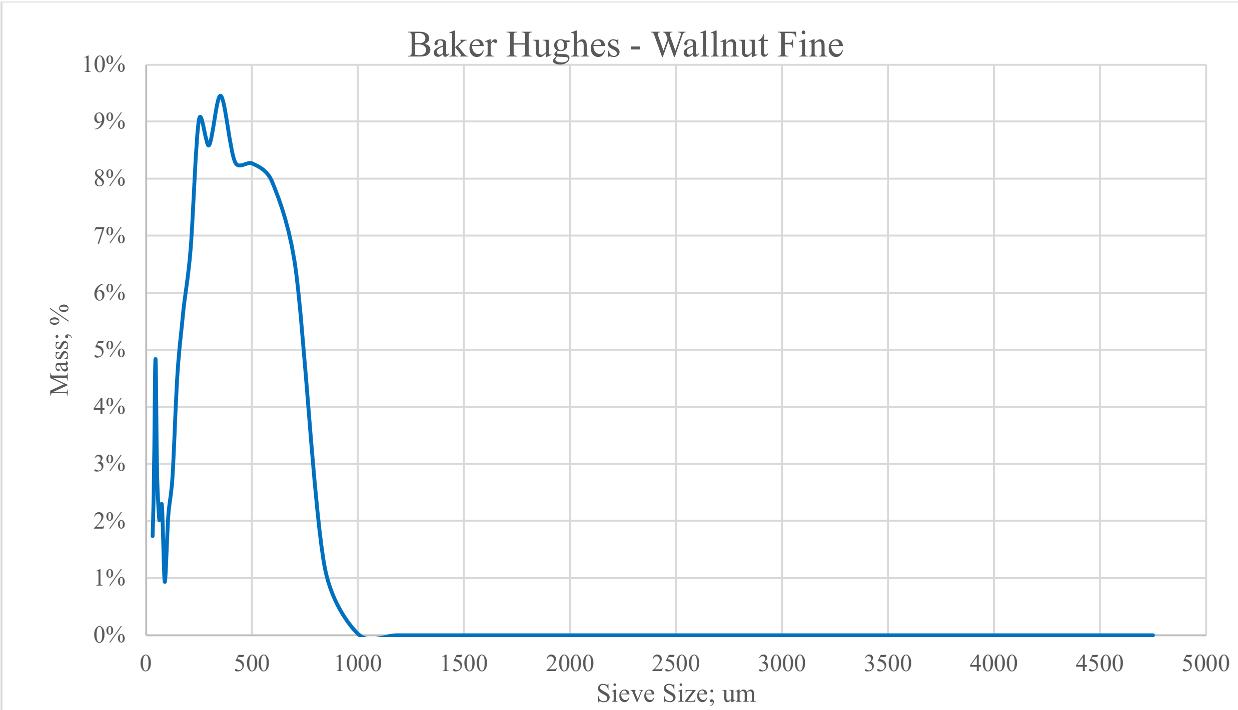

Figure C.47 Particle-size distribution determined by sieving Baker Hughes' Wallnut Fine

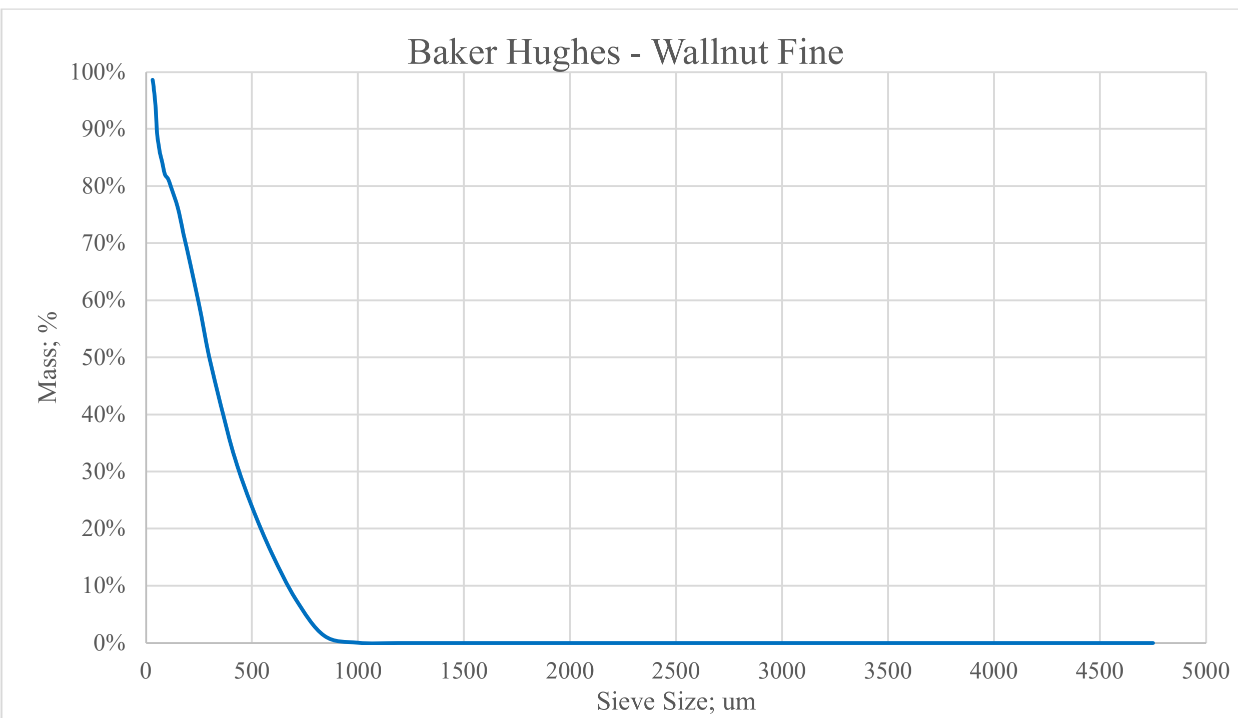

Figure C.48 Cumulative particle-size distribution determined by sieving Baker Hughes' Wallnut Fine

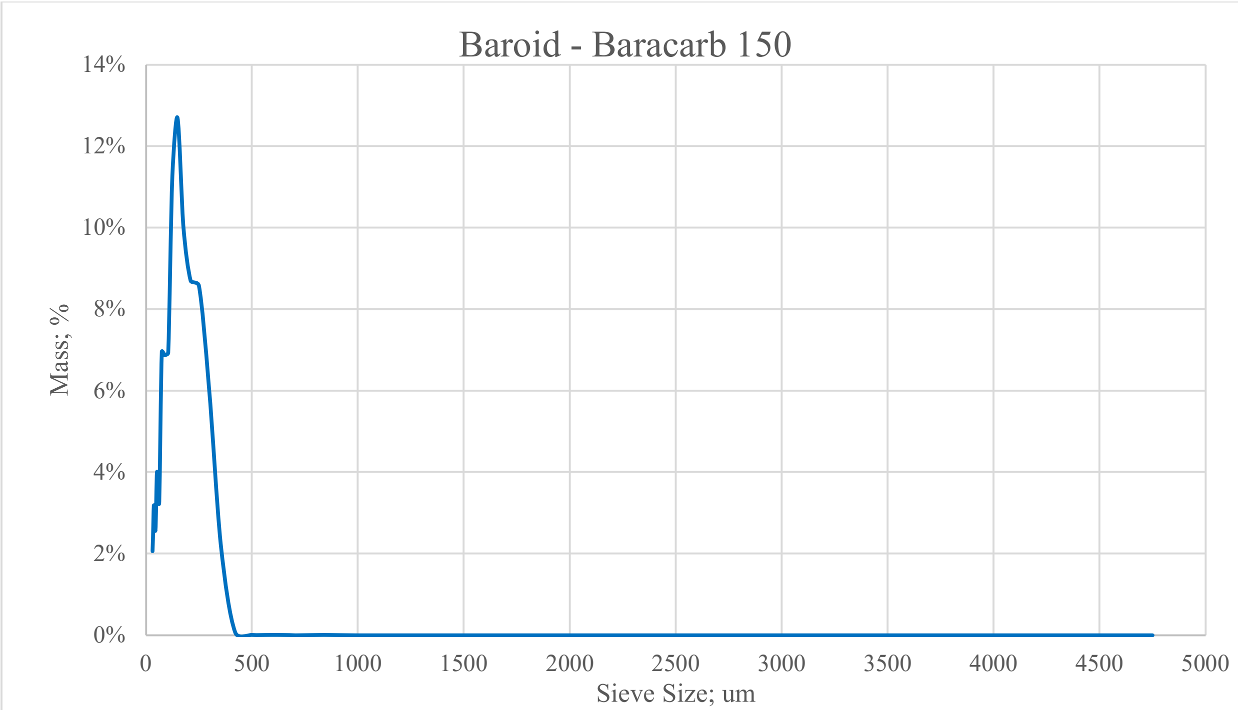

Figure C.49 Particle-size distribution determined by sieving Baroid’s Baracarb 150

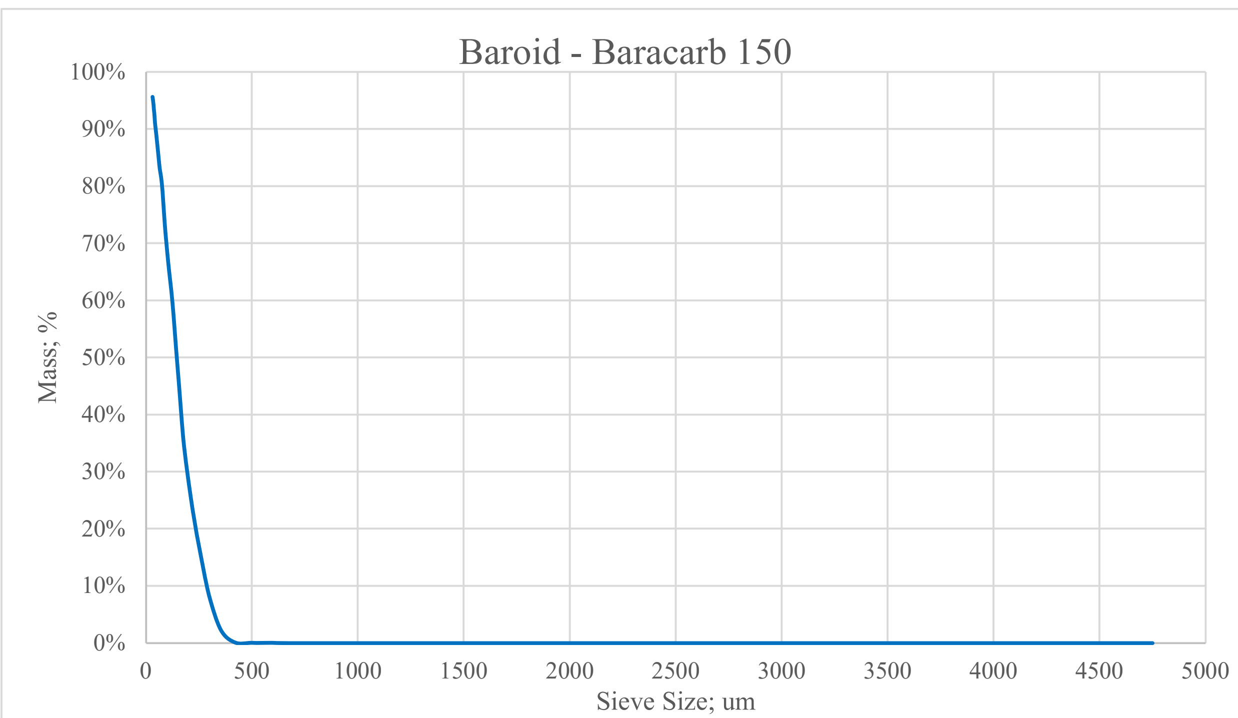

Figure C.50 Cumulative particle-size distribution determined by sieving Baroid’s Baracarb 150

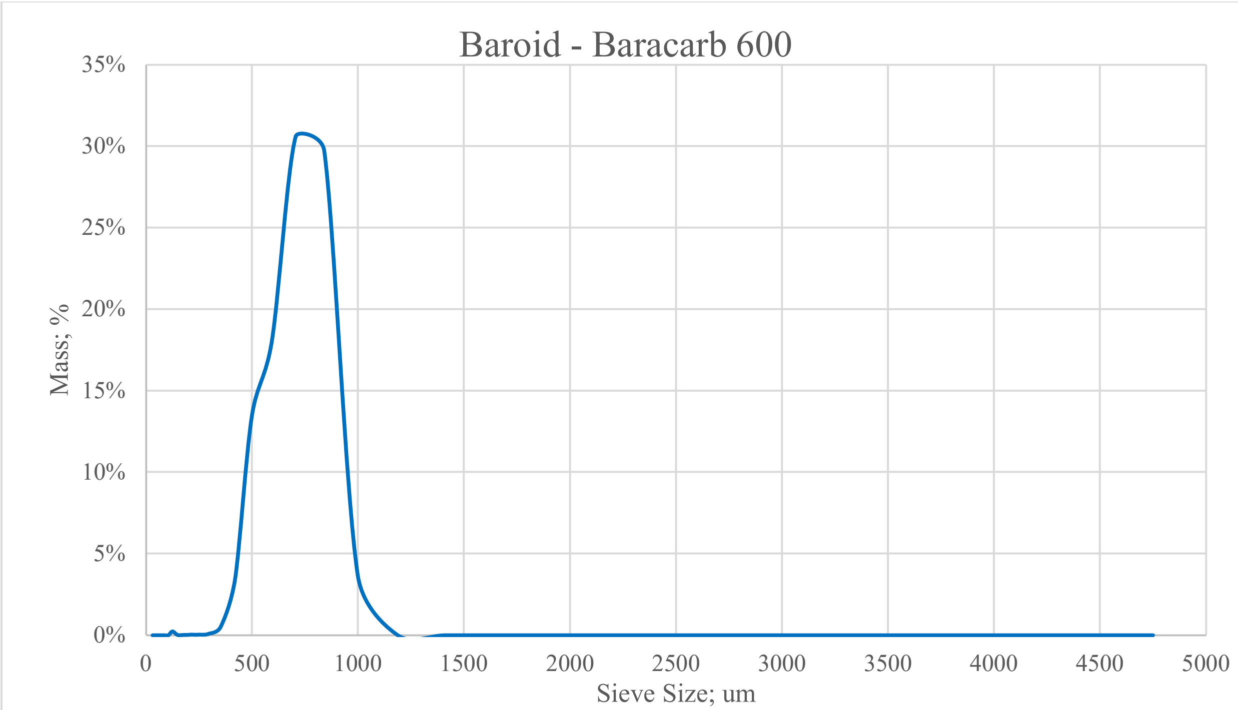

Figure C.51 Particle-size distribution determined by sieving Baroid's Baracarb 600

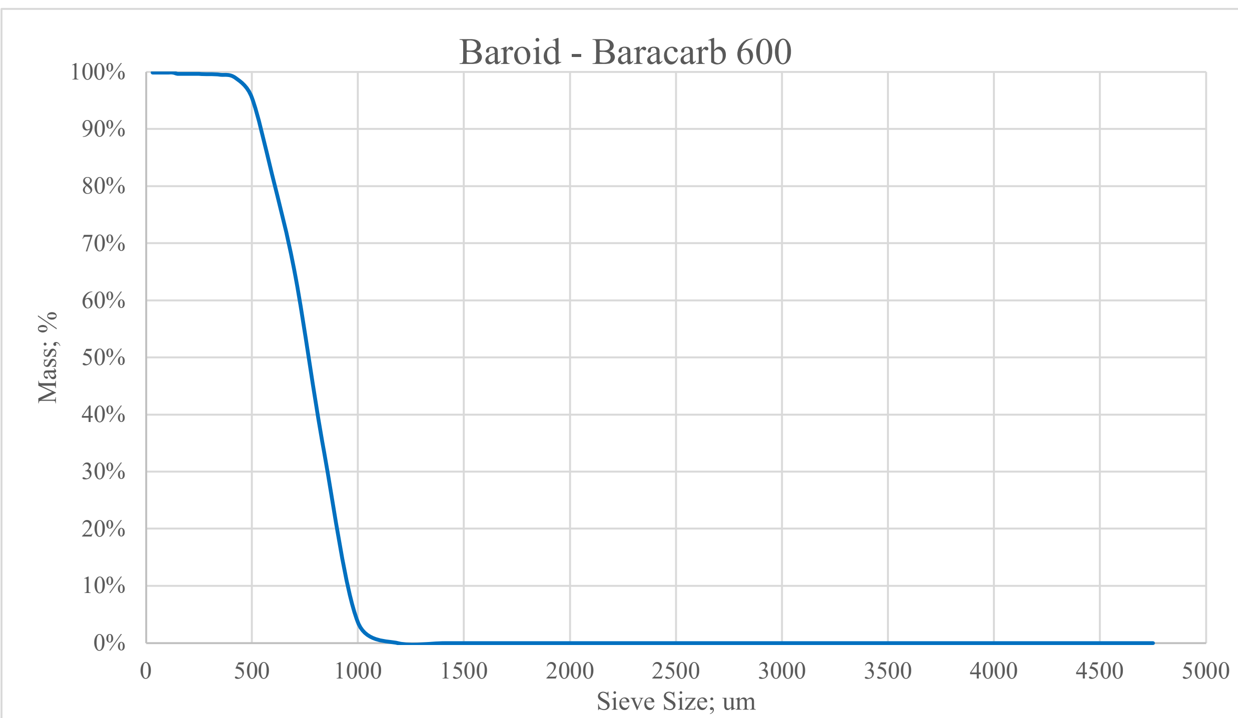

Figure C.52 Cumulative particle-size distribution determined by sieving Baroid's Baracarb 600

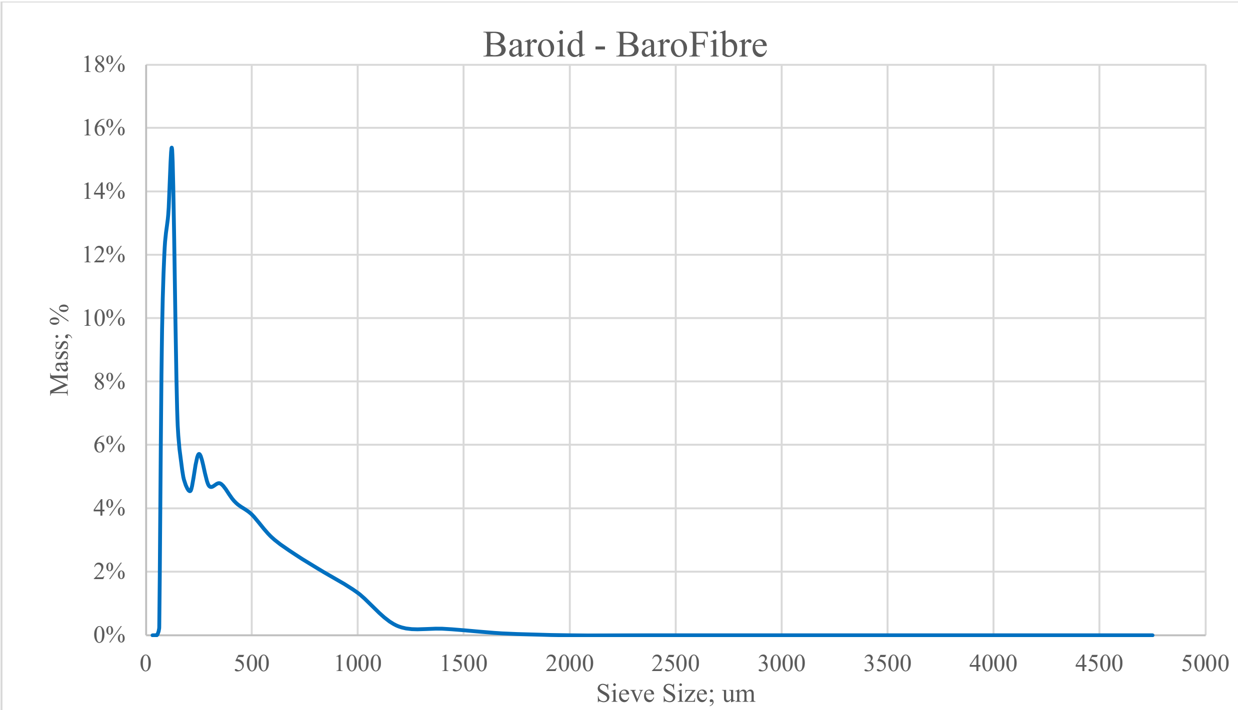

Figure C.53 Particle-size distribution determined by sieving Baroid's BaroFibre

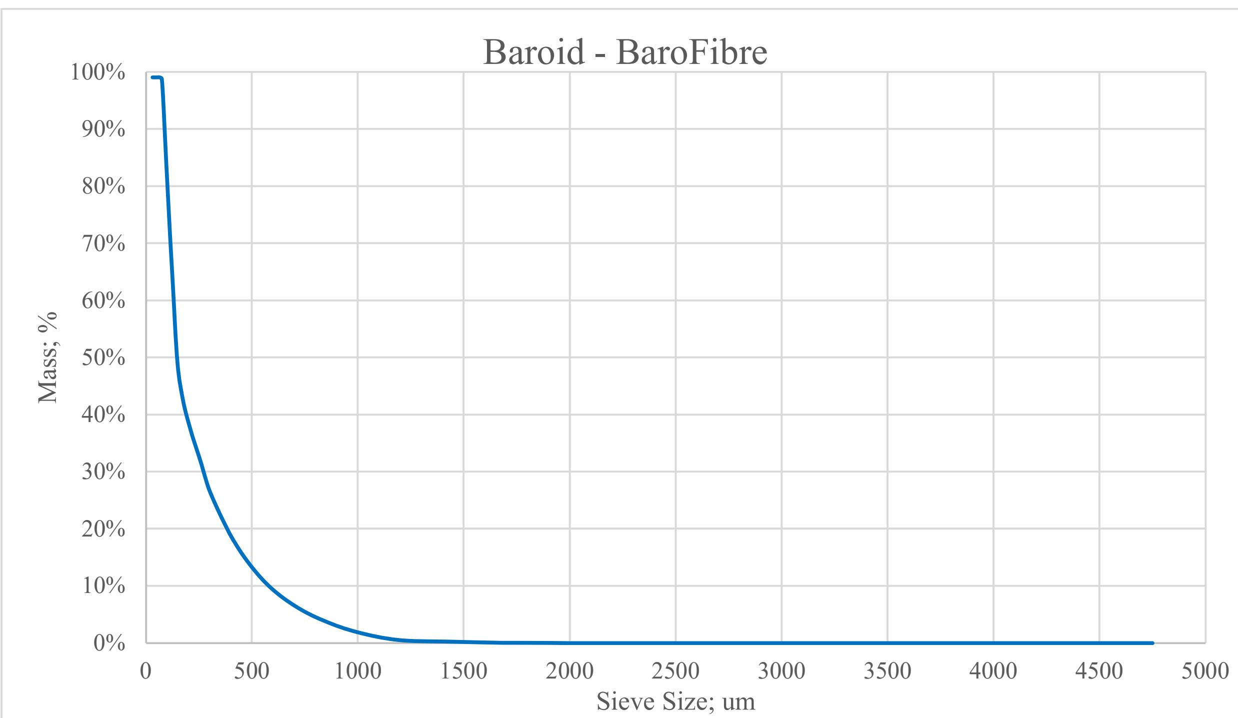

Figure C.54 Cumulative particle-size distribution determined by sieving Baroid's BaroFibre

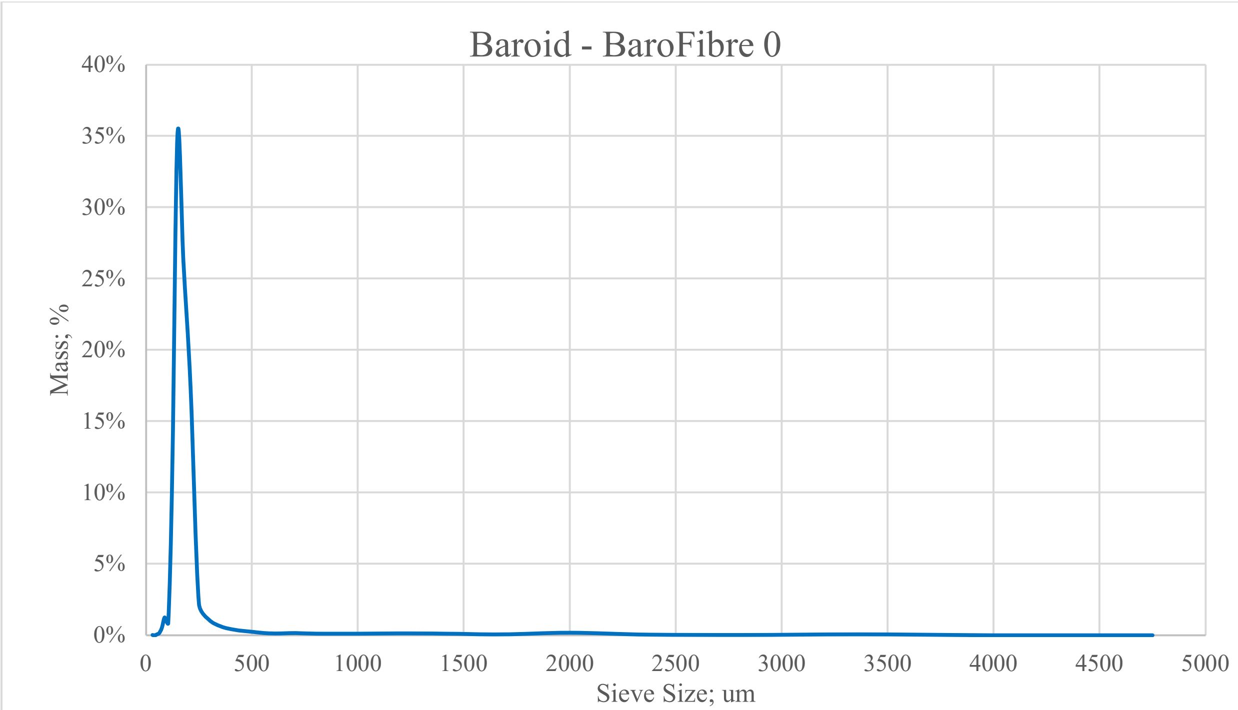

Figure C.55 Particle-size distribution determined by sieving Baroid's BaroFibre 0

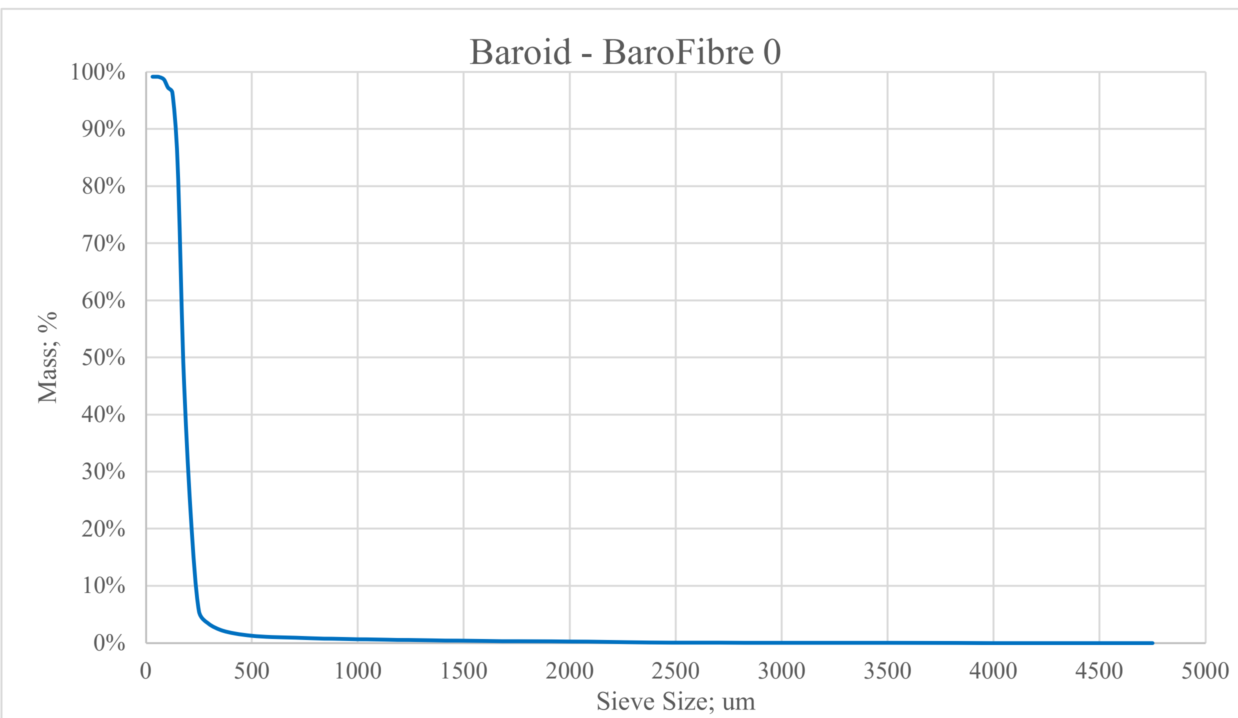

Figure C.56 Cumulative particle-size distribution determined by sieving Baroid's BaroFibre 0

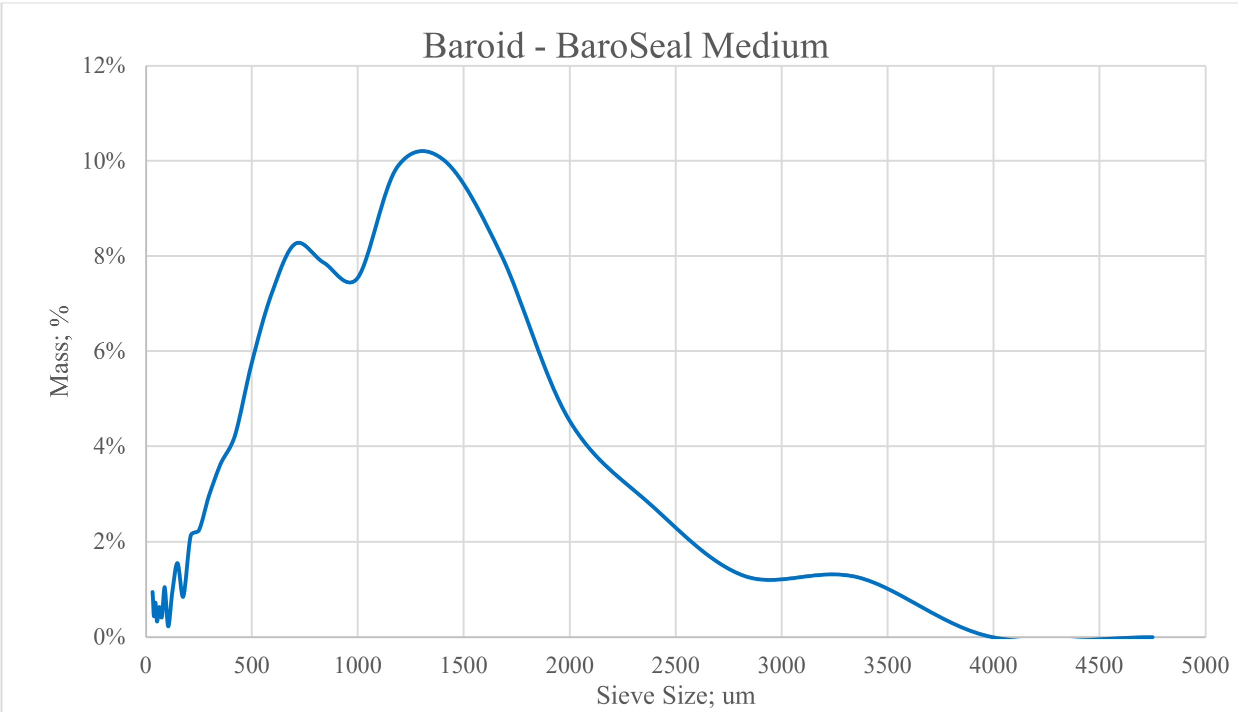

Figure C.57 Particle-size distribution determined by sieving Baroid's BaroSeal Medium

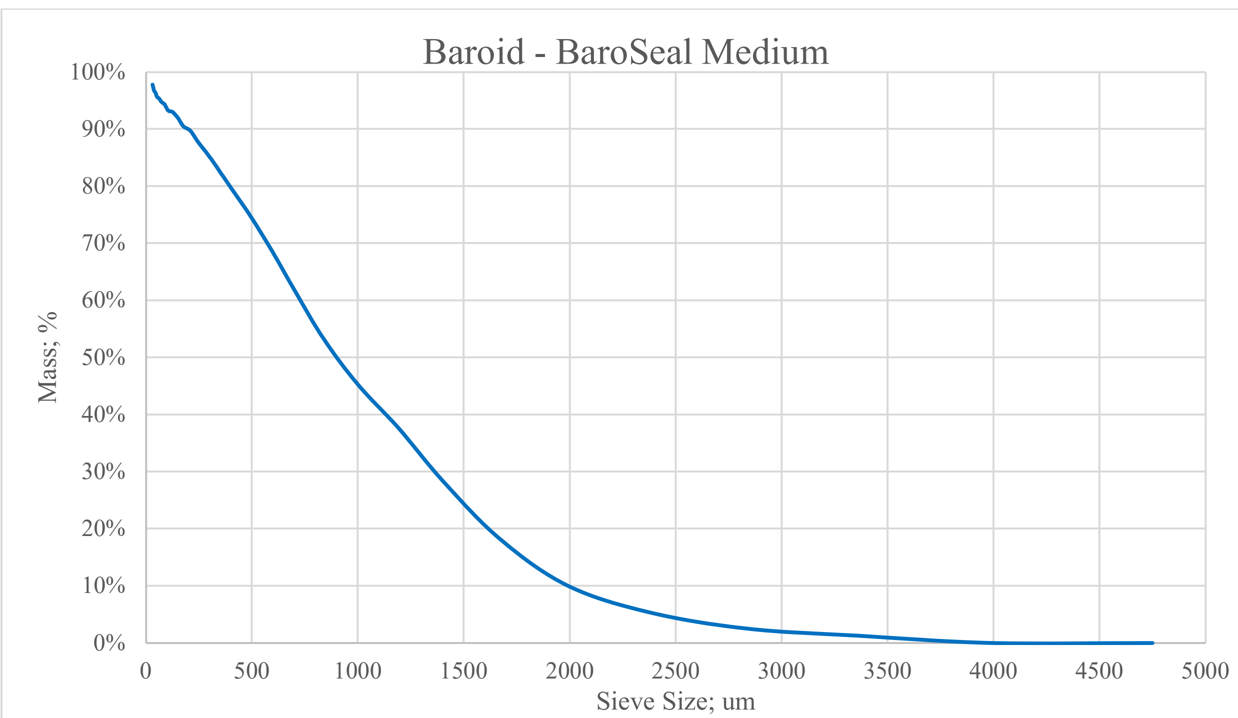

Figure C.58 Cumulative particle-size distribution determined by sieving Baroid's BaroSeal Medium

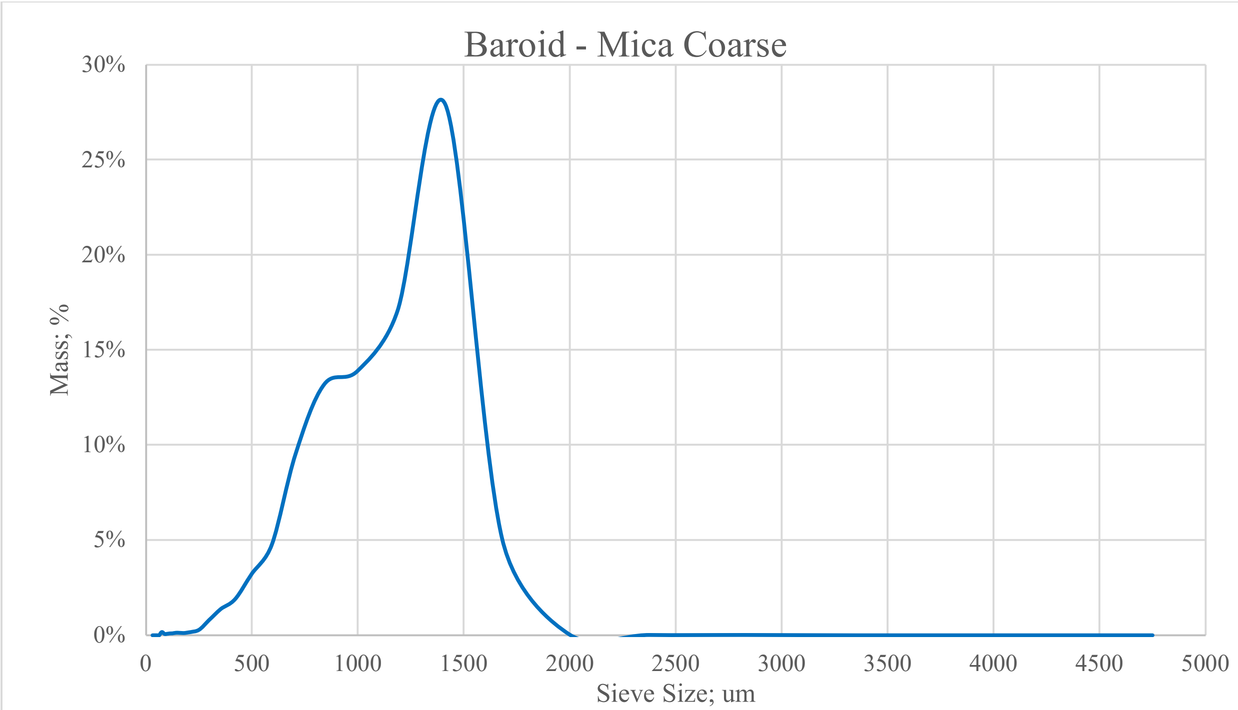

Figure C.59 Particle-size distribution determined by sieving Baroid’s Mica Coarse

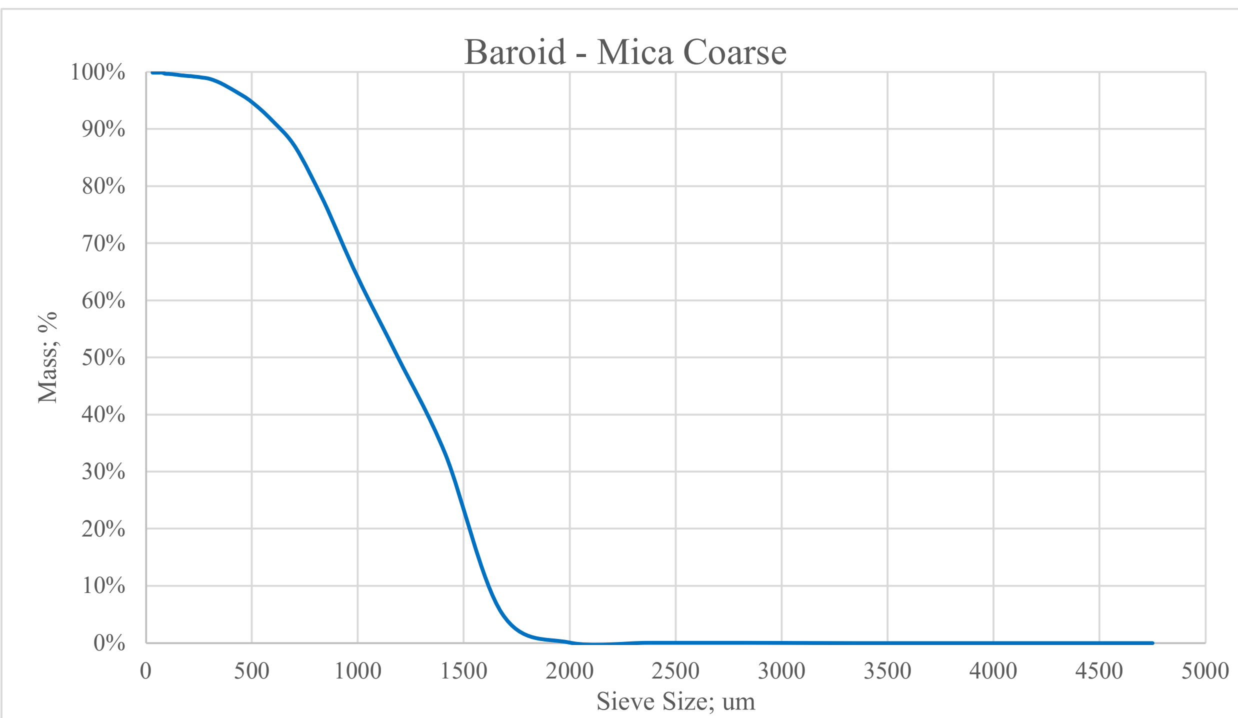

Figure C.60 Cumulative particle-size distribution determined by sieving Baroid’s Mica Coarse

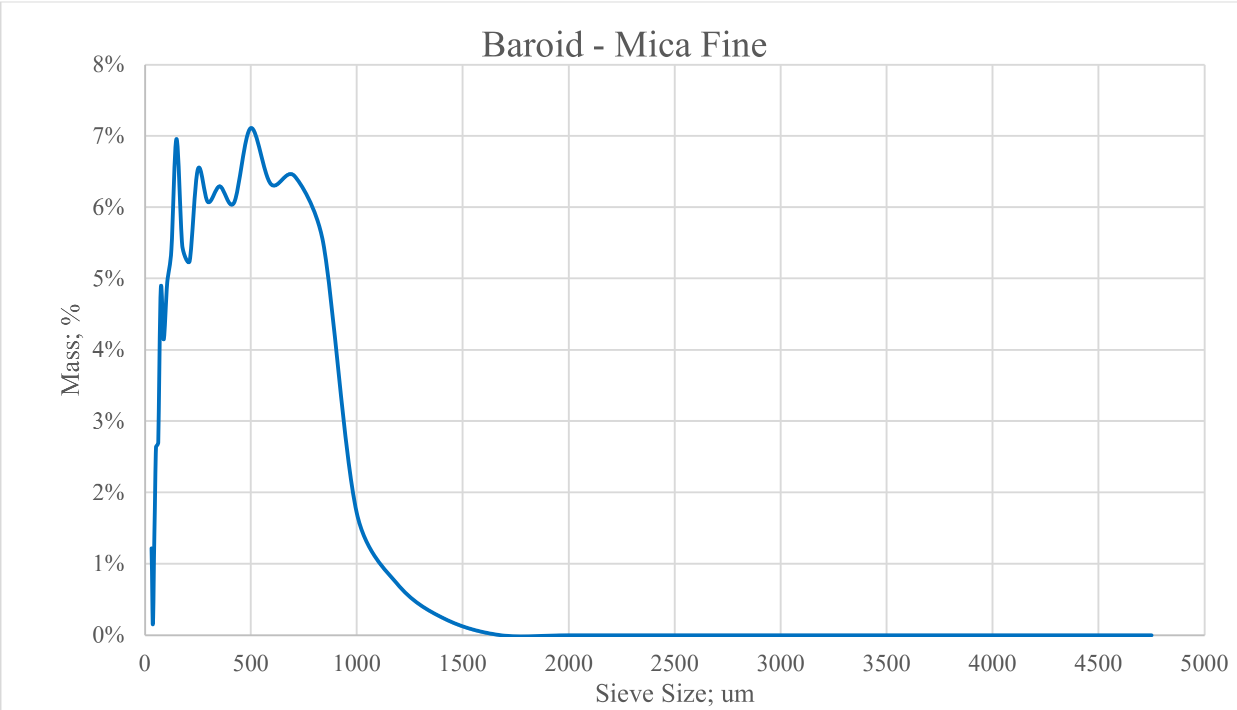

Figure C.61 Particle-size distribution determined by sieving Baroid's Mica Fine

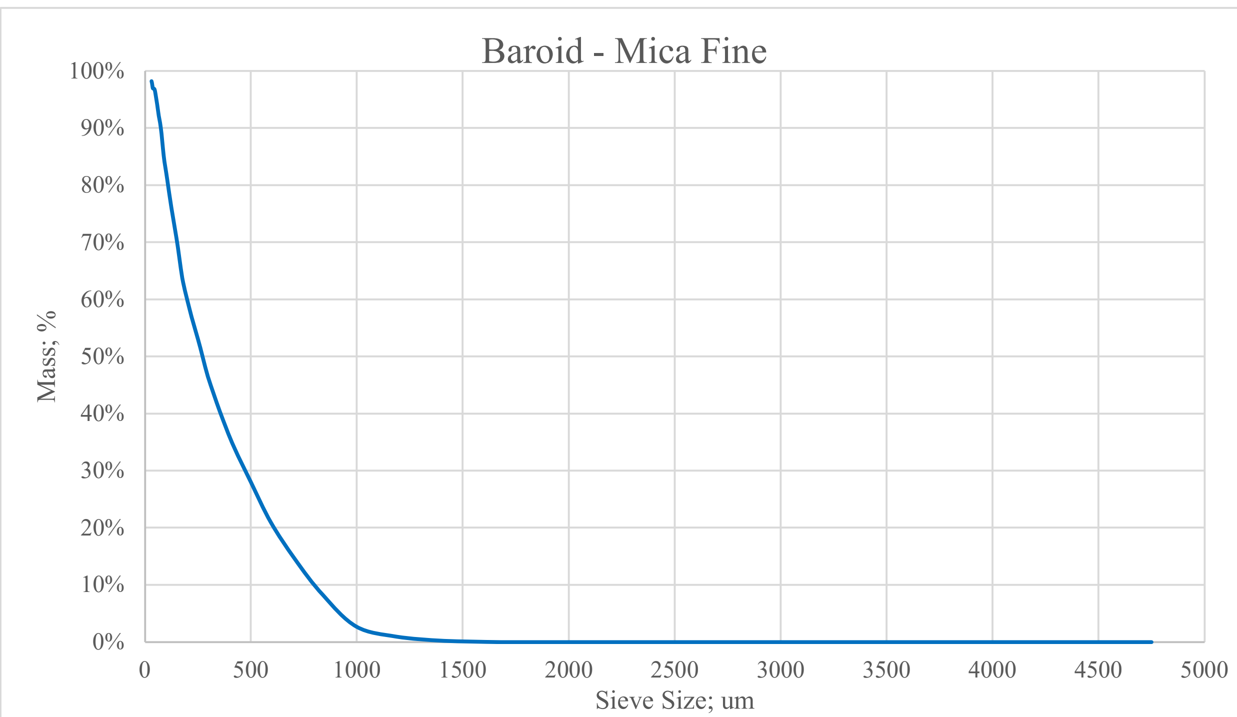

Figure C.62 Cumulative particle-size distribution determined by sieving Baroid's Mica Fine

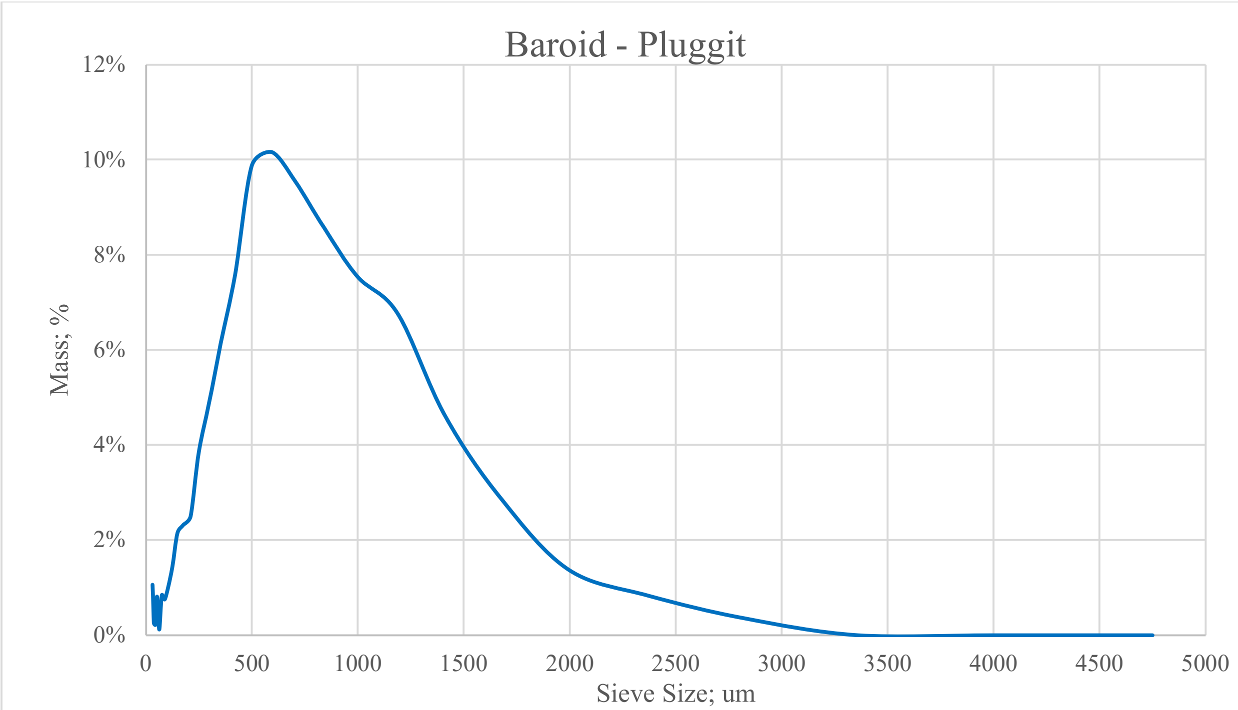

Figure C.63 Particle-size distribution determined by sieving Baroid's Pluggit

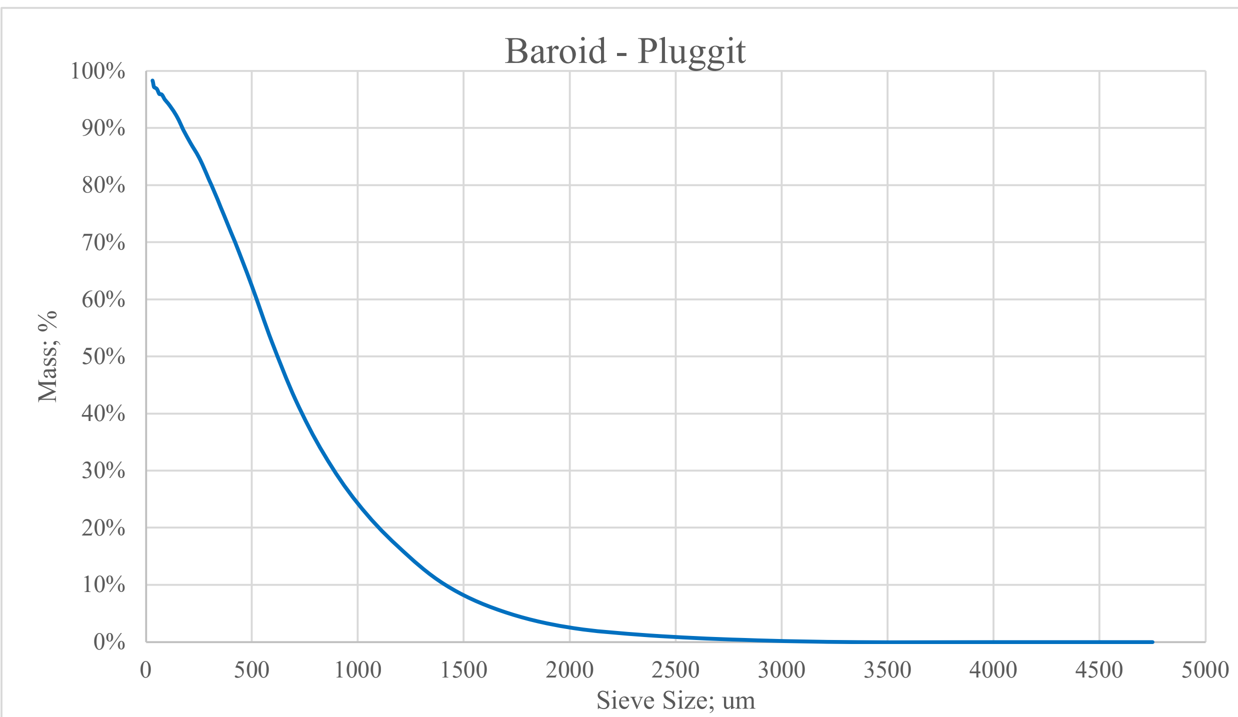

Figure C.64 Cumulative particle-size distribution determined by sieving Baroid's Pluggit

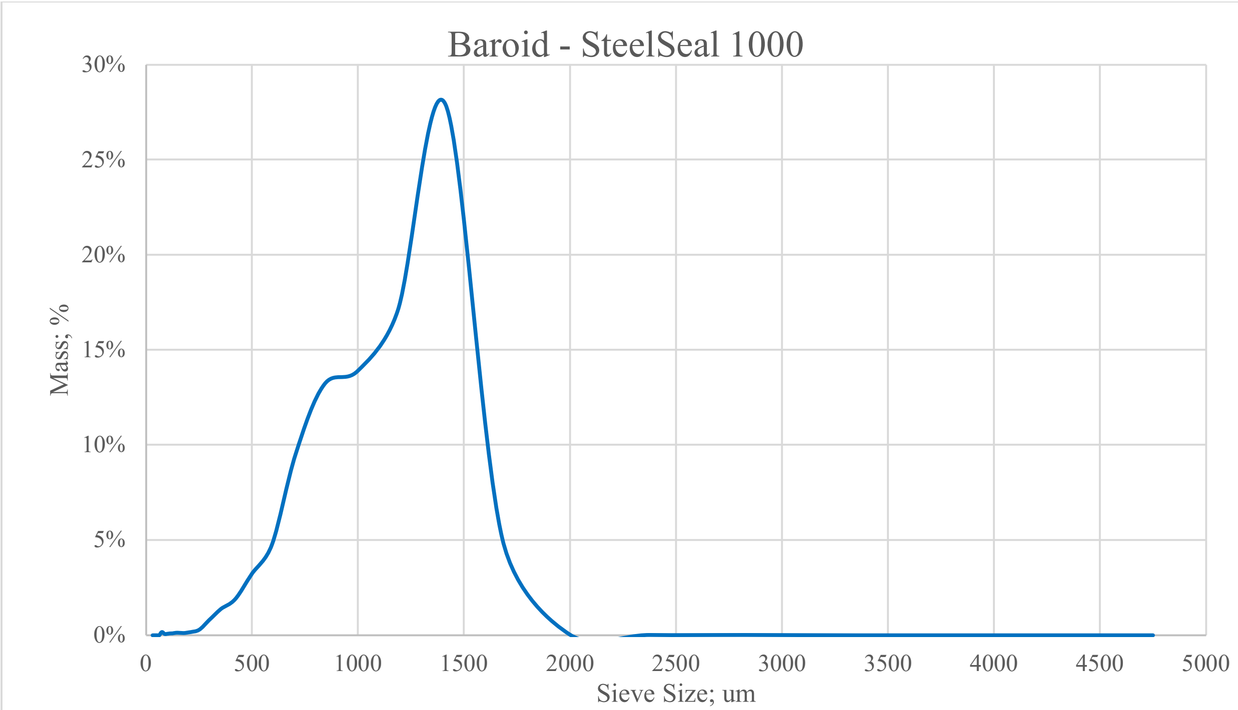

Figure C.65 Particle-size distribution determined by sieving Baroid's SteelSeal 1000

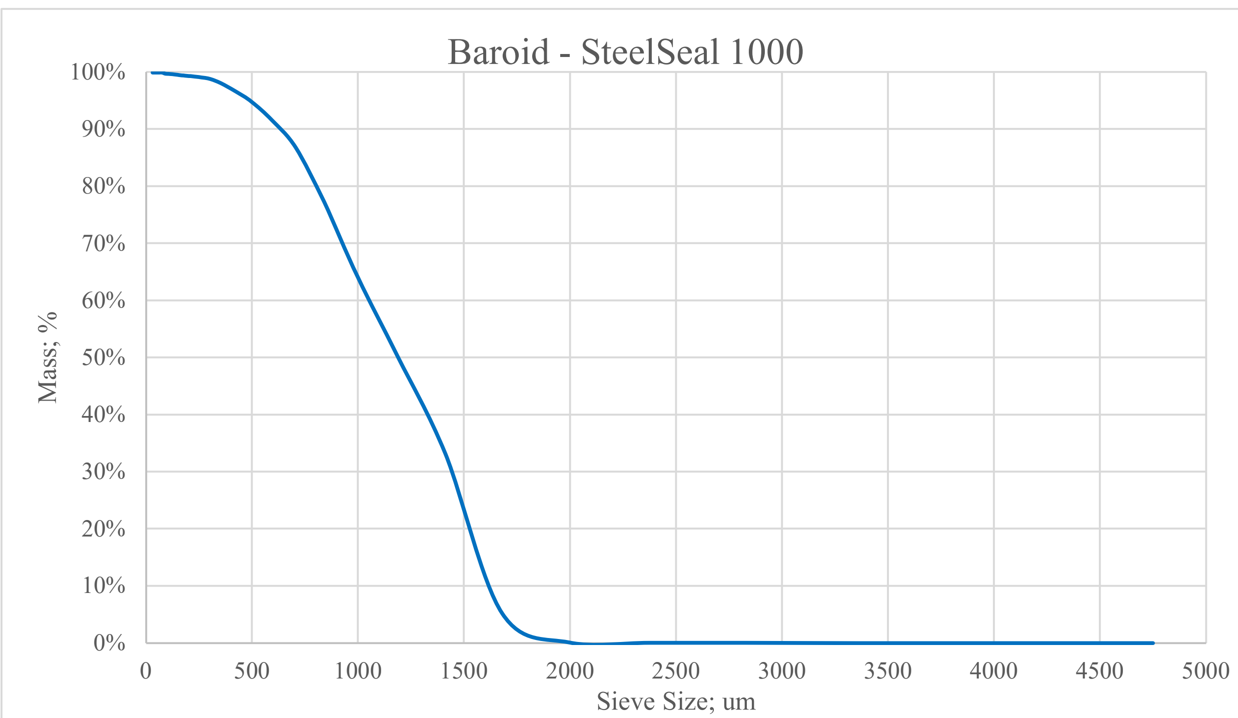

Figure C.66 Cumulative particle-size distribution determined by sieving Baroid's SteelSeal 1000

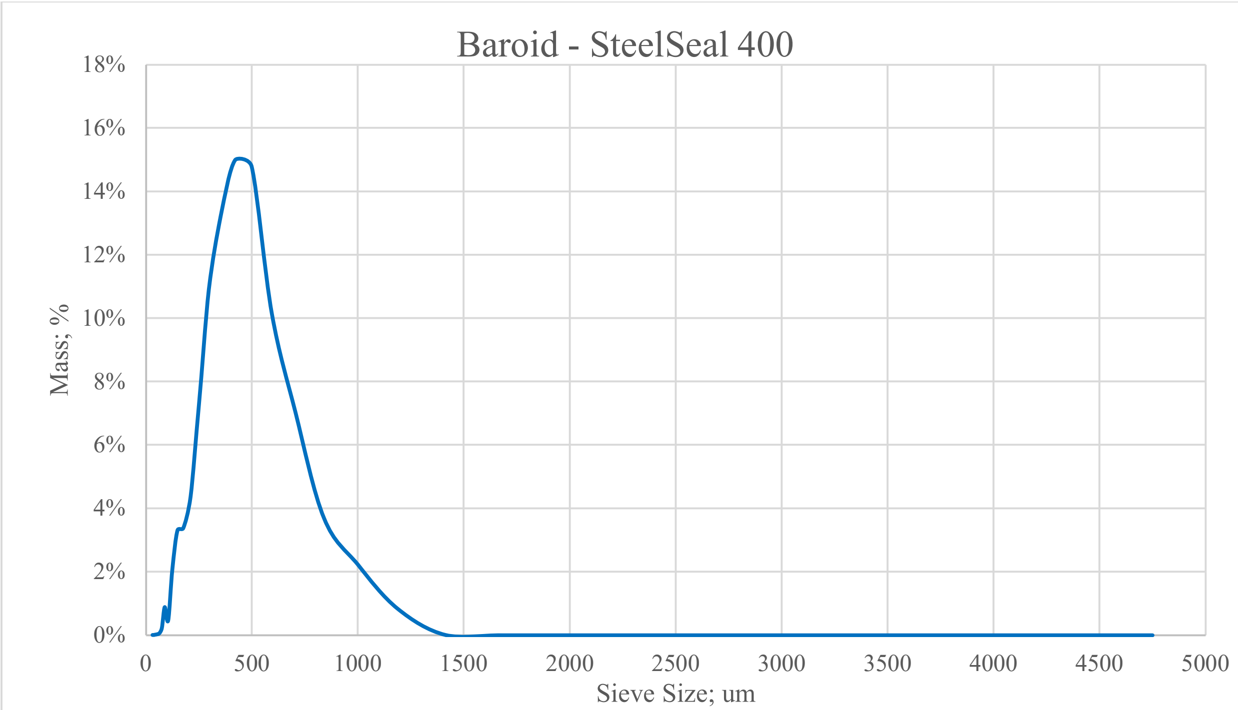

Figure C.67 Particle-size distribution determined by sieving Baroid's SteelSeal 400

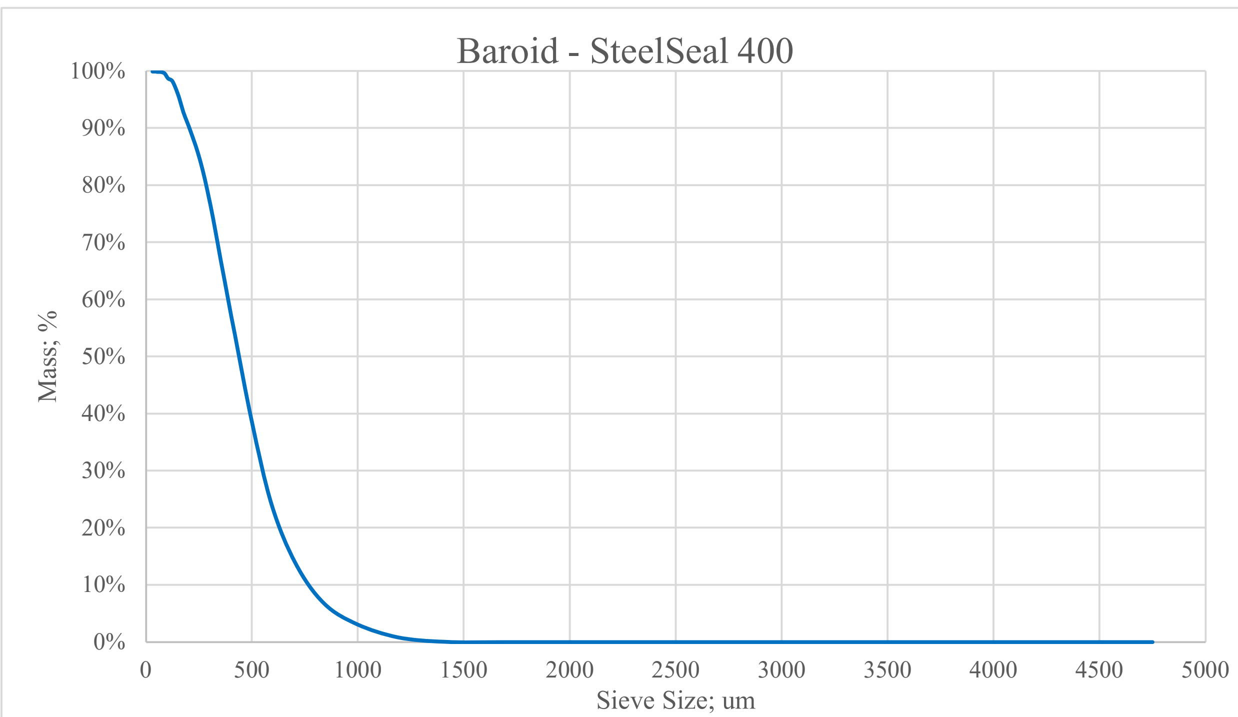

Figure C.68 Cumulative particle-size distribution determined by sieving Baroid's SteelSeal 400

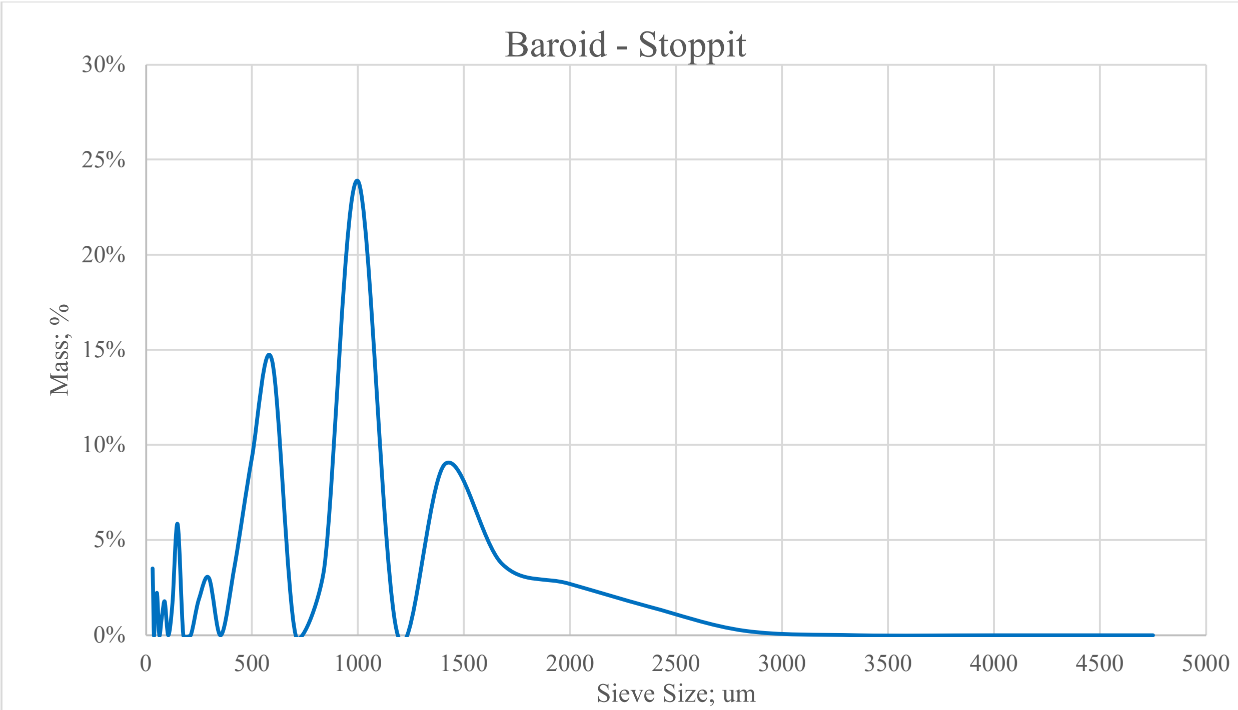

Figure C.69 Particle-size distribution determined by sieving Baroid's Stoppit

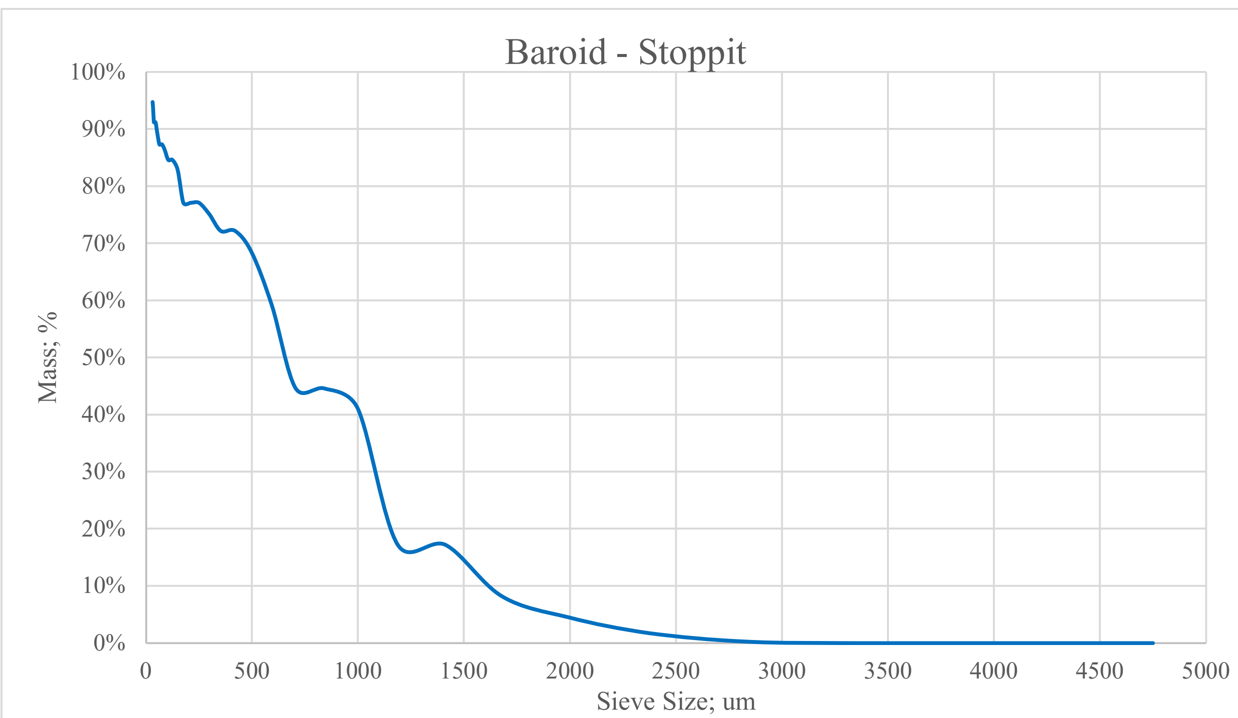

Figure C.70 Cumulative particle-size distribution determined by sieving Baroid's Stoppit

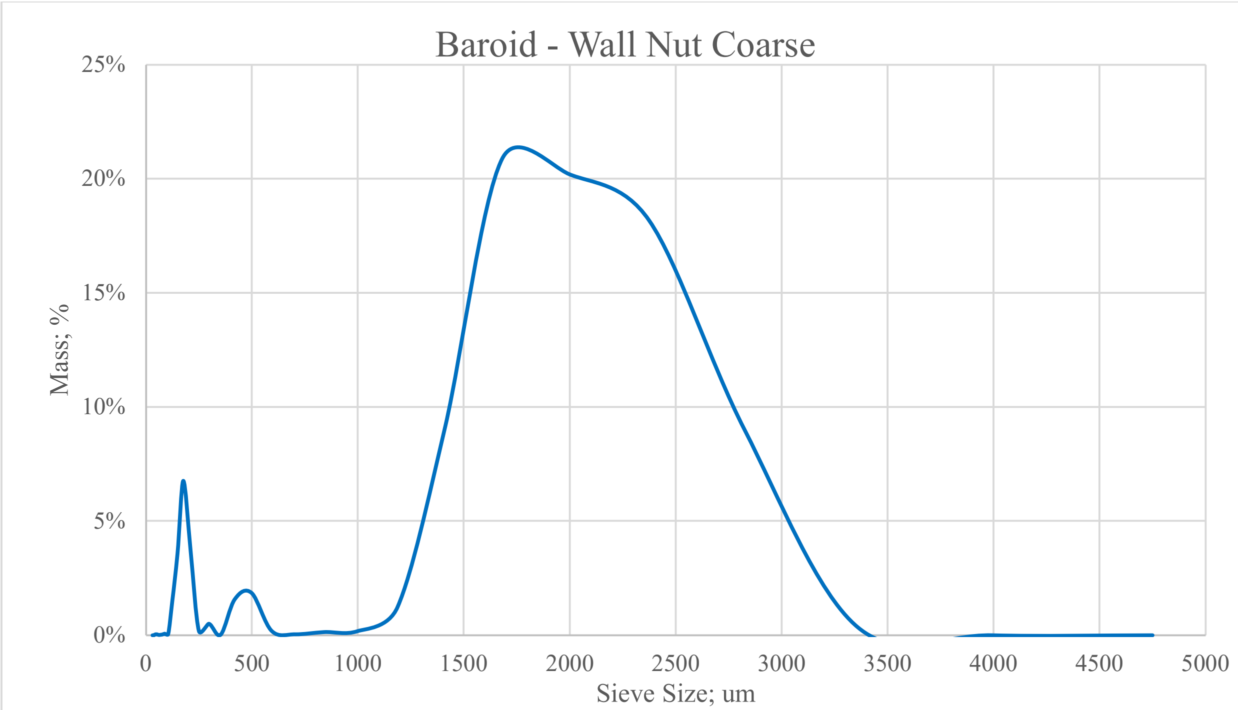

Figure C.71 Particle-size distribution determined by sieving Baroid's Wall Nut Coarse

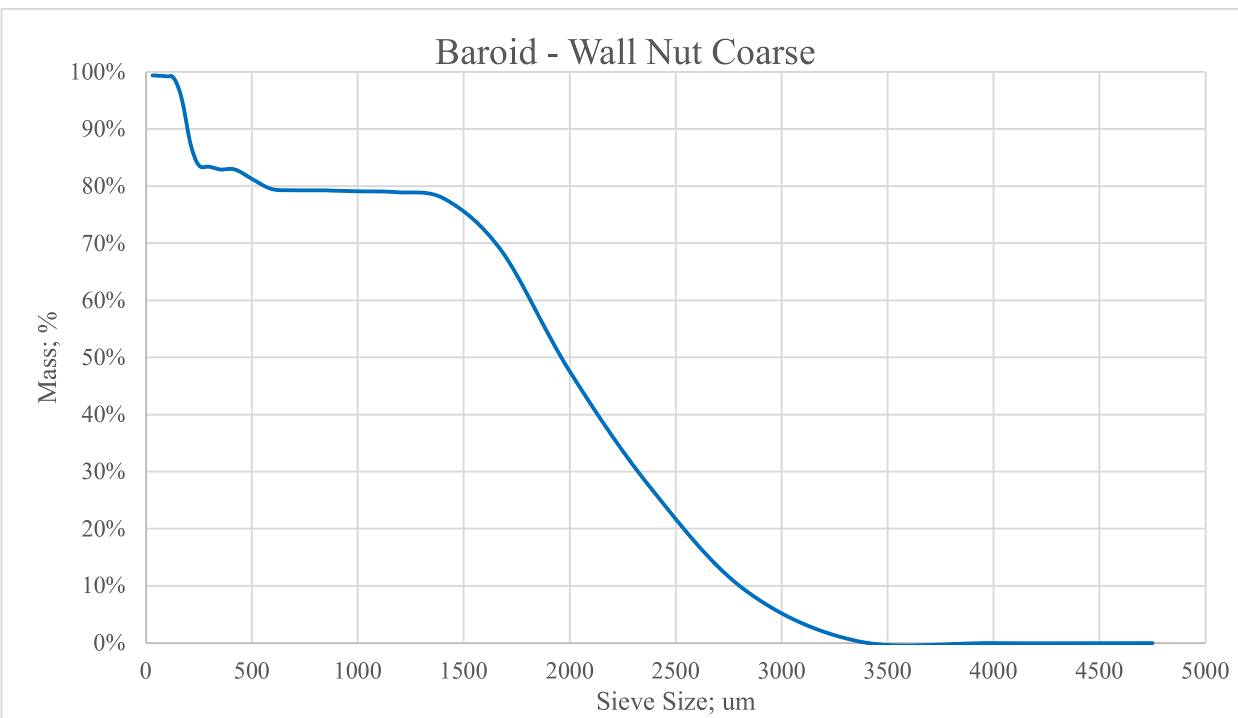

Figure C.72 Cumulative particle-size distribution determined by sieving Baroid's Wall Nut Coarse

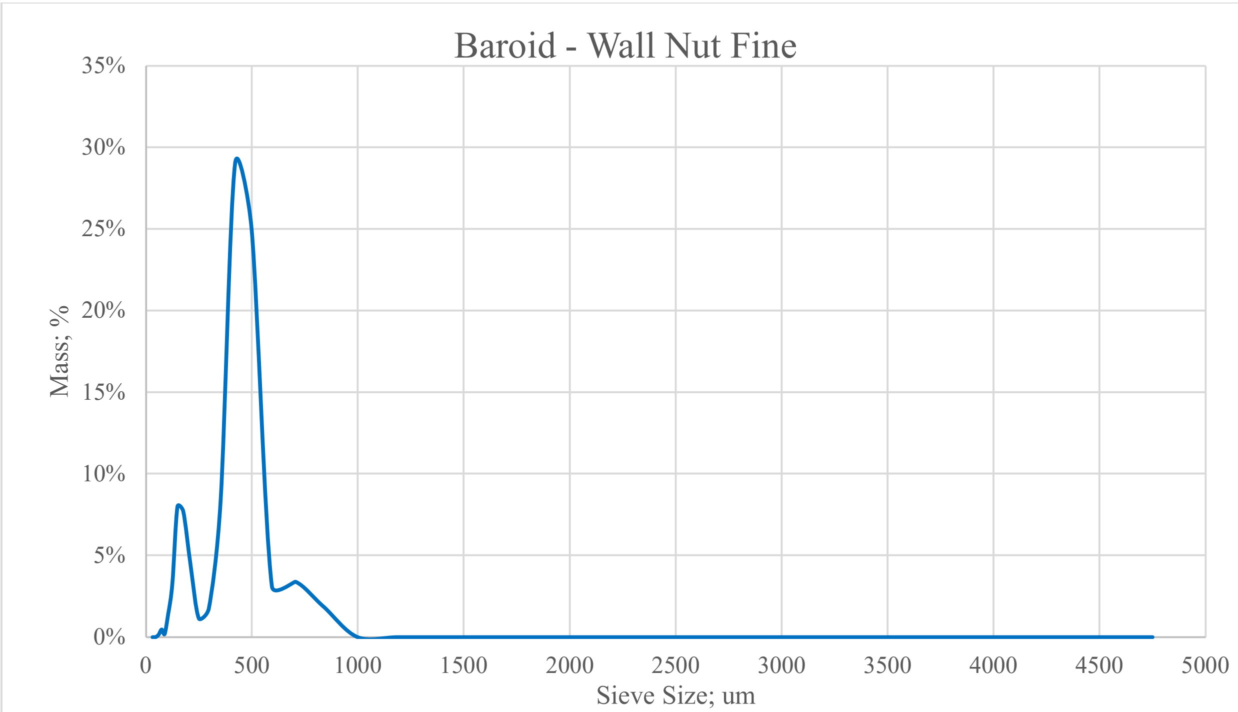

Figure C.73 Particle-size distribution determined by sieving Baroid's Wall Nut Fine

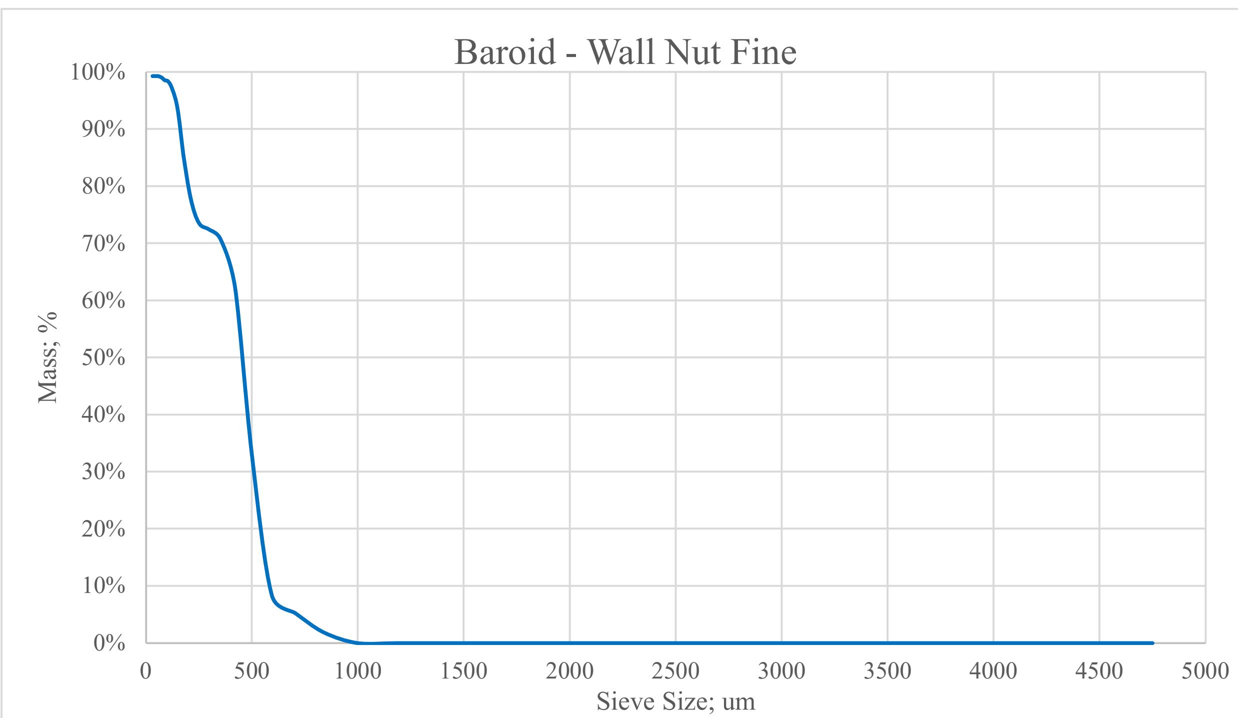

Figure C.74 Cumulative particle-size distribution determined by sieving Baroid's Wall Nut Fine

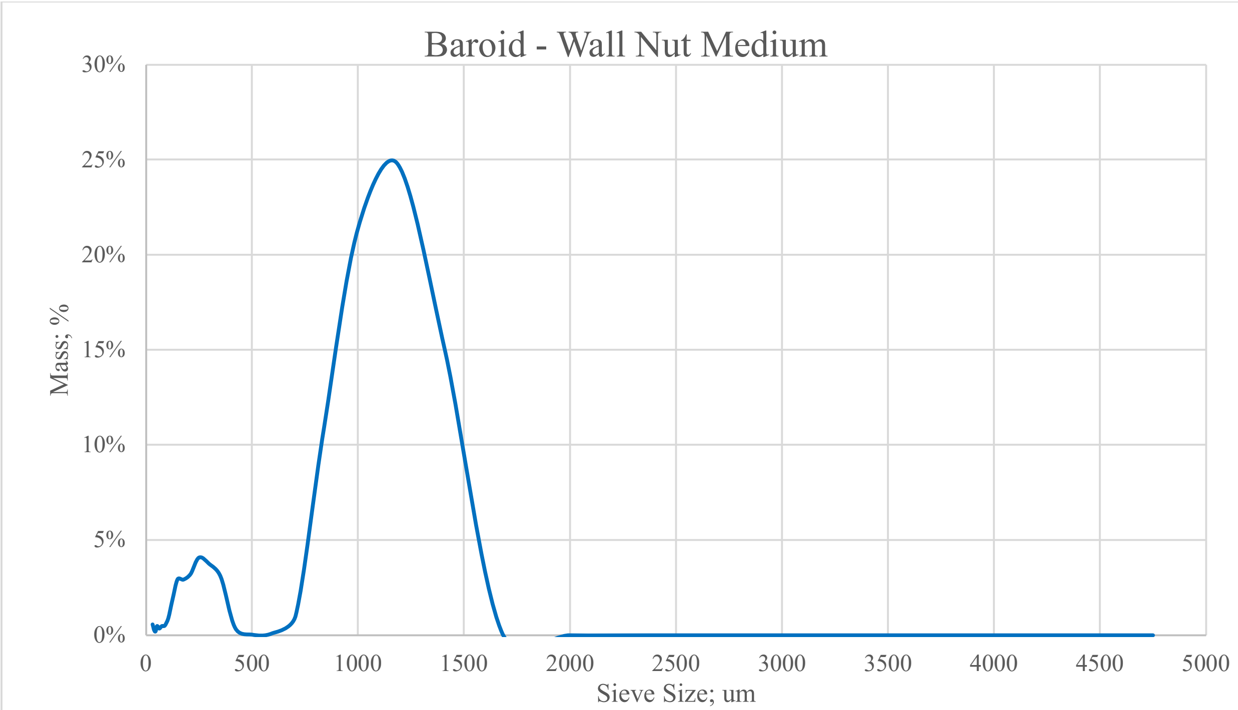

Figure C.75 Particle-size distribution determined by sieving Baroid's Wall Nut Medium

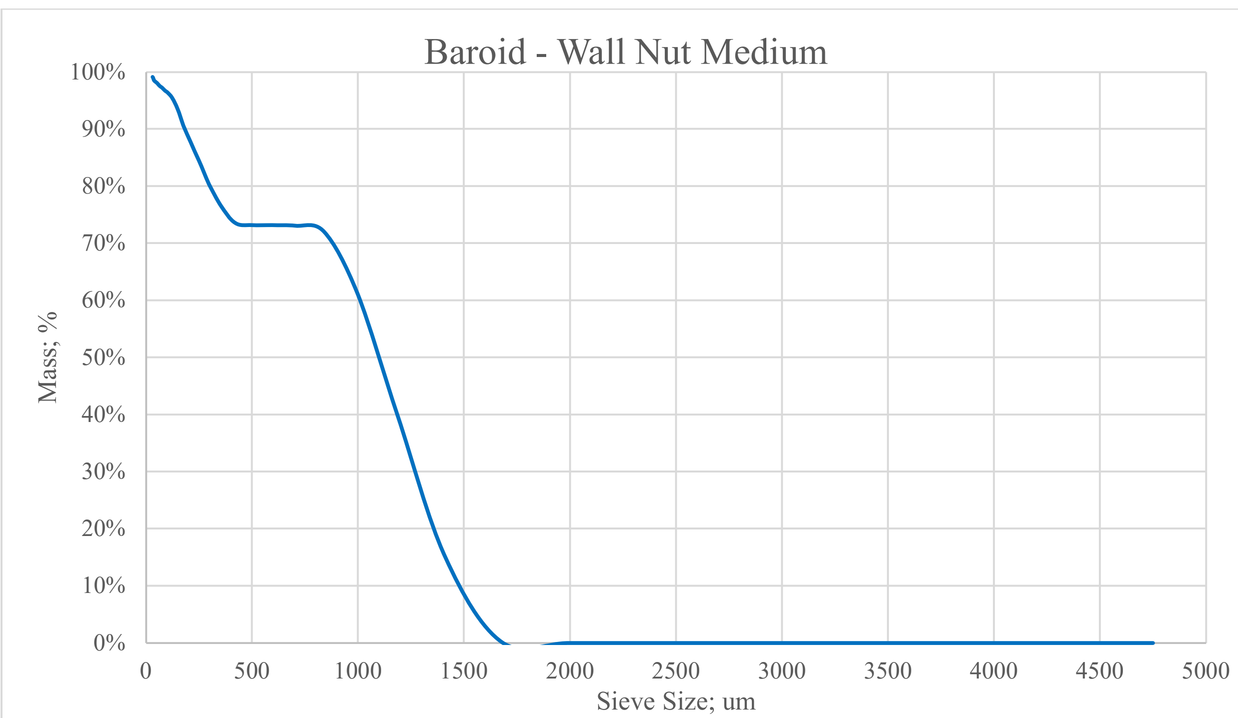

Figure C.76 Cumulative particle-size distribution determined by sieving Baroid's Wall Nut Medium

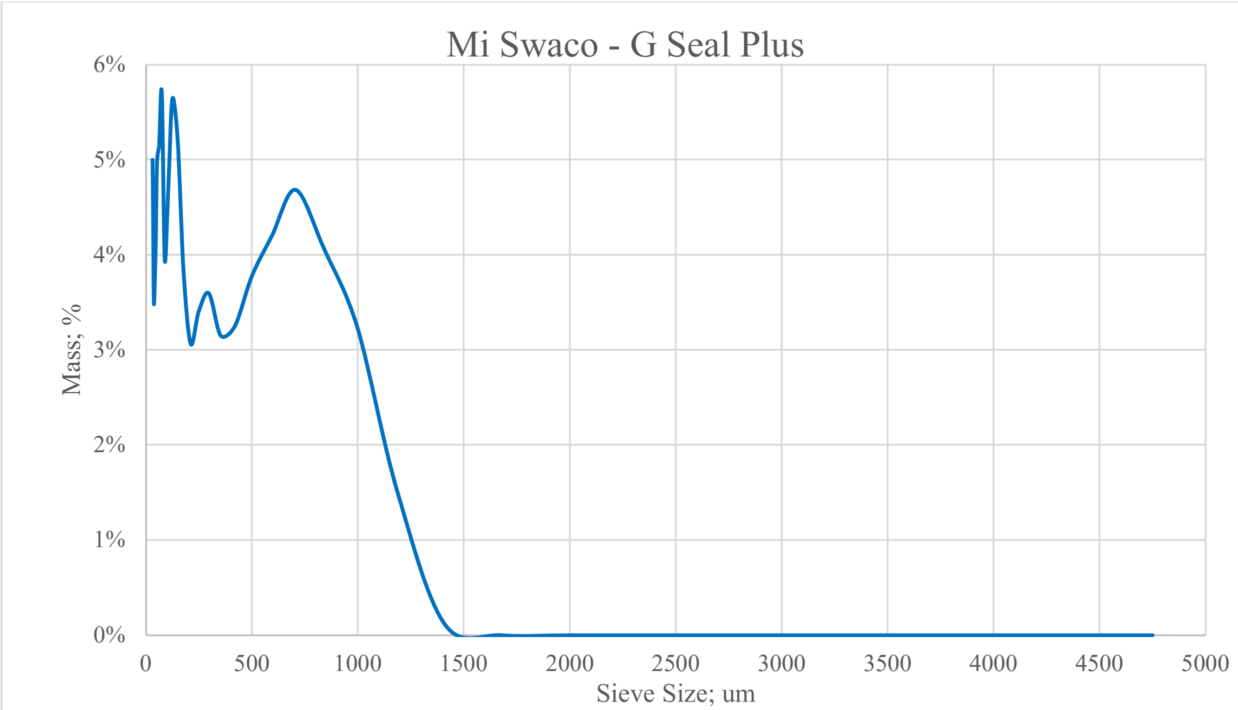

Figure C.77 Particle-size distribution determined by sieving Mi Swaco's G Seal Plus

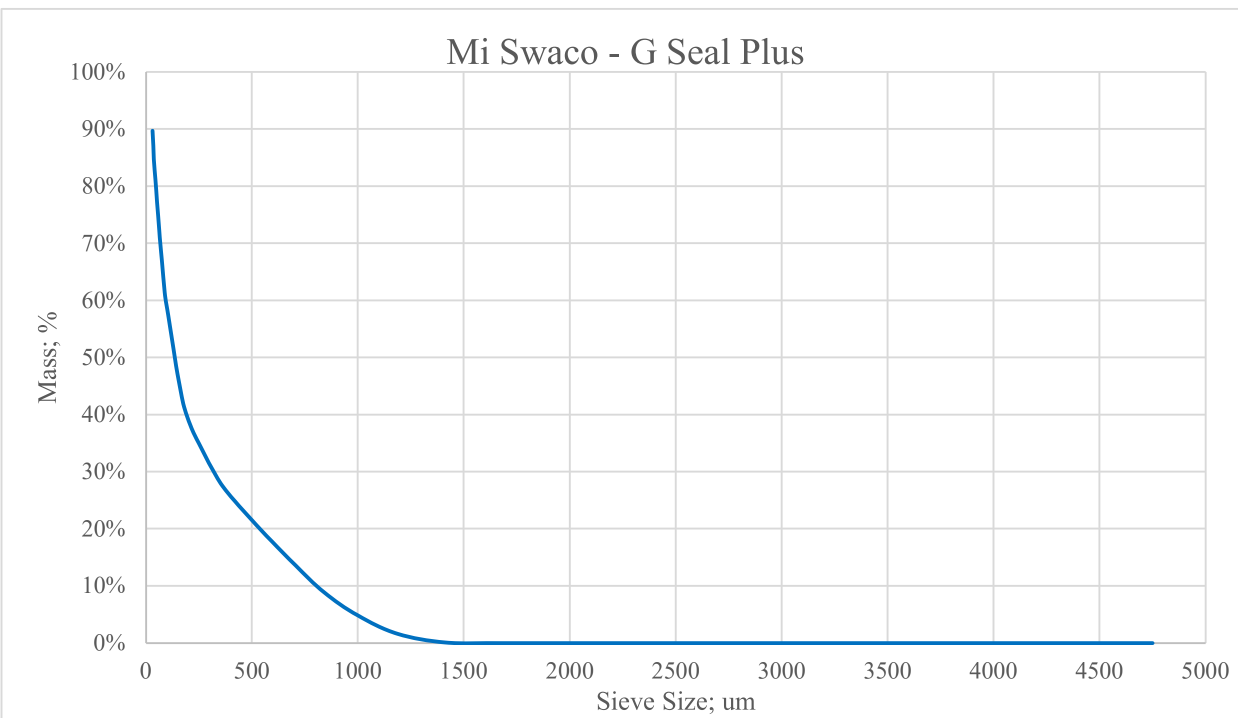

Figure C.78 Cumulative particle-size distribution determined by sieving Mi Swaco's G Seal Plus

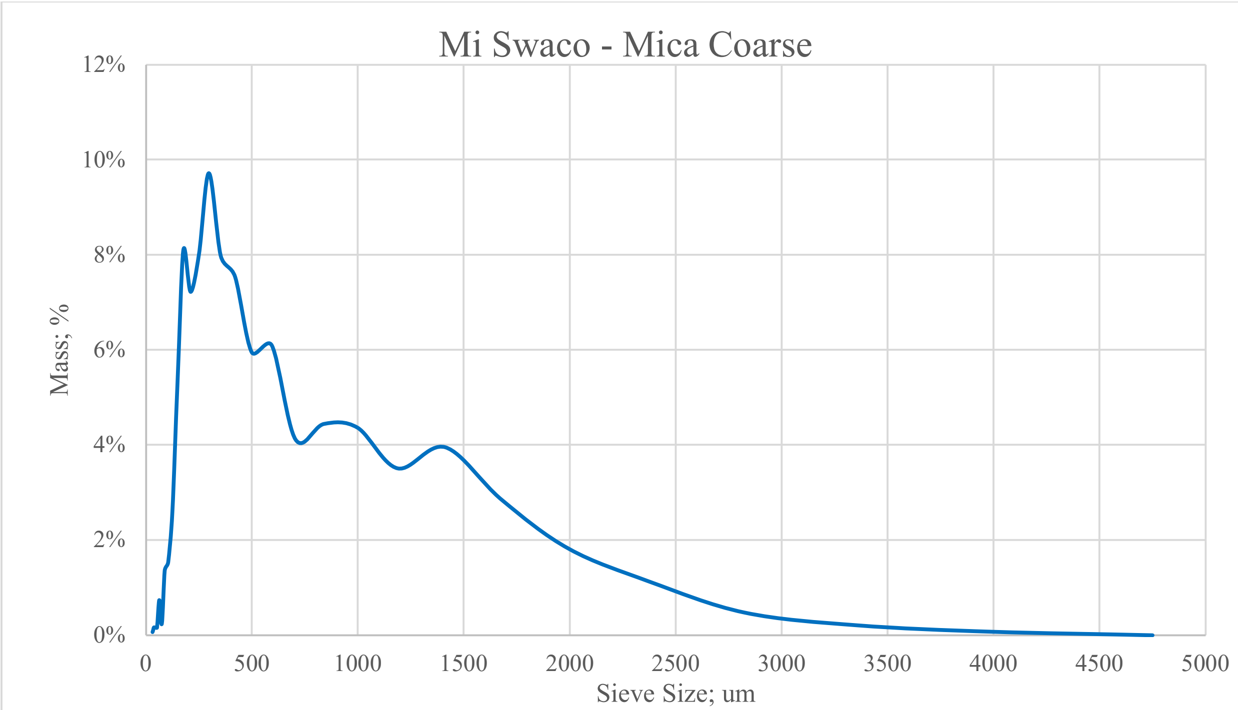

Figure C.79 Particle-size distribution determined by sieving Mi Swaco’s Mica Coarse

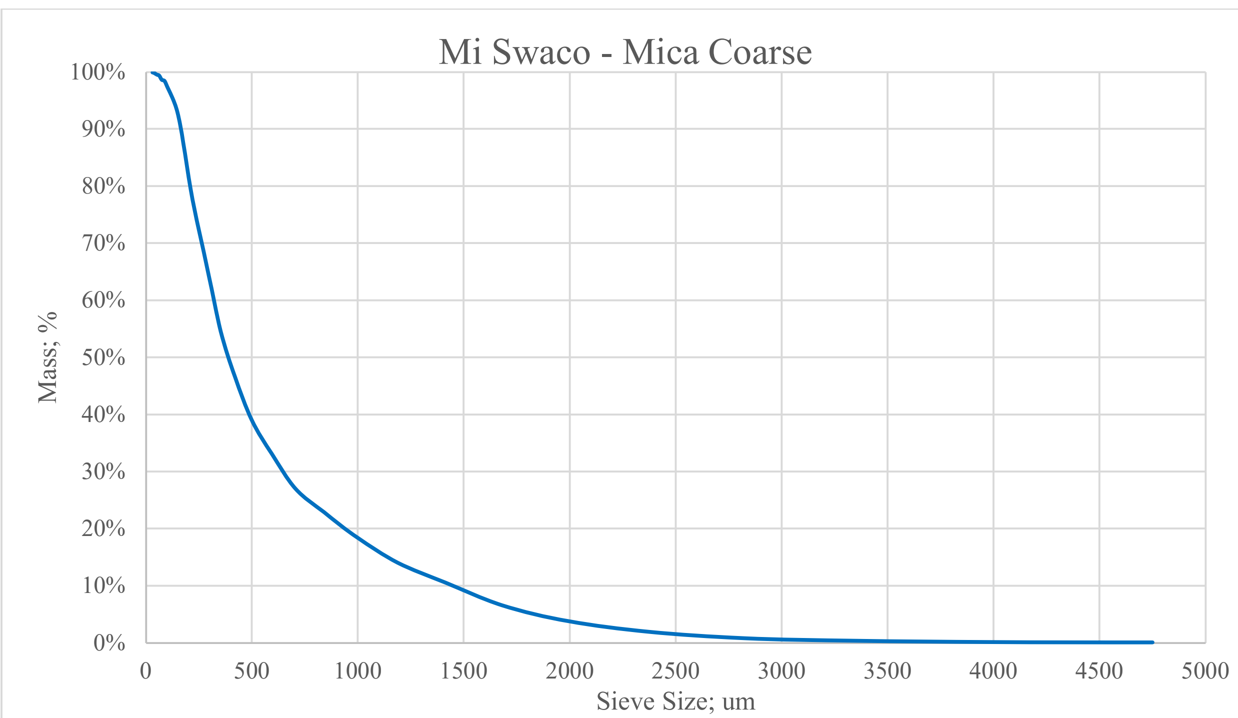

Figure C.80 Cumulative particle-size distribution determined by sieving Mi Swaco’s Mica Coarse

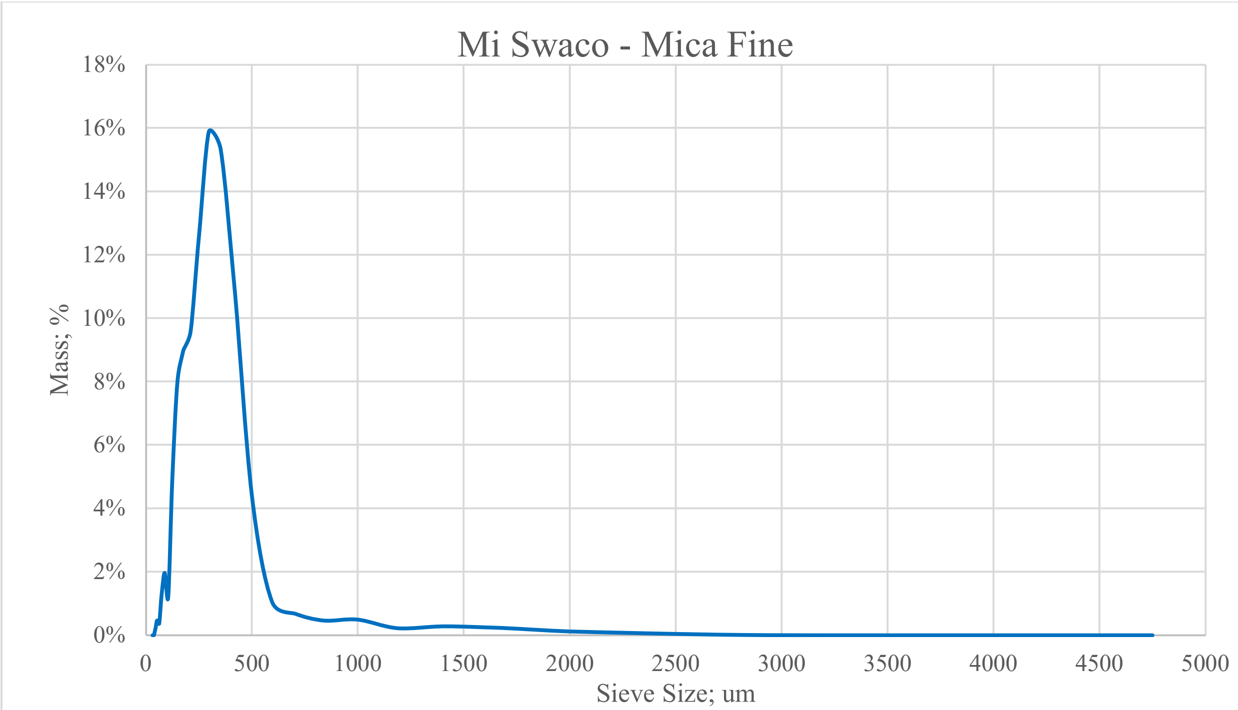

Figure C.81 Particle-size distribution determined by sieving Mi Swaco's Mica Fine

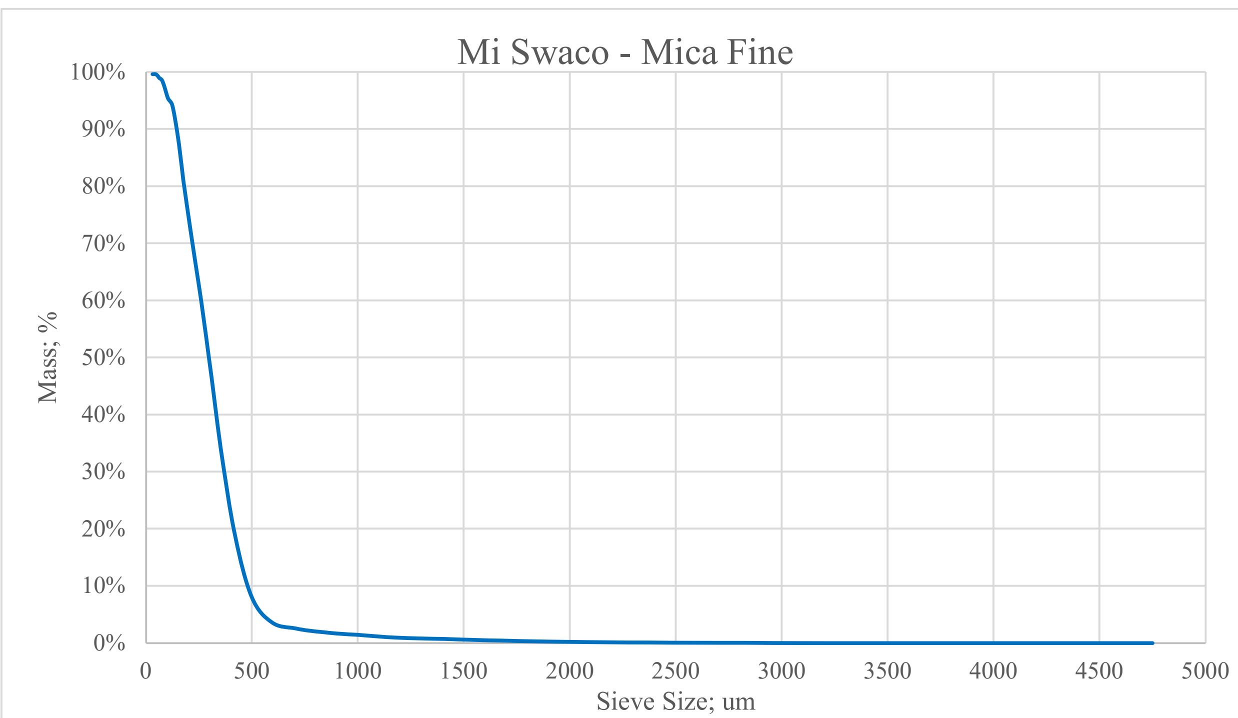

Figure C.82 Cumulative particle-size distribution determined by sieving Mi Swaco's Mica Fine

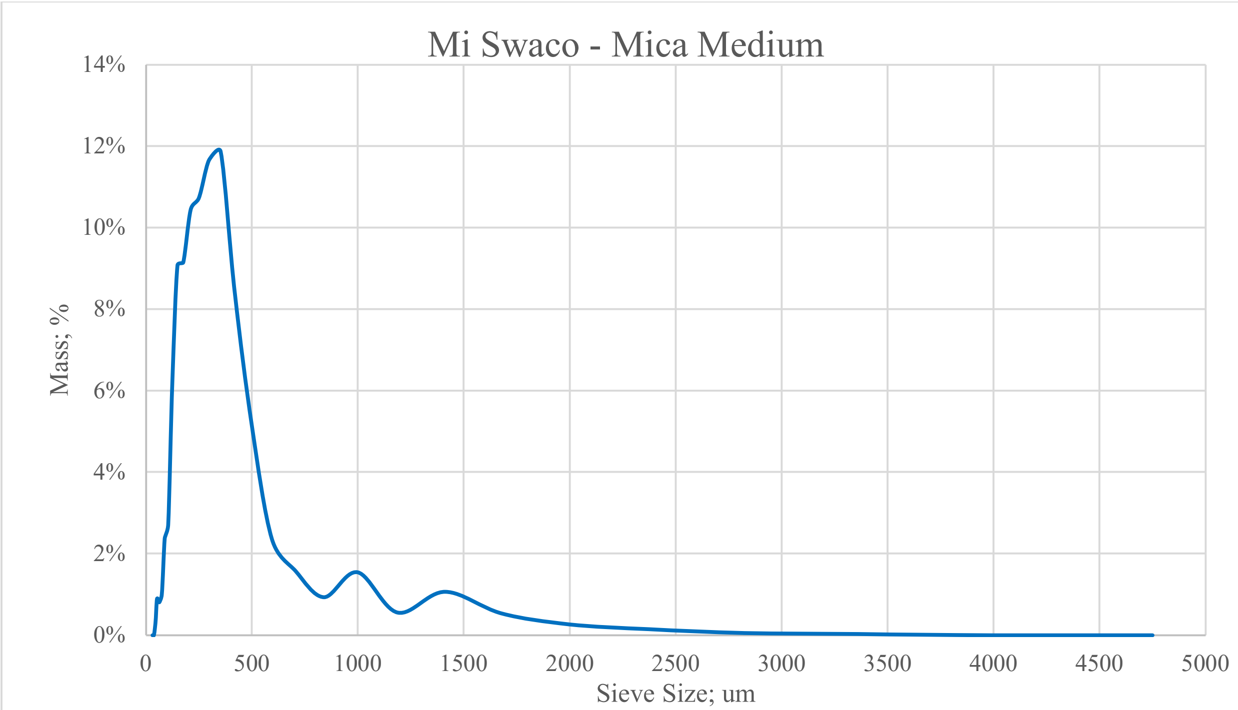

Figure C.83 Particle-size distribution determined by sieving Mi Swaco's Mica Medium

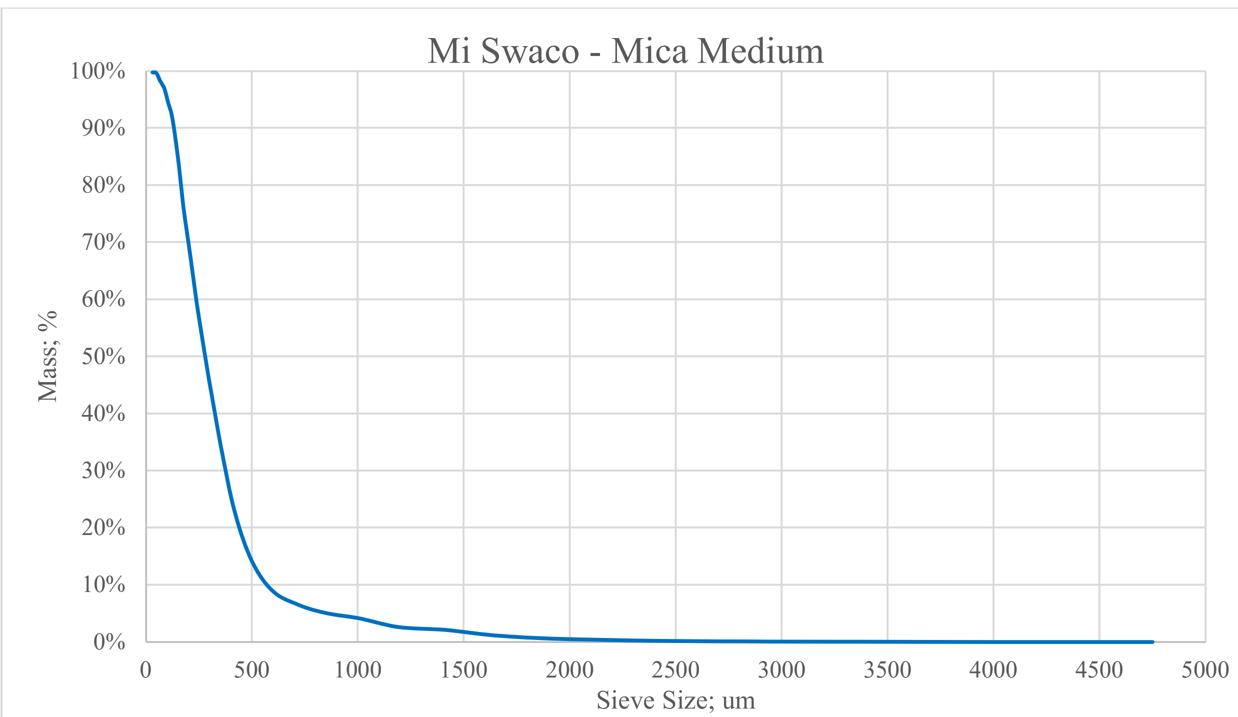

Figure C.84 Cumulative particle-size distribution determined by sieving Mi Swaco's Mica Medium

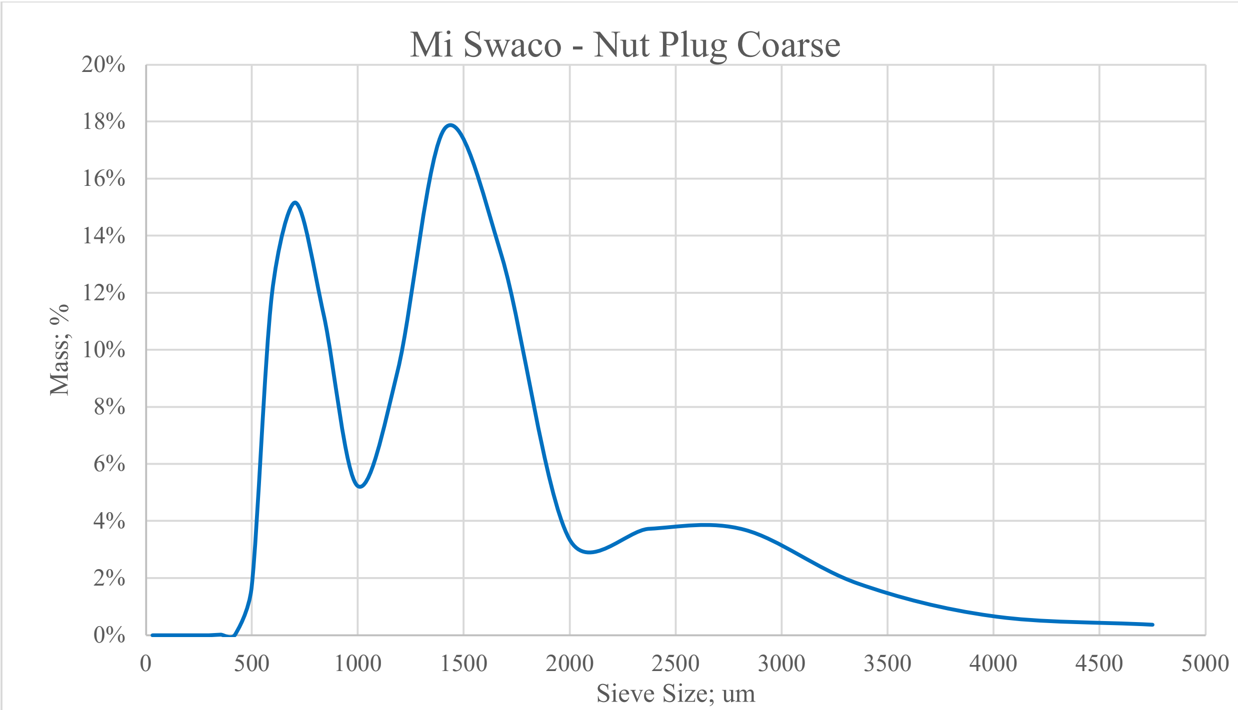

Figure C.85 Particle-size distribution determined by sieving Mi Swaco's Nut Plug Coarse

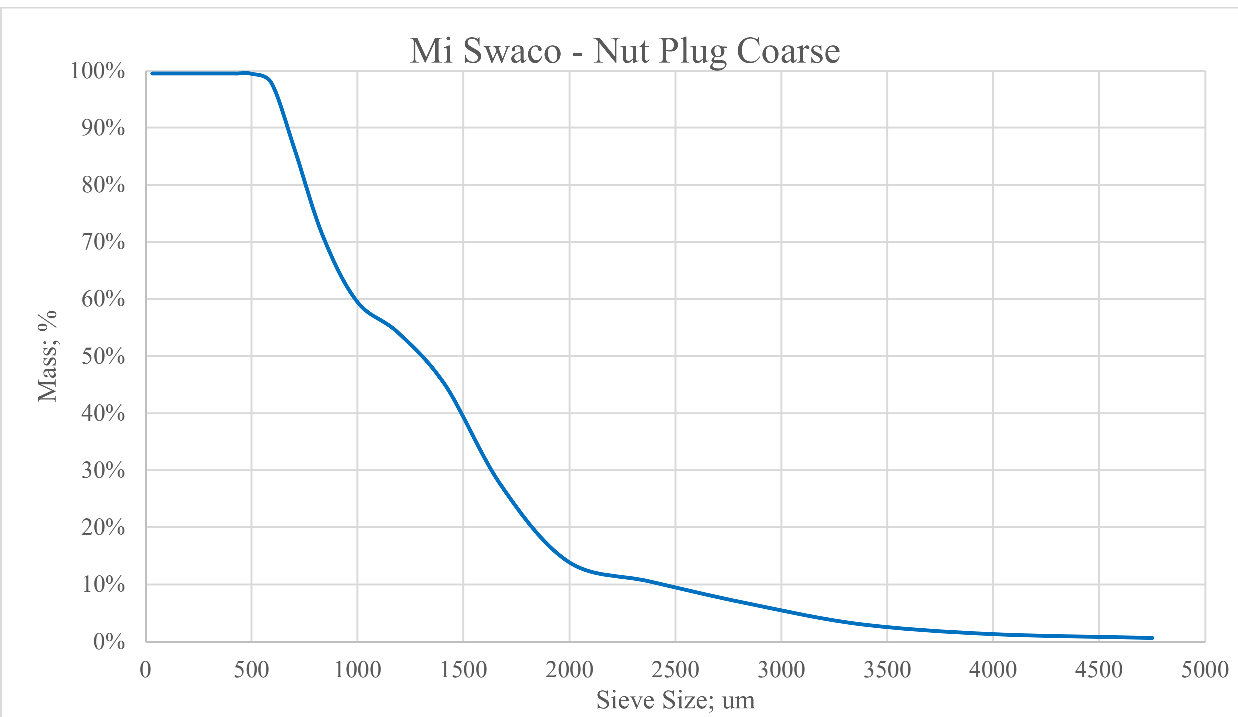

Figure C.86 Cumulative particle-size distribution determined by sieving Mi Swaco's Nut Plug Coarse

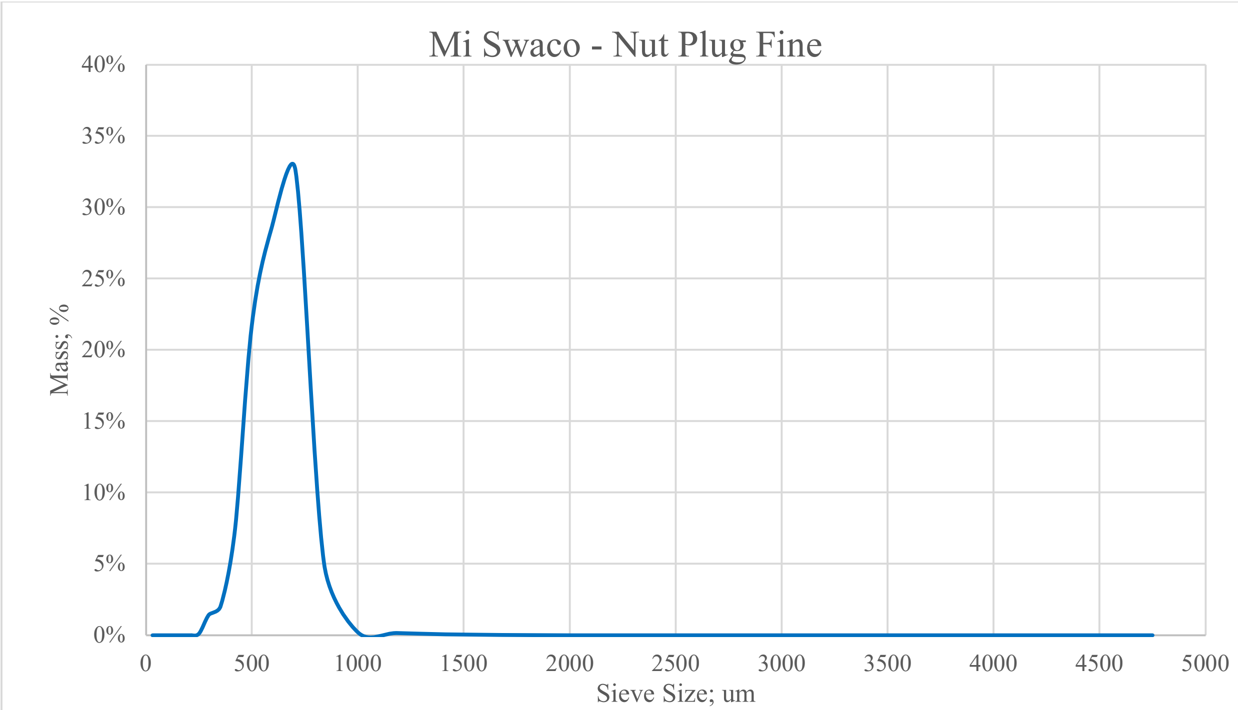

Figure C.87 Particle-size distribution determined by sieving Mi Swaco's Nut Plug Fine

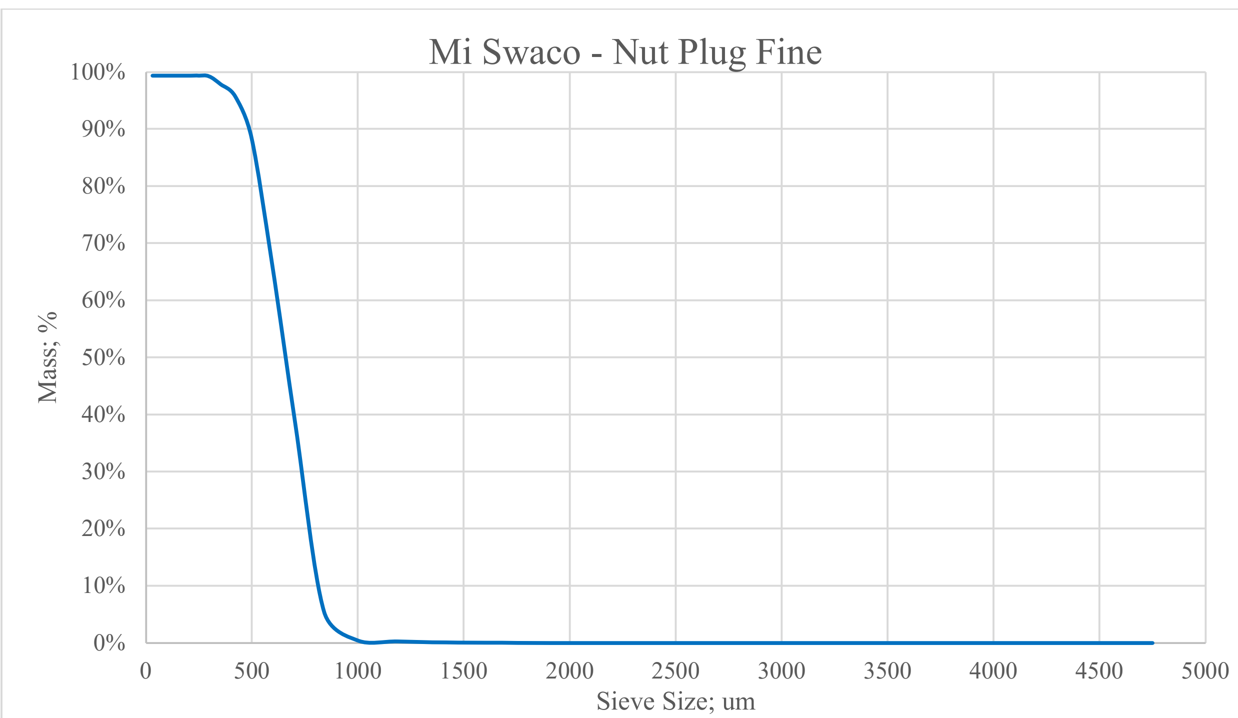

Figure C.88 Cumulative particle-size distribution determined by sieving Mi Swaco's Nut Plug Fine

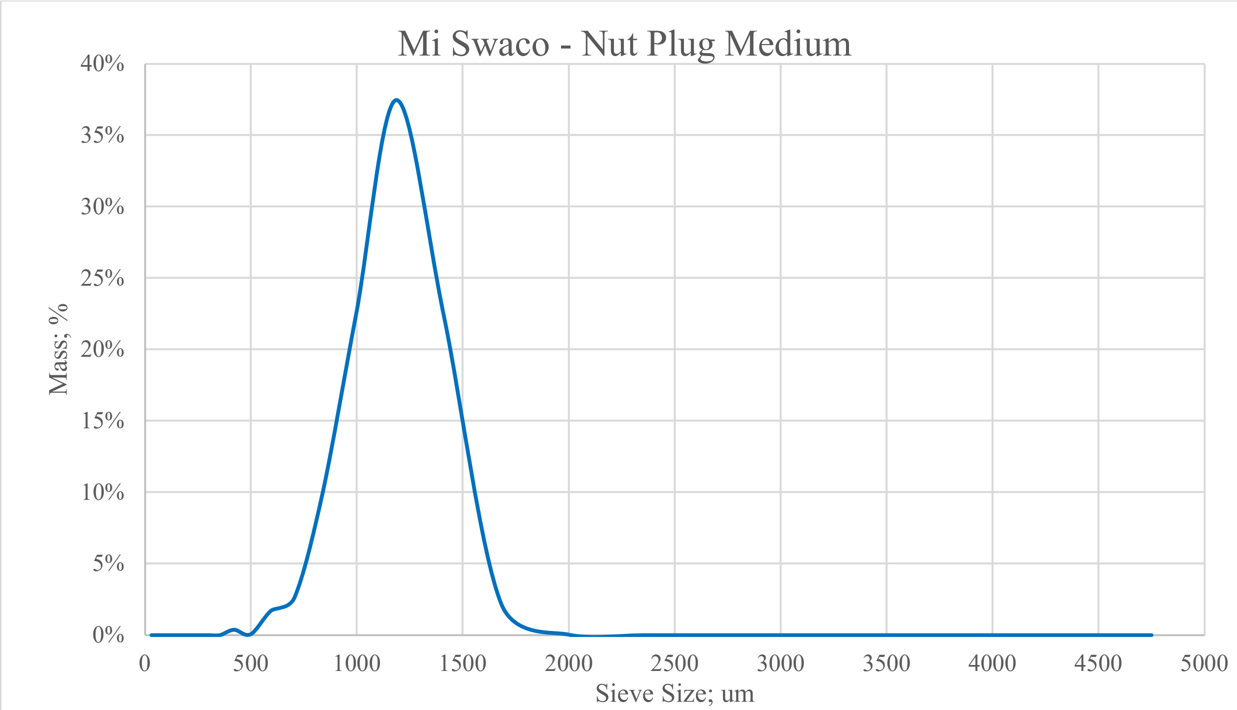

Figure C.89 Particle-size distribution determined by sieving Mi Swaco's Nut Plug Medium

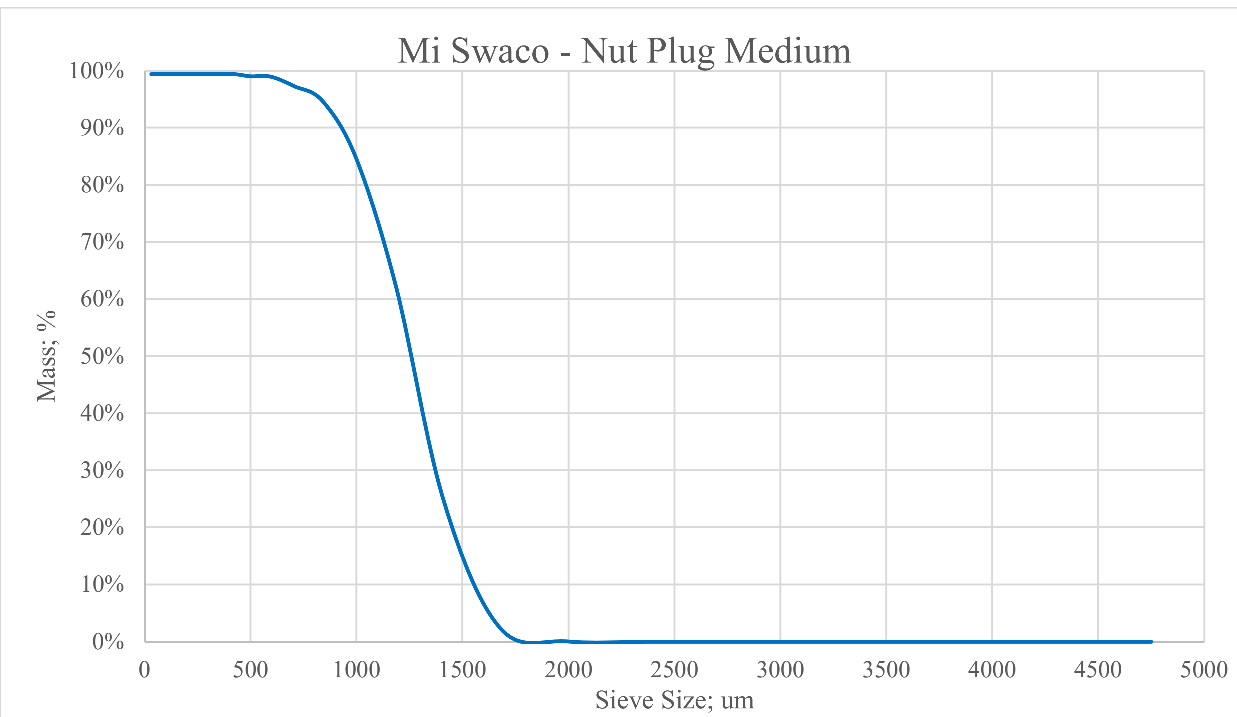

Figure C.90 Cumulative particle-size distribution determined by sieving Mi Swaco's Nut Plug Medium

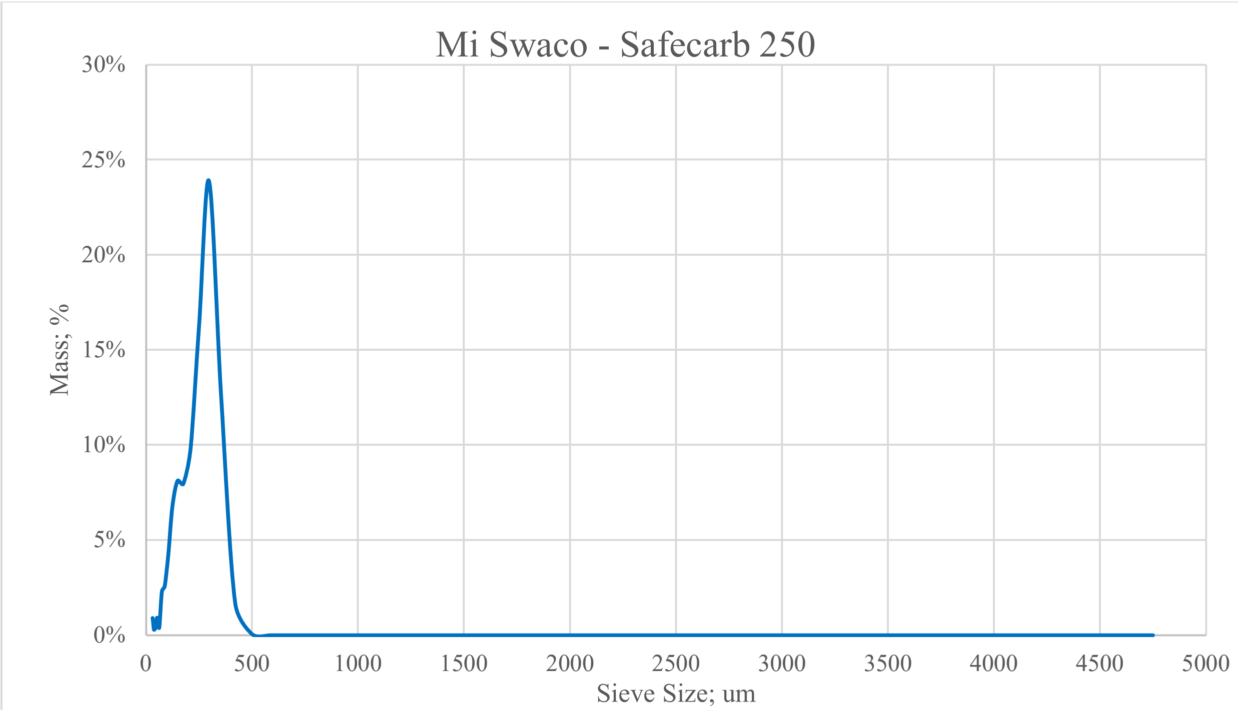

Figure C.91 Particle-size distribution determined by sieving Mi Swaco's Safecarb 250

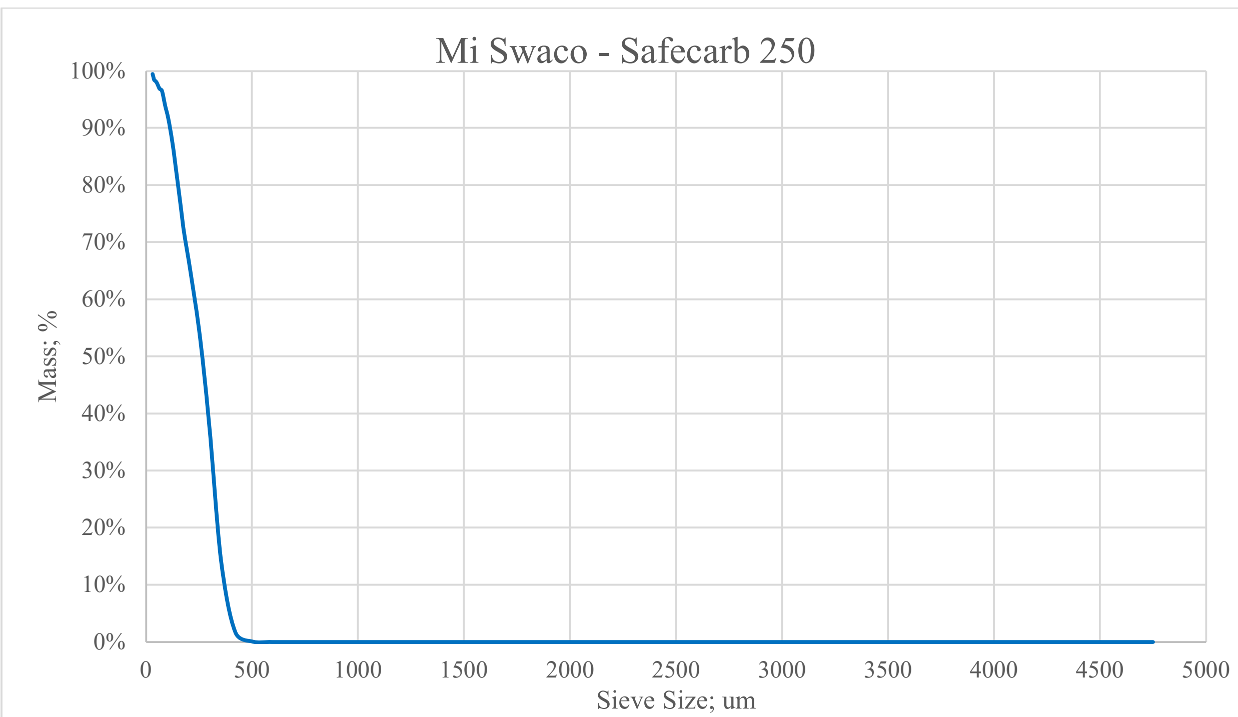

Figure C.92 Cumulative particle-size distribution determined by sieving Mi Swaco's Safecarb 250

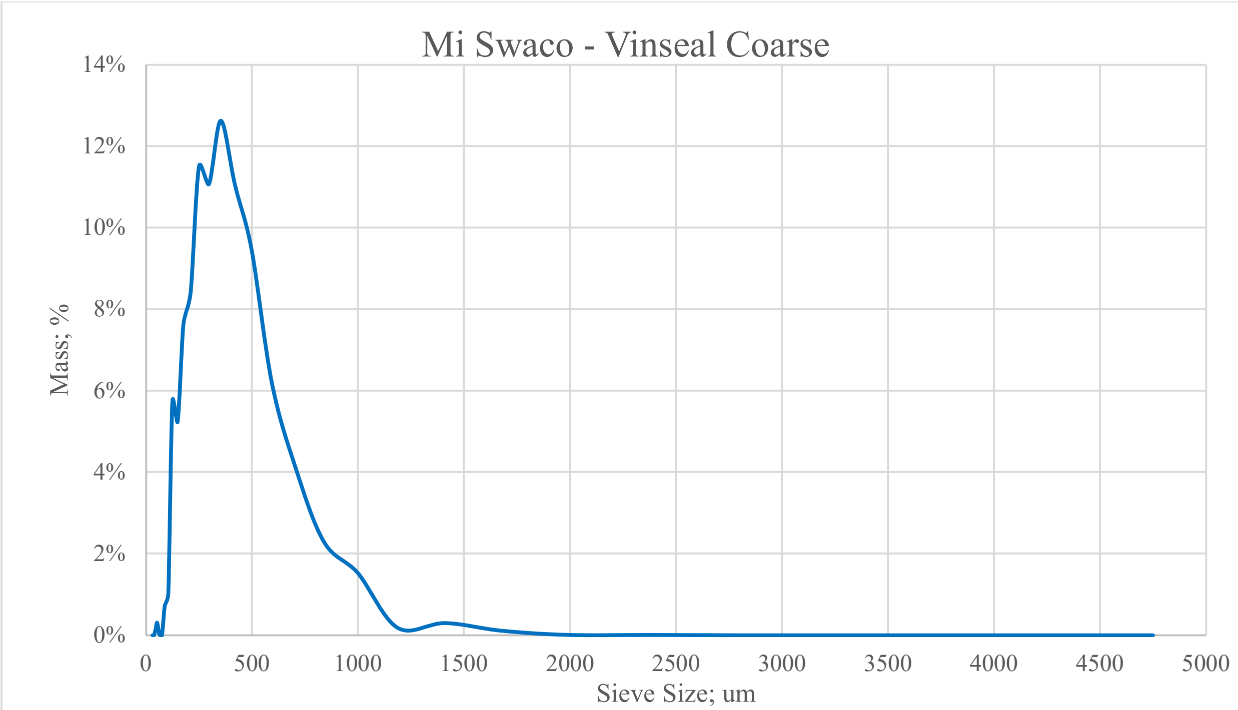

Figure C.93 Particle-size distribution determined by sieving Mi Swaco's Vinseal Coarse

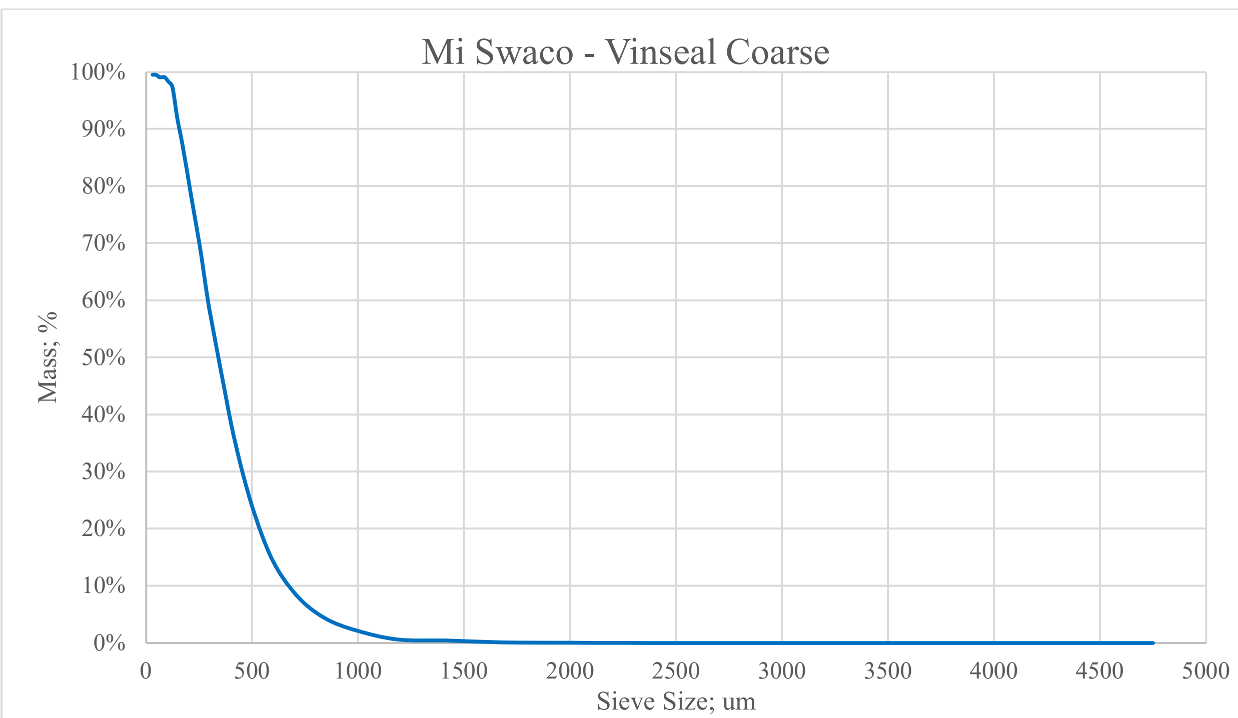

Figure C.94 Cumulative particle-size distribution determined by sieving Mi Swaco's Vinseal Coarse

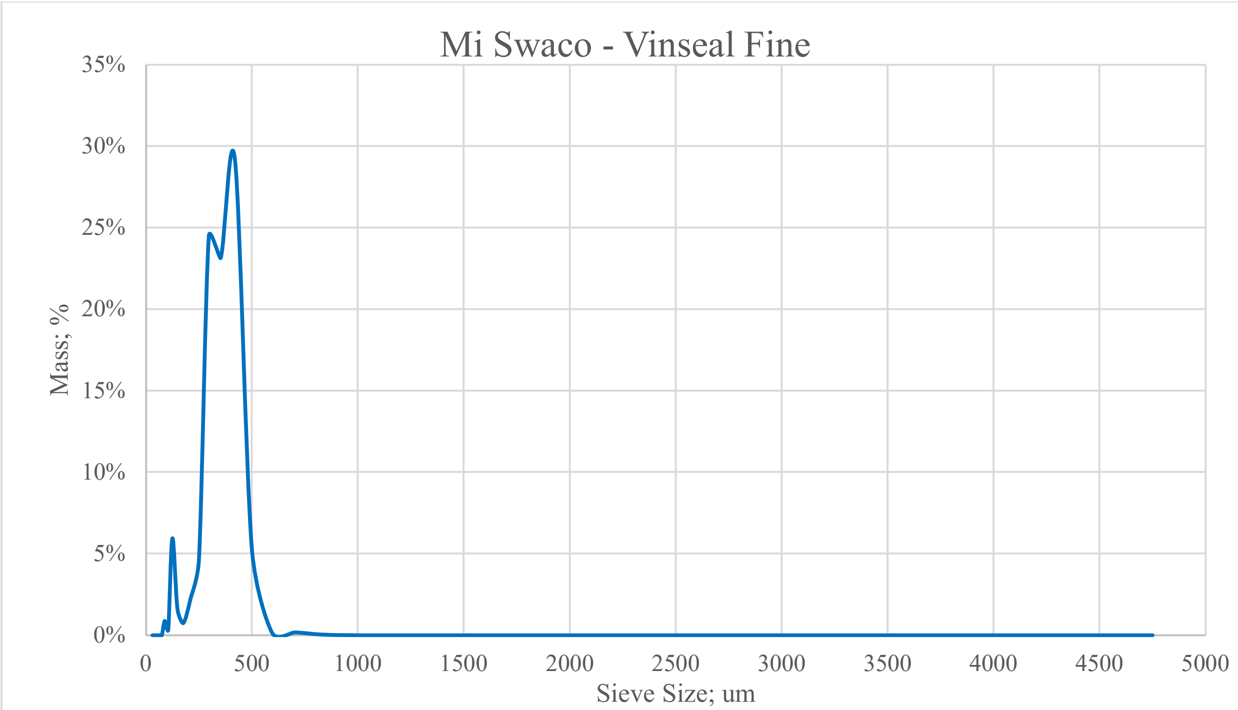

Figure C.95 Particle-size distribution determined by sieving Mi Swaco's Vinseal Fine

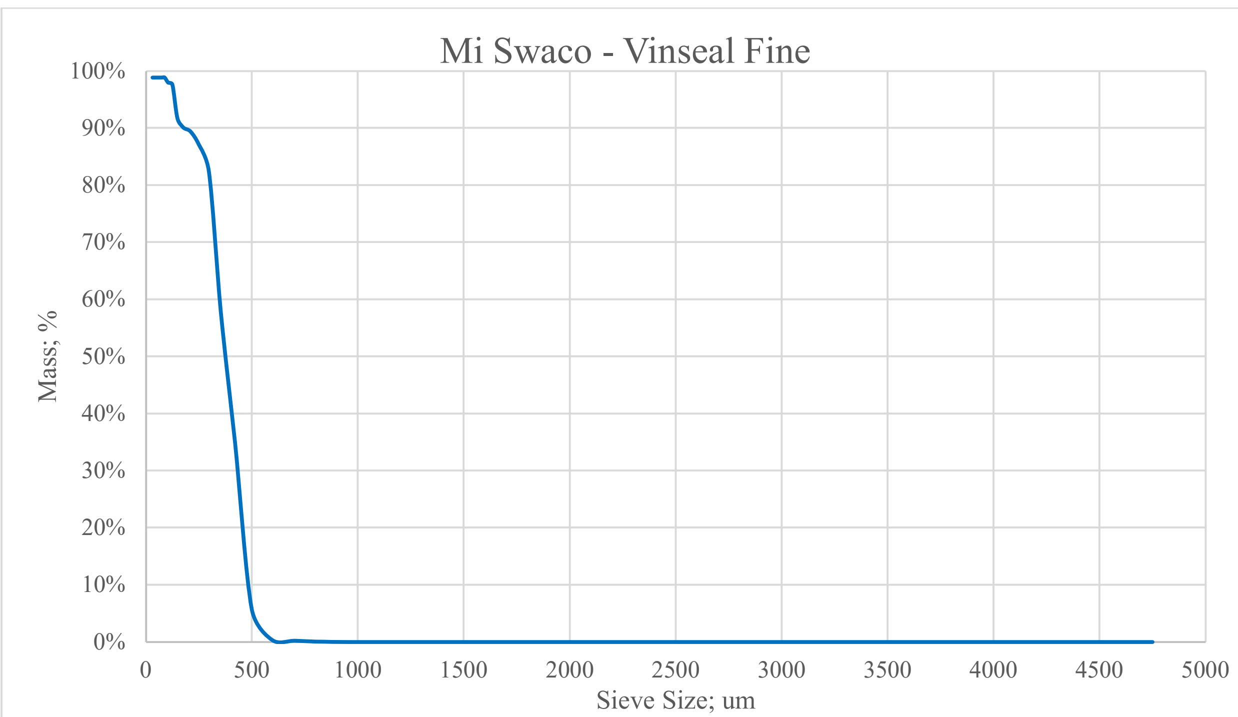

Figure C.96 Cumulative particle-size distribution determined by sieving Mi Swaco's Vinseal Fine

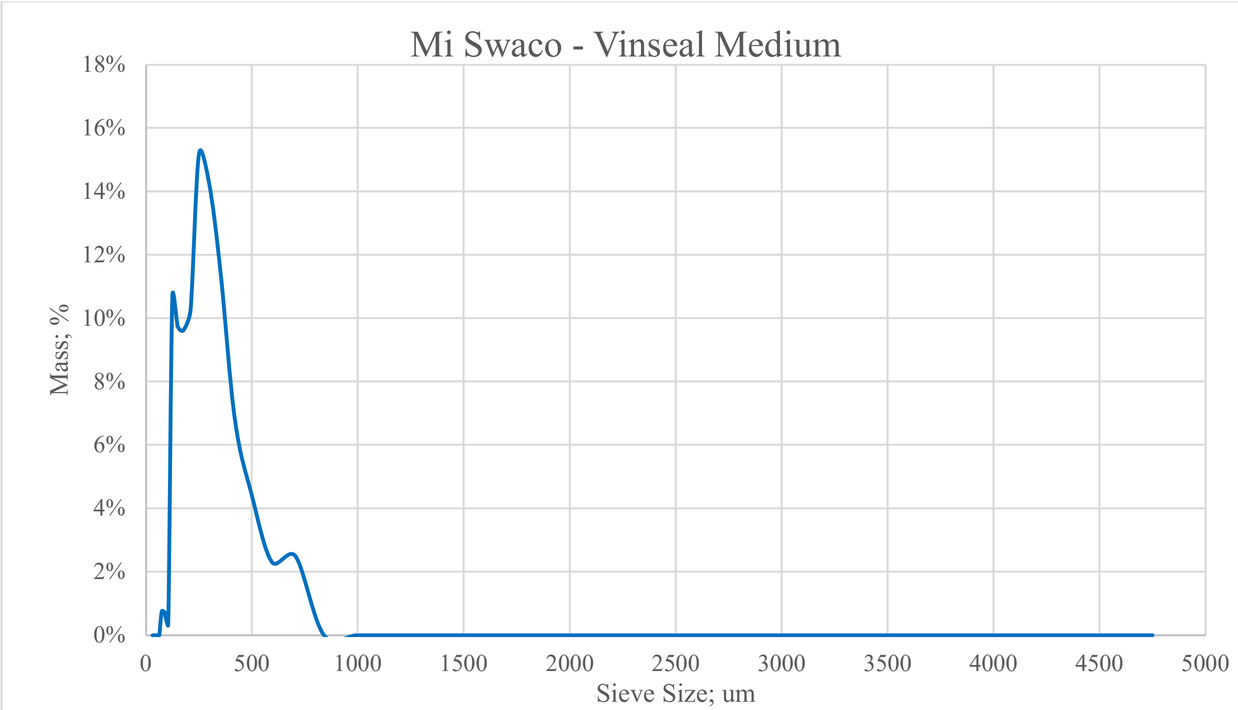

Figure C.97 Particle-size distribution determined by sieving Mi Swaco's Vinseal Medium

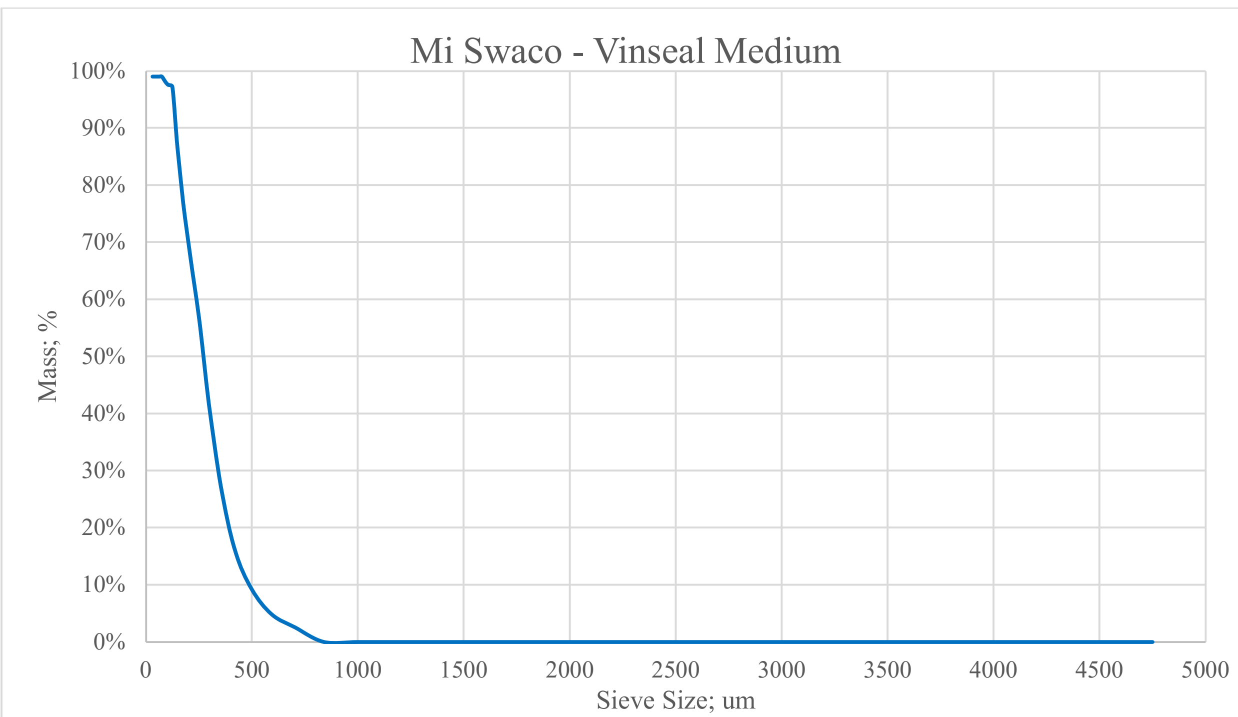

Figure C.98 Cumulative particle-size distribution determined by sieving Mi Swaco's Vinseal Medium

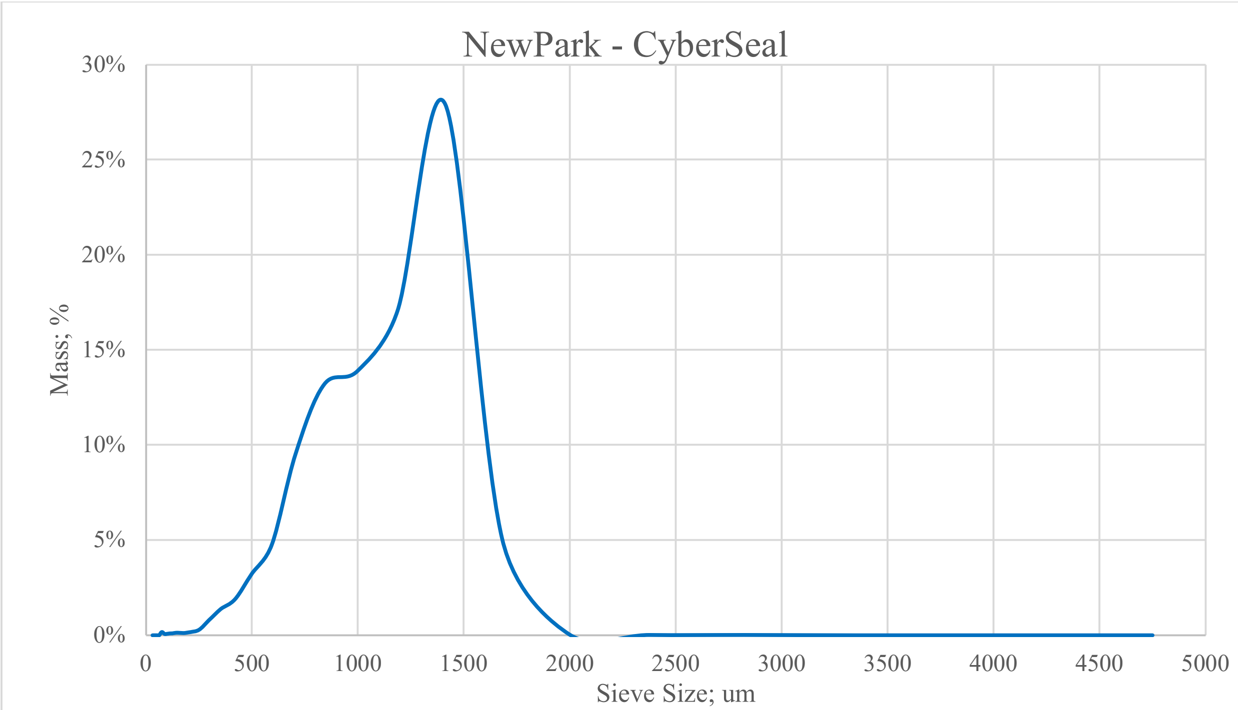

Figure C.99 Particle-size distribution determined by sieving NewPark's CyberSeal

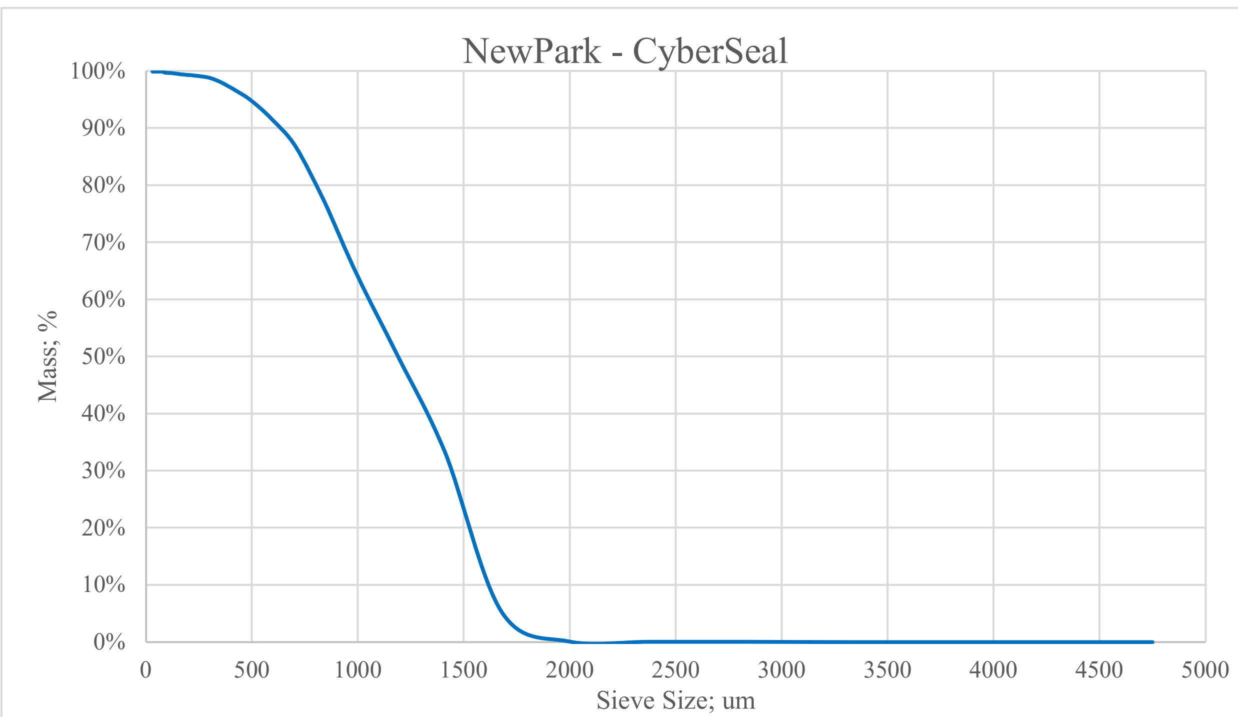

Figure C.100 Cumulative particle-size distribution determined by sieving NewPark's CyberSeal

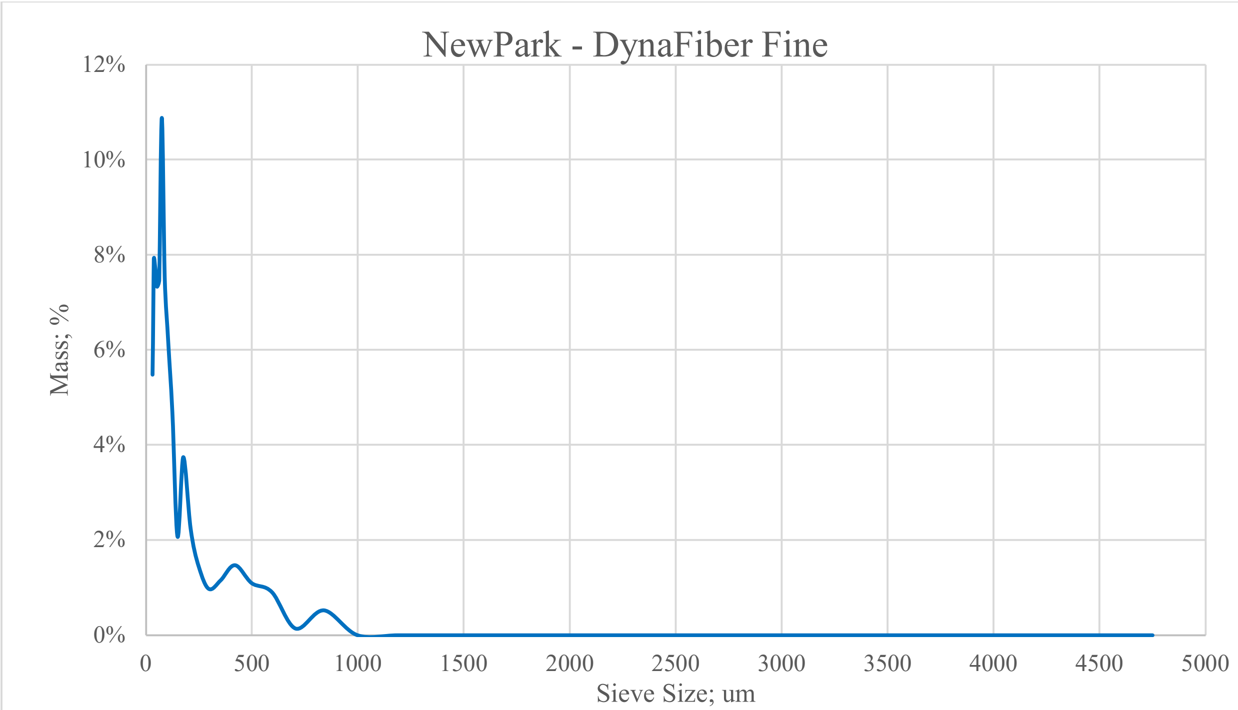

Figure C.101 Particle-size distribution determined by sieving NewPark's DynaFiber Fine

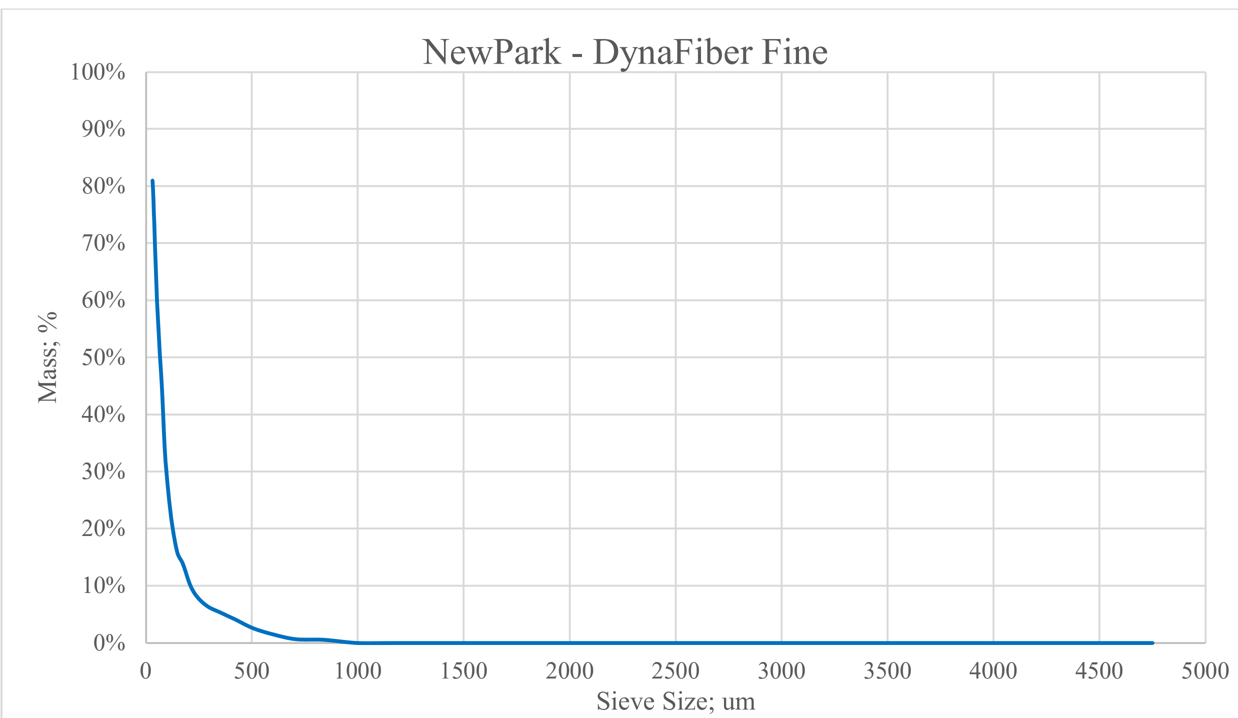

Figure C.102 Cumulative particle-size distribution determined by sieving NewPark's DynaFiber Fine

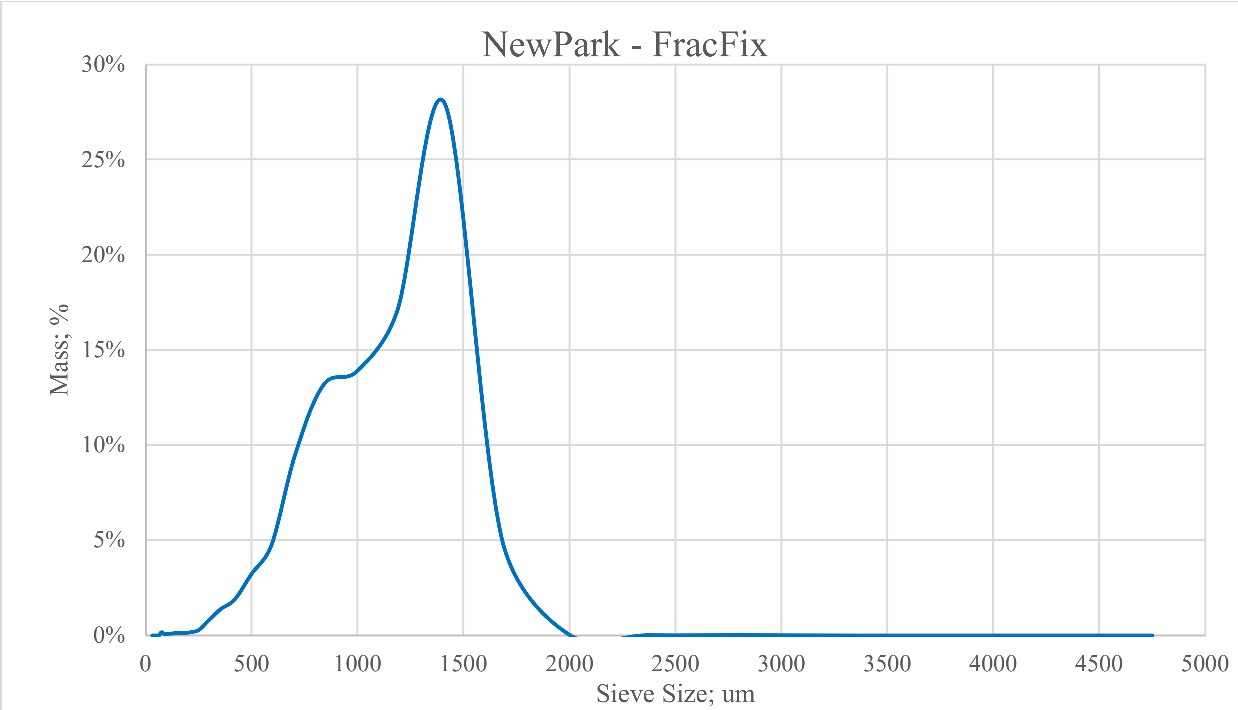

Figure C.103 Particle-size distribution determined by sieving NewPark's FracFix

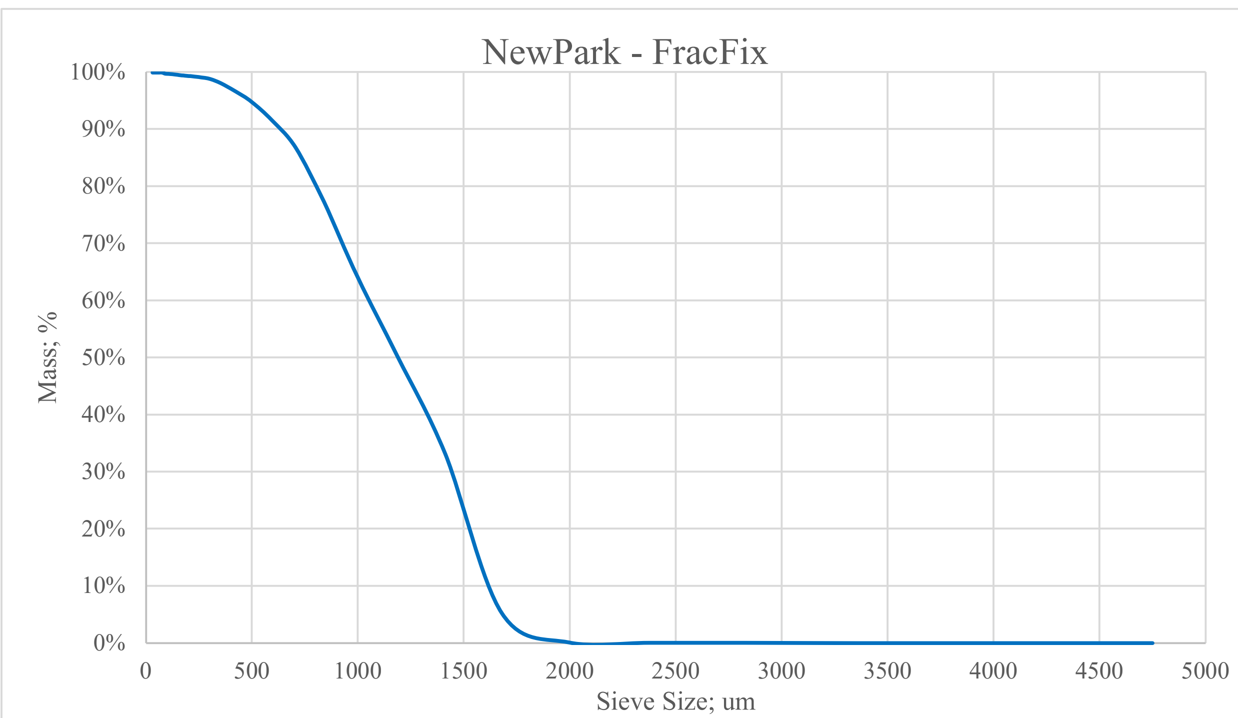

Figure C.104 Cumulative particle-size distribution determined by sieving NewPark's FracFix

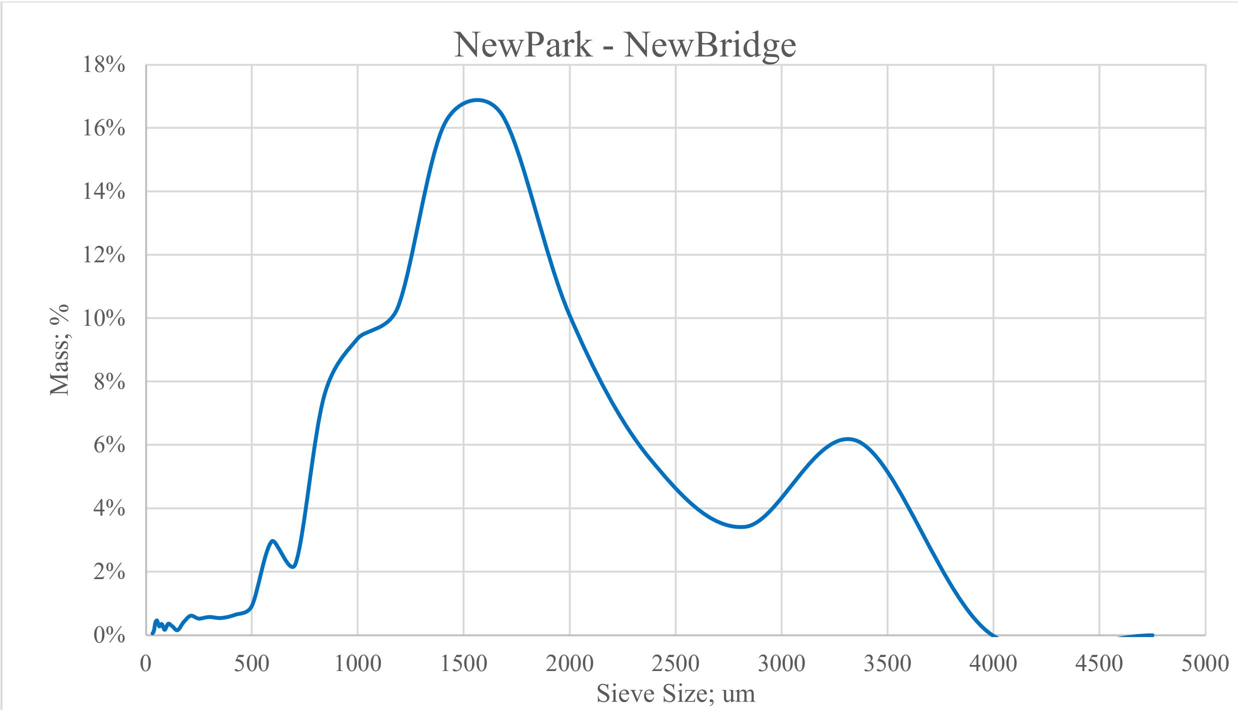

Figure C.105 Particle-size distribution determined by sieving NewPark's NewBridge

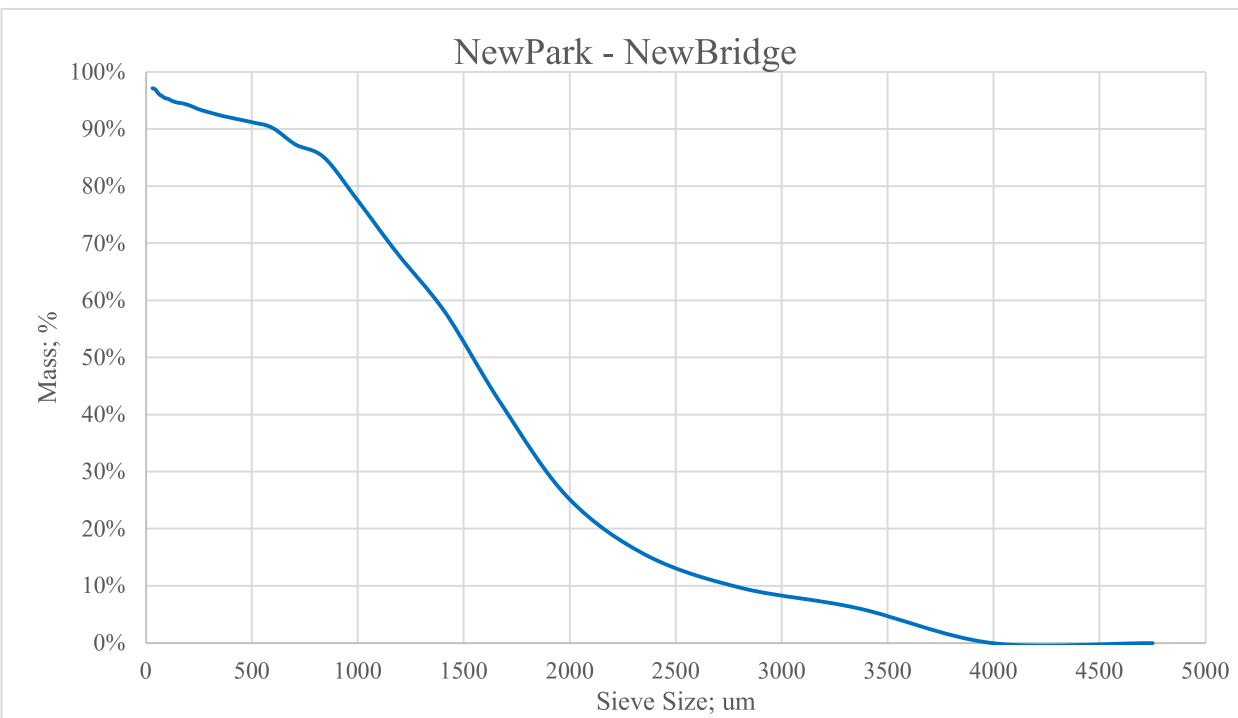

Figure C.106 Cumulative particle-size distribution determined by sieving NewPark's NewBridge

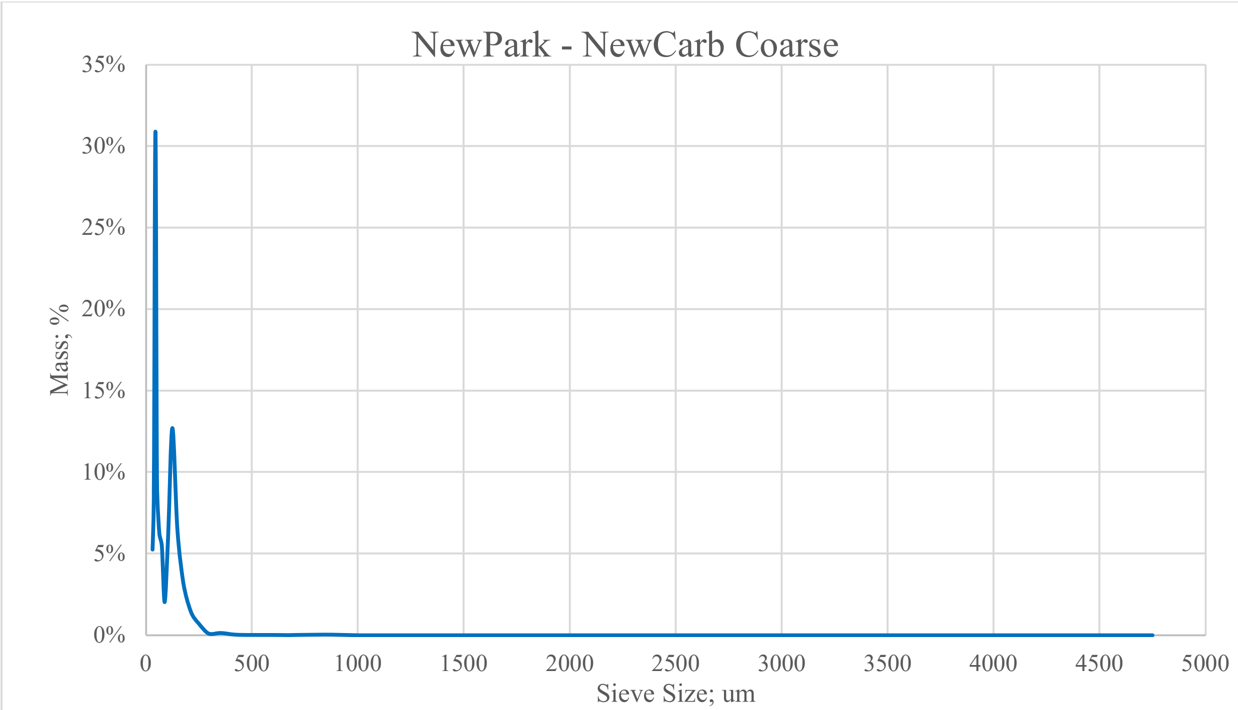

Figure C.107 Particle-size distribution determined by sieving NewPark's NewCarb Coarse

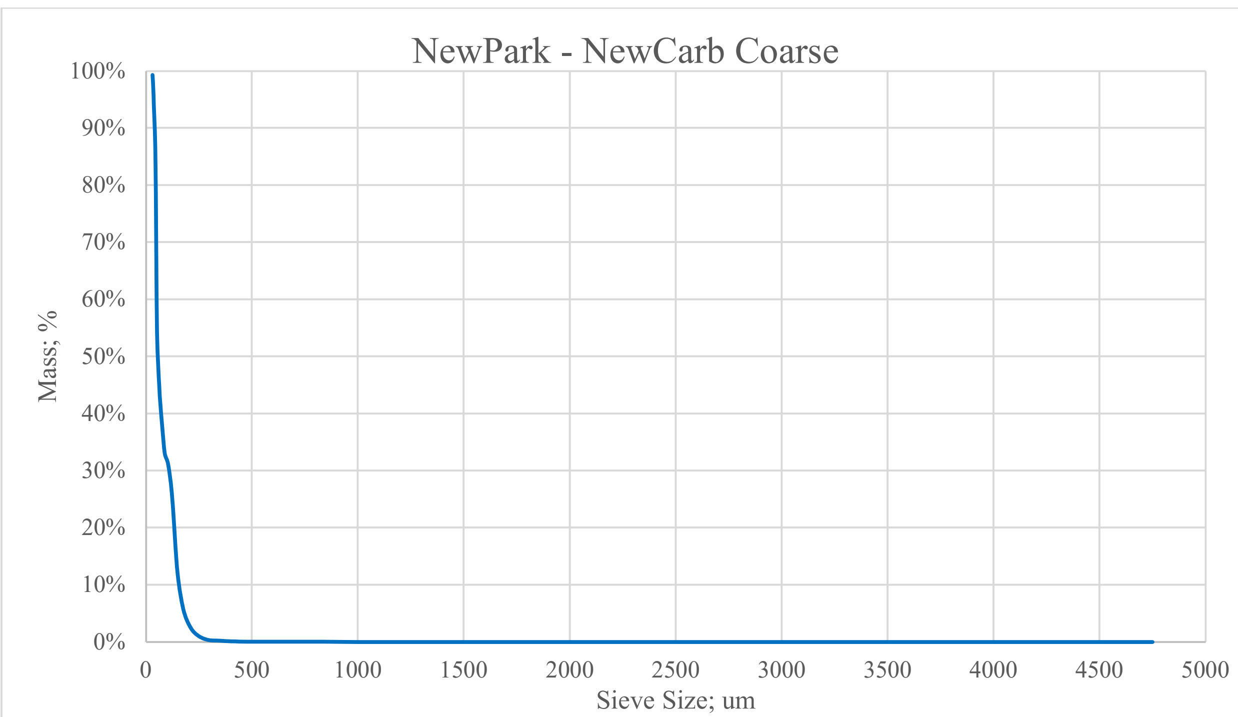

Figure C.108 Cumulative particle-size distribution determined by sieving NewPark's NewCarb Coarse

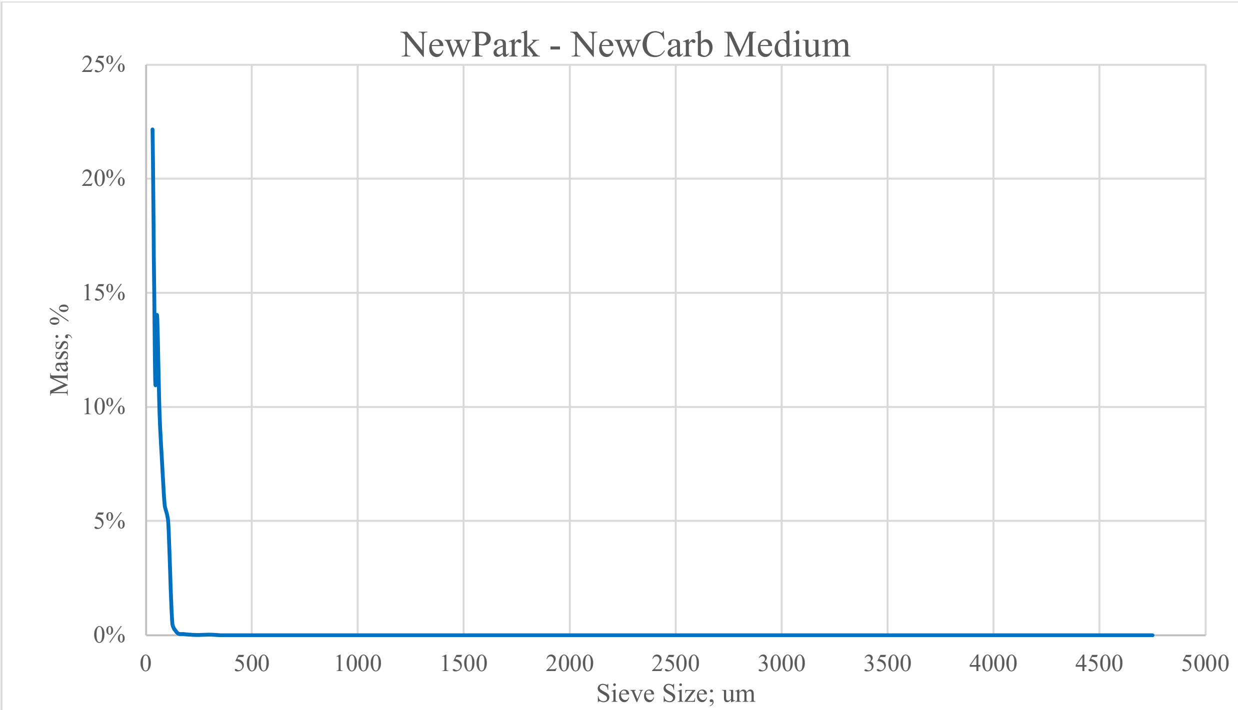

Figure C.109 Particle-size distribution determined by sieving NewPark's NewCarb Medium

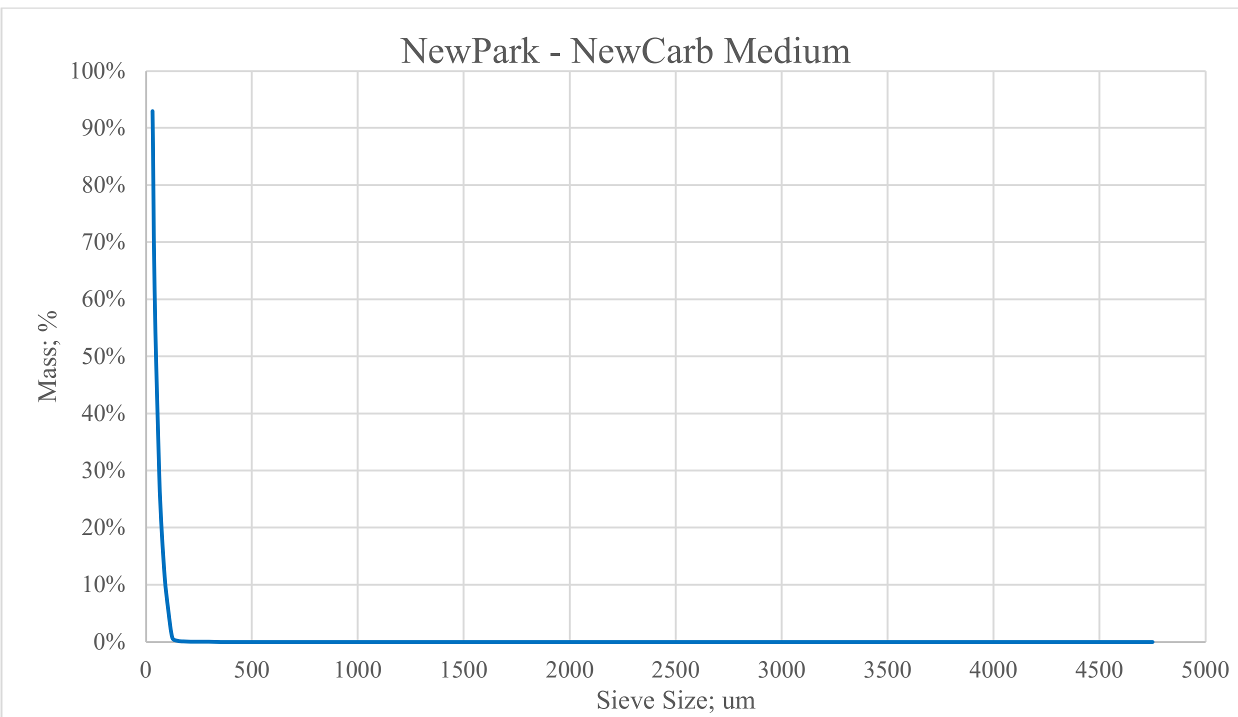

Figure C.110 Cumulative particle-size distribution determined by sieving NewPark's NewCarb Medium

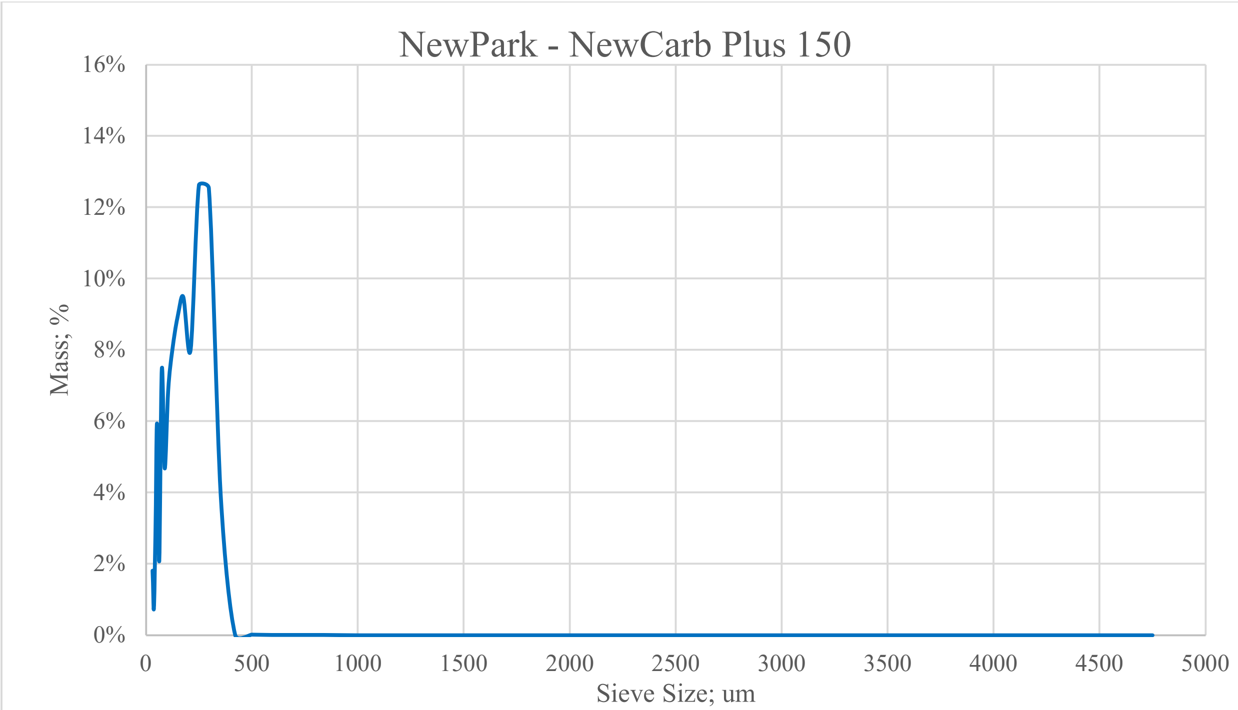

Figure C.111 Particle-size distribution determined by sieving NewPark's NewCarb Plus 150

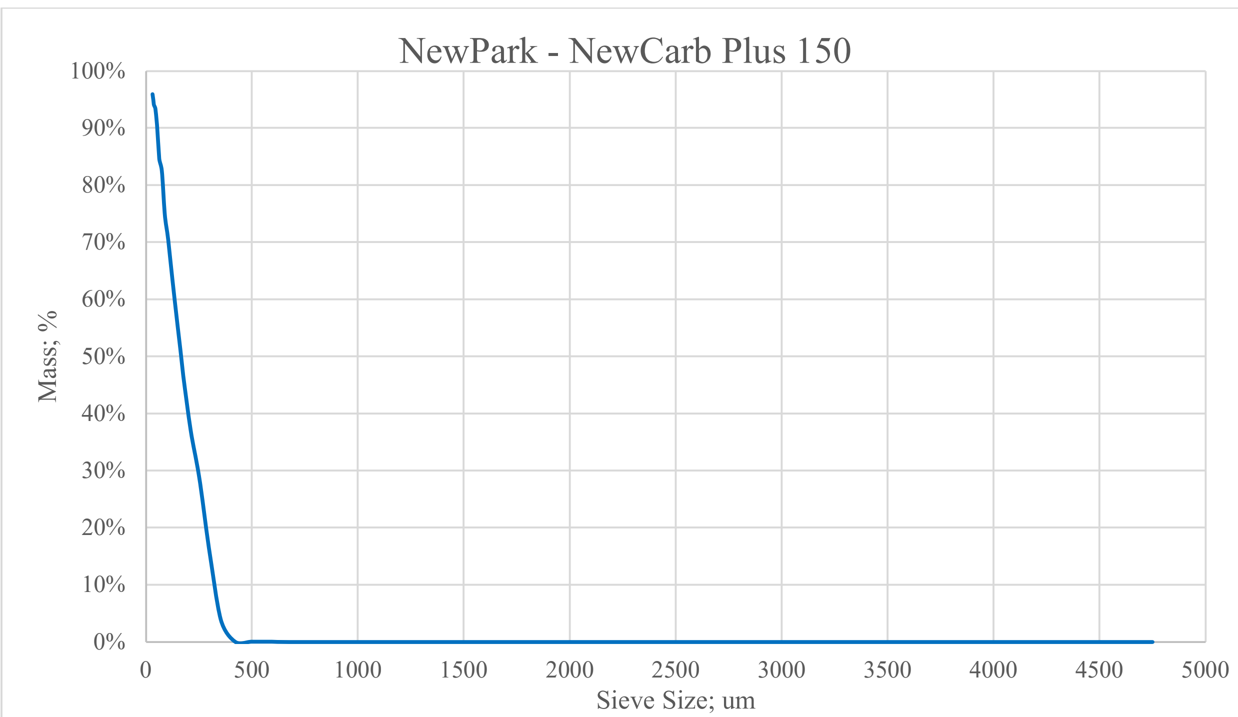

Figure C.112 Cumulative particle-size distribution determined by sieving NewPark's NewCarb Plus 150

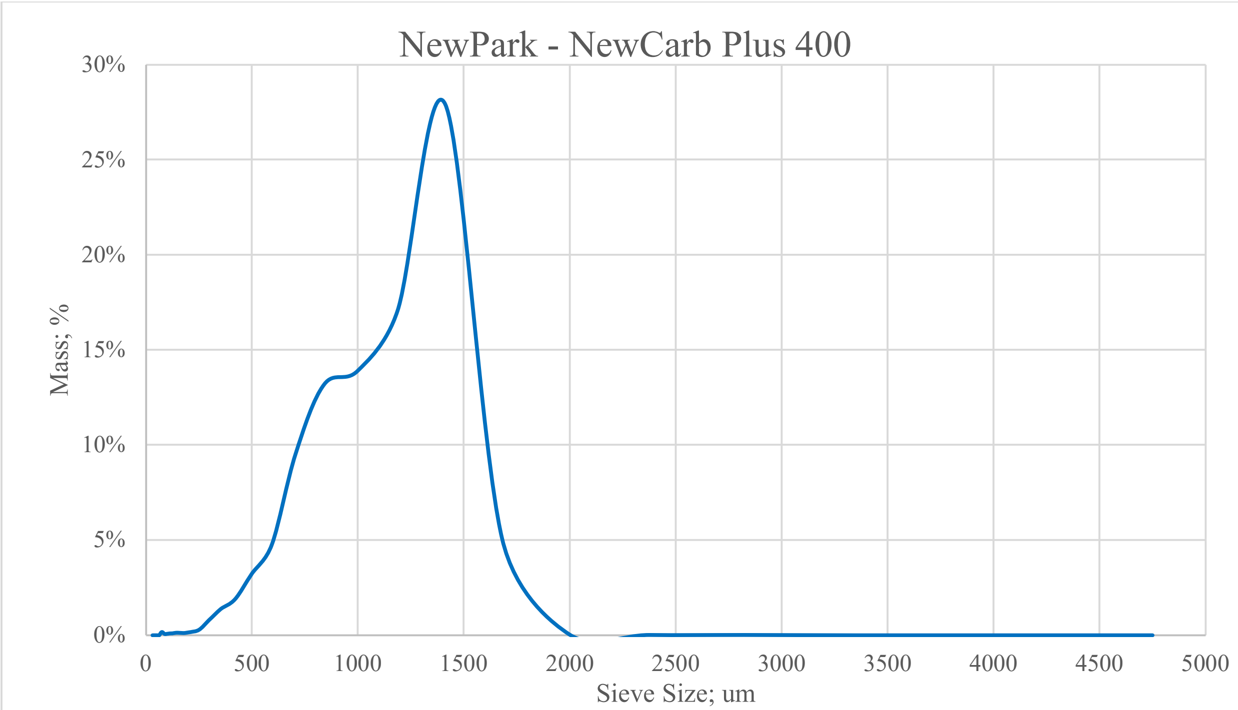

Figure C.113 Particle-size distribution determined by sieving NewPark's NewCarb Plus 400

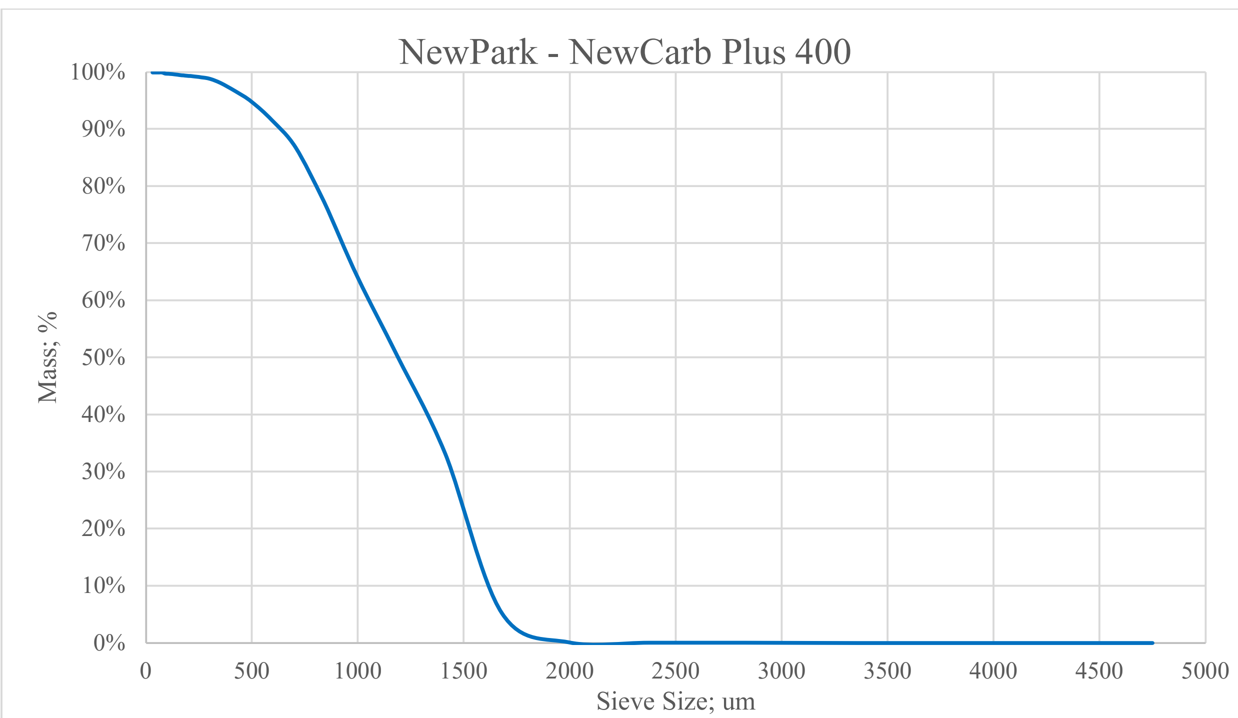

Figure C.114 Cumulative particle-size distribution determined by sieving NewPark's NewCarb Plus 400

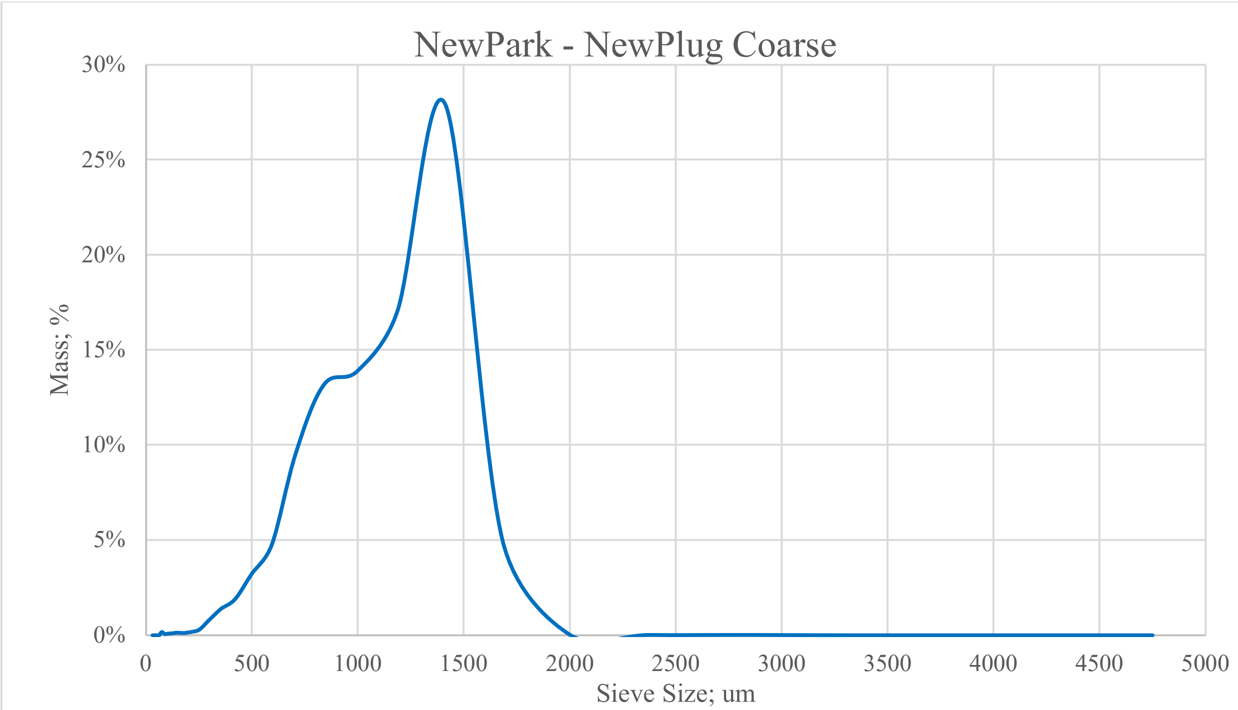

Figure C.115 Particle-size distribution determined by sieving NewPark's NewPlug Coarse

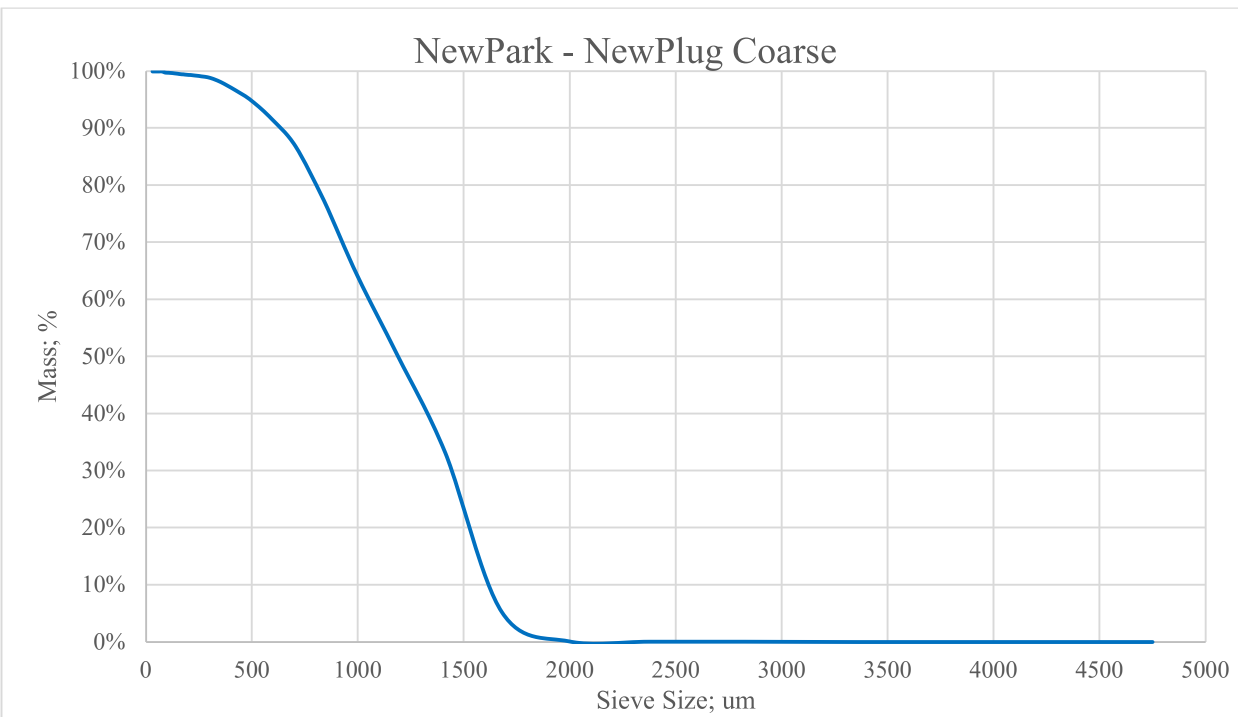

Figure C.116 Cumulative particle-size distribution determined by sieving NewPark's NewPlug Coarse

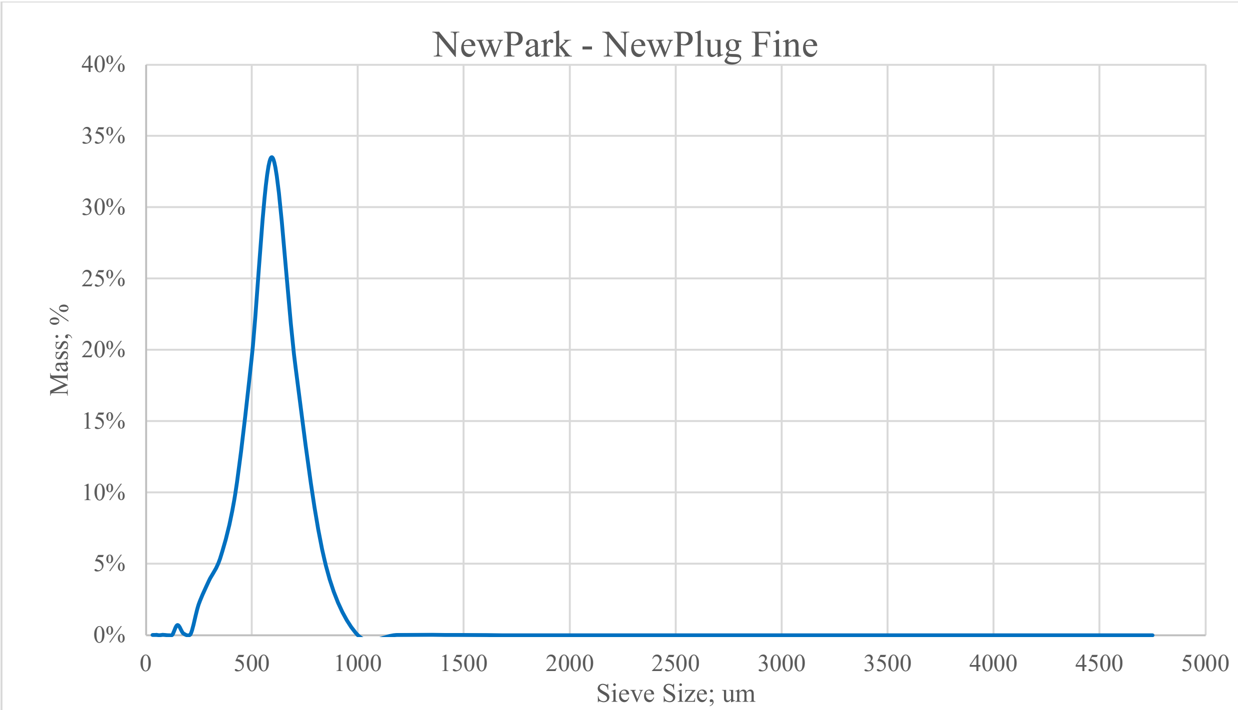

Figure C.117 Particle-size distribution determined by sieving NewPark's NewPlug Fine

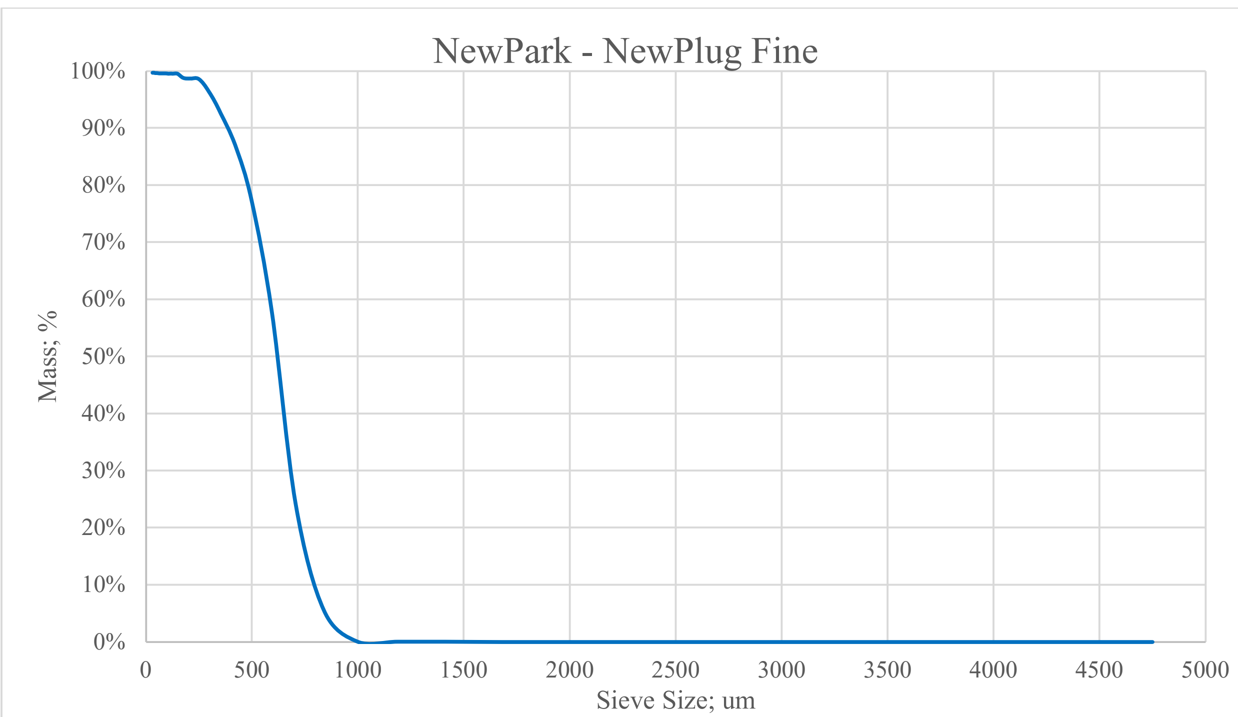

Figure C.118 Cumulative particle-size distribution determined by sieving NewPark's NewPlug Fine

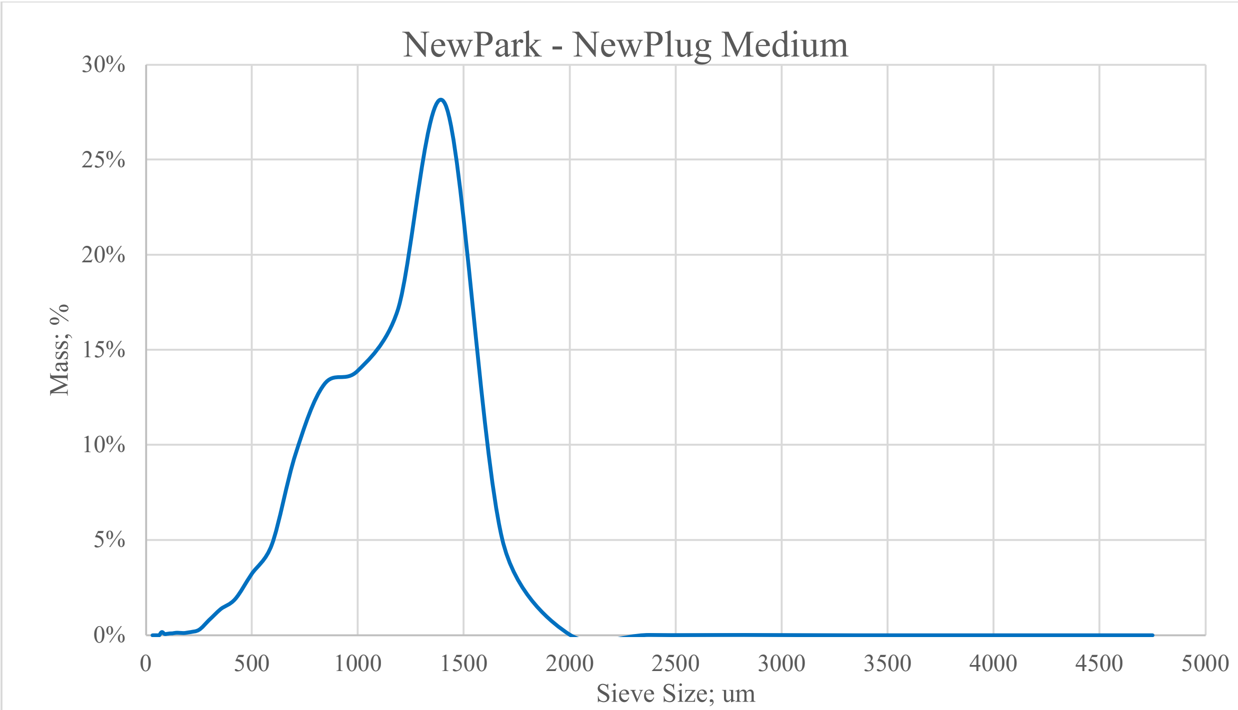

Figure C.119 Particle-size distribution determined by sieving NewPark's NewPlug Medium

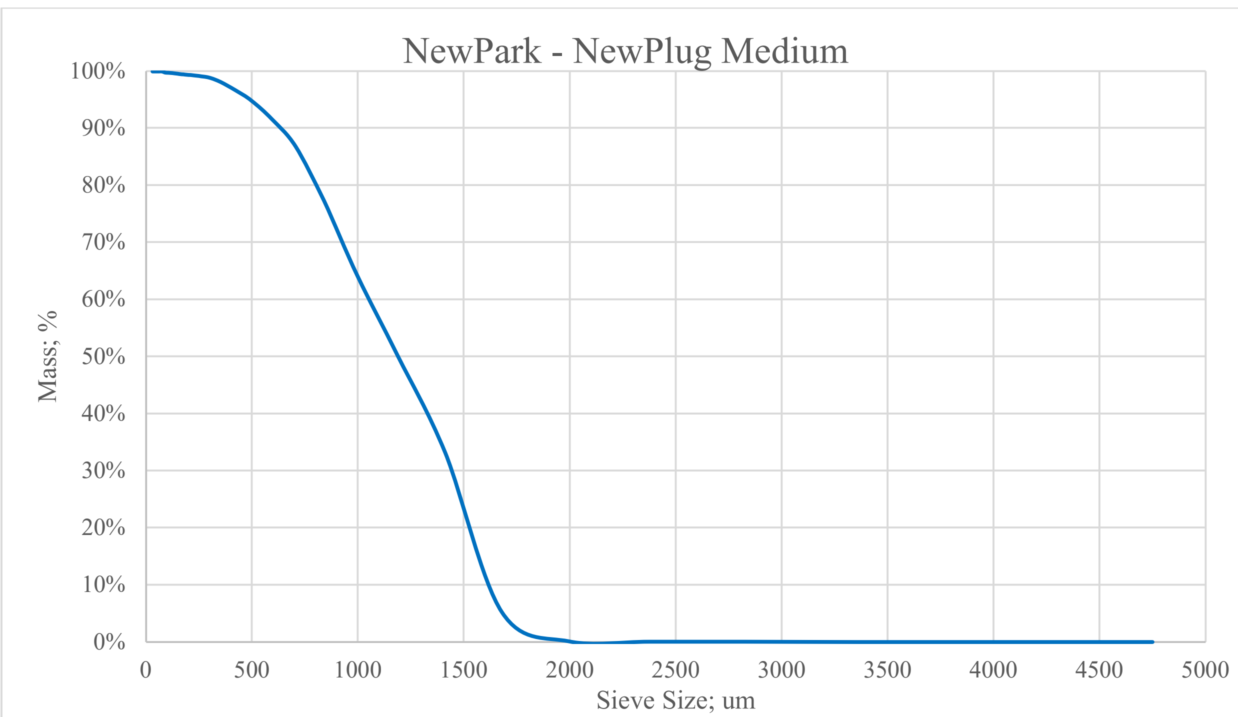

Figure C.120 Cumulative particle-size distribution determined by sieving NewPark's NewPlug Medium

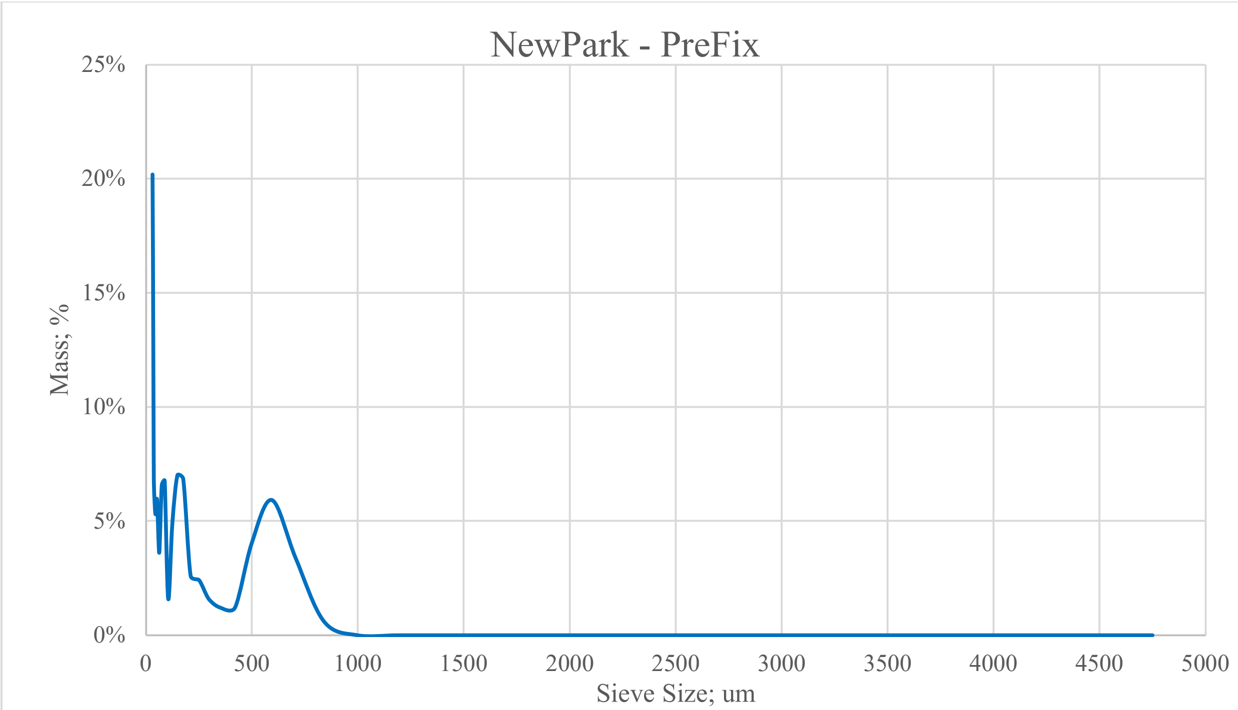

Figure C.121 Particle-size distribution determined by sieving NewPark's PreFix

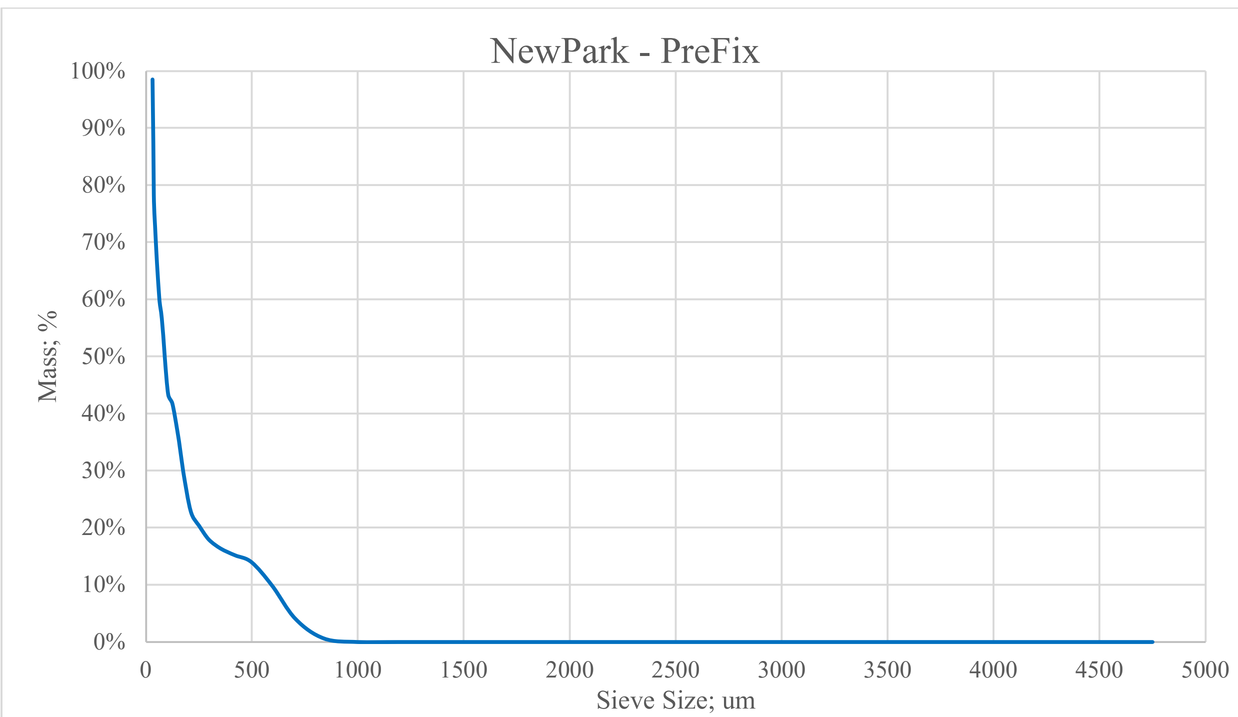

Figure C.122 Cumulative particle-size distribution determined by sieving NewPark's NewPlug PreFix

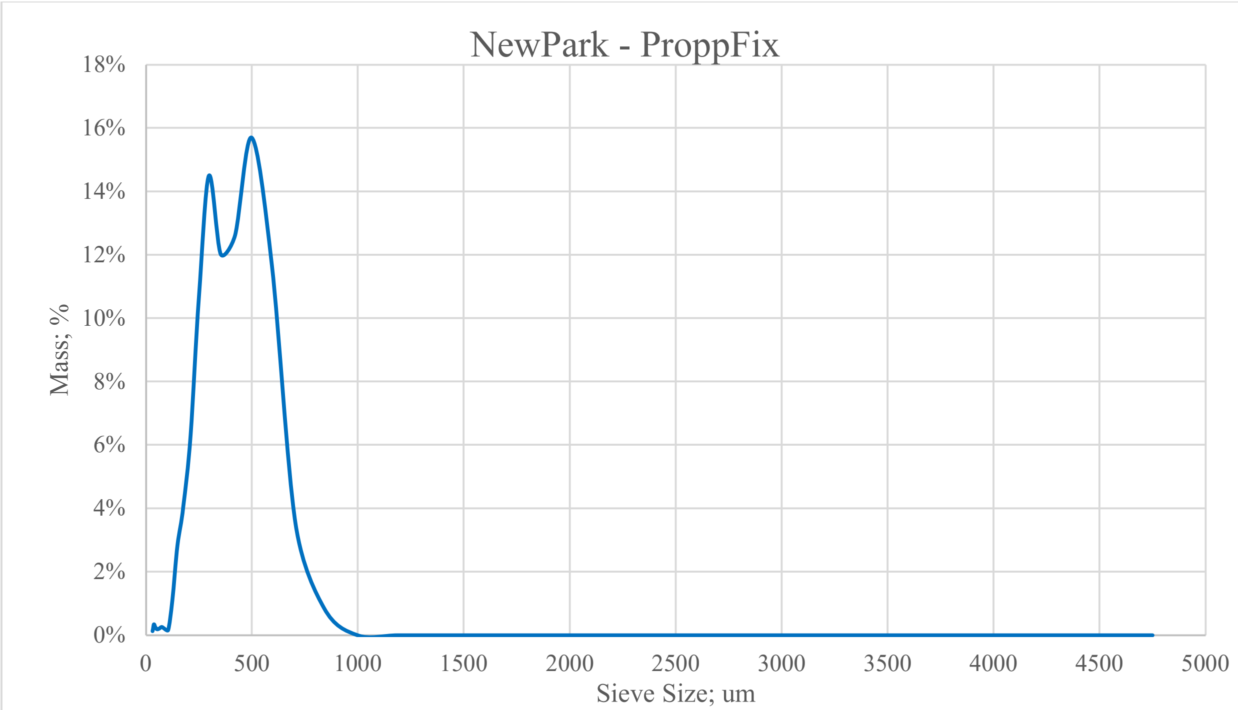

Figure C.123 Particle-size distribution determined by sieving NewPark's ProppFix

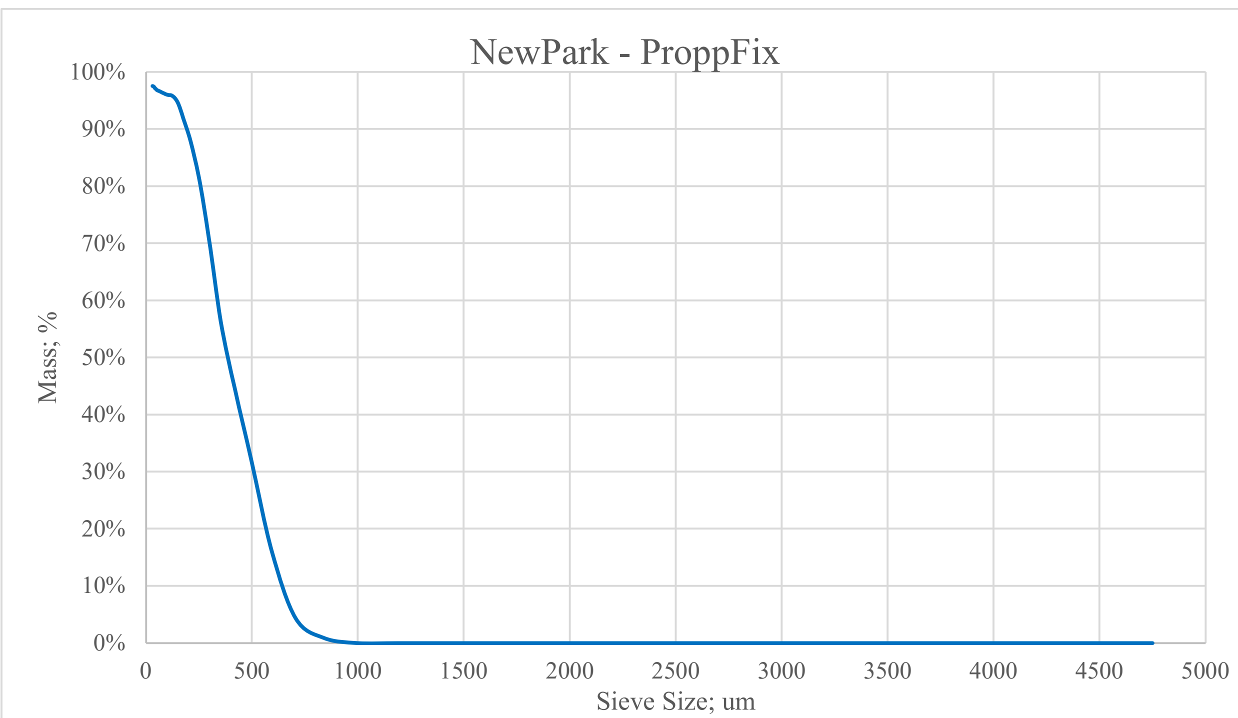

Figure C.124 Cumulative particle-size distribution determined by sieving NewPark's ProppFix

APPENDIX D

SUPPLEMENTAL FILES

The following supplemental files contain material shape, size and lab testing data sets.

D.1 Particle Shape Data

The full dataset referenced in Chapter 3; 4 & 5 can be found in Supplemental File LCM Shape Data.xlsx.

D.2 LCM Testing Data

The full dataset referenced in Chapter 3; 4 & 5 can be found in Supplemental File LCM Test Data.xlsx.